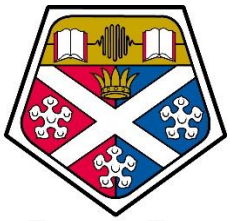

Low-cost Portable Microscopy Systems for Biomedical Imaging and Healthcare Applications

Thesis submitted by

Ziao Jiao

Department of Biomedical Engineering

Strathclyde Institute of Pharmacy & Biomedical Sciences

University of Strathclyde

This thesis is submitted for the degree of Doctor of Philosophy in Biomedical Engineering.

Declaration of Work

This thesis is the result of the author's original research. It has been composed by the author and has not been previously submitted for examination, which has led to the award of a degree.

Signed: Ziao Jiao

Date: November 23, 2023

Abstract

In recent years, the development of low-cost portable microscopes (LPMs) has opened new possibilities for disease detection and biomedical research, especially in resource-limited areas. Despite these advancements, the majority of existing LPMs are hampered by sophisticated optical and mechanical designs, require extensive post-data analysis, and are often tailored for specific biomedical applications, limiting their broader utility. Furthermore, creating an optical-sectioning microscope that is both compact and cost-effective presents a significant challenge. Addressing these critical gaps, this PhD study aims to: (1) develop a universally applicable LPM featuring a simplified mechanical and optical design for real-time biomedical imaging analysis, and (2) design a novel, smartphone-based optical sectioning microscope that is both compact and affordable. These objectives are driven by the need to enhance accessibility to quality diagnostic tools in varied settings, promising a significant leap forward in the democratization of biomedical imaging technologies.

With 3D printing, optimised optical design, and AI techniques, we can develop LPM's real-time analysis functionality. I conducted a literature review on LPMs and related applications in my study and implemented **two** low-cost prototype microscopes and one theoretical study. 1) The first project is a portable AI fluorescence microscope based on a webcam and the NVIDIA Jetson Nano (NJN) with real-time analysis functionality. The system was 3D printed, weighing ~250 grams with a size of 145mm × 172 mm × 144 mm (L×W×H) and costing ~$400. It achieves a physical magnification of ×5 and can resolve 228.1 lp/mm USAF features. The system can recognise and count fluorescent beads and human red blood cells (RBCs). 2) I developed a smartphone-based optical sectioning microscope using the HiLo technique. To our knowledge, it is the first smartphone-based HiLo microscope that offers low-cost optical-sectioned widefield imaging. It has a 571.5 μm telecentric scanning range and an 11.7 μm axial

resolution. I successfully used it to realize optical sectioning imaging of fluorescent beads. For this system, I developed a new low-cost HiLo microscopy technique using microlens arrays (MLAs) with incoherent light-emitting diode (LED) light sources. I conducted a numerical simulation study assessing the integration of uncoherent LEDs and MLAs for a low-cost HiLo system. The MLA can generate structured illumination in HiLo. How the MLA's geometry structure and physical parameters affect the image performance were discussed in detail.

This PhD thesis explores the advancement of low-cost portable microscopes (LPMs) through the integration of 3D printing, optimized optical design, and artificial intelligence (AI) techniques to enhance their real-time analysis capabilities. The research involved a comprehensive literature review on LPMs and their applications, leading to the development of two innovative prototype LPMs, alongside a theoretical study. These works contribute significantly to the field by not only addressing the technical and financial barriers associated with advanced microscopy but also by laying the groundwork for future innovations in portable and accessible biomedical imaging. Through its focus on simplification, affordability, and practicality, the research holds promise for substantially expanding the reach and impact of diagnostic imaging technologies, especially in those resource-limited areas.

Acknowledgments

I want to thank everyone who helped during my PhD career. Being a PhD is a challenging and long journey. I could only accomplish this project with their support over the past four years.

I want to thank my supervisor, Dr David Li, for his invaluable guidance, unwavering support, and mentorship. His expertise, patience, and encouragement have been instrumental in shaping the course of my research. He always encourages me with positive words and inspiration. He is also one of the few with whom I can have philosophical discussions. Also, I would like to thank the University of Strathclyde for providing funding, experimental resources, and a great platform to network with other researchers worldwide.

I want to thank my second supervisor, Dr Yu Chen. Without her support in terms of experimental equipment and facilities, I would not have been able to complete my work during my PhD.

Also, my heartfelt thanks go to my parents for their unconditional and selfless love, support, and understanding throughout this demanding journey. Your belief in me and financial and mental support motivated me to complete my studies.

Finally, I extend my appreciation to Dr Zhenya Zang. He is an innovative and talented researcher. Without his support, I could not finish my project smoothly. Also, I would like to thank my colleagues Yu Wang, Quan Wang, Dong Xiao, Wujun Xie, Mingliang Pan, Xi Chen, and Xinda Li for their support in academics and life.

Contents

List of Figures

List of Tables

Abbreviations

AI	Artificial intelligence
ANN	Artificial neural network
Avg	Average value
BF	Brightfield
BFP	Back focal plane
BPF	Band pass filter
BPP	Back pupil plane
CAD	Computer-aided Design
CLSM	Confocal laser scanning microscopy
CMOS	Complementary metal-oxide semiconductor
CNN	Convolution neural network
CPU	Center processing unit
CTF	Coherent transfer function
DC	Direct current
DF	Darkfield
DH	Digital holography
DL	Deep learning
DM	Dichromatic mirror
DMD	Digital mirror device
EM	Emission filter
ETL	Electrically tunable lens
EX	Excitation filter
FFP	Front focal plane
FISTA	Fast iterative shrinkage-thresholding algorithm
FOP	Fiber optical plate

FOV	Field-of-view
FP	Fourier ptychography
FWHM	Full width half maximum
GFP	Green fluorescent protein
GPU	Graphics processing unit
GRIN	Gradient-index
GS	Gerchberg-Saxton
GT	Ground truth
HPF	High-pass filter
IHC	In-focus high-frequency components
ILC	In-focus low-frequency components
IoT	Internet of Things
IoU	Intersection of Union
ISM	Image Scanning microscopy
LD	Laser diode
LDHM	Lensless digital holography microscopy
LED	Light-emitting diode
LOC	Lab-on-a-chip
LPF	Low-pass filter
LPM	Low-cost portable microscope
LS	Lightsheet
LSCM	Line scanning confocal microscopy
LSM	Light sheet microscopy
MAM	Modular-array fluorescence microscopy
MD	Modulation depth
MLA	Microlens array
MLM	Make-modulated microscopy

MTF	Modulation transfer function
NA	Numerical aperture
NAT	Nucleic acid testing
NJN	NVIDIA Jetson Nano
OAG	Optical absorption gap
OI	Oblique illumination
OL	Objective lens
OLED	Organic light-emitting diode
OS	Optical-sectioning
OTF	Optical transfer function
PAIM (πM)	Portable AI-enhanced fluorescence microscope
PC	Phase contrast
PDMS	Polydimethylsiloxane
PMMA	Polymethyl methacrylate
POCT	Point-of-Care Testing
PS	Polystyrene
PSF	Point spread function
RBC	Red blood cell
RI	Rheinberg illumination
RPCA	Robust principle component analysis
SBP	Space-bandwidth product
SCD	Sickle cell disease
SI	Structured illumination
SIM	Structured illumination microscopy
SLM	Spatial light modulator
SNR	Signal-to-noise ratio
SOC	System-on-chip

SOS	Smartphone-based Optical Sectioning
SR	Super-resolution
Std	Standard deviation
TIE	Transport of intensity equation
TIR	Total internal reflection
TL	Tube lens
TPEM	Two-photon excitation microscopy
TPFM	Two-photon fluorescence miroscopy
WBC	White blood cell
WFM	Widefield fluorescence microscopy
WHO	World health organization
WSI	Whole-slide imaging

Chapter 1. Introduction

The research aims and background will be introduced in this chapter. Section 1.1 will discuss the motivation and background. Following this, in Section 1.2, the first research work will be introduced, which is a portable AI-enhanced fluorescence microscope. Section 1.3 will introduce a smartphone-based optical sectioning microscope, while theoretical research aimed at reducing the cost of this smartphone-based optical sectioning microscope will be presented in Section 1.4. Additionally, Section 1.5 will outline the research aims and contributions of this work. Finally, the thesis will be outlined in Section 1.6.

1.1 Motivation and Background

Microscopical imaging is an intuitive way to observe microbiological activities and diagnose diseases. After acquiring images or videos of micro-scale objects, we can analyse their morphology, light intensities, or fluorescent signals to diagnose diseases. For example, we can diagnose sickle cell disease by observing red blood smear samples [1] and cancer cells using immunofluorescence stains and fluorescence microscopes [2]. However, commercial benchtop microscopes are bulky and expensive, and equipping benchtop microscopes can be challenging in underdeveloped or resource-limited areas.

In response to these limitations, the development of LPMs emerges as an appropriate solution. These devices, engineered for compactness, cost savings, and affordability, extend their application scenarios. LPMs can significantly facilitate disease detection and biomedical research in resource-limited areas. For the past decade, we have witnessed the fast development of miniaturized sensors, optical components, electronics, and data processing units. 3D printing techniques also significantly enhance manufacturing efficiency, facilitating the integration of low-cost portable microscopes for POCT applications. The fast development of deep-learning strategies also promises

real-time image analysis, boosting their capacities in image segmentation [3], pattern recognition [4], and imaging quality enhancement [5].

However, the widespread adoption of these low-cost portable microscopes is hindered by several critical challenges. Firstly, the intricate optical and mechanical designs of these devices are often complicated, making them less accessible to a broad user base. Secondly, the necessity for data to be transferred to a personal computer for post-analysis introduces delays and hampers the ability for real-time decision-making, a crucial factor in many clinical and field settings. Furthermore, the specificity of their design for particular application scenarios severely limits their versatility and applicability across diverse research fields. Recognizing these significant limitations, my first research project proposes the development of an innovative low-cost portable microscope characterized by its simplified optomechanical design and integrated real-time analysis capabilities. This novel microscope aims to support both brightfield and fluorescent imaging, ensuring broad applicability across various scientific disciplines.

Moreover, optical sectioning microscopy represents a transformative advancement in the diagnosis of diseases, particularly those involving complex tissue structures and cellular arrangements. It can provide high-resolution images of multiple layers within a specimen. This feature is particularly beneficial in diagnosing diseases that exhibit subtle morphological changes at the cellular or subcellular level, which might be missed by traditional microscopy techniques. Nevertheless, applying optical sectioning microscopes in resource-limited areas faces significant challenges, primarily due to their high cost, complex operation, and stringent infrastructure requirements. Consequently, proposing a low-cost optical sectioning microscope that utilizes smartphone technology presents a formidable tool for biomedical research and disease diagnosis in resource-constrained regions. The advancements in semiconductor technology have equipped most smartphones with high-quality camera sensors,

powerful illumination sources, and superior lenses, all of which hold significant promise for bioimaging applications. To bridge the gap between resource-limited areas and the availability of optical sectioning microscopy, the subsequent study introduces a smartphone-based optical sectioning microscope. This is accompanied by an in-depth theoretical investigation aimed at further reducing its costs.

Overall, I developed two LPMs in my study to meet the demands for fast disease detection and advanced POCT devices with imaging functionality. One is a low-cost, customized 3D-printed microscope capable of real-time analysis; the other is a smartphone-based HiLo optical sectioning microscope. Validation experiments were conducted on both systems to show their potential for biomedical imaging. Finally, a detailed theoretical study for applying microlens arrays (MLA) to minimize the cost of HiLo microscopy is included.

1.2 PAIM (πM): Portable AI-enhance Fluorescence Microscope

LPMs can be widely used in POCT applications [6], as well as in the detection of food and drinking water contaminants [7,8] in resource-limited areas. In these areas, the application of LPMs can significantly enhance biomedical research and disease diagnosis without incurring excessive costs. With the development of semiconductors and electronic devices, most LPMs are equipped with high-performance optical lenses and sensors at a relatively low cost. However, most of these LPMs are designed for specific applications, and their optomechanical designs are relatively sophisticated, often requiring development by professional engineers. Additionally, these LPMs function solely as microscopes, necessitating the transmission of captured data from camera sensors to computers for analysis by software, resulting in non-real-time data processing. Therefore, the research aims for this first sub-project are twofold: 1) to

develop an LPM with a simplified optomechanical design for ease of use, and 2) to integrate an AI edge computing processing unit with the LPM to enable real-time analysis without the need for data transmission to external PCs.

1.2.1 Cell counting for πM performance validation

Cell counting is a fundamental technique in both laboratory research and clinical practice, essential for quantifying the number of cells in a sample. This process is vital for understanding cell growth, viability, and function across various contexts, including the health assessment of cell cultures in biological experiments and disease diagnosis in medical settings. Traditionally, cell counting has been manually conducted using devices like hemacytometers under a microscope. However, advancements have led to automated systems and sophisticated technologies such as flow cytometry, enhancing speed and accuracy. Despite these advancements, the demand for cost-effective, accessible, and user-friendly cell counting methods persists, stimulating the development of innovative tools and techniques.

Integrating AI functionality into an LPM for cell counting offers a transformative solution, particularly beneficial for resource-limited settings, by democratizing access to advanced research tools. This integration improves usability, enabling users of various expertise levels to obtain accurate and consistent results. The device's portability and real-time analysis capabilities broaden its application to field studies and point-of-care diagnostics, facilitating immediate decision-making. Additionally, AI's adaptability promotes continuous enhancement and versatility in applications, while automated data management supports more profound, insightful research. By reducing subjectivity and errors associated with manual counting, this innovative approach promises to advance the precision and reliability of cell analysis in diverse scientific and medical domains significantly.

Employing cell counting to validate the performance of a LPM's optical imaging and AI algorithms is a strategic move, capitalizing on the universal importance and quantitative nature of cell counting in the biological and medical sciences. This methodology not only assesses the system's ability to manage the complexity and variability of biological samples but also ensures the microscope's relevance for research and clinical diagnostics. Such a validation approach effectively demonstrates the microscope's potential to revolutionize access to sophisticated imaging and analytical technologies, positioning it as an invaluable tool for a wide array of scientific inquiries and applications.

1.2.2 Use of models as biological phantoms

In this study, bead phantoms were utilized due to their uniformity in size and shape, facilitating the standardization of experimental conditions and ensuring the reproducibility of results. These model beads acted as an idealized stand-in for cells, offering a controlled setting to examine specific variables devoid of the complexity and variability typical of biological specimens. Additionally, prepared fixed blood samples were employed for counting and segmentation experiments. The use of fixed blood samples brings the benefit of long-term stability and the preservation of cellular and subcellular structures, rendering them suitable for experiments that do not necessitate functional viability. Conversely, fresh blood samples are preferred in assays that require the assessment of cellular functionality and physiological responses, as they preserve the dynamic properties and reactivity of living cells. Taking into account both effectiveness and complexity, employing beads and prepared fixed blood samples represents a suitable approach to validate the performance of the proposed LPM.

1.2.3 Method of image analysis for cell segmentation

Before the widespread use of neural networks for image analysis in cell segmentation, several traditional image processing and analysis methods were employed. These methods primarily relied on techniques that did not require the extensive training data or computational resources that neural networks demand.

For example, thresholding is one of the simplest techniques where the image is converted into a binary image based on a threshold value. Pixels above the threshold are considered part of the object (e.g., cells), and those below are considered background. This method works well when there is high contrast between the objects and the background [9]. Edge detection is also a popular way for cell segmentation, techniques like the Sobel [10], Canny [11], and Prewitt operators [12] were used to detect edges within an image. These edges would then be used to outline objects of interest, such as cells. Edge detection works by identifying sudden changes (gradients) in pixel intensity.

Although these traditional methods have provided valuable tools for analysing cell images, they are constrained by several limitations. They often struggle with low-quality images marked by poor contrast or noise and require extensive manual tuning, making them less adaptable to varying image conditions. They tend to falter when dealing with complex cell structures, such as overlapping or closely situated cells, and lack the capacity to handle the inherent variability in cell morphology. Moreover, these methods cannot realize real-time analysis and manual feature selection is necessary. For LPMs, whose imaging performance cannot compete with benchtop microscopes, using these traditional algorithms for data processing cannot always get accurate results.

CNNs have revolutionized cell segmentation by offering extraordinary accuracy,

efficiency, and robustness [13–15]. Their ability to automatically learn complex features from vast amounts of imaging data sets them apart, eliminating the need for manual feature selection and significantly reducing human error. CNNs excel in processing large datasets, adapting to various imaging conditions, showing high robustness in processing noisy data, and handling the intricate details of cellular structures. Moreover, the flexibility of transfer learning allows for leveraging pre-trained models to enhance segmentation tasks, even with limited data. This end-to-end learning capability, combined with the potential for real-time processing, positions CNNs as a cornerstone technology in advancing biomedical imaging and analysis, opening new horizons for research and clinical applications.

RBC count is a key component of a complete blood count, which is vital for diagnosing various conditions like anaemia, polycythaemia, and dehydration [16–18]. Real-time counting allows for immediate results, facilitating swift decision-making in clinical settings. In biomedical research, real-time RBC counting can provide insights into the effects of various drugs, treatments, and conditions on blood health and function [19]. It allows for the immediate observation of reactions and interactions within the blood. In these scenarios, using the microscope to acquiring blood sample images and applying algorithms to realize segmentation and counting are necessary. Counting RBCs in real time offers immediate results, enabling rapid decision-making. This is crucial in emergency situations where quick diagnosis and treatment initiation can be lifesaving [20]. Therefore, for realizing real-time RBC counting and segmentation in resource-limited area, increasing disease diagnosis level, developing a LPM with real-time functionality is a good option.

1.3 Smartphone-based Optical Sectioning Microscope

Optical sectioning microscopy stands as a cornerstone in scientific research,

particularly within biological and biomedical research areas, due to its capacity for generating high-resolution three-dimensional images without necessitating the physical sectioning of specimens. This non-invasive approach preserves the integrity of living samples, enabling continuous observation of dynamic processes. The technique's compatibility with fluorescence microscopy, combined with its ability to filter out-of-focus light, significantly enhances image clarity and contrast, thereby facilitating the detailed examination of cellular structures and molecular interactions. Furthermore, its versatility and quantitative imaging capabilities extend its applicability across a broad spectrum of scientific disciplines, making it an indispensable tool for advancing our understanding of complex biological systems and materials.

However, the high cost and substantial size of traditional optical sectioning microscopes limit their availability, especially in underfunded laboratories, remote areas, and resource-limited areas. There is a notable gap in research focused on making this technology more accessible; few studies have concentrated on designing and developing low-cost, portable versions of optical sectioning microscopes. Addressing this gap by creating affordable, portable optical sectioning microscopes could significantly enhance healthcare standards and facilitate biomedical research in resource-limited regions, thereby promoting a more equitable distribution of scientific advancement and healthcare solutions worldwide.

1.3.1 HiLo microscopy

As an advanced optical sectioning imaging technique, HiLo microscopy works by acquiring two images of a specimen: one with uniform illumination (resembling traditional wide-field microscopy) and another with structured, non-uniform illumination [21]. The structured illumination is typically achieved by projecting a striped pattern onto the specimen. These two images are then computationally combined to produce a final image that retains the high-resolution features of the

specimen while significantly reducing out-of-focus light. Detailed information can be found in chapter 4 and chapter 5.

Although there are variety of optical sectioning microscopy, like SIM [22], light-sheet microscopy [23], and confocal microscopy [24], HiLo microscopy presents unique advantages. First, implementing HiLo microscopy can be more cost-effective than setting up a light-sheet, SIM, or confocal microscopy system. It can be adapted to existing wide-field fluorescence microscopes with relatively straightforward modifications, bypassing the need for the elaborate setups and calibrations required by more complex systems like confocal and light-sheet microscopes. For instance, light-sheet microscopy necessitates an additional illumination path to generate a light-sheet illumination pattern, which is orthogonal to the observation optical path.

A critical benefit of HiLo microscopy is its minimal photodamage to biological specimens, an essential consideration for prolonged live-cell imaging to maintain specimen health. Unlike confocal microscopy, which often involves high-intensity laser scanning that may cause significant photobleaching and photodamage, HiLo microscopy employs lower light intensities. Although light-sheet microscopy also minimizes photodamage, its costs are considerably higher than those associated with HiLo microscopy. The problem with many light-sheet microscopes is the complex sample mounting requirement. Most will not be using illumination and detection through the same objective lens.

HiLo microscopy can also provide faster imaging speeds compared to confocal microscopy and SIM. Confocal microscopy involves point-by-point scanning of the specimen, which can be time-consuming, especially for large areas or when acquiring multiple z-stacks. HiLo microscopy, however, captures entire fields of view, making it faster for certain applications.

SIM, on the other hand, requires capturing multiple images with different phase shifts of the illumination pattern for each orientation, which can be time-consuming, especially for dynamic live-cell imaging, and it necessitates complex algorithms to reconstruct the super-resolution image from the multiple phase-shifted images. However, HiLo microscopy can offer faster imaging speeds because it typically requires capturing fewer images to produce a high-contrast, optically sectioned image. It relies on a simpler computational approach to combine the uniformly and non-uniformly illuminated images, and the image processing involved in HiLo microscopy is generally less computationally intensive than that required for SIM.

1.3.2 Smartphone-based HiLo

The integration of smartphone with HiLo microscopy techniques presents a compelling case for the development of low-cost, portable optical sectioning microscopes. The feasibility of utilizing smartphones for microscopic applications is underpinned by the continuous advancements in their camera technology and LED illumination capabilities. Modern smartphones are equipped with high-resolution cameras, featuring sensors with high pixel density and sensitivity, enabling the capture of detailed and clear images. The LED flash and torch functions serve as adaptable and bright light sources, providing necessary illumination for viewing specimens. Moreover, the computational power of smartphones supports sophisticated image processing and analysis through various applications, enhancing the microscopy experience.

On the other hand, HiLo microscopy, enhances image quality by combining high-resolution and wide-field imaging, yielding clear and detailed images with improved contrast and reduced background noise. This technique is simple and cost effective when comparing with other advanced optical sectioning microscopy. By merging the convenience and accessibility of smartphone-based imaging with the advanced optical

sectioning capabilities of HiLo microscopy, it becomes possible to create a powerful, low-cost microscopy solution. Such a system would open new avenues for field-based studies and point-of-care diagnostics. The synergy of these technologies making advanced microscopy more accessible and practical for a wide range of applications.

The integration of smartphones with HiLo microscopy stands out as more suitable compared to combinations with light sheet, confocal, or SIM due to several key factors spanning hardware requirements, software compatibility, and overall accessibility. First, HiLo microscopy requires minimal hardware alterations, making it highly compatible with the compact and integrated design of smartphones. Unlike light sheet or confocal systems, which necessitate elaborate setups with precise alignment and high-power light sources, HiLo can be implemented with simple optical modifications, aligning well with the portability of smartphones, and the LED flash in smartphones, while suitable for basic illumination in HiLo microscopy, may not provide the intensity or coherence required for techniques like light sheet or confocal microscopy, which often rely on laser sources for illumination. Moreover, HiLo microscopy leverages the high-resolution sensors of smartphone cameras effectively, requiring only modest computational reconstruction to achieve optical sectioning. This is less demanding compared to the complex illumination patterns and high-speed imaging required in SIM, which may exceed the capabilities of standard smartphone cameras.

Therefore, the combination of smartphones with HiLo microscopy offers a compelling balance of advanced imaging capabilities, ease of use, and affordability. This makes it particularly suited for applications where portability, cost, and user accessibility are key considerations, thus providing a strong case for its development and use over more complex and hardware-demanding techniques like light sheet, confocal, or SIM microscopy.

1.3.3 Data processing for smartphone-based HiLo microscopy

In the proposed smartphone-based HiLo microscopy, SI images and widefield images are directly recorded by the iPhone original camera application, and then processed with HiLo algorithms on computer. Using smartphone providing a cost-effective alternative for capturing high-quality images. In some cases, Smartphones are being used in microscopy to capture images directly through the eyepiece of microscopes.

However, the use of smartphones in microscopy is not without challenges. Dealing with the built-in image filters and processing algorithms of smartphones can be tricky, as these are typically optimized for general photography and can alter the raw data of microscopic images. This alteration can lead to inaccuracies in colour representation and detail, which is critical in scientific imaging. Moreover, smartphones have limitations in terms of optical zoom capabilities and sensor sensitivity compared to dedicated microscopy cameras, which can affect the resolution and quality of the captured images, particularly in low-light conditions. These limitations are discussed in detail in chapter 6.

Despite these limitations, the use of smartphones in microscopy continues to grow, driven by ongoing advancements in smartphone camera technology and the development of specialized apps and attachments that aim to mitigate these challenges, making microscopy more accessible and versatile than ever before.

1.4 Using Microlens Arrays (MLAs) for Minimizing the Cost of HiLo Microscopy

The primary objective of this research is to explore cost-effective alternatives for implementing HiLo microscopy (see details in chapter. 5). The conventional approach

employs a DMD for producing Structured Illumination (SI). Despite its efficacy, the DMD's high cost necessitates the investigation of more economical solutions for SI generation, with the potential to significantly reduce overall expenses.

This study proposes the use of microlens arrays (MLAs) as a viable, low-cost substitute for DMDs in creating SI for HiLo microscopy. The main reason for considering MLAs as an alternative is quite straightforward: they are simple and affordable tools for creating the necessary light patterns for structured illumination. Unlike more complex systems, MLAs use basic optical principles to focus light into regular, repeating patterns, which is exactly what we need for this kind of microscopy, but without the high cost. In contrast to DMDs, which require complex and expensive microfabrication processes to precisely control mirror orientations for light modulation, MLAs utilize fundamental optical refraction principles. By concentrating incident light into uniform, periodic focal points, MLAs can produce the necessary SI patterns with minimal hardware complexity and reduced manufacturing costs.

MLAs present a cost-effective alternative to DMDs in HiLo microscopy. The cost advantage of MLAs over DMDs is underpinned by the availability of low-cost fabrication methods for MLAs, which significantly reduce the overall expense involved in their production and implementation. For instance, techniques such as microplastic embossing [25,26], microdroplet jetting [27,28], and laser swelling [29,30] have been identified as simple methods for producing MLAs at a fraction of the cost associated with the microfabrication of DMDs. These methods are particularly notable for their suitability for mass production, owing to their minimal complexity and reduced requirement for sophisticated equipment. Moreover, the advent of 3D printing technology has further expanded the possibilities for economical MLA fabrication, enabling the production of high-quality MLAs with minimal investment in specialized infrastructure [31,32].

It should be noticed that the fabrication of MLAs using Polydimethylsiloxane (PDMS) and exploiting surface tension methods has shown promising results for creating cost-effective, high-quality optical components. One notable technique involves utilizing the interfacial tension force as the dominant mechanism for lens formation during spin coating under a multiphase system. This method leverages the unique properties of PDMS and the dynamics of surface tension to precisely shape microlenses [33].

To assess the feasibility of employing MLAs in HiLo microscopy, I conducted simulations of the HiLo imaging process using MLAs with varied parameters. The results of this analysis not only confirm the potential of MLAs in HiLo microscopy but also provide insights into how the specific characteristics of MLAs influence the quality of HiLo optical sectioning images. Although MLAs cannot be easily tuned when comparing with DMD, this study paves the way for understanding how MLA-generated patterns effect the final HiLo images and how to choose appropriate MLAs.

1.5 Research Aims

The key aims and goals of this PhD project are:

1. To review current LPMs and corresponding biomedical applications and compare their performance and differences.
2. To develop an AI-enhanced customized LPM with real-time target detection ability that can be used for RBC counting.
3. To develop a low-cost HiLo optical sectioning microscope based on the smartphone. HiLo is a widefield optical sectioning algorithm, which will be introduced in the related section.
4. To further minimize the cost of the HiLo optical sectioning microscope, a theoretical study about using the microlens array (MLA) with specific parameters to generate structured illumination (SI) is discussed.

1.6 List of Contributions

A list of contributions of this PhD project are listed below:

1. PAIM (πM): portable AI-enhanced fluorescence microscope for real-time target detection.
    - Proposed a LPM with an easy optical path and mechanical design. 3D printed model constructs its body without any help of alloy or metal structure, and anyone can design it without sufficient mechanical design experience. Users can customize their artificial neural networks (ANNs) for applications on πM, such as feature extraction, pattern recognition, and cell counting. They can also connect πM to the internet and share real-time analysis results.
    - The edge computing technique makes πM acquire a powerful AI-enhanced real-time analysis function. The NJN makes πM can be customized appropriately for different applications, and data transfer to the cloud and servers for analysis are exempted because of the NJN's edge computing power.
    - Even though those resource-limited regions have poor network and communication conditions, πM can also realize real-time analysis without any network data transfer because users can implant well-trained ANNs into the NJN in advance. This powerful AI module can immediately give users results after capturing microscopic images during the experiments. In the worst case, even if users want to realize functions that cannot be achieved in pre-trained ANNs, they can use πM to collect data and directly train their customized ANNs. After that, they can use πM to solve their given problems.
2. Smartphone-based Optical Sectioning (SOS) Microscopy with A Telecentric Design for Fluorescence Imaging.

- Proposed a smartphone-based optical sectioning microscope with an easy optical path and mechanical design. We built our SOS with off-the-shelf optical mechanical cage systems with 3D-printed adapters to seamlessly integrate the smartphone with the SOS main body.
- The broadband smartphone LED torch can effectively excite fluorescent polystyrene (PS) beads. The liquid light guide can be integrated with the adapter, guiding the smartphone's LED light to the digital mirror device (DMD) with neglectable loss.
- The smartphone in our SOS microscope acts as a complementary metal-oxide semiconductor (CMOS) sensor to decrease the cost of traditional HiLo microscopes. High-resolution coloured images can be acquired without external colour filters because of the smartphone's Bayer filter and the small pixel size.
- The electrically tunable lens (ETL) was conjugated to the back pupil plane (BPP) of the objective lens for realizing a telecentric axial scan, which can stabilize SOS's lateral magnification at different depths.
- To our knowledge, the proposed SOS is the first smartphone-based HiLo optical sectioning microscopy. It is a powerful, low-cost tool for biomedical research in resource-limited areas.

3. Optimizing microlens arrays for incoherent HiLo microscopy.
    - To our knowledge, this is the first numerical study about using proper MLAs to realize HiLo microscopy.
    - This study can guide a more detailed analysis for further investigation in the theoretical research field, including a more comprehensive numerical aperture (NA) range, a larger microlens pitch, the ratio between NA and the lens pitch, and multiple microlens arrangements.
    - This study can guide more researchers to establish low-cost MLA-based HiLo microscope systems in the experiment and engineering aspects.

1.7 Thesis Outline

A summary of the following chapters of this thesis is shown below:

Chapter 2: A literature review of LPMs

This chapter will review different types of LPMs. They will be classified into smartphone-based, customized, and lensless LPMs. The hardware aspect will be first discussed. Their differences and performance will be introduced. LPMs for biomedical applications will also be discussed in detail. Finally, how to choose appropriate LPMs for different biomedical applications will be discussed.

Chapter 3: PAIM (πM): portable AI-enhanced fluorescence microscope for real-time target detection

This work presents a PAIM (πM) based on a webcam and the NJN, integrating with edge computing techniques for real-time target detection. πM only costs ~$400 and its structure was constructed by a 3D printer, weighing only ~250 grams with dimensions of 145mm × 172 mm × 144 mm (L×W×H). It achieves a physical magnification of ×5 and can resolve 228.1 lp/mm USAF features. Prepared microscopic samples, fluorescent PS beads, and human RBCs can be imaged in brightfield and fluorescence mode. The NJN exempts πM from time-consuming data transfer and image processing. Users can customize their ANNs for feature extraction, pattern recognition, and cell counting applications. They can also connect πM to the internet to share real-time analysis results. We used πM for fluorescent beads and human RBC observation. We demonstrated a convolution neural network (CNN) to realize real-time foreground feature extraction and counting functions without data transfer and image processing. With a miniature size and real-time analysis, πM has potential in point-of-care testing, field microorganism detection, and clinical diagnosis in resource-limited areas.

Chapter 4: Smartphone-based Optical Sectioning (SOS) Microscopy with A Telecentric Design for Fluorescence Imaging.

This work presents a SOS microscope with a telecentric design for fluorescence imaging. SOS microscope uses the HiLo principle to realize the optical sectioning function, with a single smartphone replacing a high-cost illumination source and a camera sensor. It costs around £7,035 cheaper than a traditional HiLo microscope equipped with a scientific camera sensor and an illumination source. We used an ETL instead of a mechanical translation stage to realize low-cost axial scanning. SOS has a 571.5 μm telecentric scanning range and a 5.5 μm axial resolution. We successfully used SOS for high-contrast fluorescent PS beads imaging with different wavelengths and optical sectioning imaging of accumulated fluorescent PS beads. SOS is a low-cost, compact optical sectioning microscope that is easy to replicate in a portable style. It has the potential for biomedical research in resource-limited areas.

Chapter 5: Optimizing microlens arrays for incoherent HiLo microscopy

This work presents a new low-cost HiLo microscopy technique using MLAs and incoherent LED light sources. We simulate SI patterns and HiLo image generation based on Fresnel diffraction and incoherent imaging theories. To observe how MLAs affect HiLo images, we used three common MLAs (cross-, cylinder-, and hexagon type) with specific microlens pitch and NA to generate periodic illumination patterns. According to the detailed mathematical deduction and numerical simulation, we analyse how different MLAs affect SI patterns' appearance, modulation depth, and axial resolution. We also study how these SI patterns alter the final HiLo images' performance. We conclude that increasing MLA's lens pitch can enhance the HiLo image's contrast and optically-sectioned ability. However, this pitch size has a valve value. Beyond that, we also find that the hexagon-type MLA is the most susceptible to artifacts, and we can get HiLo images with the mildest artifacts using cylinder-type MLA. To our knowledge, this is the first study about using proper MLAs to realize

HiLo microscopy.

Chapter 6: Conclusion

This chapter concludes the results and contributions of this PhD study. Future works and prospects of current studies are predicted and discussed.

Chapter 2. A Literature Review of LPMs

Low-cost and portable microscopes can significantly facilitate disease detection and biomedical research in resource-limited areas. Recent advances in AI further boosted their capacities in image segmentation, pattern recognition, and imaging quality enhancement. This chapter will review recent advances in low-cost and portable microscopes for biomedical imaging applications. They can be categorized as smartphone-based, customized, and lensless microscopes. Then, I will discuss detailed case studies in biomedical imaging applications. At this chapter's final, I will summarize the key characteristics of LPMs under investigation. Additionally, I will provide insights into the criteria and considerations for selecting the most suitable LPMs tailored to specific biomedical applications. This discussion aims to distil the essential features and functionalities of LPMs, offering a practical guide for researchers and practitioners in choosing the appropriate microscope for their distinct biomedical needs. The comprehensive evaluation of LPM characteristics and the subsequent guidelines for selection will enhance the understanding and utilization of these portable imaging tools in diverse biomedical contexts.

2.1 Introduction

To fully develop the capabilities and potential applications of LPMs, it's crucial to recognize their role in transforming remote diagnostics, field research, and POCT applications. LPMs, characterized by their affordability and portability, enable immediate microscopic investigations in environments far from conventional laboratories. This innovation is particularly beneficial for field researchers and healthcare professionals who require quick and reliable diagnostic tools in remote or resource-limited settings. The ability of these microscopes to provide immediate

insights into the microscopic realm makes them invaluable tools in advancing healthcare diagnostics and environmental research. Considering about different type of LPMs, their corresponding characterizations, and application scenarios, many aspects should be discussed to get a better understand of LPMs:

1. **Choosing LPMs Appropriately:** Considering the increasing diversity in LPMs, understanding how to select these devices correctly for various applications is crucial.
2. **Performance Enhancement:** Exploring ways to enhance the performance of LPMs will contribute to their efficacy in diverse settings.
3. **Unique Features and Drawbacks:** A comprehensive discussion on the unique features and potential drawbacks of LPMs is essential for a nuanced understanding of their capabilities and limitations.
4. **Future Development:** Addressing the future development of LPMs is vital to anticipate emerging trends, technological advancements, and potential applications.

These discussions will offer valuable insights for researchers, fostering a deeper understanding of the current landscape and guiding future developments in LPMs.

There are many reviews about portable microscopes. Most of them are focused on detailed discussions of hardware systems, algorithms, and specific biomedical applications. For example, Wei et al. discussed portable microscopy platforms for single-molecule and particle detection [34]; Yang et al. reviewed the recent development of portable imaging platforms for cells analysis [35]; Cabodi et al. reviewed low-cost and portable lab-on-chip devices for malaria elimination [36]; Gopinath et al. discussed how to use low-cost portable devices for bacterial detection [37]. These review articles emphasized LPMs for specific biomedical applications. Cristobal et al. published a short review and commented on 23 articles in the last decade [38]; Kuang et al. reviewed computational portable microscopes and summarised their applications in POCT and telediagnosis cases [39]; Henriques et al. reviewed

customized microscopes for life sciences. He gave a field guide about how to design and use 3D printing to construct microscopes with different modalities [40]; Coté et al. classified LPMs into three imaging modalities (bright-field, fluorescence, and cross-polarised) [41]; Ozcan et al. concentrated in mobile-phone-based microscopes and proposed potential diagnosis applications [42]. This gives the review a clearer clue for readers with different backgrounds and aims. Other review articles about LPMs and sensing platforms in environmental detection scenarios are out-of-scope, which can be found in [43–45].

In this review section, I take a macroscopic approach to discuss LPMs, distinguishing my approach from the reviews mentioned above by providing a broad overview and technical trajectory from system design to its associated applications. From a systemic perspective, I categorize LPMs into three types: Smartphone-based, customized, and lens-less (or lens-free). I focus on their distinctive mechanical and design features, exploring imaging modalities and optical performance in each category. For each imaging platform, the advantages and drawbacks will be discussed.

In the application segment, my emphasis lies on biomedical imaging applications, while non-imaging sensing applications are covered in References [42,46,47]. Here, four popular applications (Fig. 2-1) that can be realized on LPMs are chosen for detailed discussion. Additionally, how different hardware imaging platforms can be appropriately employed for various biomedical imaging applications will be discussed.

Fig. 2-1 illustrates the structure of this review section. The primary objective is to bridge the gaps between multidisciplinary subjects, encompassing optics, electronics engineering, and biology. By presenting a cohesive structure, hardware microscopists can focus on the practical aspects of biomedical imaging applications. Simultaneously, this review is a valuable resource for biologists, introducing how low-cost portable

microscopes can support their biomedical and healthcare research endeavours.

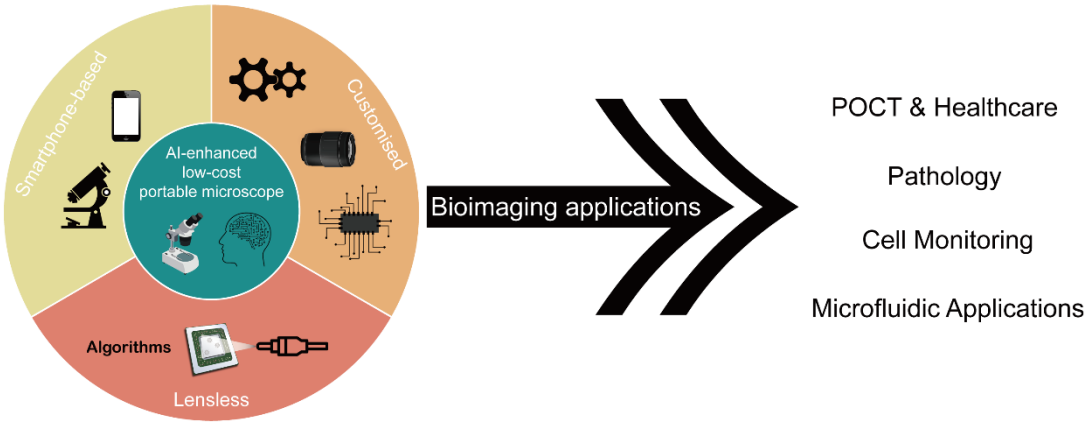

Fig. 2-1. The review's structure. Three types of LPMs: smartphone-based, customized, and lensless. Four appropriate bioimaging applications which can be realized on LPMs.

2.2 System Configuration of Low-cost Portable Microscopes

There are three main categories of LPMs: smartphone-based, customized, and lensless (Fig. 2-1). Within each category, this analysis begins with a literature review and examines specifications about mechanical structures and optical properties. The characteristics and limitations are subsequently discussed in the final section.

2.2.1 Smartphone-based Low-cost Portable Microscopes

Modern smartphones have high-performance chips, internal memory, advanced optical sensors, and low-aberration lenses. They usually provide good imaging quality and fast data analysis functions. After combining smartphones with external optical lenses and filters, they can work as microscopes [48]. These smartphone-based LPMs are compact and user-friendly. They can obtain cellular scale resolution [49,50]. After examining recently published smartphone microscopes, I concluded that smartphone microscopes could be realized in three configurations: 1. Applying polymer [51] or liquid droplets

[52] onto the smartphone camera surface; 2. Putting a reversed smartphone lens before the smartphone camera to constitute a 1:1 magnification system [53]; 3. Designing proper mechanical adapters for harnessing external optical paths to the smartphone [54–56]. Table. 2-1 lists smartphone-based microscopes with different configurations. The corresponding imaging modality, resolution, and biomedical imaging application are also described.

Table. 2-1. Smartphone-based microscope classified by three configurations. BF: Brightfield, DF: Darkfield, PC: Phase contrast, OI: Oblique illumination, RI: Rheinberg illumination, FP: Fourier ptychography, WBC: White blood cell.

Configuration	Imaging modality	Resolution	Biomedical imaging application	Reference
Droplet	BF	3.91 μm	Pathology imaging	[57]
		1 μm		[58]
		2.19 μm	Microfluidic particle detection	[59]
	BF/Fluorescence	2.76μm	Cell and tissue imaging/Cell counting/ Plasmid transfer evaluation/Superoxide production analysis	[51]
		3.1 μm	fluorescently labelled M. smegmatis detection	[60]
Reversed smartphone lens	BF	<=5 μm	Blood smear imaging	[53]
		<=5 μm	Schistosoma haematobium infection diagnosis	[61]
		<=6.5 μm	L. loa microfilariae detection in whole blood	[62]
		<=4 μm	WBC screening	[63]
	BF/Fluorescence	1.21 μm	Blood cells morphology recognition and cell counting	[64]
	BF/Fluorescence with UV illumination	<1 μm	Pathology imaging/Mucosal smear imaging/ Bacterial imaging	[65]
Mechanical adapter	Fluorescence	<=1.5 μm	Single DNA molecules/nanoparticles/virus detection	[66]
				[67]
	BF/DF/Fluorescence	0.98 μm	DNA sequencing and in situ mutation analysis	[68]
		5.35 μm	Cell sorting	[69]

	Quantitative phase	0.98 μm axial	RBC quantitative phase imaging	[70]
	BF/DF/PC	5 μm axial	Human blood, cells, and bacterial imaging	[71]
	BF/PC	N/A	Pathology imaging	[72]
	BF/DF/OI/Fluorescence/RI/PC	1.7 μm	Tissue/cells/fungus imaging	[73]
	FP	870 nm	Blood smear imaging	[74]
	Fluorescence	1.2 μm	Single-molecule detection	[75]

a. Droplet

Applying droplets onto the smartphone camera surface is a straightforward method for magnification. The formation of liquid lenses is facilitated by surface energy minimization, requiring no intricate parameter control [76]. Among polymers, PDMS is an ideal choice for crafting droplet lenses due to its capacity for high-temperature curing without significant shape deformation or viscosity alterations. Ekgasit et al. fabricated planoconvex lenses by dripping PDMS droplets onto small circular disks [77]. Kamal et al. introduced a passive droplet dispensing and capturing approach specifically designed for producing high-quality droplet lenses [78]. Hu et al. innovatively presented the concept of effective surface tension, enabling the modelling of fast-cured polymer droplets as conventional liquid droplets with a constant viscosity [79]. In a related study, Szydlowski employed oil droplets dripped onto the sample surface for microscopic image observation [52]. These studies showed that integrating droplet lenses with smartphones is a potent and cost-effective solution.

Lee et al. successfully integrated the droplet lens with a smartphone, achieving an impressive 60x magnification. They applied this setup for imaging human pathology slides, pollen grains, and skin samples [57]. Similarly, Sung et al. investigated the properties of droplet lenses with varying volumes and curing temperatures, employing the droplet lens smartphone microscope for pathology imaging [58]. Salafi et al.

adopted a comparable approach, incorporating microfluidic devices for real-time particle detection. To facilitate this, they devised a 3D-printed adapter to seamlessly integrate microfluidic chips and droplet lenses with a smartphone, enabling particle counting at 240fps with an accuracy of (93.6 ± 2.0) % (average particle speed = 2.2mm/s) [59].

The studies highlighted above concentrated on brightfield imaging. However, to extend the capabilities of the droplet smartphone-based microscope to fluorescence imaging, Dai et al. [51] and Long et al. [60] employed a strategy of dyeing PDMS with silicon dyes. This innovative approach allowed for the combination of droplet lenses and absorption optical filters. Consequently, various applications such as plasmid transfection evaluation, superoxide production analysis, immunofluorescence pathology imaging [51], and detecting fluorescently labelled bacteria [60] became easily achievable. Diagrams extracted from the related research articles are depicted in Fig. 2-2.

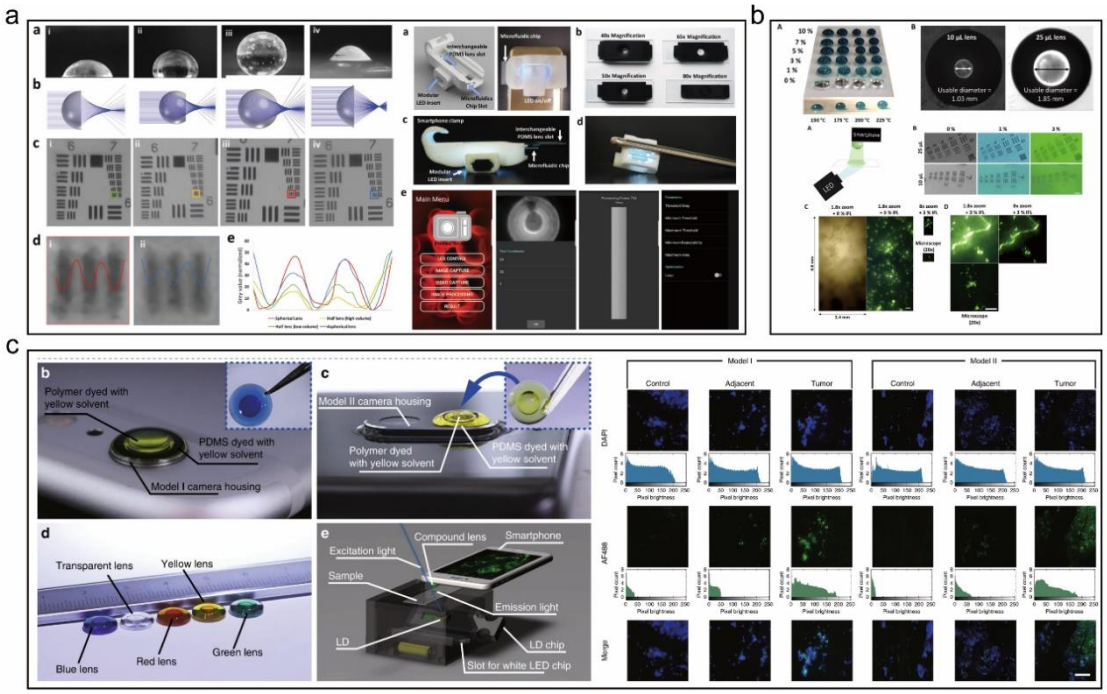

Fig. 2-2. Droplet lens smartphone-based microscopes for biomedical imaging applications. (a) Salafi et al. fabricated PDMS droplet lenses with different volumes to

obtain different magnifications. They designed a 3D-printed adapter to harness the droplet lens and the microfluidic chip into the smartphone for microfluidic particle counting [59]. (b) The smartphone is equipped with a silicon-dyed PDMS droplet lens for fluorescently labelled bacteria detection [60]. (c) The smartphone is equipped with different colour compound droplet lenses for various wavelength fluorescence observation [51].

b. Reversed Smartphone Lens

An alternative method to implement a smartphone-based microscope involves positioning a reversed lens before the camera. This configuration creates an imaging relay system by combining the reversed and original smartphone lenses. The magnification is determined by the f-number ratio between the two lenses. When the reversed lens matches the specifications of the original smartphone lens, a 1:1 imaging relay system is established. Additionally, employing the same lens allows the creation of a symmetrical imaging system, effectively reducing off-axis aberrations [80].

In contrast to droplet-based methods, this approach does not necessitate a sophisticated fabrication process. Moreover, most smartphone lenses feature five to seven carefully designed plastic aspherical lenses, effectively minimizing optical aberrations while maintaining cost control. Switz et al. affixed the reversed lens to the phone using double-sided tape and devised a straightforward mechanical stage (costing less than $30). This system, boasting a resolution of less than 5μm, demonstrated the capability to observe human red blood cells (Fig. 2-3a) [53]. In another study [61], Ephraim et al. applied the same method for *S. haematobium* detection, achieving a system sensitivity and specificity of 68% and 100%, respectively. Ambrosio et al. utilized a reversed lens to create a smartphone microscope for capturing and analysing videos of microfilaria motions in the blood (Fig. 2-3b). In a clinical application, they examined 33 potentially *Loa-infected* patients in Cameroon, achieving a specificity and sensitivity of 94% and

100%, respectively [62]. In Central Africa, this device can potentially exclude patients from ivermectin-based treatment at the point of care in Loa-endemic regions, thereby facilitating the extension of drug administration programs for onchocerciasis and lymphatic filariasis.

In 2020, Sánchez et al. presented a smartphone microscope employing a reversed lens and oblique 520nm illumination. This device demonstrated the capability to resolve optical absorption gaps (OAG) in nail fold capillaries, as illustrated in Fig. 2-3c. Leveraging the absorption of 520nm light by human RBCs, the technique facilitates quantitative screening of WBCs. In their experiments, a recording rate of 60fps proved sufficient to resolve an average frequency of 37 OAGs/minute passing through nail fold capillaries [63]. Similarly, Rabha et al. utilized the reversed lens and devised a 3D-printed mechanical adapter to create a multimode (brightfield, fluorescence) imaging system [64]. This system achieved a lateral resolution of 1.21 μm over a satisfactory FOV (~4530 μm^2). Well-established brightfield and fluorescence imaging of blood cells and automatic cell counting were demonstrated. Additionally, they developed an algorithm and programmed the smartphone for cell counting (Fig. 2-3d).

Liu et al. made a groundbreaking contribution by demonstrating the first ultraviolet surface excitation microscope on the smartphone platform, utilizing a reversed lens (Fig. 2-3e). Their approach involved using sub-285nm UV light for illumination, penetrating only a few microns into typical specimens. This method achieves strong optical sectioning near the sample surface without degrading image contrast due to subsurface signals. Furthermore, sub-285nm UV light can effectively excite many fluorescent dyes (such as DAPI, fluorescein, rhodamine, etc.), providing a straightforward mechanism for general fluorescence imaging. The platform successfully realized pathology and immunofluorescence imaging, plant and environmental samples imaging, and mucosal smear imaging [65].

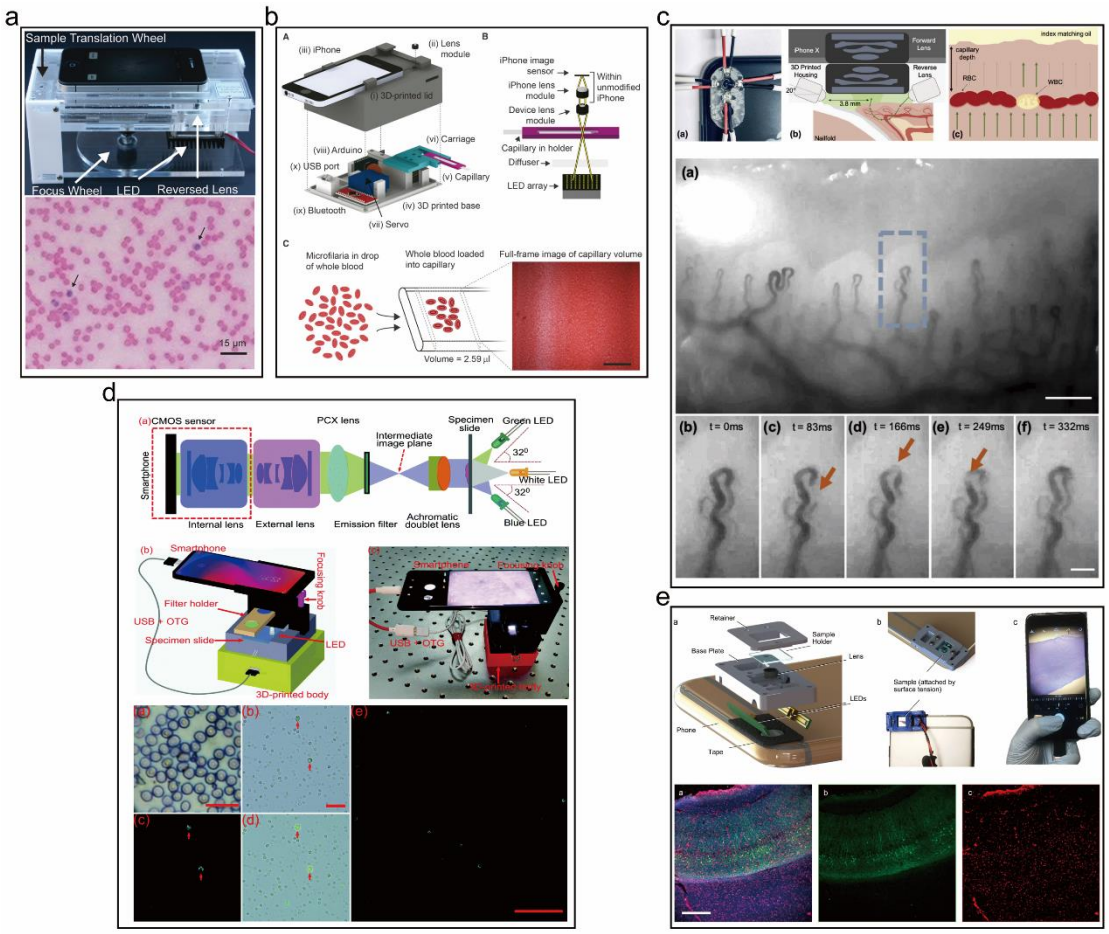

Fig. 2-3. Reversed lens smartphone-based microscope for (a) human RBC imaging [53], (b) microfilaria detection in whole blood [62], (c) WBC screening [63], (d) blood cells morphology recognition and cell counting [64], and (e) pathology imaging, mucosal smear imaging, and bacterial imaging [65].

c. Mechanical Adapter

To augment the functionalities and imaging modalities of smartphone-based microscopes, researchers employ CAD software and 3D printing to create mechanical adapters seamlessly compatible with specific smartphones. These adapters enable the integration of various optical devices and paths into the smartphone microscope, facilitating the realization of diverse imaging modalities, including fluorescence [81,82], DF [83], PC [84], and FP [74]. Unlike droplet and reversed lens smartphone-based microscopes, mechanical adapters offer the advantage of combining more advanced

imaging modalities with smartphones. Furthermore, these precisely engineered adapters contribute to the system's stability.

The research group led by Aydogan Ozcan has put forth a diverse range of mechanical adapters tailored for various bioimaging applications with smartphones. These applications encompass imaging of blood cells on a fibre-optic array [85], detection of *Giardia lamblia* cysts [56], enhanced detection of plasmonic nanoparticles [86], smartphone microscopy enhanced by DL [87], detection of pathogenic bacteria [82], and blood cell detection [1,88]. Wei et al. [66] introduced a portable smartphone microscope for nanoparticle and virus detection. Their approach involved combining a smartphone with a mechanical adapter that integrated an illumination laser source, an optical filter, and an objective lens, effectively creating a fluorescent microscope. Remarkably lightweight at only 186g, the system achieved a resolution of 1.5μm and successfully demonstrated fluorescent single-virus imaging (Fig. 2-4a). In 2014 [67], they utilized a similar device to image single DNA molecules of various lengths, achieving a length measurement accuracy of <1 kbp for DNA molecules 10 kbp and longer (Fig. 2-4b).

Kühnemund et al. established a smartphone platform for imaging and analysing DNA sequencing reactions and in situ point mutation detection assays in preserved tumour samples [68]. The system featured a half-pitch resolution of 0.98μm and an imaging FOV ~0.8mm^2. It accurately quantified individual RCA products over a 4-log dynamic range (1fM-10pM) (Fig. 2-4c). Knowlton et al. innovatively designed a smartphone-based microfluidic cytometry incorporating magnets beside the microfluidic chip to generate a magnetic field inside the channel. This setup allowed sorting RBCs and other magnetically combined samples using magnetic force. The system could realize fluorescence, brightfield, and darkfield imaging modalities [69,89].

To enhance the accuracy of single-molecule detection on the smartphone platform for POCT applications, Trofymchuk et al. successfully integrated DNA origami nanostructures to scaffold addressable NanoAntennas with Cleared HOtSpots (NACHOS). The incorporation of NACHOS significantly increased the brightness of single emitters, with the researchers building a smartphone microscope to achieve single-molecule detection for DNA specific to antibiotic-resistant *Klebsiella pneumonia* [75] (Fig. 2-4f).

Researchers can leverage customized mechanical adapters to integrate smartphone microscopes with various illumination methods. Phillips et al. developed an adapter featuring a domed LED array, providing easy smartphone attachment. The domed LED design supports the smartphone microscope with BF, DF, and PC illumination [71]. Meng et al. introduced a smartphone microscope designed for quantitative phase imaging of RBCs using the transport of intensity equation (TIE). This setup achieves an axial resolution of 0.98 μm [70]. Rabha et al. engineered a smartphone microscope with seven illumination modes within a single setup. They employed a programmable OLED display as the illumination source, allowing for the imaging of tissues, cells, and fungal specimens [73] (Fig. 2-4d). Lee et al. proposed a smartphone-based FP microscope utilizing the display screen for illumination. This device attains a half-pitch resolution of 870 nm across a broad FOV measuring 2.1 × 1.6 mm^2. Notably, the device can reconstruct unstained blood smear samples (Fig. 2-4e) [74].

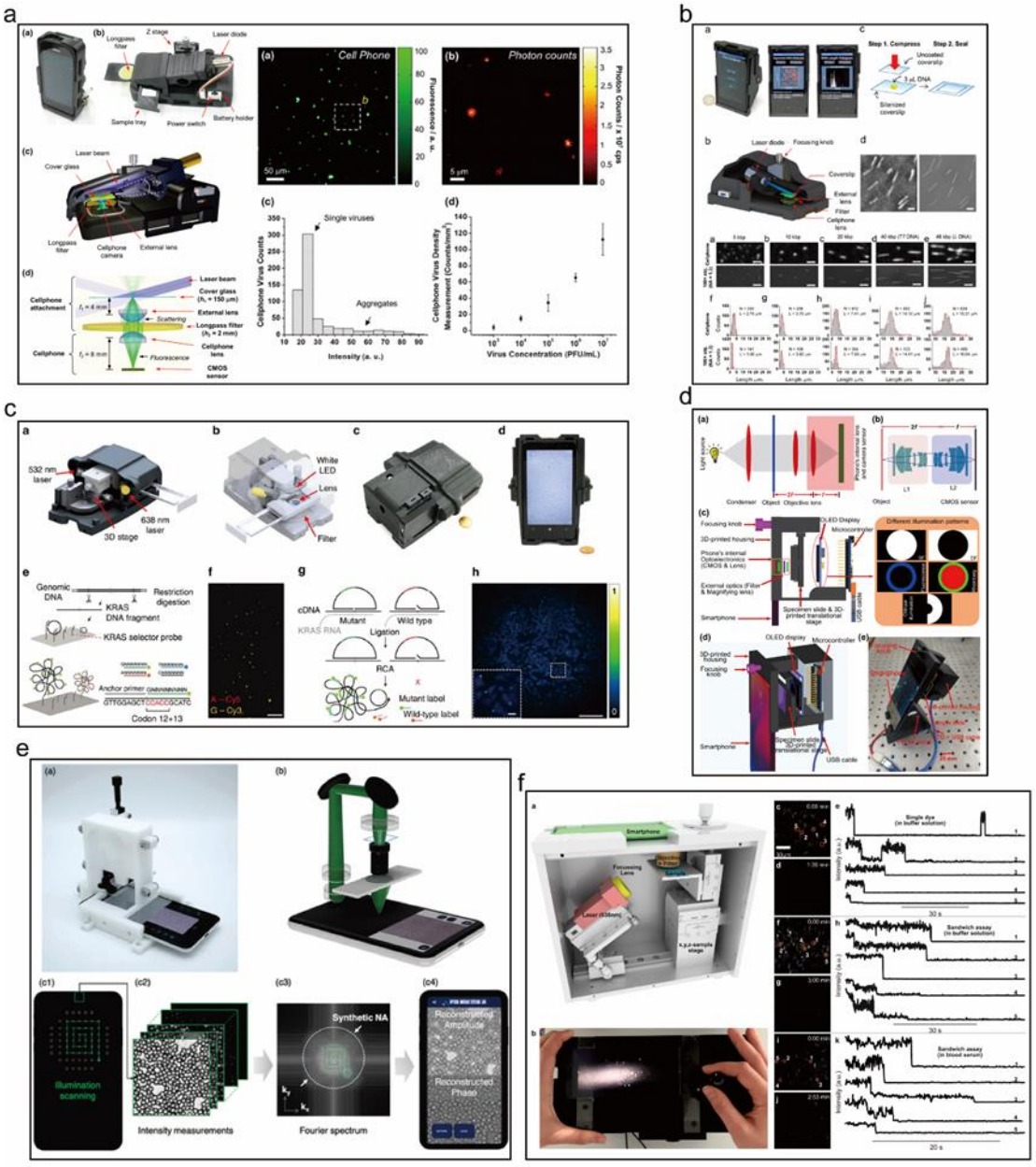

Fig. 2-4. Smartphone-based microscope using mechanical adapters for (a) fluorescent single-virus imaging [66], (b) imaging single DNA molecules of various lengths [67], (c) analysing DNA sequencing reactions and in situ point mutation detection assays in preserved tumour samples [68], (d) multimode imaging of tissues, cells, and fungus specimens [73], (e) Fourier ptychographic microscope [74], and (f) single-molecule detection for DNA specific to antibiotic-resistant *Klebsiella pneumonia* [75].

2.2.2 Customized Low-cost Portable Microscopes

Customized microscopes offer a broader range of imaging modalities compared to their smartphone-based counterparts. They can facilitate various functions, spanning from basic fluorescence microscopes [90,91] to advanced single-molecule [92,93] and SR microscopes [94,95]. Additionally, the meticulous mechanical design, precise alignment, and utilization of readily available components contribute to the enhanced optical performance of these customized microscopes.

A notable advantage lies in the accessibility provided by open-source initiatives and microscopy societies, which encourage researchers to share their hardware designs openly. This collaborative effort enables the seamless downloading of customized components and mechanical designs [96,97]. Consequently, even biologists lacking extensive microscopy expertise can swiftly assemble a microscope tailored to their research needs, guided by the readily available open-source guidelines.

Utilizing 3D printing proves to be a suitable technique for constructing budget-friendly mechanical structures and tailored components [40]. Researchers have demonstrated effective strategies for reducing the expenses associated with imaging sensors [98] and illumination sources [95,99,100]. Table. 2-2 presents a compilation of customized microscopes designed for specific biomedical applications. The evaluation of their system complexity is categorized into three levels: simple, medium, and complex.

Table. 2-2. Customized microscope classified by the system complexity. BF: Brightfield, DF: Darkfield, PC: Phase contrast, DH: Digital holography, RI: Rheinberg illumination, LS: Lightsheet, TPFM: Two-photon fluorescence microscopy, SR: Super-resolution, SIM: Structured illumination microscopy, ISM: Image Scanning microscopy

Complexity	Imaging modality	Resolution	Biomedical imaging application	Reference
Simple	BF/DF/Fluorescence/LS	< 2.2 μm	Monocyte to macrophage cell differentiation monitoring/ Zebrafish expressing green fluorescent protein (GFP) observation	[101]
	BF/Fluorescence	< 2 μm	Cell motility monitoring/Cell and tissue viability analysis/ Oxygen microenvironment measurement inside organoids	[102]
		1.3 μm	Blood and faecal smears with parasite imaging	[103]
		1.62 μm	RBCs segmentation and counting	[104]
	DH	0.594 μm	RBCs analysis for COVID-19 screening	[105–107]
	Fluorescence	3 μm	*In situ* live-cell imaging and analysis	[108]
Medium	BF/Fluorescence/Polarised	0.48 μm	Giemsa-stained blood smear sample imaging	[109]
	BF/DF/PC/RI/Fluorescence	N/A	RBCs with Plasmodium parasites imaging	[110]
	BF/Fluorescence	0.793 μm	RBCs parasitemia measurements	[111]
		2-3 μm	Automated sample preparation and cell imaging	[112]
		1.187 μm	Single cells assay in microwells and cell tracking in the microfluidic chip	[113]
	ISM/SIM	156 nm-300 nm	Fluorescent-stained Hela cells imaging	[114]
Complex	TPFM	0.44 μm lateral 1.68 μm axial	Mice brain Ca2+ imaging	[115]
	SR (DNA-PAINT)	10 nm	Microtubules/ Mitochondrial/ DNA origami imaging	[116]
	LS	N/A	Zebrafish imaging/ Nervous system dynamic observation	[94]
	BF	7 μm	Longitudinal live imaging of *Xenopus tropicalis* embryonic/ In-incubator imaging of human embryonic stem cells and brain organoids	[117]

a. OpenFlexure

The Richard Bowman Group has established the OpenFlexure, a fully open-source and automated microscope, as illustrated in Fig. 2-5. This microscope features a customized 3-axis translation stage with a travel capacity of 12 mm * 12 mm * 4 mm and impressive resolutions of 70 nm in the x-y-axis and 50 nm in the z-axis [118,119]. With a compact volume of 15 cm * 15 cm * 20 cm and a weight of 500 g, the OpenFlexure offers a

resolution of 0.48 μm and supports brightfield, epi-fluorescence, and polarized imaging modalities. Notably, it has been deployed extensively, with over 100 units produced and utilized in Tanzania and Kenya for educational, scientific, and clinical purposes, particularly in imaging blood smears for malaria diagnosis [109].

Stirling et al. expanded the capabilities of OpenFlexure by introducing additional imaging modalities such as DF, RI, and PC [110]. Furthermore, they integrated it with the Raspberry Pi for automated control and real-time analysis. Moreover, OpenFlexure can be freely integrated various applications, including SIM [120] and microfluidic antibiotic susceptibility testing [121]. The versatility and accessibility of the OpenFlexure contribute significantly to advancing microscopy applications in diverse research fields.

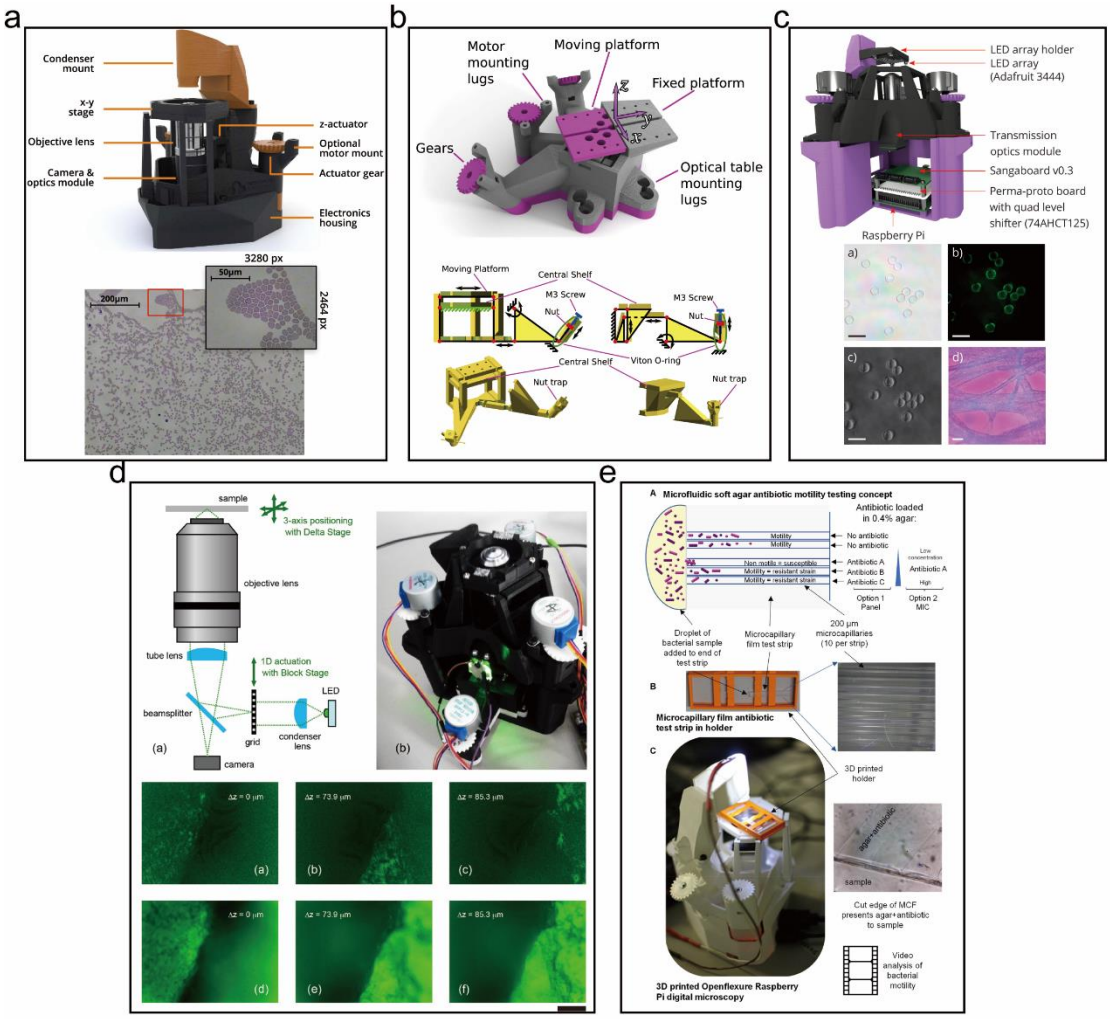

Fig. 2-5. OpenFlexure microscope and its variations for biomedical imaging. (a) OpenFlexure for RBCs imaging [109]. (b) The self-designed 3-axis translation stage of OpenFlexure was fabricated by 3D printing [118]. (c) Multi-modal OpenFlexure combined with Raspberry Pi for realizing automatic control and real-time analysis [110]. (d) SIM is realized on the OpenFlexure platform [120]. (e) Using OpenFlexure for testing antibiotic susceptibility in microfluidic chips [121].

b. µCube and UC2

Delmans and Haseloff introduced µCube, an assembly standard designed to standardize the creation of modular optical devices [122]. Resembling a fundamental building block like LEGO, µCube allows the integration of optical, electrical, and mechanical components into its structure, as depicted in Fig. 2-6a. This modular approach

empowers biologists to construct personalized microscopes tailored to their unique applications and preferences. Furthermore, the innovation extends beyond standalone use, as Delmans and Haseloff have ingeniously developed an adapter that facilitates seamless connection with the OpenFlexure platform. This interoperability enhances the versatility of both μCube and OpenFlexure, providing researchers with a flexible toolkit for addressing a wide array of microscopy needs.

Similarly, Diederich et al. introduced UC2, a 3D-printed, open-source, and modular microscope that offers easy replication, modification, and extension capabilities, as illustrated in Fig. 2-6b [101]. These basic cubes can be assembled in various configurations to suit specific biological applications, as depicted in Figure 2-6c. One notable application of UC2 involves monitoring monocyte-to-macrophage cell differentiation inside an incubator over a seven-day period, as shown in Fig. 2-6d.

Moreover, UC2's adaptability is demonstrated by its transformation into a LSM for imaging transgenic Zebrafish expressing green fluorescent protein (GFP) at only 400 Euros. Expanding its functionalities, Want et al. enhanced UC2 by incorporating consumer-grade DMD and laser projectors, thereby upgrading it to perform ISM and SIM. This upgraded system successfully imaged Alex Fluor 647- and SiR-stained HeLa cells [114]. The birth of UC2 facilitates cost-effective customization and innovation in microscopy applications.

Ouyang et al. have pioneered an open-source modular framework designed for automated pipetting and imaging applications [112]. Integrating various components such as OpenFlexure [109], Opentrons [123], ImJoy [124], and UC2 [101], they have created a seamless, automated pipeline aimed at simplifying protocols and eliminating the risk of suboptimal data quality resulting from human error. The system, depicted in Fig. 2-6(e), can be remotely controlled through software, facilitating sample preparation

and imaging analysis.

With an impressive resolution ranging from 2 to 3 μm, this framework successfully executed a comprehensive protocol, which included staining of HeLa cells, in situ microscopic observations, and data analysis—all performed through a user-friendly interface accessible in a web browser. Ouyang et al.'s integrated system showcases the potential for efficiently and precisely conducting complex experimental procedures in a modular, automated fashion.

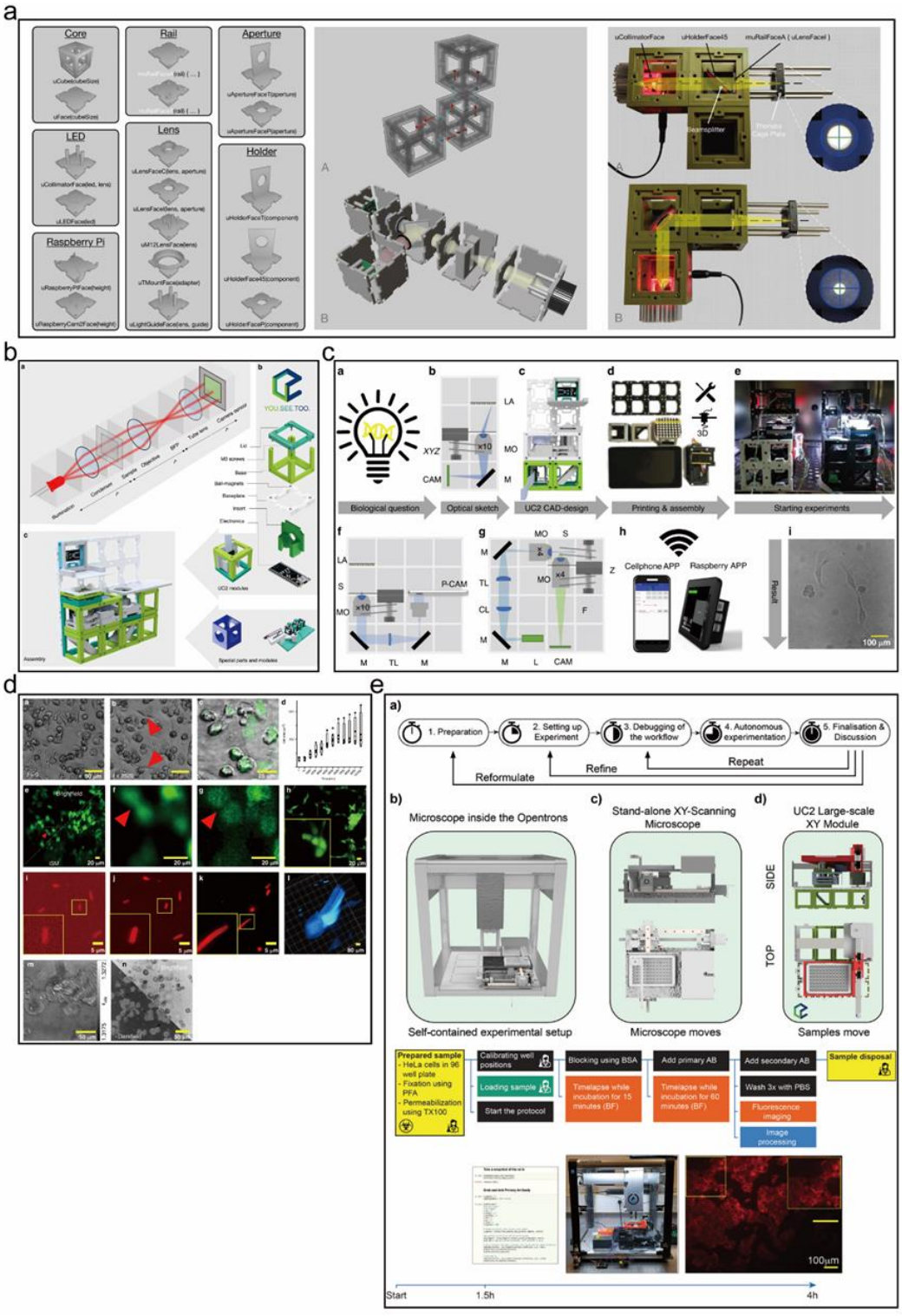

Fig. 2-6. Customized microscopes based on modular designs. (a) µCube, a fundamental building block. Different components can be directly installed into it [122]. (b-d) UC2 open-source microscope for various imaging modalities [101]. (e) An open-source modular framework is constructed by different customized microscopes and open-source systems for automated pipetting and imaging applications [112].

c. Others

Zhang et al. innovatively created a mini-microscope using off-the-shelf components and a webcam [102]. This portable device is adept at real-time monitoring of cell migration and analysing the activities of microfluidic liver and cardiac bioreactors. Remarkably, it can seamlessly integrate with various platforms such as cell culture plates, microfluidic devices, and organs-on-a-chip systems, potentially serving as a versatile alternative to traditional bench-top microscopes for prolonged in-situ imaging, as depicted in Fig. 2-7a.

Javidi et al. employed 3D printing to fabricate a cost-effective digital holographic microscopy setup, showcased in Fig. 2-7b. They developed sophisticated algorithms and utilized deep learning methods to quickly detect COVID-19 from RBCs [105–107]. Similarly, Tristan-Landin et al. designed a 3D-printed fluorescence microscope for single-cell detection, incorporating a Raspberry Pi for image analysis, as illustrated in Fig. 2-7c [113]. Ojaghi et al. proposed a portable microscope utilizing ultraviolet illumination featuring microfluidic chips for label-free neutropenia detection [125].

Aidukas et al. ingeniously transplanted FP into a 3D-printed portable device, successfully reconstructing lung carcinoma intensity and phase images (Fig. 2-7d) [126]. Zhu et al. engineered a portable microscope by integrating a camera lens with a smartphone [91]. Jang et al. constructed a miniature darkfield microscope for prolonged cell monitoring [127]. MicroHikari3D, a low-cost microscope platform transformed by a 3D printer, boasts automated sample positioning, autofocus, and multi-illumination modalities (Fig. 2-7e). Bueno et al. harnessed this platform for whole 2D slide imaging and observation of 3D live specimens [128].

In [129], Niu et al. introduced a quantitative phase microscope designed for phase

imaging of RBCs. The system demonstrates impressive temporal and spatial sensitivities of 0.65 nm and 1.04 nm, respectively, as shown in Fig. 2-7f. These diverse and innovative approaches showcase the potential of low-cost and portable microscopes in various research and application domains.

Customized microscopes offer the advantage of being compact and capable of remote control, making them particularly valuable for real-time monitoring of cell cultures within an incubator. A noteworthy example is the miniaturized modular-array fluorescence microscopy (MAM), a compact system designed for living cell imaging [108]. The MAM system comprises twelve miniature microscopes, each consisting of a gradient-index (GRIN) lens, a filter, and an imaging lens. Deployable within an incubator, it can simultaneously capture images from twelve cell culture chambers of a 12-well plate, as illustrated in Fig. 2-7g.

MAM achieves an impressive lateral resolution of 3 μm with a rapid 60 Hz frame rate. Son et al. demonstrated the efficacy of MAM by successfully recording in vitro cell imaging of living COS-7 cells within the incubator. This capability positions MAM as a valuable tool for real-time observation and analysis of dynamic cellular processes in a controlled environment.

Another comparable device is the Picroscope, which features 24 cameras designed for longitudinal biological imaging [117]. This innovative tool is compatible with standard 24-well cell culture plates and can capture 3D z-stack image data. Furthermore, the Picroscope can be remotely controlled, enhancing its versatility and ease of use. Ly et al. demonstrated the capabilities of the Picroscope by utilizing it to capture longitudinal whole-organism image data for frogs, zebrafish, and planaria worms.

The adaptability of the Picroscope extends to its deployment within an incubator, where

it successfully recorded both 2D monolayers and 3D mammalian tissue culture models, as depicted in Fig. 2-7h. This feature underscores its utility for observing dynamic biological processes in various experimental settings over time. The Picroscope stands as an advanced tool for comprehensive longitudinal imaging in biological research.

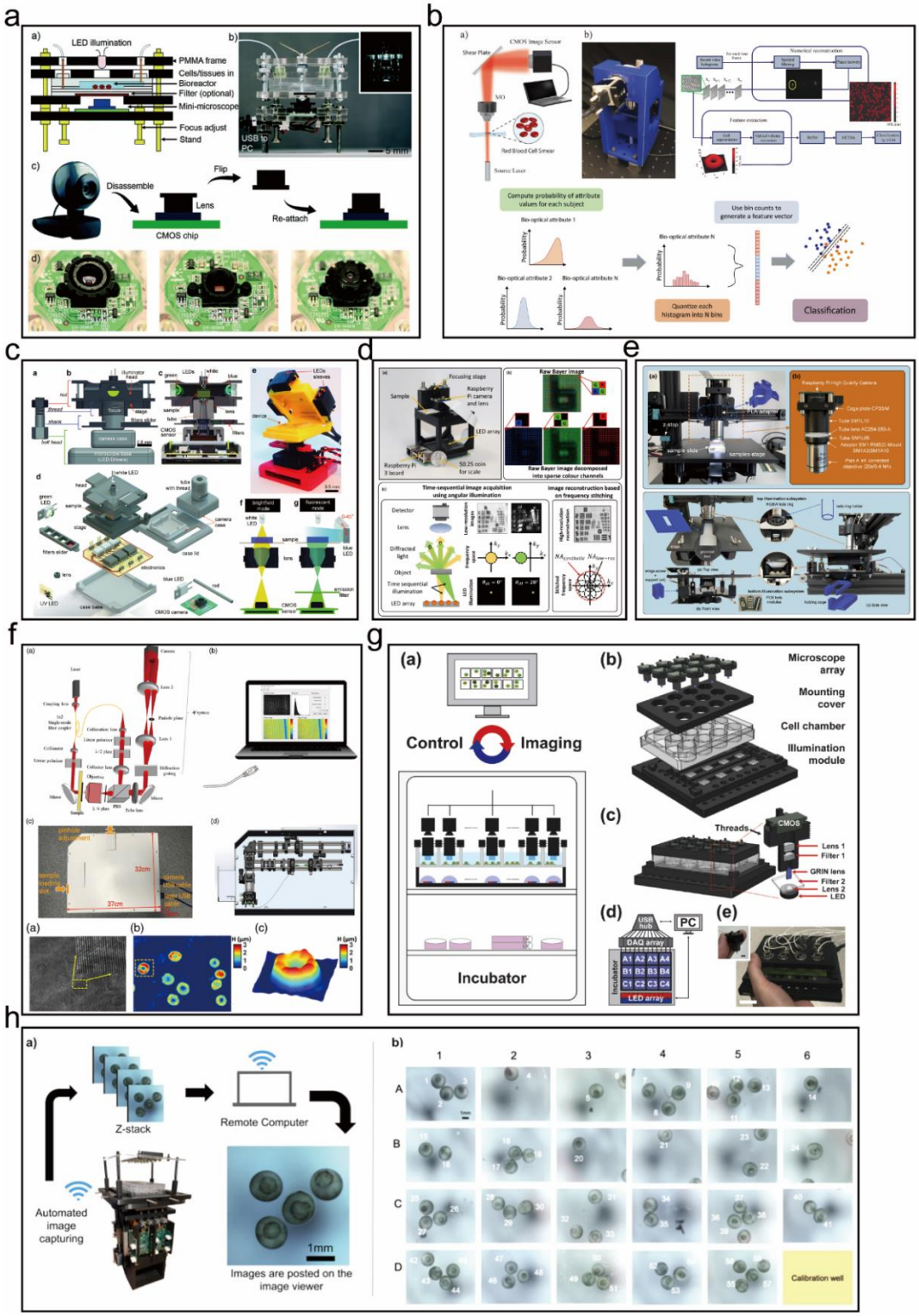

Fig. 2-7. Other customized microscopes for bioimaging applications. (a) Low-cost customized microscope for microfluidic applications [102]. (b) Digital holography microscope for COVID-19 diagnosis assisted by deep learning [105–107]. (c) 3D printed microscope for single-cell analysis [113]. (d) 3D printed FP microscope [126]. (e) MicroHikari3D automatic microscope [128]. (f) Portable quantitative phase microscope for RBCs phase imaging [129]. (g) The miniaturized MAM for the in vitro cell imaging of living COS-7 cells in the incubator [108]. (h) Picroscope for longitudinal whole organism imaging [117].

2.2.3 Lensless Low-cost-Portable Microscopes

In lensless microscopy, as opposed to employing optical lenses for the magnification of microscopic targets onto an image sensor, the approach involves recording object-generated diffraction patterns by the image sensor, subsequently reconstructed through post-processing algorithms. Traditional microscopes are subject to a 'Resolution-FOV' trade-off, imposing constraints on the space-bandwidth product (SBP). Lensless microscopy addresses this limitation by reducing the distance between samples and the sensor, enhancing the system's FOV. Nevertheless, the spatial resolution of the lensless imaging system remains contingent upon the pixel size of the sensor, thereby limiting the SBP. To surmount this pixel-induced limitation in resolution, researchers have employed subpixel resolving techniques such as microfluidic flow [130–133], light source shifting [134–140], and synthetic aperture [141].

Lensless microscopes can be integrated with lab-on-a-chip (LOC) and microfluidic devices. The advancement of edge computing and system-on-chip (SOC) capabilities facilitates the on-the-fly processing of data acquired through lensless microscopy. This integration enables real-time analysis and enhances the overall efficiency of the imaging system. Ozcan and McLeod conducted a comprehensive review of lensless imaging, sensing methodologies, and their associated biomedical applications [142].

Robinson et al. delved into lensless imaging applications encompassing photography, refocusing, 3D imaging, and microscopy in a more macroscopic exploration. Their classification of lensless imaging systems includes illumination-modulated, mask-modulated, and programmable-modulated categories. Additionally, they provided an overview of algorithms and deep learning techniques employed in lensless image reconstruction [143].

In this context, the emphasis is placed on lensless microscopy and its applications in bioimaging. It should be noted that lensless imaging applications such as photography, compressive sensing, and macroscopic 3D imaging fall outside the scope of this discussion. References are recommended [144,145] for those interested in these specific areas. Lensless microscopy is herein categorized into shadow imaging, digital holography, mask-modulated imaging, and fluorescence imaging. Refer to Table. 2-3 for a comprehensive list of pertinent articles detailing resolution, image reconstruction methodologies, and bioimaging applications.

Table. 2-3. Lensless portable system for bioimaging applications. LDHM: Lensless digital holography microscopy, MLM: Mask-modulated microscopy. RPCA: Robust principle component analysis. FISTA: fast iterative shrinkage-thresholding algorithm. CNN: Convolution neural network.

Modality	Resolution	Image reconstruction	Biomedical imaging application	Reference
Shadow imaging	40 μm	N/A	*C. Elegan* screening	[146]
	3 μm		Cell monitoring	[147]
	0.24 μm		Urine analysis	[148]
	0.9 μm		*C. Elegen* and cell imaging	[131]
	0.66 μm	Pixel super-resolution algorithm	Continuous cell culture monitoring	[137]
LDHM	2 μm	N/A	Cells detection and cytometry	[149]
	N/A		Prostate epithelial cells analysis	[150]
			Real-time label-free cell detection	[151]
		Gerchberg-Saxton algorithm	3D cell culture imaging	[152]
	0.98 μm	Phase retrieval and TIE	Pathology imaging	[153]
	3 – 5 μm	Phase retrieval	Real-time cell functions monitoring	[154]
	1.55 μm	Phase retrieval	Sperm and platelet imaging	[155]
MLM	1.6 μm	RPCA/FISTA	3D imaging of moving fluorescent beads in the microfluidic chip	[156]
	0.78 μm	Customized recovery algorithm	Cancer slides imaging	[157]
	N/A	CNN	RBC classification	[158]
			Sickel cell disease identification	[159]
	8 μm lateral 50 μm axial	FISTA	3D zebrafish imaging	[160]
	< 9 μm lateral 80 μm axial	RPCA	In vivo brain calcium dynamics imaging	[161]
Lensless fluorescence imaging	10 μm	Compressive sampling	Transgenic *C. Elegan* imaging	[162]
	<4 μm		*Giardia muris* cysts imaging	[163]
	36 lp/mm	N/A	Brain slice imaging	[164]
	0.22 mm	N/A	Cancer cell detection	[165]
	12 μm	Customized	Cell culture monitoring	[166]
	1.2 μm	N/A		[167]

a. Shadow Imaging

Shadow imaging represents the most straightforward manifestation of lensless microscopy, requiring solely a stable illumination source and an image sensor,

rendering image reconstruction algorithms unnecessary. This technique positions specimens between the illumination source and the sensor (Fig. 2-8a). Notably, the illumination-to-sample distance spans approximately centimetres, surpassing the sample-to-sensor distance, which typically ranges from 1 μm to millimetres. To mitigate diffraction patterns effectively, researchers should set a minimal sample-to-sensor distance [146], typically less than 500 μm [142]. However, an incremental increase in this distance transforms shadow imaging into digital holography (as elucidated in section 2.3.2). In such instances, image reconstruction is imperative to restore amplitude and phase information [149].

Lange et al. utilized a compact shadow imaging apparatus with a microfluidic chip to investigate C. elegans [146]. Penwill et al. showcased the application of a lensless shadow imaging device for screening the growth phenotype of Schizosaccharomyces pombe [168]. Ozcan et al. introduced a lensless shadow imaging prototype (LUCAS) characterized by a wide FOV (37.25 mm * 25.70 mm) for monitoring and quantifying diverse cell types [147]. Zhang et al. seamlessly integrated a lensless shadow imaging device with a microfluidic chip, facilitating the automated recording of sperm movement within a microfluidic channel [169].

While lensless shadow imaging proves to be a compact means for particle detection [170], urine analysis [148], and cell monitoring [171,172], it is essential to acknowledge its limitation in resolution dictated by the pixel size of the sensor.

Yang et al. devised a solution to address the inherent limitation imposed by pixel size, which involved the fabrication of a linear sub-micrometre aperture array positioned above the CMOS. Each aperture within the array is precisely centred on an individual pixel. In contrast, the microfluidic channel, positioned at a tilted angle over the aperture array, facilitates a line scan when the sample is introduced. Through the controlled flow

of the specimen, the adjacent linear aperture array functions as a scanning line, ultimately enabling the acquisition of sub-micrometre images upon the rectification of the line scan and estimation of flow velocity (Fig. 2-8d) [131,132,173].

Instead of modifying the hardware configuration, Zheng et al. retained the original hardware setup. However, they altered the illumination angle to capture low-resolution images from diverse perspectives (Fig. 2-8e, f). Subsequently, employing algorithms and leveraging these low-resolution images, they successfully reconstructed high-resolution images [130,137].

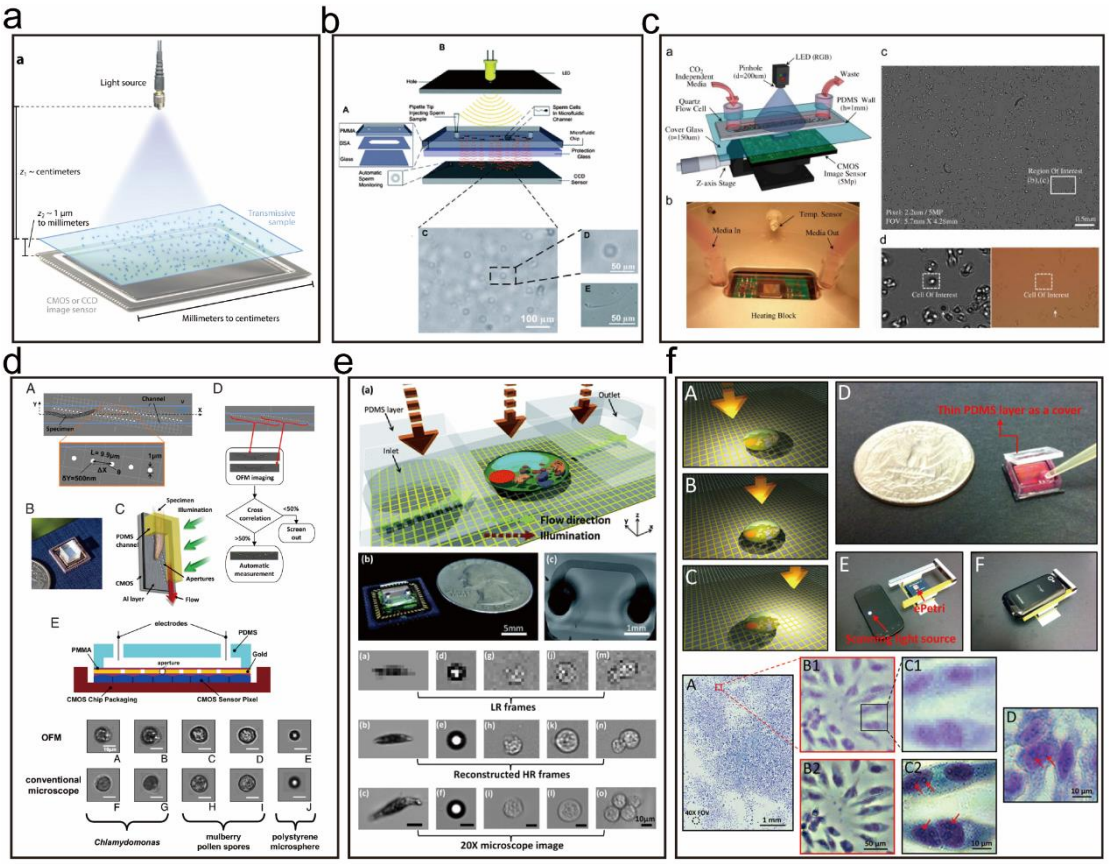

Fig. 2-8. Lensless microscopy using shadow imaging principles. (a) Lensless shadow imaging principle, cropped from [142]. Lensless shadow imaging for sperm monitoring (b) [169] and continuous cell monitoring (c) [172]. SR shadow imaging by flowing samples (d) [131] and modulating illumination [130,137] (e,f)

b. Lensless Digital Holography Microscopy

Lensless Digital Holography Microscopy (LDHM) employs either coherent or partially coherent light to illuminate samples, with the sensor capturing the resulting diffraction pattern [174,175]. This technique is extensively applied in LOC microscopy contexts [176]. The hardware setup closely resembles that of shadow imaging (Fig. 2-8a), with the notable distinction that the distance (z2) between samples and sensor can be increased for diffraction pattern recording [142].

In contrast to shadow imaging, LDHM excels in retrieving complex-field information encompassing both amplitude and phase. This capability enables the reconstruction of three-dimensional information, resulting in enhanced resolution and signal-to-noise ratio (SNR) compared to shadow imaging [150,174,177]. LDHM necessitates a coherent light source, commonly employing LEDs instead of lasers. By adjusting the source's size, bandwidth, and distance to the sample, LEDs' spatial coherence can be finely tuned, approximating the sample as illuminated by a partially coherent plane wave [174–176]. Despite lasers offering superior spatial and temporal coherence, they are susceptible to speckle noise.

The coherent interference pattern captured on the sensor can be effectively modelled as an in-line hologram [178–180]. In this context, the intensity pattern arises from the interference between the scattering wave induced by the sample and the unobstructed reference wave transmitted from the source through the specimen. Leveraging the Fresnel diffraction integral to reverse-propagate the interference pattern allows for the reconstruction of the specimen in high resolution [181–183]. However, this digital holographic reconstruction approximation has limitations, particularly when applied to sparsely distributed samples. This constraint stems from the requirement that the sample-induced scattering wave must be less pronounced than the reference wave.

In a broader sense, the coherent interference pattern can be treated as a coherent diffraction pattern, challenging the validity of the clear reference wave assumption. Consequently, specific approaches, such as incorporating prior knowledge of the sample [174] or employing multiple measurements [141,153,177,184], become necessary for accurate sample recovery.

LDHM exhibits sensitivity to sample sparsity, with the twin-image artifact becoming particularly pronounced in instances of high sample density [185,186]. Researchers use diverse approaches, such as employing varied sample-to-sensor distance measurements [153] and different illumination angles [141] to enhance sample information recovery. Additionally, the application of iterative phase recovery algorithms, such as the Gerchberg-Saxton (GS) algorithm [187,188] and the TIE [189,190], proves beneficial in improving reconstruction accuracy and convergence performance. For a more comprehensive exploration of LDHM and its intricacies, readers should consider authoritative sources [142,143,175].

LDHM emerges as a potent technique for cell and pathology imaging, analysis, and the recovery of phase information, particularly advantageous for sparse samples. Zora et al. undertook a cost-effective initiative, investing $52.82 to construct an open-source LDHM for bioimaging (Fig. 2-9a) [191]. Sobieranski et al. innovatively integrated LDHM with computational pixel super-resolution through multi-frame processing. Their prototype, employing the angular spectrum method, successfully recovered both intensity and phase information for sperm analysis, achieving a spatial resolution of 1.55 μm over a FOV of 30mm² (Fig. 2-9b) [155].

Mundanyali et al. showcased a lensless on-chip microscope capable of realizing differential interference contrast imaging and imaging various blood cell types (RBC,

platelet, neutrophil). This system boasts a resolution of 1~2 μm across a 24mm² FOV and weighs approximately 46 grams (Fig. 2-9c) [174]. For target recognition using the lensless on-chip microscope, Seo et al. custom-tailored an algorithm for matching captured diffraction patterns to a predefined database (Fig. 2-9d) [149]. Furthermore, in their work [151,154], LDHM was leveraged for real-time cell culture monitoring, enabling the quantification of cell functions such as cell-substrate adhesion, cell spreading, cell division, cell division orientation, and cell death (Fig. 2-9e).

Indeed, overcoming challenges posed by dense samples is achievable through various measurement and illumination strategies. Greenbaum et al. introduced a multi-detection approach by tilting the image sensor, employing the TIE, pixel SR, multi-height phase recovery, and colorization algorithms to capture detailed images of human pathology samples (Fig. 2-9f) [153]. Luo et al. incorporated the synthetic aperture method into LDHM for colour pathology imaging, achieving a system NA of 1.4 and a resolution of 250 nm at a wavelength of 700 nm under unit magnification (Fig. 2-9g) [141]. Rivenson et al. employed two in-line holograms acquired at different sample-to-sensor distances and successfully recovered samples using multi-height phase recovery techniques (Fig. 2-9h) [192].

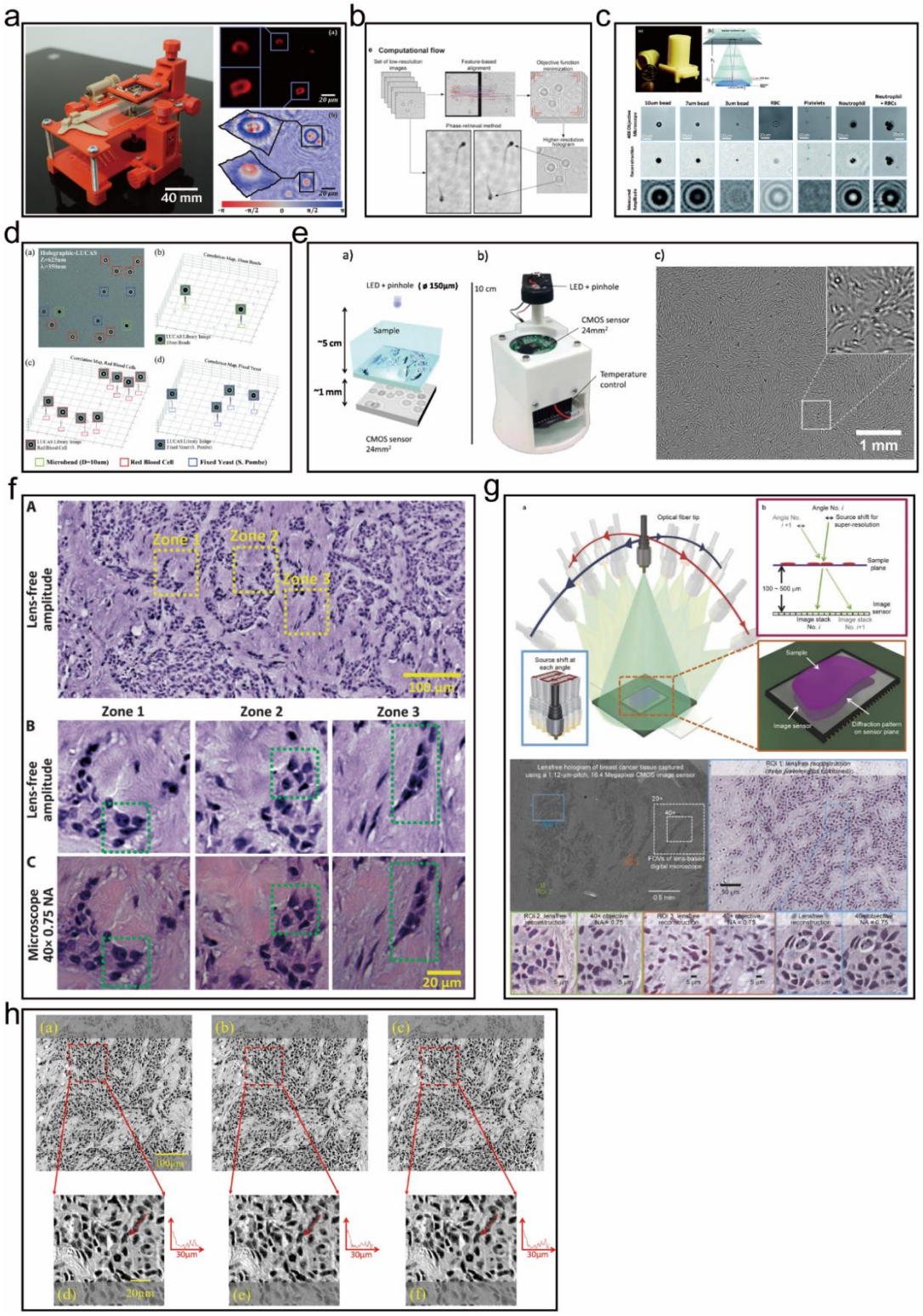

Fig. 2-9. Portable LDHM for bioimaging applications. (a) A low-cost portable LDHM for RBC imaging [191]. (b) LDHM with computational pixel super-resolution for sperm monitoring [155]. (c,d) LDHM for cell recognition [149,174]. (e-h) LDHM for dense sample imaging [141,151,154,192].

c. Mask-modulated Lensless Microscopy

In the preceding section (2.2.3.b), we observed that LDHM offers a compact dimensional profile, and its versatility in sample recovery extends from sparse to dense configurations through the application of phase retrieval algorithms. However, the recovery process presents an exceptionally ill-posed inverse problem intricately linked to experimental conditions and algorithmic performance. The recovery process becomes challenging if the differences between multiple detections are too subtle [143,193]. To address this issue, LDHM adopts strategies such as altering illumination patterns or adjusting the sample-to-sensor distance to acquire multiple detection results.

Another approach to mitigate this challenge involves using mask-modulated lensless microscopy (MLM). In MLM, targets undergo illumination by a light source and are directly modulated by a mask before reaching the sensor. The resultant image on the sensor is a convolution between the sample and the PSF of the mask (Fig. 2-10). Generally, these masks fall into two categories: amplitude-based [156,194–198] and phase-based [194,199–203].

Amplitude-based masks are relatively easy to fabricate and cost-effective [156,194–196]. However, due to the mask's attenuation and obstruction of specific light components, the SNR is compromised, limiting its efficacy in low-photon scenarios such as fluorescence imaging.

On the other hand, phase-based masks modulate the light phase using wave optics without significant photon loss. This property makes them suitable for photon-limited scenarios like microscopy [156,160,161,204]. However, this advantage comes with a trade-off of high costs and intricate fabrication procedures [161,199,200,205].

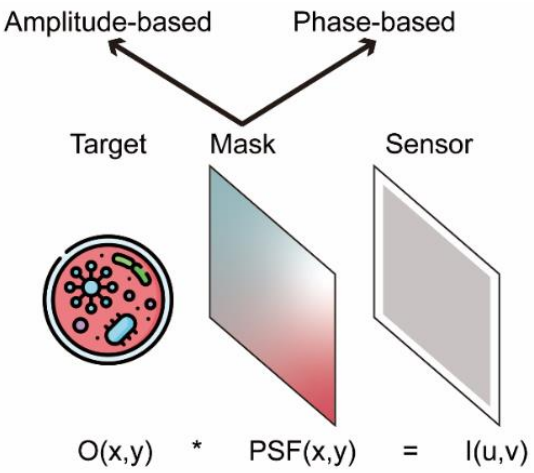

Fig. 2-10. The principle of MLM. The target is modulated by the mask and imaged to the sensor. At the sensor plane, the captured image is the convolution of the target and PSF of the mask. This image could be meaningless. Algorithms can reconstruct the final image.

MLM exhibits versatility across various applications beyond microscopy and bioimaging, including photography, volumetric imaging, light field and refocusing, as well as compressive sensing [206]. In this discussion, the focus will be on reviewing references about MLM in microscopy and bioimaging. For a more comprehensive understanding of MLM and its applications in other domains, we strongly encourage readers to refer to the recommended sources [207].

Adams et al. introduced an amplitude-based lensless microscope named Flatscope, an ultra-lightweight device weighing only 0.2 grams and with a thickness of less than 1mm (Fig. 2-11a). Flatscope achieves a minimum resolution of 1.6 μm. The researchers employed Flatscope to record 3D volumetric videos of flowing fluorescent beads within microfluidic chips. To streamline the calibration and image reconstruction processes, they meticulously designed a mask pattern that could be decomposed by the outer product of two 1D functions. The reconstruction procedure was treated as solving a Tikhonov regularized least-squares problem [156].

Jiang et al. implemented a diffuser between the object and the image sensor for modulation in their lensless microscope configuration. Utilizing the FP technique, they employed blind scanning of the sample in x-y positions using an illumination source for quantitative intensity and phase recovery (Fig. 2-11b). This system achieved a resolution of 0.78 μm over a 6.4mm * 4.6 mm FOV. Beyond biomedical slide imaging, they utilized the platform for cell segmentation based on quantitative phase maps captured by the lensless microscope [157].

Similarly, the research group led by Bahram Javidi incorporated a diffuser mask to realize lensless microscopy. They employed a low-cost, portable lensless microscope using an LD laser as the illumination source, with 3D printing facilitating device fabrication (Fig. 2-11c). Additionally, they integrated CNNs into their devices to achieve RBC classification and identify sickle cell disease [158,159].

MLM holds significant promise for advancing 3D biomedical imaging capabilities, facilitated by the masks' ability to encode light from various depths, enabling 3D imaging from a single acquisition [208]. Grossrubatscher et al. implemented a random microlens diffuser between the object and the image sensor (Fig. 2-11d). This setup allowed them to achieve 3D in vivo zebrafish imaging, with an 8 μm resolution in the lateral direction and a 50 μm resolution in the axial direction [160].

To address challenges such as light loss and low SNR inherent in amplitude-based mask lensless microscopes, Adams et al. introduced a novel phase-based mask lensless microscope called Bio-Flatscope (Fig. 2-11e). Bio-Flatscope exhibited improved performance compared to their previous Flatscope. The researchers designed a unique phase mask to generate the PSF using the near-field phase retrieval algorithm. The modulation transfer function (MTF) of Bio-Flatscope indicated the preservation of most spatial frequencies, allowing for the successful reconstruction of dense, low-contrast

samples such as biological tissue. Their investigations employed Bio-Flatscope to achieve 3D volume reconstruction of Hydra samples, stimulus-evoked Ca2+ brain monitoring in freely moving mice, and imaging of the human oral mucosa [161].

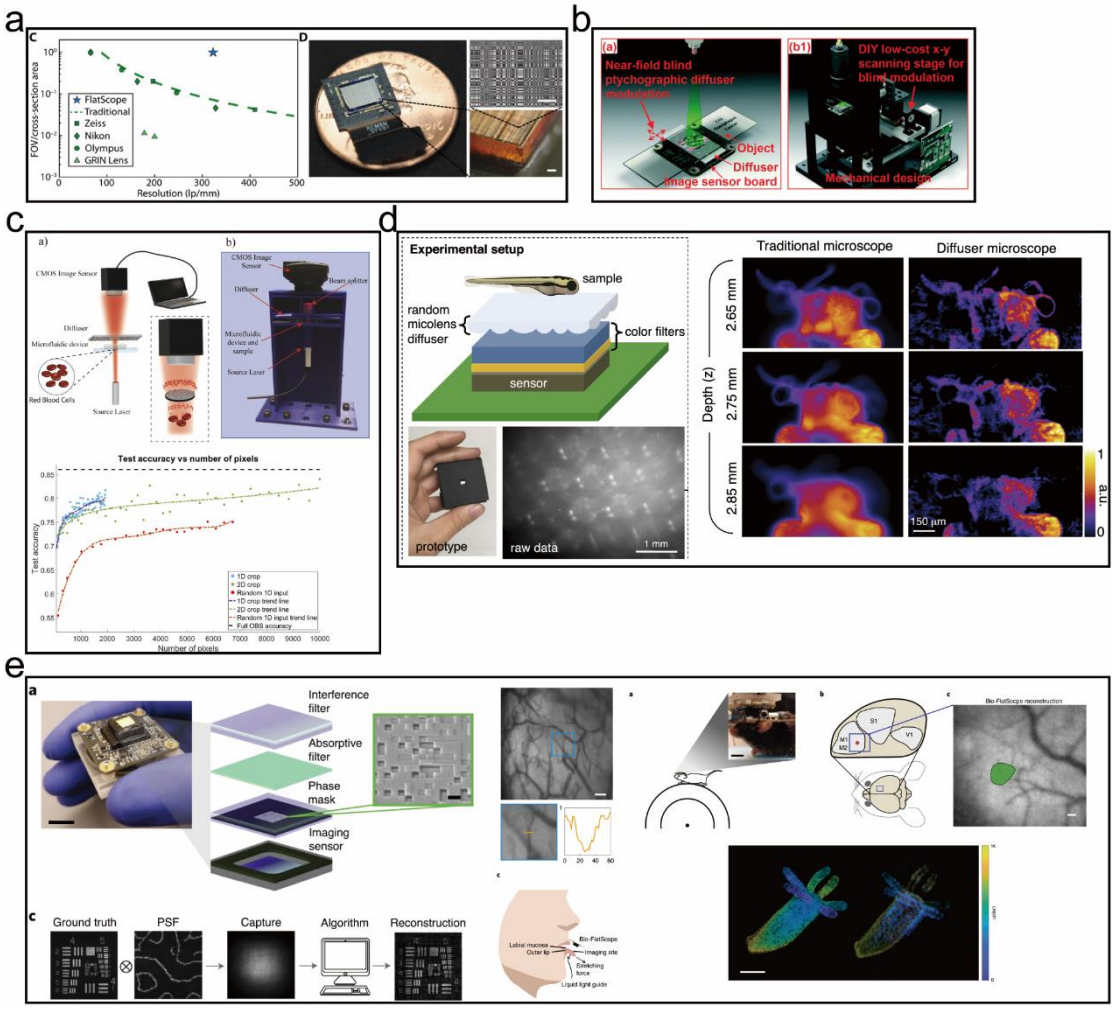

Fig. 2-11. Different types of mask-modulated lenless microscopes. (a) The FlatScope, an amplitude mask lensless microscope, cropped from [156]. (b) Using a diffuser as a modulator to realize mask-modulated lensless microscopes. The Fourier ptychography method is used for high-resolution images and phase recovery, cropped from [157]. (c) A low-cost diffuser-based lensless microscope for RBC detection. The CNN is used for sickle cell identification, cropped from [158,159]. (d) The lensless 3D fluorescent microscope, a random microlens diffuser is used as a modulator, cropped from [160]. (e) In Bio-Flatscope, the particular phase mask can generate contour PSF to modulate

the light signal. It can be used for 3D imaging, brain activity monitoring, and human oral mucosa imaging [161].

d. Fluorescence Imaging

Fluorescence imaging can be successfully implemented in a lensless configuration [162,163,209]. The underlying principle is similar to shadow imaging, with the distinction that the collected light comprises incoherent fluorescent signals rather than scattered light. Moreover, in many fluorescence imaging scenarios, the emission light typically possesses a distinct wavelength from the excitation light. To attain images with a high SNR, excluding the excitation light from being captured by the image sensor is essential.

Effectively rejecting excitation light can be achieved by incorporating an emission filter between the sensor and the sample. While Fabry-Perot film-coated filters offer superior filtering performance, their thickness is often impractical for lensless configurations, potentially compromising resolution [210]. Many filters can be directly fabricated or coupled to the sensor without significant spatial impact [211–214]. However, this approach may not eliminate all excitation light, occasionally leading to a low SNR in the images.

An alternative strategy is to leverage total internal reflection (TIR) to prevent the collection of excitation light by the sensor [213]. Coskun et al. implemented a prism above the sensor to establish a TIR geometry (Fig. 2-12a). This configuration effectively avoids undesired scattering and excitation light, enabling the realization of Calcein-labeled white blood cell (WBC) imaging with a system resolution of about 40-50 μm [209]. In a subsequent work [162], they employed compressive decoding processes to enhance the resolution to 10 μm, achieving lensless on-chip fluorescent imaging of transgenic C. elegans (Fig. 2-12b).

Another approach involves using optical fibre bundles to transmit the image to the sensor (Fig. 2-12c). In this setup, the sample is positioned on the surface of the optical fibre bundles, and the fluorescent signal can be relayed to the sensor. Inserting the emission filter between the fibre taper and the image sensor helps selectively capture the fluorescent signal. As the fibres carry the light toward the image sensor, the fibre bundle widens, providing a moderate on-chip magnification without needing a lens [163,215].

Sasagawa et al. developed an integrated fibre optical plate with optical filters named FOP, which can be directly coupled with the image sensor (Fig. 2-12d). The resolution of fluorescence imaging achieved with FOP is approximately 12 μm. The researchers successfully utilized FOP for time-lapse monitoring of cell culturing in a CO2 incubator [166] and imaging brain slices from a green fluorescent protein transgenic mouse [164] (Fig. 2-12e). To achieve high excitation light rejection performance, Kulmala et al. fabricated a high-performance dual-colour hybrid filter, combining it with FOP and mounting it onto a commercially available colour image sensor (Fig. 2-12f). Image processing effectively differentiated between green and red fluorescent beads by analysing images acquired through alternating excitation light sources [214].

Employing SI represents an effective strategy for enhancing the resolution of lensless fluorescence microscopy. Han et al. devised a lensless fluorescence microscope for longitudinal cell culture monitoring within an incubator (Fig. 2-12g). The system relies on the Talbot effect for imaging [216]. Their prototype achieves a resolution limit of 1.2 μm over a 13 mm^2 FOV [167].

Tian et al. introduced a miniaturized light field lensless fluorescence microscope, GEOMScope, designed for 3D imaging (Fig. 2-12h). This setup combines an optical

filter with a thin microlens array, employing an innovative algorithm that integrates geometrical-optics-based pixel back projection and background suppressions for image reconstruction [204].

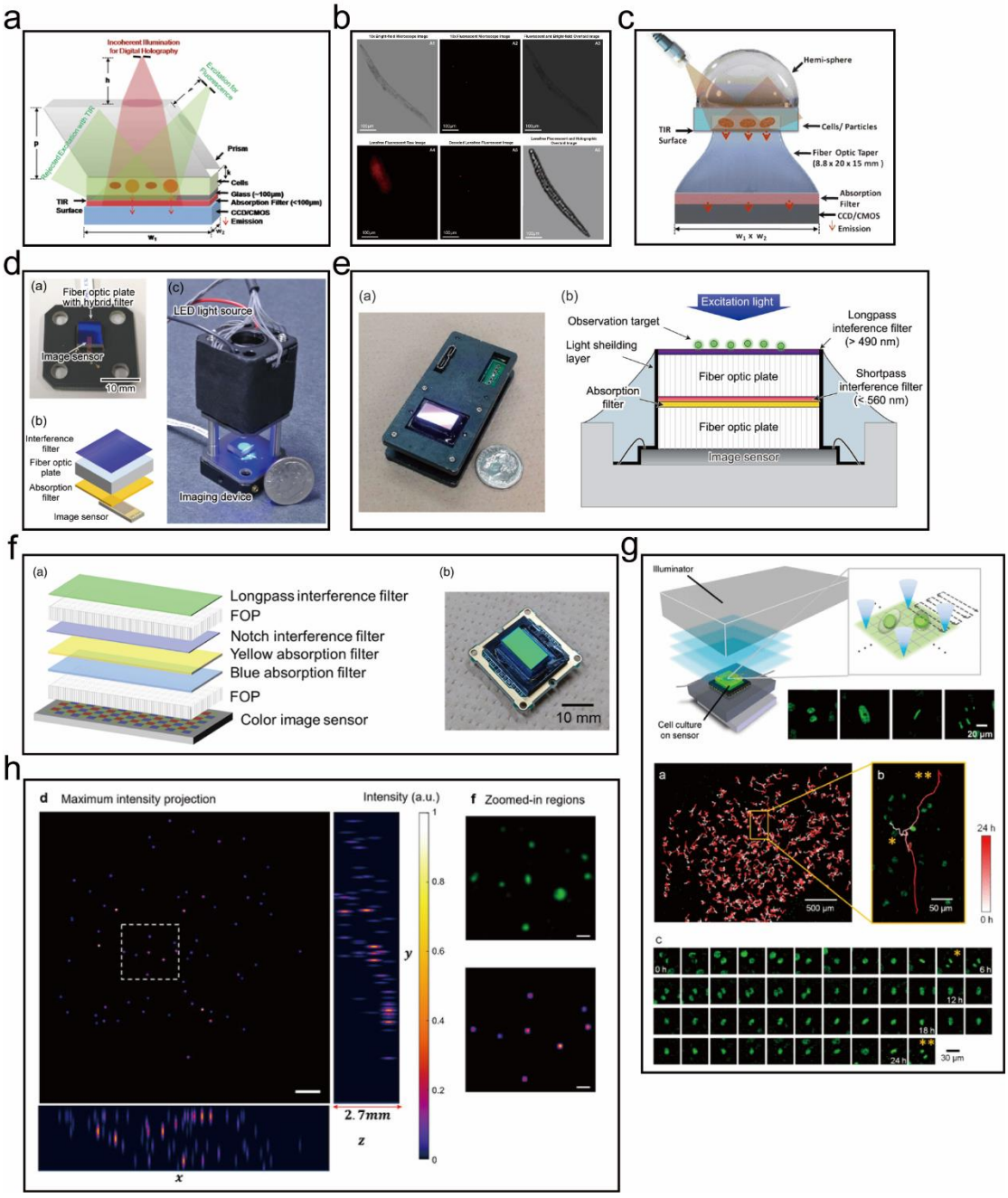

Fig. 2-12. Lensless microscopes for fluorescence imaging. (a-b) Using the TIR principle to reject excitation illumination. (a) [209]. (b) [162]. (c-f) Using optical fibre bundles to relay the image to the sensor. (c) [163]. (d) [166]. (e) [164]. (f) [214]. (g) A lensless fluorescence microscope for longitudinal cell culture monitoring from within the

incubator. The structured illumination is used for enhancing resolution [216]. (h) A miniatured light field lensless fluorescence microscope [204].

2.2.4 Discussion

Section 2 comprehensively examines three LPM categories: smartphone-based, customized, and lensless. Within this segment, we have delved into the distinctive features inherent to each configuration, identifying their respective optimal application domains. The synthesis of information about each configuration is presented in Table. 2-4, which encapsulates various facets of their attributes.

The smartphone-based (droplet) configuration exhibits the lowest level of complexity, with optical magnification achieved using droplets. Nevertheless, owing to the inherent influence of hydrodynamics on lens shape control, this configuration manifests the least favourable imaging performance compared to other configurations. Concurrently, its imaging modality displays suboptimal results, particularly in BF and fluorescence imaging, as detailed in Table. 2-1.

Due to their optomechanical design and incorporation of additional optical components, the other two smartphone-based microscopes (reversed smartphone lens and mechanical adapter) exhibit enhanced imaging quality and offer a broader range of imaging modalities. However, this improvement comes at the cost of intricate hardware configurations. For different smartphones, mechanical structures should be designed into various forms, which means these designs cannot be general. Deploying distinct algorithms and customized mobile applications allows for automated outcomes and real-time analysis in smartphone microscopes. These algorithms necessitate tailoring for specific applications, ensuring high-efficiency computing performance for seamless smartphone operation.

Notably, smartphone-based microscopes yield meaningful images directly, obviating the requirement for computationally intensive data recovery algorithms. Nevertheless, they must meet the demands of applications such as multi-target detection and high-frame-rate video recording, which necessitate robust computational resources. Given their compact size and efficient computing capabilities, smartphone-based microscopes prove most suitable for POCT and healthcare applications in resource-limited areas. Examples include the detection of abnormal cells and the identification of parasites/bacteria in drinking water.

Customized microscopes have a sophisticated optomechanical design tailored precisely to diverse biomedical applications, resulting in superior imaging performance and a broader array of imaging modalities. However, their primary limitation lies in the necessity for meticulous design and construction by experts in optomechanics for each specific application. In contrast to smartphone-based and lensless microscopes, the cost associated with customized microscopes is relatively higher. In terms of software capabilities, customized microscopes are equipped with external data processing units such as laptops, personal computers, and embedded systems (e.g., NJN, Raspberry Pi), enhancing compatibility and facilitating easy customization of software and algorithms for diverse applications. Integration with AI functionalities can be seamlessly realized on these platforms, given their high-performance processors. This attribute renders customized microscopes well-suited for laboratory and community hospital applications, including pathology studies and disease detection.

Furthermore, the remote controllability of most embedded systems associated with customized microscopes extends their utility to real-time cell monitoring in specific chemical environments or incubators, amplifying their versatility in research settings.

In contrast to smartphone-based and customized microscopes, lensless microscopes do

not directly capture images. Instead, the sensor initially captures diffraction patterns or modulated optical intensity fields. Subsequently, recovery algorithms are employed to reconstruct meaningful images from the acquired patterns. The data processing unit for lensless microscopes is also an external computational device. However, the original diffraction patterns or modulated optical intensity fields are susceptible to scattering, reflection, and sensor noise—random phenomena that introduce variability. Consequently, the same algorithm may yield different results across devices, diminishing the software compatibility of lensless microscopes compared to customized microscopes.

The performance of lensless microscopes can vary for different applications and operational environments. In scenarios with low SNR, lensless microscopes may struggle to reconstruct meaningful images. Developing robust algorithms becomes crucial in such cases, though this aspect is beyond the scope of the current study.

The hardware configuration of lensless microscopes is straightforward, comprising a sensor, a light source, and a thin glass cover to protect the sensor. Additional components such as modulation masks, optical filters, and fibre arrays become necessary in MLM and fluorescence imaging setups. The uncomplicated hardware design renders lensless microscopes particularly well-suited for applications in microfluidics and in vivo imaging. However, the rapid dynamic processes inherent in microfluidic movements and in vivo imaging signals pose significant challenges for the sensors employed in these setups.

Table. 2-4. Characteristic ranking of different low-cost and portable microscopes.

Configuration		Hardware			Software		
		Complexity	Imaging performance	Imaging modality	Compatibility	Algorithms necessity	Performance
Smartphone-based	Droplet	✪	✪	✪✪	✪✪	✪✪✪	✪✪✪
	Reversed smartphone lens	✪✪✪	✪✪✪	✪✪✪			
	Mechanical adapter	✪✪✪✪	✪✪✪✪	✪✪✪✪			
Customized		✪✪✪✪✪	✪✪✪✪✪	✪✪✪✪✪	✪✪✪✪✪	✪✪✪	✪✪✪✪✪
Lensless	Shadow imaging	✪✪	✪	✪	✪✪✪	✪✪✪✪✪	Depend on applications
	LDHM	✪✪	✪✪✪✪	✪✪✪			
	MLM	✪✪✪✪	✪✪✪	✪✪✪✪			
	Fluorescence imaging	✪✪✪	✪✪	✪			

2.3 Applications of Low-cost Portable Microscope

LPMs hold promise as diagnostic and analytical instruments, contributing to enhanced healthcare outcomes and the progression of scientific investigations across diverse domains, mainly focusing on resource-limited regions and developing nations. This section encapsulates the most prevalent LPM applications, carefully chosen from prior reviews. We elucidate their biomedical implications and scrutinize various instances of low-cost and portable microscopes employed in each application. In contrast to their applications, we deliberate upon the merits and limitations of distinct devices.

2.3.1 Point-of-Care Testing and Healthcare

POCT plays a pivotal role in contemporary healthcare, denoting medical testing carried out close to the patient, typically at or near the care site, as opposed to the conventional practice of dispatching samples to a central laboratory for analysis. This methodology facilitates real-time test results, empowering healthcare providers to make prompt clinical decisions. Implementing POCT enables the early detection of diseases, facilitating timely interventions and ultimately enhancing patient outcomes.

Particularly in remote or resource-limited regions, POCT devices empower users to attain diagnoses without relying on elaborate laboratory protocols. The streamlining of laboratory processes through POCT contributes to a reduction in healthcare costs.

Notably, the recent advancements in the IoT and high-speed telecommunication technologies, such as 5G, have synergized with POCT, giving rise to a convergence with telemedicine services. This integration allows patients to conduct tests in the comfort of their homes and share the results remotely with healthcare professionals.

Using smartphone-based microscopes emerges as a compelling option for POCT and various healthcare applications. Most smartphones are equipped with high-performance optical lenses and sensors, complemented by robust computational capabilities within their chips. Leveraging the inherent strengths of smartphones, small neural networks such as MobileNets [217], VGG16 [218], and Alexnet [219] can be seamlessly integrated into these devices for real-time diagnostics. Additionally, the rapid communication and data transfer capabilities facilitated by telecommunications infrastructure further amplify the potential of smartphone-based microscopes, thereby advancing the landscape of telemedicine services. However, from both application and engineering perspectives, designing sample holders and mechanical adapters with broader compatibility is imperative to accommodate diverse smartphone models, which ensures versatility and accessibility in deploying smartphone-based microscopes across various devices.

In their work, Knowlton S et al. [69] innovatively crafted a smartphone microscope for cell sorting, employing magnetic focusing in conjunction with fluorescence imaging to facilitate specific clinical assays. This compact system, costing a modest $105.87, proficiently identifies cell types and activities through brightfield, darkfield, or fluorescent imaging modes. Nevertheless, it fails to achieve real-time analysis, as data

processing relies on computer software. The adapter, unfortunately, lacks generalization and is tailored to a specific smartphone model.

Addressing smartphone versatility, Ilyas S et al. [220] devised an external device compatible with various smartphones equipped with external lenses for magnification. Their Matlab algorithm enables the detection of sickle cell disease (SCD) from a drop of whole blood in POCT. Despite this advancement, the real-time analysis application was not transferred to the smartphone, and data analysis requires external devices.

To enhance smartphone-based microscopes, Ozcan et al. harnessed DL technology, designing specific neural networks for SCD diagnosis [1] and image enhancement [87]. Despite generating commendable diagnostic results and high-quality image data, the reliance on external devices for data processing persists.

Dacal E et al. [221] strived towards real-time applications by developing a smartphone-based microscope with real-time DL for quantifying Trichuris trichiura infection. They transplanted the novel DL algorithm to the smartphone, enabling automatic assessment and quantification of parasitological infections by Soil-transmitted helminths in real-time. However, it is worth noting that the entire system exhibits a relatively large volume as a drawback.

2.3.2 Pathology

Pathology is dedicated to examining tissues to diagnose and monitor diseases [222]. Within pathology, capturing high-resolution images with a large FOV is imperative to acquire informative insights and ensure the accurate and efficient diagnosis of diseases.

Medical professionals and researchers have employed benchtop microscopes equipped with high-magnification objective lenses and scanning mechanisms to capture multiple

pathological images. However, this approach comes with inherent limitations, primarily a restricted FOV. To overcome this limitation, researchers employ image registration to stitch multiple images into a comprehensive pathology slide image, achieving both high resolution and a broader FOV. Nevertheless, the scanning mechanism introduces inefficiencies. Furthermore, the process is susceptible to artifacts from unstable mechanical scanning, thereby impacting the quality of the final registered images. Moreover, implementing a precise mechanical stage incurs substantial costs, presenting an additional challenge in the conventional pathology imaging approach.

The primary challenge in pathology imaging is obtaining images with high SBP, which is addressed effectively by applying FP [223]. FP achieves high SBP images by illuminating samples from various directions. For in-depth insights into the detailed implementations and concepts of FP, refer to [223]. Notably, recent advancements have enabled the realization of FP microscopes using low-cost, off-the-shelf devices and 3D printing [74], rendering them well-suited for pathology studies in resource-limited areas.

Aidukas. T et al. successfully implemented a low-cost FP microscope, incorporating a Raspberry Pi embedded system and a cost-effective Bayer sensor. This setup enables the reconstruction of 25-megapixel images with a resolution of 780nm [126]. The system is designed with a 3D-printed microscope structure, weighing a mere 250 grams and boasting external dimensions of 6cm * 9cm * 11cm. Noteworthy innovations include the development of novel image-construction techniques aimed at compensating for misalignments inherent in mechanical movement. The outcome of this approach is the reconstruction of an aberration-free, full FOV lung carcinoma image (~4 mm^2) in both the intensity and phase domains, as illustrated in Fig. 2-8d.

Lee et al. [74] introduced a novel approach to FP microscopy by developing a customized system. Diverging from conventional FP microscopes, they utilized the

smartphone screen as a programmable illumination source instead of an LED array, with the front built-in camera as the imaging device. This unique configuration integrates compact and lightweight optics modules with the smartphone through a self-designed mechanical adapter (Fig. 2-5e). The resulting device achieves a resolution of 870nm over a FOV measuring 2.1*1.6 mm^2, and it encompasses amplitude, phase, and colour imaging capabilities. They developed an Android application for capturing and recovering images in network-disconnected scenarios to enhance practicality. The system successfully reconstructed full FOV amplitude and phase images of unstained blood and Tilia stem samples.

While FP microscopy stands as an effective method for pathology studies, it does present several challenges. Careful calibration of the illumination angle is required, and the arrangement of the light source significantly impacts the final image reconstruction. A multi-illumination scan becomes necessary, and the recovery of phase and amplitude images demands high-robustness algorithms. These factors collectively impede the imaging speed and quality of the FP microscope.

In contrast, researchers can employ lensless microscopy, particularly LDHM, to obtain high SBP images in both amplitude and phase domains, thereby enhancing the efficiency of pathology studies. The LDHM approach involves only two optical components: a partially coherent illumination source and a sensor. This streamlined configuration offers a potentially more efficient and simplified solution for pathology imaging.

In lensless microscopy, samples are directly positioned atop the sensor's cover glass, where the microscope's FOV and resolution are intricately linked to the sensor's active area and pixel size. Given the typically high density of pathology slides, achieving robust phase and amplitude recovery necessitates capturing more than 6-8 images at

different sample-to-sensor distances.

To streamline the image reconstruction process, Rivenson et al. [192] identified that natural images often exhibit sparsity in specific domains. Leveraging this observation, they introduced a sparsity-based phase reconstruction technique implemented in the wavelet domain. This innovative approach reduces the number of required images for reconstruction by at least 2-fold. By successfully integrating their sparsity-based phase reconstruction algorithm with a simple lensless microscope, they accomplished imaging of breast cancer tissue slides over a substantial FOV of approximately 20 mm^2, as depicted in Fig. 2-10h.

Luo et al. [141] pursued a similar objective in a parallel effort. Rather than varying the sample-to-sensor distance for robust image reconstruction, they embraced the synthetic aperture-based principle. This principle involves scanning the illumination angle across the dome surface, similar to FP microscopy, to enhance the effective NA of the reconstructed lens-free image (Fig. 2-10g). Remarkably, this approach allows the system's NA to reach 1.4, achieving a resolution of approximately 250nm at a wavelength of 700nm. Additionally, their method enables colour imaging of pathology slides without requiring multi-height scanning. The researchers successfully applied their technique to image colour-stained cancer tissue slides and unstained Papanicolaou smears over a substantial FOV of 20.5 mm^2.

In the realm of pathology studies, customized FP microscopes and LDHMs emerge as the most fitting methodologies. While FP microscopes tend to boast more intricate mechanical structures than LDHMs, their recovery algorithms are notably more robust. Conversely, LDHMs rely heavily on advanced recovery algorithms and feature more compact dimensional sizes. It is worth noting that LDHMs can be combined with the FP illumination method to achieve high NA images. Nevertheless, both technologies'

reliance on multi-illumination or multi-height detection approaches is a common challenge. Overcoming this challenge by reducing the number of required detections and enhancing overall efficiency is a crucial goal for future studies in these fields. Efforts toward streamlining and optimizing these imaging techniques will undoubtedly contribute to advancing pathology studies.

2.3.3 Cell Monitoring

LPMs find extensive applications in cell monitoring studies. In the field of biology, cell monitoring involves the study of cell behaviours, measurement of cellular activities, and observation of cellular processes [224]. Microscopy is crucial in cell monitoring, particularly in live-cell imaging [225] and cell culture monitoring [226]. In many cell monitoring studies, observing how cells respond to various environments necessitates the live recording of microscopic images or videos under specific physical conditions, such as within a CO_2 incubator, which implies that imaging devices should be remotely controlled under these specific environments. In such application scenarios, customized and lensless microscopes emerge as favourable choices due to their adaptability and versatility.

Customized microscopes, as discussed in section 2.2.2, offer the advantage of easy construction for various applications. The incorporation of 3D-printed mechanical structures enhances their adaptability and cost-effectiveness. The evolution of semiconductor technology has resulted in the production of compact-sized embedded systems. This development allows for direct integration with customized microscopes, enabling the application of data analysis and remote-control functionalities. Consequently, a high level of integration can be achieved with customized microscopes, where optical systems, electronic devices, and mechanical components are seamlessly combined into a single platform. This integrated approach contributes to enhanced functionality and efficiency in diverse applications.

A notable example of a customized compact live-cell imaging platform is the MAM, proposed by Son. J et al. [108]. MAM integrates twelve miniature microscopes, a 12-well plate, an LED array, and a USB hub for connecting to control systems, such as computers or embedded systems. Positioned as a cell monitoring platform, MAM is designed to be placed inside an incubator for time-lapse recording. Each miniature microscope within MAM is equipped with a GRIN objective and features individually addressed illumination and digital components. This design allows for the time-lapse recording of a specific well in the 12-well plate (Fig. 2-8g). MAM provides high fluorescence efficiency and low photo-toxicity for fluorescence observation, enabling parallel data acquisition. It achieves approximately 3μm lateral resolution with a temporal resolution of 60Hz.

Researchers have successfully utilized MAM for imaging fixed COS-7 populations stained with HCS NuclearMask Deep Red and recording time-lapse videos of living COS-7 cells within the incubator. Despite its strengths as a potent cell monitoring platform suitable for incubator use, MAM does have some limitations. Firstly, it is limited to 12-well plates and cannot be adapted to other biological containers. Additionally, it requires cable connections, posing a constraint on its flexibility and manoeuvrability.

To achieve remote control and automated image recording, Ly. V et al. developed a customized low-cost multi-camera and robotic imaging platform called Picroscope, designed for simultaneous cell monitoring [117]. Picroscope has 24 individual objectives, offering a resolution of approximately 7μm. The platform incorporates several Raspberry Pi Hubs and Arduino Uno for remote control and automatic image capture, eliminating the need for cable connections (Fig. 2-8h). Notably, the embedded systems in Picroscope are equipped with temperature and gas sensors, enabling

environmental monitoring during cell culture. Picroscope can perform automated image recording of a 24-well cell culture plate within the cell incubator. The captured data is then transferred to a remote computer or server for real-time results viewing during post-processing. Additionally, Picroscope can automatically execute brightfield z-stack imaging throughout the imaging process.

In assessing Picroscope's performance, researchers employed the system to monitor various animal embryonic models (Xenopus tropicalis, Danio rerio, and planaria worms) during development and regeneration in the longitudinal direction. Furthermore, Picroscope was utilized for imaging human embryonic stem cells and 3D cortical organoids within a standard tissue culture incubator. Compared with MAM, Picroscope offers remote control and additional automatic functions. However, it currently encounters limitations in brightfield imaging, and its physical size is relatively substantial. Like MAM, Picroscope is specifically designed for use with a particular well plate and lacks broader applicability.

Due to their compact design, lensless microscopes offer increased accessibility for cell monitoring within incubators. In a study by Ohta. J et al. [166], a lensless fluorescence imaging device was developed specifically for cell culture monitoring in a CO_2 incubator. Maintaining a short distance between the sensor and the sample is essential in lensless microscopes. To overcome this limitation and extend the sensor-sample distance, researchers implemented an FOP above the sensor, serving as a relay for the image to reach the sensor. A sandwich structure was also employed, placing the FOP between interference and an absorption filter to enable fluorescence observation (Fig. 2-12d). A small cell culture chamber was also fabricated, allowing direct integration with the lensless microscope. The resolution achieved by this imaging system is approximately 12μm.

For validation, time-lapse imaging of GFP-transfected HEK293 cells was captured at 10-minute intervals for 22 hours, all within the confines of the incubator. This lensless microscope configuration showcases its potential for real-time and long-term cell monitoring applications within controlled environments like CO_2 incubators.

While lensless microscopes offer the advantage of compactness, they face challenges when it comes to easy integration with commercial cell culture plates, such as 12-well or 96-well plates. Additionally, data analysis and post-processing can be intricate in lensless microscopy. Moreover, due to their compact size, implementing remote control and automated mechanisms on these platforms can be challenging. The limited dimensions pose difficulties, mainly because most mechanical components are larger than the camera sensor. As a result, realizing efficient remote control and automation features requires careful consideration and engineering efforts to overcome the constraints posed by the compact design of lensless microscopes.

2.3.4 Microfluidic Applications

Microfluidic involves the operation and control of tiny fluids from microliters to nanolitres. Generally, the core of microfluidics is the microfluidic chips, which are fabricated by semiconductor microfabrication technologies. Inside the chips are many intricate networks of channels and chambers on a small scale for chemical reactions. These devices are often called LOC systems, enabling precise control of fluid flow, mixing, and reaction processes [227]. For biomedical and healthcare research, microfluidic can reduce sample and reagent volumes, increase reaction times, and improve sensitivity. Moreover, thanks to its small size, microfluidic chips can integrate multiple analytical functions into a single platform. Some of the applications of microfluidics are POCT, environmental monitoring, chemical synthesis, and biological research [228].

Using microscopes in microfluidic applications is essential. It plays a crucial role in

enabling precise microscale observation and analysis of fluidic processes. Microscopes allow researchers to visualize fluid dynamics, particle interactions, and biochemical reactions in real time, offering insights into the intricate details of microscale phenomena. This visual feedback is essential for optimizing device performance, validating theoretical models, and ensuring the reliability of microfluidic systems. Moreover, microscopy facilitates the examination of cells, particles, and other biological entities within microfluidic environments, advancing applications in fields such as biology, medicine, and diagnostics. Integrating microscopes with microfluidic platforms enhances our ability to explore and exploit the full potential of these miniature systems, contributing significantly to advancements in research, diagnostics, and various industrial applications.

Both customized and lensless microscopes are suitable for microfluidic applications. In [113], Tristan et al. constructed an portable fluorescence microscope that operates in bright-field mode and in three fluorescence channels: UV, green, and red. The system is assembled by six 3D printed parts and cost only 122 USD. A Raspberry Pi was programmed in Python to capture time-lapse images and videos. They successfully used the proposed microscope to realize single-channel microfluidic device observations. They injected THP-1 cells stained with Calcein-AM at a speed of ~150 μm/s, and recorded a video while cells flowed through the channel (Fig. 2-8c).

To obtain large FOV images efficiently, Zhang et al. established a LDHM for large number of sperms tracking in the microfluidic chip [169]. They integrated a lensless charge-coupled device (CCD) with a microfluidic chip to facilitate a wide field of view (FOV) and automatic recording while sperm traverse a microfluidic channel. This integrated system allows for the sorting and tracking of a population of sperm within the microfluidic channel. Similar to the clinically employed swim-up column method, the channel can be observed in both horizontal and vertical configurations. The motility

of sperm can be quantified by tracing the shadow paths of individual sperm. Additionally, as sperm are sorted by swimming from the inlet toward the outlet of the microfluidic channel, motile sperm reaching the outlet can be extracted from the channel after the process.

As previously discussed in Sections 2.3.2 and 2.3.3, customized microscopes exhibit sophistication in hardware design, whereas lensless microscopes demonstrate sophistication in algorithms. Considering their distinctive characteristics and varied microfluidic applications, choices can be tailored to specific scenarios. The lensless microscope stands out as a suitable option for LOC applications involving slow-speed activities, such as organ-on-chip monitoring. Because lensless microscopy highly relies on post-processing algorithms, processing high frame-rate video data imposes a significant computational burden, influencing the final reconstruction results. Moreover, lensless microscopy is appropriate for acquiring high SBP images without a mechanical scanning process.

Conversely, customized microscopes are more adept for high-speed LOC applications like flow cytometry and high-throughput particle tracing. Implementing advanced algorithms in High-Performance Embedded Systems, exemplified by NJN and Raspberry Pi, facilitates image reconstruction and data analysis. Additionally, researchers can design high-magnification and NA optical paths to counteract sampling loss in the spatial domain when utilizing multi-pixels instead of a single pixel in a CMOS sensor for processing high-speed events.

2.3.5 Discussion

This section comprehensively discusses selecting suitable LPMs for various biomedical applications. Considering the configuration of LPMs and the distinctive features of different biomedical applications, researchers can employ LPMs in resource-limited

settings across four biomedical scenarios: POCT and healthcare, pathology, cell monitoring, and microfluidics. Table. 2-5 guides on selecting appropriate LPMs for distinct biomedical applications, accompanied by corresponding challenges. This framework is intended to direct researchers towards the correct path for the future development of diverse LPMs.

Choosing smartphone-based microscopes in POCT and healthcare applications proves advantageous owing to their compact size and integrated communication capabilities. Results can be conveniently obtained through dedicated smartphone applications and transmitted to designated users or professionals. However, this platform encounters two challenges: Firstly, researchers and engineers must design mechanical adapters tailored for various smartphone models to ensure broader compatibility. Secondly, smartphones are constrained by limited computing power, restricting their applicability to relatively straightforward tasks such as target recognition, counting, fluorescent signal analysis, and segmentation.

In pathology applications, opting for lensless microscopy proves to be a superior choice. While FP microscopy can also be employed to capture high-resolution images, its configuration is more intricate than lensless microscopy, and using a multi-illumination method requires precise LED calibration. Furthermore, a lensless microscope can be seamlessly integrated with an FP illumination setup to enhance overall image quality. The primary challenge associated with the lensless microscope lies in the requirement for multi-height detection. This hurdle could be overcome by exploring more robust algorithms and applying deep learning techniques.

Considering the dimensions and mechanical structure of cell culture containers, as detailed in section 2.3.3, customized microscopes are highly practical for cell monitoring experiments. These microscopes can be conveniently situated within the

incubator, seamlessly integrating with cell culture containers for continuous real-time monitoring. Achieving remote control is feasible by employing an embedded system as the processing unit. However, a challenge similar to smartphone-based microscopes arises, emphasizing the necessity for a highly compatible mechanical design.

As outlined in section 2.3.4, while both customized microscopes and lensless microscopes are viable options for microfluidic applications, the latter is a more favourable choice, particularly when considering the compact size of microfluidic chips. However, the imperative need for high-frame-rate video recording arises in situations involving high-speed events such as particle tracking and cytometry. This requirement means the algorithms should be highly robust to highly efficient data processing and image reconstruction.

Table. 2-5. Proper LPMs and corresponding characteristics for different biomedical applications.

Biomedical applications	Proper LPM	Problem
POCT & Healthcare	Smartphone-based microscope	● Mechanical adapters should be designed with broader compatibility. ● Computing power is limited
Pathology	Lensless microscope	Multi-height detection
Cell monitoring	Customized microscope	Compatible mechanical design is necessary
Microfluidic	Lensless microscope	Algorithms with high robustness is necessary for high frame rate videos processing and image reconstruction

2.4 Conclusion

In this chapter, a comprehensive review is conducted on articles about three distinct types of LPMs: Smartphone-based, customized LPMs, and lensless microscopes. Each type is carefully discussed, focusing on introducing the corresponding hardware

configurations and inherent characteristics. Subsequently, a critical analysis is presented, addressing the identified limitations and proposing viable solutions for each type. Following an extensive examination of prevalent application scenarios for LPMs, emphasis is placed on four prominent biomedical applications: POCT and healthcare, pathology, cell monitoring, and microfluidics. A choice of optimal platforms is provided for each application, accompanied by a comprehensive discussion of prevailing challenges. This examination offers valuable insights that can guide researchers in shaping the trajectory of future investigations in this domain.

Chapter 3. PAIM (πM): portable AI-enhanced fluorescence microscope for real-time target detection

In this research, a portable AI fluorescence microscope (πM) has been introduced, utilizing a webcam in conjunction with the NVIDIA Jetson Nano (NJN) for immediate target detection through edge computing techniques. πM offers a physical magnification of ×5 and demonstrates the ability to resolve 228.1 lp/mm (line pairs per millimetre) USAF features, making it suitable for imaging microscopic samples and fluorescent polystyrene (PS) beads. πM's body was fabricated using a 3D printer, with a weight of approximately 250 grams and physical dimensions measuring 145mm in length, 172mm in width, and 144mm in height (L×W×H), costing ~$400. It has a similar brightfield imaging quality to benchtop microscopes (~$13,000). The customized Convolutional Neural Network (CNN) integrated into the NJN can perform feature extraction, real-time counting of PS beads, and red blood cell counting without the need for data transfer or image processing. Compared to two model-free image processing methods (OpenCV and CLIJ2), our CNN approach demonstrates robustness in counting beads at various concentrations. It achieves an accuracy of 80% in counting six aggregated beads. In terms of feature extraction and human red blood cell (RBC) counting, our CNN method demonstrated results that were closer to the ground truth (GT) when compared to the CLIJ2 method (GT: 201; CNN 196; CLIJ2: 189). With its compact size and real-time analytical capabilities, πM has potential in point-of-care testing, field microorganisms detection, and clinical diagnosis in resource-limited areas.

3.1 Introduction

Microscopes can reveal biological and biochemical processes. Over the past two decades, advancements in technology, such as 3D printing methods, MEMS (Micro-

Electro-Mechanical Systems) systems, and diffractive optical elements have led to the miniaturization of microscope systems. Additionally, integrating new CMOS sensors and well-crafted optical lenses into smartphones has allowed for the development of compact microscopes. These miniaturized microscope systems are user-friendly, portable, and cost-effective compared to traditional laboratory microscopes. They have the potential to support various applications, including the diagnosis of conditions like sickle cell disease [220,229], sperm cell monitoring [230,231], and the detection of hazardous materials in drinking water in resource-limited areas [83,113].

Numerous researchers utilize 3D printing technology to create compact and cost-effective microscope systems. For instance, Bowmen et al. established the OpenFlexure microscope [109,118,119], which has applications in education, scientific research, and clinical settings in Tanzania and Kenya. Delmans and Haseloff proposed the μCube framework for 3D printing optomechanical parts for users to reconfigure their microscopes rapidly [122]. Diederich et al. also developed similar work. They developed microscopic components as LEGO-like building blocks to establish more complex systems [101]. The cheapest microscope, the Foldscope, was fabricated through origami techniques, with a production cost of less than $1. This innovative device can perform both brightfield and fluorescence imaging [232].

Furthermore, more scientific and precise experiments can be achieved in open-source portable microscopes, such as real-time in-vivo neuron imaging [233] and single-molecule detection [92]. ANNs have recently enhanced portable microscopes' data processing capacity. Shen et al. used only one aspherical lens to build a microscope. They used a deep learning (DL) algorithm to improve the resolution power and minimize optical aberrations [234]. Besides these intensity-based microscopes [90,102,235], Ozcan et al. used off-the-shelf devices and 3D printers to develop portable quantitative phase microscopes and holographic microscopes [129]. They used

ANNs or iterative algorithms to recover samples' morphology instead of optical lenses [155,184,236,237]. Harvey et al. developed a low-cost 3D-printed Fourier ptychography microscope based on a Raspberry Pi. This system can computationally construct images with a high space-bandwidth product (25-megapixel with sub-micron resolution). They also used a novel algorithm to minimize aberrations [126]. Cacace et al. published design guidelines for a compact off-axis holographic microscope. They successfully used their prototype image flowing marine microalgae, polystyrene beads, E.coli bacteria, and microplastics [238]. To solve the problem of malaria diagnosis in remote regions where benchtop microscopes are unavailable, Gordon et al. designed a portable microscope with monochromatic visible illumination with a long working distance singlet aspheric objective lens. The detection limit can reach 0.18 parasites per 100 red blood cells [111].

Smartphone-based microscopes are easier to operate than open-source microscopes which are mentioned above. Ozcan et al. developed different smartphone-based microscopes for imaging viruses [66] and DNA molecules [67], detecting Giardia lamblia cysts [56], and screening sickle cells [1]. They combined a smartphone with optical fibre arrays to develop a high-resolution computational microscope. They used the Wiener deconvolution algorithm to reconstruct images of blood smear samples [85]. Trofymchuk et al. built a smartphone microscope and carried out a single-molecule detection assay for DNA specific to antibiotic-resistant Klebsiella pneumonia [75]. Lee and Yang developed a lensless smartphone-based microscope by removing the camera lens [239]. They made a compact system using ambient light illumination. This microscope can capture ultra-wide field-of-view (FOV) images with a sub-micron resolution. Dai et al. coupled different coloured polymer droplet lenses on smartphones to realize brightfield and fluorescence microscopes without optical lenses and filters. It can observe cells and tissues, count cells, and evaluate plasmid transfection and superoxide production [51]. Sung et al. developed a multicolour fluorescence

smartphone microscope [81]. They used total-internal-reflection (TIR) guided illumination inside the glass slide. This configuration can enhance images' signal-to-background ratios. Müller et al. optimized a peptide nucleic acid (PNA) based fluorescence in situ hybridization (FISH) assay and used a smartphone microscope for rapid identification of pathogenic bacteria [82]. Liu et al. demonstrated a portable smartphone microscope called MUSE, the first practical implementation of microscopy with ultraviolet surface excitation. This MUSE is a powerful tool for point-of-care diagnostics, health monitoring, and environmental studies [65]. McKay et al. used iPhone and an additional iPhone camera lens to resolve optical absorption gaps in nailfold capillaries. The system has a 4μm resolution with 1 mm^2 FOV [63]. Moreover, computational microscopes, such as Fourier ptychography microscopes [240], phase contrast microscopes [71,72,241,242], and 3D phase microscopes [44,45], can also be constructed using smartphones.

Several deep-learning techniques have been developed to process images captured from portable microscopes [87,243–246]. Göröcs et al. developed a portable deep-learning imaging flow cytometer for drinking water analysis [247,248]. Zhang et al. constructed a magnetically modulated lensless cytometry for blood cell detection [249]. Wu et al. developed a lensless microscope for herpes simplex virus detection and used DL to reconstruct high-quality images [250]. O'Connor et al. developed a compact digital holographic microscope. The built-in long short-term memory (LSTM) neural networks successfully classified different animals' blood cells, normal and sickle blood cells from human blood [251]. The system can also screen blood cells for COVID-19 tests [106].

In this project, I proposed a portable AI-enhanced fluorescence microscope equipped with real-time AI capabilities. Most open-source microscopes have complex optomechanical structures and rely on external devices such as laptops or computers for operation. Smartphone microscopes, while compact, often need more computational

power for image processing. In contrast, the πM microscope offers a balanced solution. Table. 3-1 provides a comparative analysis between πM and several similar existing systems. Compared to these systems, our approach stands out due to its innovative integration of optical imaging components and a data processing unit within a straightforward mechanical structure, all while maintaining a low cost. The utilization of a readily available off-the-shelf webcam lens yields excellent imaging quality without the need for intricate optimization algorithms or complex optical designs. Furthermore, the neural network can be easily tailored to various applications. The ease of configuration and cost-effective design make it well-suited for on-site network training and data collection.

πM costs ~$400 and weighs 670g with a size of 145 mm × 172 mm × 144 mm. It has a ×5 physical magnification and can resolve 228.1 lp/mm using the USAF target as an object. πM has two key innovations: First, it has a simplified optical path and mechanical design, making it accessible for individuals with limited mechanical design experience, allowing anyone to design it; Secondly, πM enables real-time AI-enhanced analysis using NJN-embedded neural networks for specific applications, and data transfer to the cloud or servers is unnecessary.

I demonstrated πM by imaging samples and different fluorescent PS beads, realizing real-time feature extraction and counting of beads and human RBCs. We compared the OpenCV, CLIJ2, and our customized CNN methods in bead and human RBC counting experiments. Our CNN can recognize six aggregated beads with 80% accuracy (OpenCV: three aggregated beads with 26% accuracy; CLIJ2: six aggregated beads with 64% accuracy). It shows results closer to the ground truth (GT) than the CLIJ2 method (GT: 201; CNN: 196; CLIJ2: 189) in human RBC recognition and counting. These experimental results provide a proof-of-principle debut of πM.

Table. 3-1. Comparative analysis between recent similar schemes.

	Optomechanical complexity	AI function	Resolution	Application	Dimensional size (L*W*H)	Cost
Bowman et al. [109]	High	No	0.48μm	Brightfield, fluorescence, and polarization imaging	150*150*200 mm^3, ~500g	~ $ 250
Heintzman et al. [101]	High	No	0.6μm	Observations of a transgenic Zebrafish expressing green fluorescent protein (GFP)	200*50*200 mm^3 (Alterable)	$ 140~ $ 680 (Altertable)
Zhu et al. [234]	Low	Yes	0.66μm	Brightfield imaging	200*200*400 mm^3	N/A
Zhou et al. [129]	Medium	No	1.15μm	PRCs phase imaging, material metrology	370*320*80 mm^3	~ $ 5000
Ferraro et al. [238]	Low	No	0.58μm	Holographic microscope, flowing marine microalgae, polystyrene beads, E.coli bacteria and microplastics imaging	~50*30*150 mm^3	~ $ 880
Gordon et al. [111]	High	Yes	0.8μm	Automated malarial parasitemia quantification in thin blood smears	300*200*130 mm^3	~ $ 1318
Ozcan et al. [1]	Medium	Yes	< 1μm	Sickle cell disease detection	Smartphone+350g	$ 60+Smartphone
Trofymchuk et al. [75]	Medium	No	1.2μm	DNA origami single molecule detection	~ 200*150*200 mm^3	~ $ 4600
Jenkins et al. [65]	Medium	No	3-4μm	Ultraviolet Surface Excitation microscopy	138.3*67.1*7.1 mm^3 (iPhone 6s size)	iPhone 6s + $ 10
Durr et al. [63]	Low	No	< 4μm (central FOV) < 6μm (peripheral)	Quantification of optical absorption gaps in nailfold capillaries, neutropenia screening	143.6*70.9*7.7 mm^3 (iPhone X size)	N/A
Kuang et al. [72]	Medium	Yes	N/A	Virtual phase contrast imaging	120*100*170 mm^3 400g	Smartphone + $ 1~10
This work	Low	Yes	1.62μm	Aggregated RBCs segmentation and counting	145*172*144 mm mm^3, 250g	$ 300

3.2 Method

3.2.1 πM Framework

Fig. 3-1(a) shows the πM framework. The NJN acts as the CPU to control the system. It incorporates illumination LEDs and a CMOS camera. Users can train and implement ANNs inside the NJN for real-time analysis. While we used a laptop to manage πM in this project, it can be seamlessly replaced with a touch screen interface. Ray-tracing simulations (OpticStudio 2017) and experiments determine πM's dimensional size and optical paths. The construction of πM's main body components was carried out using

CAD software (Solidworks, 2020), and these components were subsequently 3D-printed.

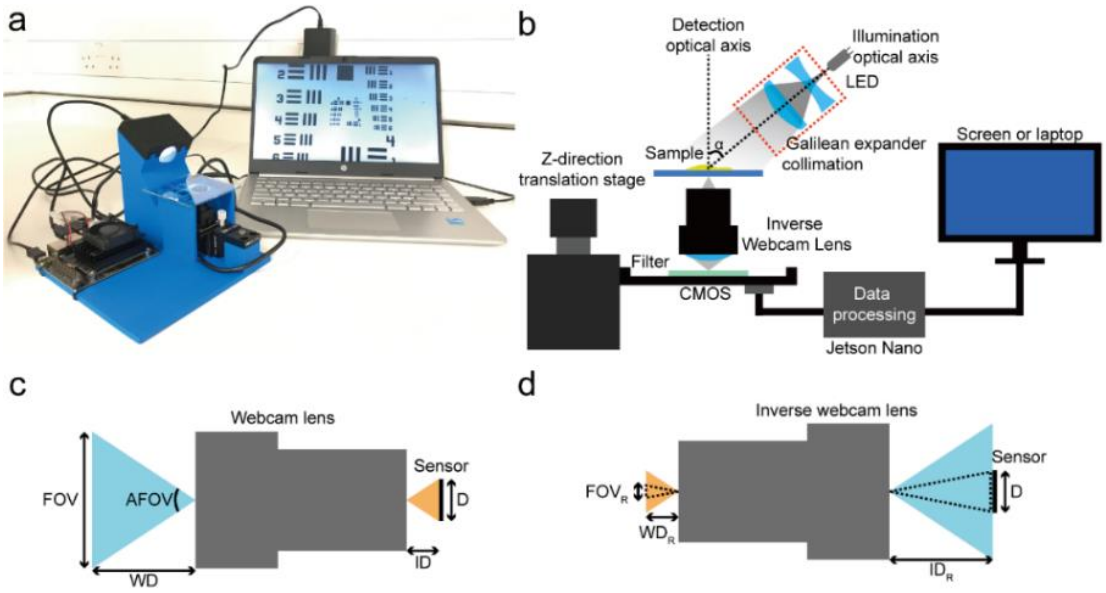

Fig. 3-1. (a) πM diagram. (b) πM optical path. A filter is inserted between the CMOS and the inverse webcam lens for observing fluorescent signals. The customized ANN in the NJN can realize real-time image analyses. (c) The original webcam optical path. (d) πM's optical path. Dashed triangle lines indicate the effective FOV in both object and image spaces (FOV: field of view, WD: working distance, ID: image distance, D: sensor's horizontal size, FOVR: πM's effective field of view, WDR: πM's working distance, IDR: πM's image distance).

3.2.2 Imaging System Design

Fig. 3-1(b) illustrates πM's optical path. It provides the flexibility to utilize a white LED for brightfield imaging or substitute it with a different wavelength for fluorescence imaging. A biconcave and a scattering aspherical condenser lens were used for Galilean expander collimation. The biconcave lens expands the light, while the condenser lens collimates it.

One notable feature is the angle α (where α = 60°) between the illumination and detection optical axes. This configuration enhances the image contrast of transparent biological samples while preventing the direct collection of excitation light by the inverted webcam lens when πM is used for fluorescence observation.

In the optical detection path, a webcam lens from an off-the-shelf internet webcam was disassembled (ELP, Shenzhen, China) and reversed as an objective lens for our system. A specialized holder was designed to integrate this lens with the camera sensor and the optical filter. Subsequently, the refitted webcam with an inverted webcam lens was harnessed to a z-direction translation stage, allowing for precise adjustment of the focal plane. It is important to note that the webcam lens we utilized was already well-optimized. Therefore, this setup substantially magnifies the samples with minimal optical aberrations, particularly regarding spherical aberration.

Before designing mechanical structures, the distances between optical elements (ID_R and WD_R in Fig. 3-1(d)) were first calculated. Since only a few parameters of the webcam lens working in the webcam optical path were known (Fig. 3-1(c)), we first used these parameters in combination with the paraxial approximation to calculate approximate values in Fig. 3-1(c). Then, we reversed the system and obtained the corresponding parameters in Fig. 3-1(d).

Here we first consider the monochrome camera sensor. According to the Nyquist sampling requirement, the sampling frequency should be two times as high as the spatial frequency. To get a better resolution, we increase it to three. The magnification ($PMAG_R$) is:

$$PMAG_R = \text{ceiling}\left(\frac{3\times Pixel\ pitch}{L_{res}}\right), \tag{3-1}$$

where L_{res} is the theoretical resolution and the pixel pitch is the distance between neighbour pixels (1.62 μm).

The minimum resolution is set to 1μm for πM to observe biological samples and $PMAG_R = 5$. The imaging system functions for the webcam optical path in Fig. 3-1(c) are:

$$F = \frac{horizontal\ pixel\ number \times \text{pixel pitch} \times WD}{FOV} \approx ID, \tag{3-2}$$

$$PMAG = \frac{1}{PMAG_R} = \frac{horizontal\ pixel\ number \times \text{pixel pitch}}{FOV}, \tag{3-3}$$

where the sensor's horizontal pixel number and the pixel pitch are 3840 and 1.62μm, respectively. $PMAG_R$ is 5, and F (back focal length) is 3.6mm. As a result, W_D is approximately 18mm, WD_R is 3.6mm, and ID_R is 18mm.

It should be noticed that the formulas presented here are not exact solutions but rather approximations intended to guide us in determining an optimal starting point for the reversed webcam lens experiment. Due to the lack of specific details about the webcam lens, these estimated values provide a useful foundation for establishing a starting point and range for our tests aimed at achieving the desired outcomes. In practice, when employing a colour sensor equipped with a Bayer filter, the sampling rate should be quadrupled compared to the minimum required by the Nyquist criterion. Additionally, in equation 3-2, we simplify the webcam lens in its standard configuration to a thin lens model, which is an imprecise representation. Nonetheless, these approximations serve primarily to narrow down the initial testing range for subsequent experiments. For attaining accurate results, relying on simulations and hands-on experimentation is the most reliable approach.

Meanwhile, choosing a 1μm resolution is for RBCs counting. RBCs typically ranging between 6 to 8 micrometres in diameter.

I estimated ID_R = 13 ~ 18mm in ray-tracing simulations and plotted WD_R vs ID_R, $PMAG_R$ vs ID_R, and $PMAG_R$ vs WD_R curves in Fig. 3-2(c-d). WD_R and $PMAG_R$ were tested at each data point five times to obtain mean values and standard variations (the error bars). ID_R is chosen as 14mm to achieve the average WD_R of 5.41mm and an average lateral magnification of ×5.14.

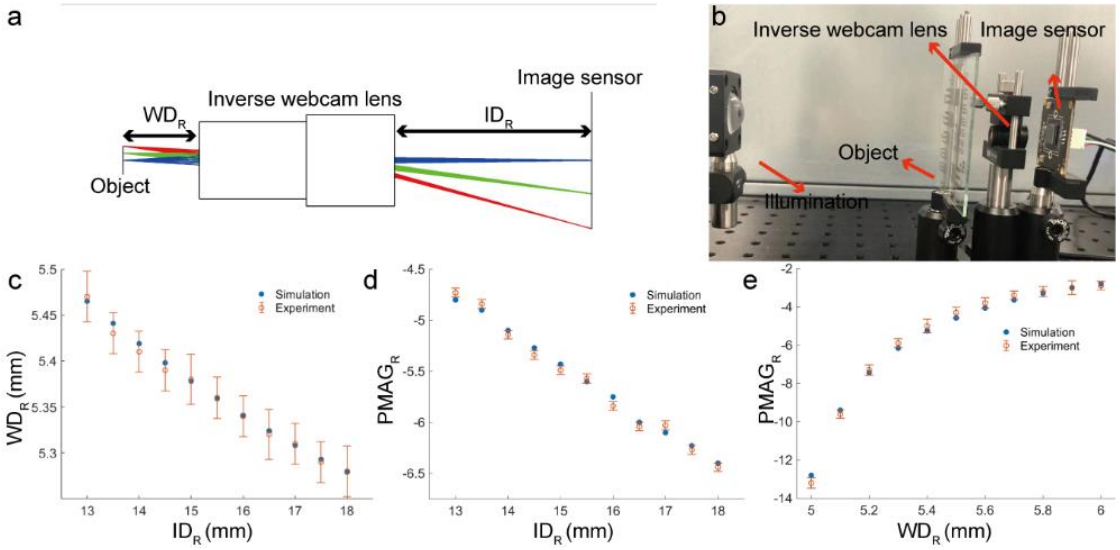

Fig. 3-2. Inverse webcam lens measurements. (a) Ray-tracing simulations of the inverse webcam lens. Blue, green, and red rays correspond to 0mm, 0.5mm, and 1mm object height. (b) The experiment configuration. The object (R3L3S1P, Thorlabs) is illuminated by the white LED (LEDW7E, Thorlabs). Illumination lights are collimated by a diffusive surface aspherical lens (ACL2520U-DG15, Thorlabs). (c), (d) and (e) are relationships between ID_R, WD_R, and lateral magnifications.

3.2.3 Illumination Path

Simulated and experimental results were used to optimize πM's illumination path to obtain even illumination at the object plane, as shown in Fig. 3-3(a). A concave lens

(LD2746, Thorlabs) and an aspherical lens (ACL2520U-DG15, Thorlabs) were used to constitute a Galilean collimator. This configuration can collimate light at a shorter distance. *D1* and *D3* were set as 10mm and 50mm, respectively. The Zemax RAID operand was used to calculate *D2* = 8.037mm. During the experiment, we positioned a piece of white paper at the target location, situated 50 mm from the rear surface of the aspherical lens, as illustrated in Figure 3-3(a). The light illuminated the white paper, creating an intensity profile. A camera was placed on the opposite side to capture this intensity profile. Fig. 3-3(b) shows experimental results before and after collimation. Corresponding line profiles are shown in Fig. 3-3(c). The LED's intensity was concentrated at the centre, leading to excessive illumination power from the uncollimated LED. This high power caused saturation in the camera sensor, creating an uneven light intensity distribution across the surface of the target plane. This resulted in a profile that appeared almost flat in the central region of the surface.

To better understand how collimated illumination affects the spatial resolution of brightfield and fluorescence microscopes, I compared the πM illumination with the critical and the Köhler illumination. The USAF-1951 (R3L3S1P, Thorlabs) was used as the test target, and the white LED (LEDW7E, Thorlabs) illumination source was chosen for brightfield imaging. Three different PS beads were used as samples (blue-green, Ex 430/Em 465; yellow-green, Ex 505/Em 515; red, Ex 580/Em 605; Thermofisher) for fluorescence imaging and chose appropriate single wavelength LED sources (430nm, 505nm, Lumex; LED591E, Thorlabs) for illumination.

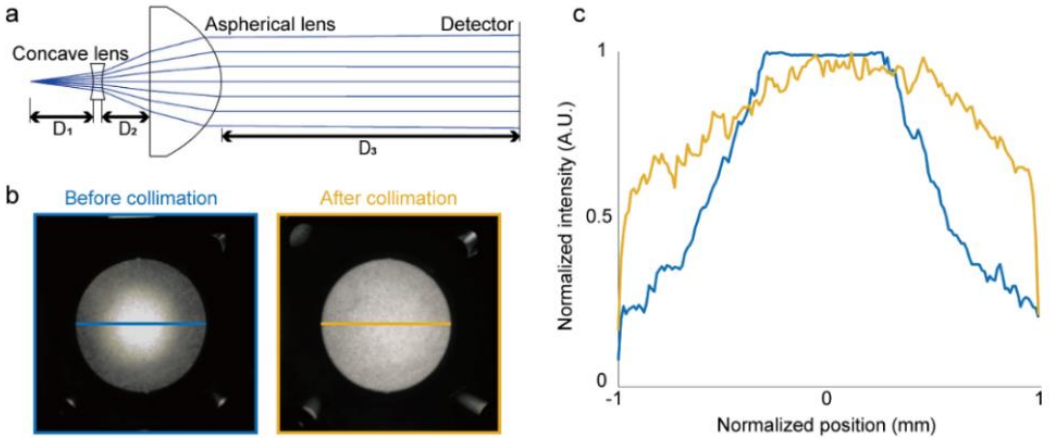

Fig. 3-3. Collimation light path. (a) The simulated collimation optical path. (b) Intensity distribution before and after collimation. (c) Corresponding line profiles of (b).

Fig. 3-4(a) illustrates three different illumination types. The light source is projected to the sample plane in critical illumination by a single convex lens (LD2746, Thorlabs). While this setup is the simplest, it has the drawback of imaging the light filament onto the sample plane, which can adversely affect image quality. Moreover, it can only illuminate a small region. On the other hand, Köhler and πM illuminations can collimate light and providing even illumination across larger areas at the sample plane. In experiments, Köhler illumination was constructed by a collector lens (LD2746, Thorlabs), a condenser lens (ACL2520U-DG15, Thorlabs), and two diaphragms (ID25, Thorlabs). Fig. 3-4(b) shows brightfield captured images with different illumination types. The corresponding line profiles of the sixth element of Group 7 (depicted in Fig. 3-4(b)) are shown in Fig. 3-4(c). To judge the image quality:

$$C(\%) = \frac{I_{max} - I_{min}}{I_{max} + I_{min}}, \tag{3-4}$$

where I_{max} and I_{min} are maximum and minimum pixel intensities, and a higher C means better image quality.

I also tested how the illumination field affects fluorescence images. Fig. 3-4(d) shows images of three different PS beads under different illumination types. The corresponding line profiles are shown in Fig. 3-4(e). It is important to note that the emission wavelength determines the resolution of fluorescent signals, and the optical filter is employed to block the excitation light. Consequently, the differences observed in these fluorescent bead images, resulting from different illumination types, are relatively insignificant. In contrast, in brightfield imaging, the imaging formation is due to the illumination light modulated by the object. According to the Abbe theory of microscope image formation, the image quality relies on the illumination light. Under the PAI-M illumination, we successfully discerned the sixth element in Group 7 of the USAF-1951 target (228.1 lp/mm). Additionally, we were able to observe 10μm PS beads exhibiting red, blue, and green fluorescence. We believe that the resolution constraints stem from the limited NA and the non-Koehler lighting setup, along with the poor quality of the commercial webcam's lens and sensor used in our system.

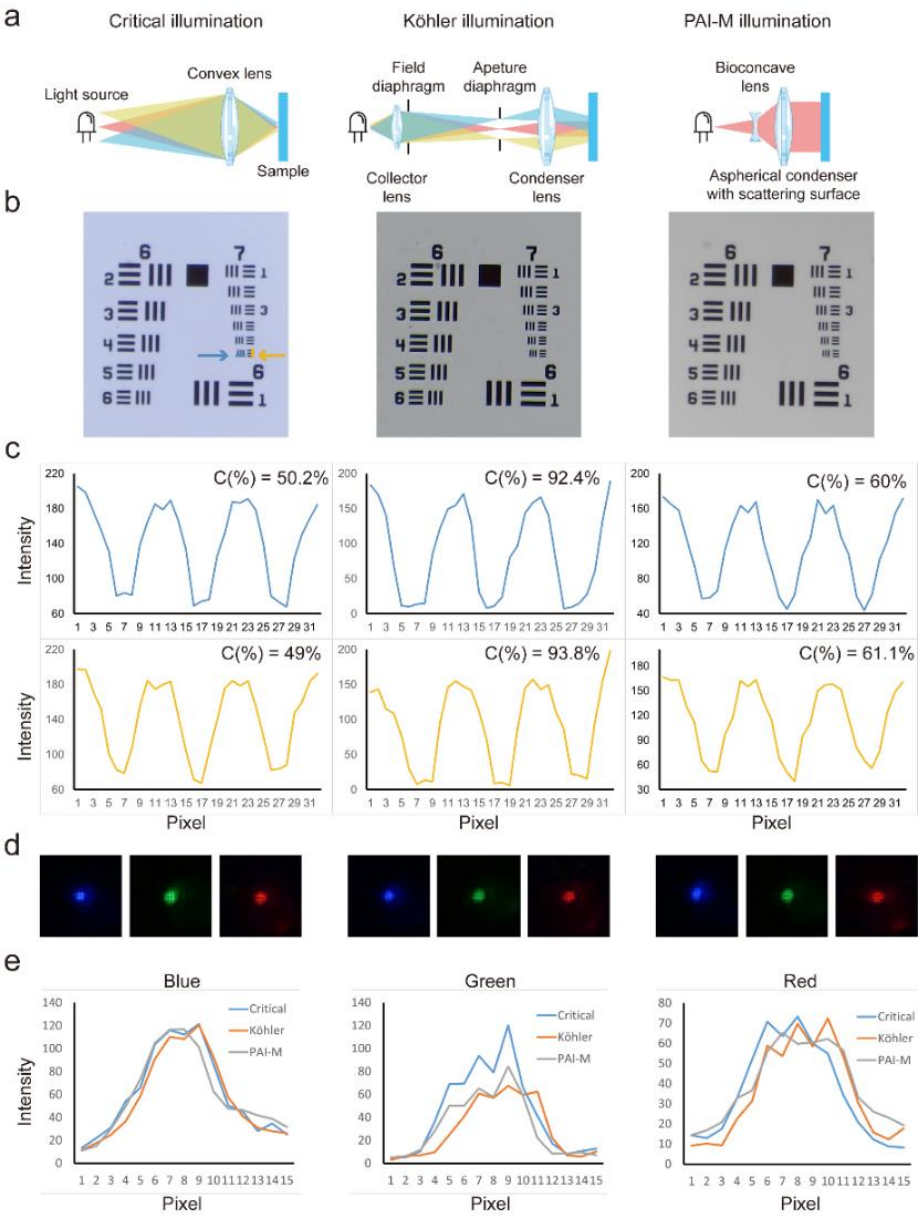

Fig. 3-4. Brightfield and fluorescence images are captured under different illumination setups. From (a)-(d), each column is related to the following illumination setup in Fig. 3-4(a). (a) Illustration of three different illumination setups. (b) Corresponding brightfield images were captured under different illumination types. (c) Horizontal and vertical line profiles of the 6th element of Group 7 in Fig. 3-4(b). (d) Blue, green, and red fluorescence images of PS beads. Corresponding line profiles are shown in Fig. 3-4(e).

3.2.4 Body Structures Construction

The development of πM was facilitated through Solidworks software and a 3D printer, as depicted in Fig. 3-5, with a twenty-cent coin serving as the dimensional reference. The specific details regarding determining element sizes and arrangement have been discussed in previous sections (Sections 3.2.2 and 3.2.3).

The overall dimensions of πM measure 172mm in length, 175mm in width, and 144mm in height. Galilean expander collimation was realized with a biconcave lens and a scattering aspherical condenser lens to collimate light (Fig. 3-5(b)). Furthermore, we replaced the original webcam lens holder with a redesigned one to realize πM's optical path, as demonstrated in Fig. 3-5(c).

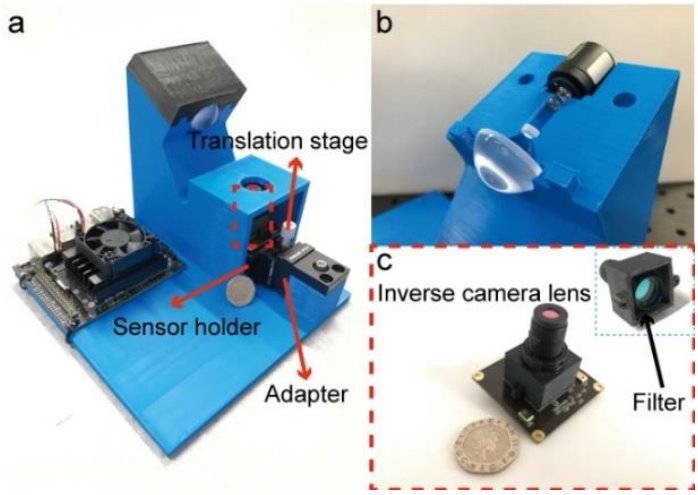

Fig. 3-5. Models of πM parts. (a) πM's schematic. (b) Illumination part. (c) The redesigned inverse webcam (Zoomed-in part in (a)). The vignette shows the back side of the webcam lens holder.

Fig. 3-6 shows CAD models of πM's parts. There are four components: the main body (Fig. 3-6(a)), the illumination cover (Fig. 3-6(b)), the webcam lens holder (Fig. 3-6(c)), and the sensor holder (Fig. 3-6(d)). The main body accommodates an NJN and contains

an LED socket (LEDMT1F, Thorlabs), a concave lens (LD2746, Thorlabs), an aspherical convex lens (ACL2520U-DG15, Thorlabs), and an illumination cover stabilizing components. The webcam lens from the webcam was disassembled and mounted into the corresponding position (Inverse webcam lens) indicated in Fig. 3-6(c). The grey opaque parts in Fig. 3-6(c) are screw holes for coupling the webcam lens holder into the CMOS webcam. The sensor holder equipped with the redesigned microscopic webcam can be mounted to the Z-direction translation stage (DT12, Thorlabs) for adjusting the focus (Fig. 3-6(d)). Finally, the refitted webcam with a Z-direction translation stage was installed to πM's main body through an adapter (DT12A, Thorlabs).

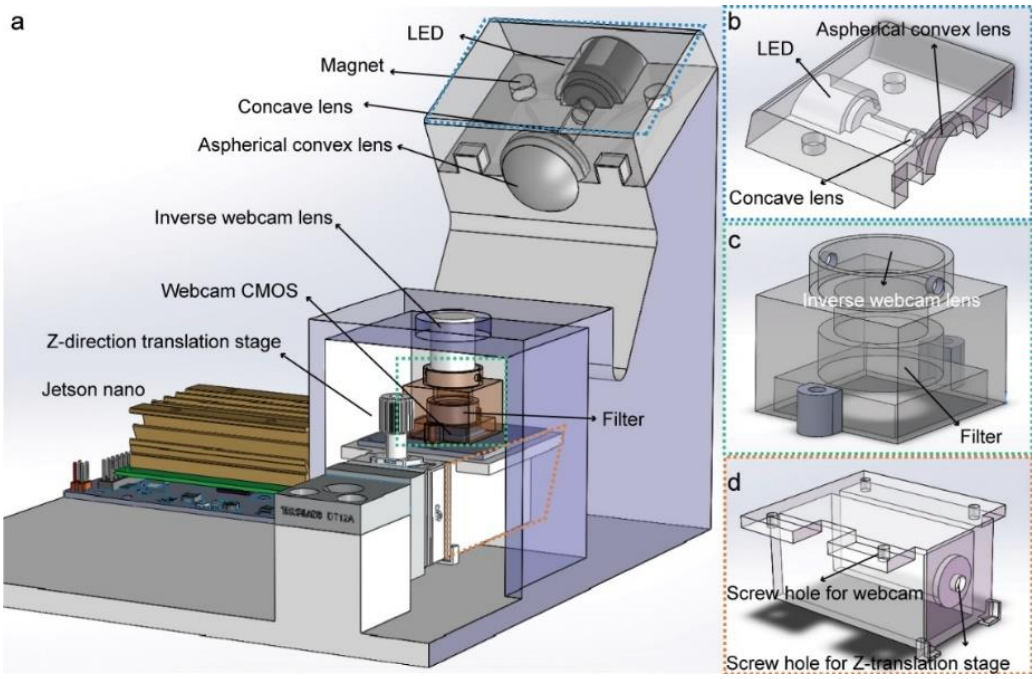

Fig. 3-6. CAD Models of πM parts. (a) The main body for assembling all components. Four screw holes under NJN hold NJN to the main body. (a) πM's schematic. (b) The illumination cover is used for fixing LED and optical lenses. (c) Webcam lens holder for carrying the inverse webcam lens and an optical filter. (d) Sensor holder for holding the inverse webcam.

3.2.5 Foreground features extraction and the counting function

The proposed CNN-enhanced foreground feature extraction and counting functions was implemented based on a cascade neural network composed of a U-Net [252] and a VGG [218] network. To acquire results efficiently, two networks were combined to simultaneously realize segmentation and counting functions. The first output segmentation maps of the U-net network can seamlessly link to the VGG network for target counting. The U-net contains six down- and up-sampling layers, eventually producing precisely segmented images. The training data Broad Bioimage Benchmark Collection (BBBC 005) was used [253], including the pervasive cellular morphology captured by a fluorescence microscope. Despite unfocused cells, the U-Net can segregate foreground and background. This segregated image offers a solid pre-requisite for the counting task. The VGG network has seven convolutional and one fully connected (FC) layer. After two convolutions, the intensity and segregated images are fused to extract more spatial features. The FC layer then generates a scaler output indicating the number of cells. In experiments, the sensor's frame rate was from 30fps to 250fps (4ms to 33ms processing time). The average processing time on the Jetson Nano for each RGB 256*256 image is about 35fps (28.6ms).

While there are numerous image-processing algorithms available for counting aggregated beads or cells, CNN is more accessible to combine with various neural networks. The layer structures and their corresponding input and output features can be readily customized, providing a high degree of adaptability. Additionally, using transfer learning and open-source pre-trained neural networks can significantly save time. Furthermore, the NJN is an ideal Graphics Processing Unit (GPU) acceleration unit for parallel matrix manipulations. Compared to other iterative algorithms, CNN can outperform them considerably when executed on the NJN, demonstrating its superior

efficiency in various image-processing tasks.

In addition, CNN can easily acquire many feature maps of aggregated and high-quantity targets. We compared the proposed method with the OpenCV and CLIJ2 [254] (an open-source unsupervised method) methods (Sections 3.3.3 and 3.3.4).

3.2.6 Cascade neural network design and working flowchart

U-Net is a prestigious network architecture for image segmentation [255–258]. Some derivatives of U-Net, such as Eff-UNet [259], Dense-UNet [260], and U-Net++ [261], etc., exhibit superior accuracy than naive U-Net. However, numerous skip connections in these architectures lead to big model sizes. In this project, the objective is to adopt compact, efficient neural networks for portable devices, where the model's size is crucial to achieve a reasonable trade-off between accuracy and computing efficiency. Visual Geometry Group (VGG) [218] was demonstrated to realize counting due to its unified, hardware-friendly topology, where the depth of down-sampling layers can be easily configured. Although ResNet [262] is a ubiquitous backbone that can prevent gradient vanishing and accelerate convergence, achieving faster inference, its generalization deteriorates more seriously as the network becomes deeper. Conversely, VGG can be generalized to different applications, and results also demonstrated the feasibility of cell counting (Sections 3.3.3 and 3.3.4).

The network was implemented with PyTorch. Two networks were trained separately on an NVIDIA RTX 5000 GPU. Images in the training dataset were divided into 2200 for training and 200 for validation. The batch size was set to 64 and the number of epochs was set to 200. A batch normalization module follows each convolutional layer to prevent gradient vanishing. An early stopping strategy was used to avoid overfitting during the training stage, which means the training process could stop at a pre-defined patient number (ten in this case) before the loss function is divergent. Adjustable,

exponentially decreasing learning rates were utilized for both networks to accelerate training processes. Adam was used as the optimizer. MSELoss(·) and BCEWithLogitsLoss (·) were VGG and U-net loss functions. After the U-net training is completed, its pre-trained model acts as a pre-processing function to create foreground feature extraction images in the VGG training. To compare the neural network with conventional OpenCV approaches, we employed contour extraction (cv2.findContours(·) and cv2.contourArea(·)) functions to realize feature extraction and counting. Fig. 3-7 illustrates workflow charts of two solutions (Route A for the OpenCV approach and Route B for the cascade neural network approach). Beyond that, we also used the CLIJ2 [254] (an unsupervised method combining Ostu's thresholding [263] and Voronoi diagrams [264]) as a comparison. The CNN neural networks implement both feature extraction and counting functions. For the OpenCV method, feature extraction is obtained by model-free image processing, and a VGG network realizes the counting function. In contrast, both functions are model-free for the CLIJ2 method.

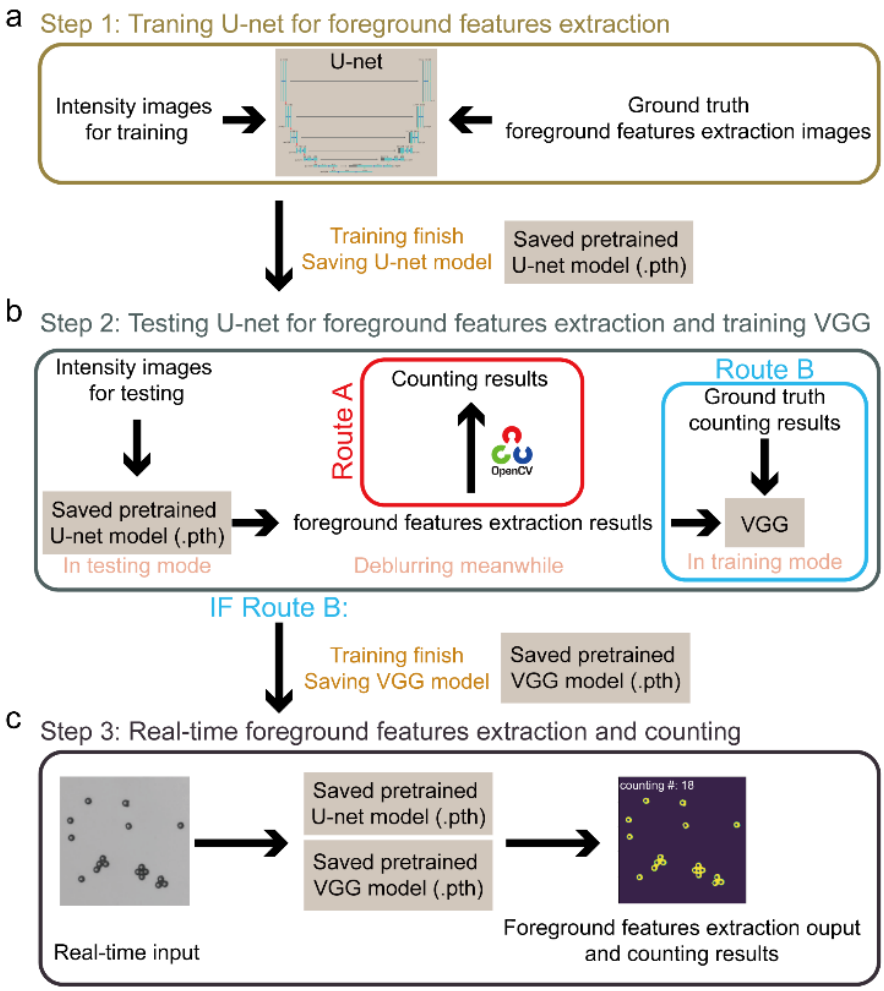

Fig. 3-7. The cascade neural network architecture for foreground masking and counting. (a) A U-net is initially trained to generate mask images, and the optimal model is saved to serve the counting neural network afterwards. (b) The pre-trained U-net model operates as the test model to generate clear mask images to improve the robustness of the counting network. In contrast, OpenCV utilizes mask images for counting. The optimal VGG model is also saved when training is completed. (c) Both networks work in the test mode, and the intensity image goes through them sequentially. The corresponding mask image and the number of counts are the output.

3.2.7 Foreground extraction performance

It is essential to define and present appropriate metrics for the segmentation performance of the U-Net network for foreground feature extraction. The IoU is utilized

to evaluate the foreground extraction, which is defined as:

$$IoU = \frac{TP}{(TP + FP + FN)}, \tag{3-5}$$

$$TP = m \&\& \tilde{m}, \tag{3-6}$$

$$FP = (m \,||\, \tilde{m}) - m, \tag{3-7}$$

$$FN = (m \,||\, \tilde{m}) - \tilde{m}, \tag{3-8}$$

Where m and $\tilde{m}$ are ground truth and predicted masks, respectively. IoU ranges from 0 to 1, where a greater IoU means the predicted mask exhibits more overlap areas regarding the ground truth mask. 100 images was randomly selected from our test dataset and evaluated predicted masks. The average IoUs obtained from OpenCV, CNN, and CLIJ2 are 0.35, 0.8, and 0.79, respectively. Fig. 3-8 shows the performance of three different algorithms which were used to generate the segmentation masks. OI is the original image from the dataset, GT is the ground truth binary mask of OI, and the other three masks are OI's mask generated by corresponding algorithms. The link of the dataset can be found in the appendix.

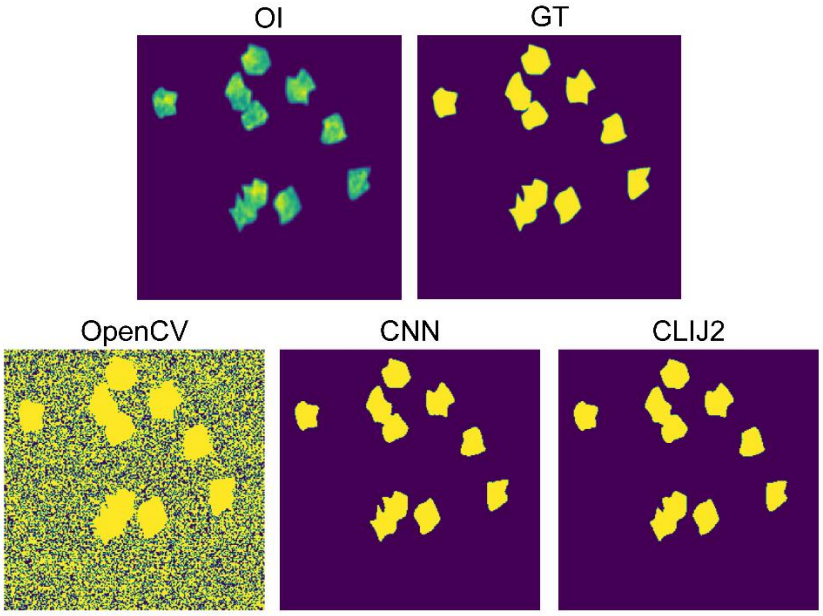

Fig. 3-8. Intersection of union plot for three different methods. GT is the ground truth.

3.2.8 Sample Preparation

We used distilled water (ThermoFisher, USA) to prepare PS bead solutions with five concentrations (0.225×10^6, 0.45×10^6, 0.9×10^6, 1.8×10^6, and 3.6×10^6 beads/mL). The diameter of all PS beads is 10μm. For fluorescent imaging, we used three different PS beads (blue-green, Ex 430/Em 465; yellow-green, Ex 505/Em 515; red, Ex 580/Em 605; Thermofisher) solutions with 1.8×10^6 beads/mL concentration. PS beads (505/515, Thermofisher) at different concentrations were used to test πM's real-time image foreground feature extraction and bead counting performances. Each sample was prepared on the glass side (Corning, USA) with a 10μL volume.

3.3 Results

3.3.1 Brightfield Imaging

To assess the brightfield imaging capabilities of πM, we compared πM and a benchtop microscope (Olympus BX51, JP). Prepared microscope slides containing dog skeletal muscle, Hydrilla leaf, and rabbit spinal cord samples (AmScope, UK) were captured under brightfield illumination. When using the benchtop microscope, we employed a ×5 objective lens and the same sensor (IMX317-Sony) to observe the samples. It is important to note that this comparative experiment is limited to a magnification of ×5 because πM's magnification also matches this value. Therefore, the magnification of the objective lens of the benchtop microscope was chosen to be equivalent to that of πM, limiting the comparison to ×5 magnification.

As shown in Fig. 3-9, the images of the prepared microscope slides are presented. The colour temperature of different illumination sources may lead to variations in background colour. Furthermore, our experiments revealed that images captured with a benchtop microscope contain more out-of-focus signals compared to those captured

with the πM, attributed to the differences in the NA of the objective lenses used. The πM's webcam lens has an NA of 0.2 and a magnification of ×5, whereas the benchtop microscope's objective lens, which is an Olympus model, has an NA of 0.15 and a magnification of ×4. The higher NA in the πM setup enables better rejection of out-of-focus signals.

It should be noticed that the Olympus benchtop microscope in our laboratory does not offer a ×5 magnification lens option (only ×4, ×10, ×20, ×60 are available), leading us to choose the ×4 lens for comparison purposes. While a Mitutoyo objective lens with ×5 magnification is available (https://www.thorlabs.com/thorproduct.cfm?partnumber=MY5X-802), budget constraints prevented us from acquiring a new microscope equipped with it. Future comparisons will aim to include off-the-shelf microscopic objective lenses that match the magnification of the πM's webcam lens.

To validate πM's resolution, the USAF-1951 resolution target was illuminated by six different LEDs (LED405E, LED465E, LED528HP, LED591E, LED630E, LEDW7E, Thorlabs). 228 line pair/mm targets (Element 6 of group 7) can be resolved under different wavelengths (Fig. 3-10, indicated by arrows).

In Fig. 3-10, a notable deviation is observed between the anticipated theoretical resolution and the actual empirical resolution achieved by πM. Theoretically, given the NA (0.2 for πM) and illumination at 523nm, the system is expected to achieve a resolution of approximately 1.33μm. However, the empirical data suggest a significantly lower resolution of about 4.5μm, highlighting a discrepancy that warrants further examination. This gap between theoretical predictions and practical outcomes can be attributed to several factors inherent in the design of the πM system. The constraints imposed by the need for a portable and cost-effective design may inherently

limit the optical system's resolving power. Optical aberrations, both chromatic and spherical, are particularly challenging to correct in compact optical systems and likely contribute to the reduced resolution. Furthermore, the quality of the optical components, the precision of their alignment, and the capabilities of the imaging sensor may not be fully optimized to realize the system's potential resolution.

To solve these problems, improvements in the quality of optical components, the implementation of advanced aberration correction strategies, and enhanced alignment precision could significantly narrow the gap between theoretical and observed resolution (Section 3.4).

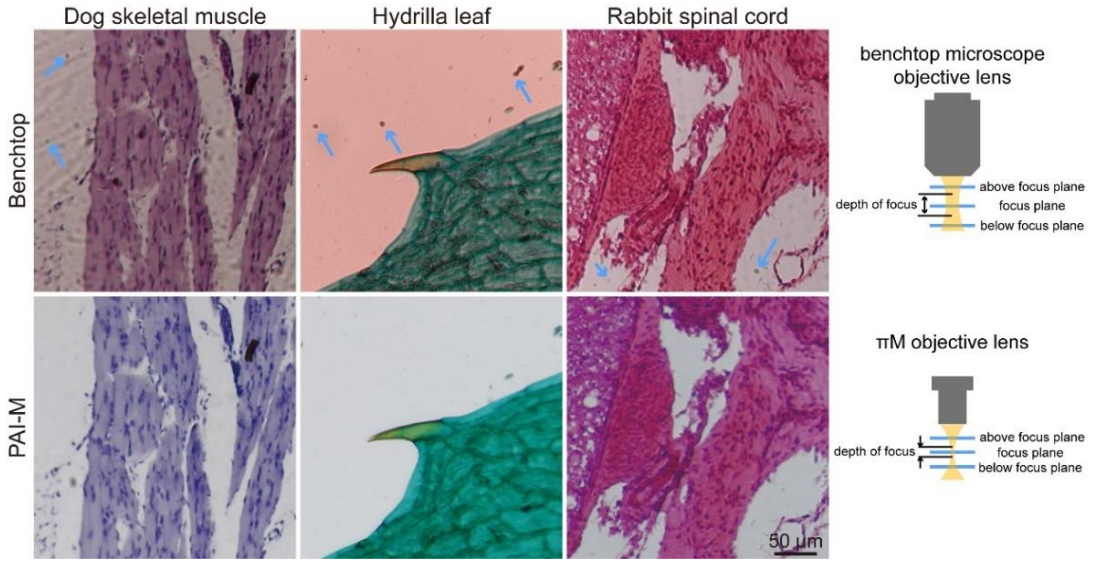

Fig. 3-9. Prepared microscope slides images captured by both PAI-M and benchtop brightfield microscope. I cropped these images for the same size and FOV for comparison, and the 50μm scale bar is for all images. Blue arrows depict dusts and scratch on microscopic slides captured by benchtop microscope with x4 magnification. The benchtop microscope objective lens has a more extended depth of focus, so the sensor will collect information in this range simultaneously. However, the πM's objective lens has a smaller depth of focus range because of its higher NA and magnification.

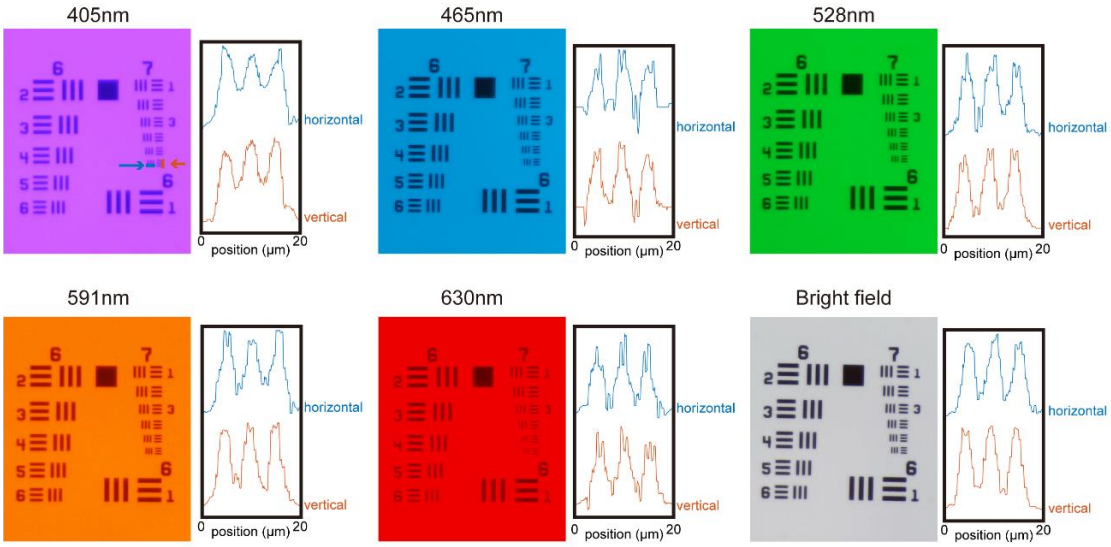

Fig. 3-10. πM's resolution under different illumination wavelengths. Each picture is cropped from the centre FOV. Horizontal and vertical line profiles of the 6th element, Group 7 (indicated by arrows), are depicted beside each picture.

3.3.2 Fluorescence Imaging

For the fluorescence imaging of various PS beads, we employed different LED light sources and optical filters. Specifically, a blue LED (430nm, Lumex) was used to excite blue-green beads, a yellow LED (505nm, Lumex) was used to excite yellow-green beads, and an orange single-wavelength LED (LED591E, Thorlabs) was used to excite red beads. Optical filters with specific wavelengths (473/10, 520/10, 610/10, Edmund Optics) were selected to observe the fluorescent signals effectively.

To capture brightfield images, the system is initially set up in its standard configuration without the need for specialized filters. However, for fluorescence imaging, a crucial modification involves the disassembly of the adapter that houses the optical filter. This step is undertaken with precision to ensure the integrity of the optical path and components is maintained. Following the removal of the adapter, the optical filter specifically chosen for the fluorescence imaging application—based on the fluorophores' excitation and emission wavelengths—is carefully positioned within the

optical pathway. Once the appropriate filter is in place, the system is reassembled, ensuring the webcam lens holder and other components are securely and accurately repositioned. This reassembly is critical for maintaining the optical alignment and ensuring the system's overall functionality. The meticulous process of changing the optical filter and adjusting the webcam lens holder allows for a seamless transition between brightfield and fluorescence imaging, enabling the comprehensive characterization of samples using both modalities. This adaptability in imaging techniques underscores the πM system's versatility, making it a valuable tool for diverse applications in microscopy.

However, this process introduces a notable limitation in maintaining precise optical alignment. The manual adjustment required for switching imaging modalities, despite being meticulously conducted, inherently carries the risk of slight deviations in alignment. This misalignment, even if minimal, can potentially affect the quality and accuracy of the captured images, thereby impacting the overall performance of the system. Addressing this challenge necessitates innovative solutions in future iterations of the πM system. Detailed discussions can be found in section 3.4.

Fig. 3-11 shows the brightfield, fluorescence, and merged images of various PS beads. It also includes zoomed-in images highlighted by yellow-dashed rectangles. The zoomed-in images clearly show the aggregated beads, indicated by yellow arrows. Notably, both the brightfield and fluorescence images of the samples can be captured within the same FOV by changing the webcam lens holder (Fig. 3-5(c)) and adjusting the optical filter, offering a versatile and efficient imaging solution.

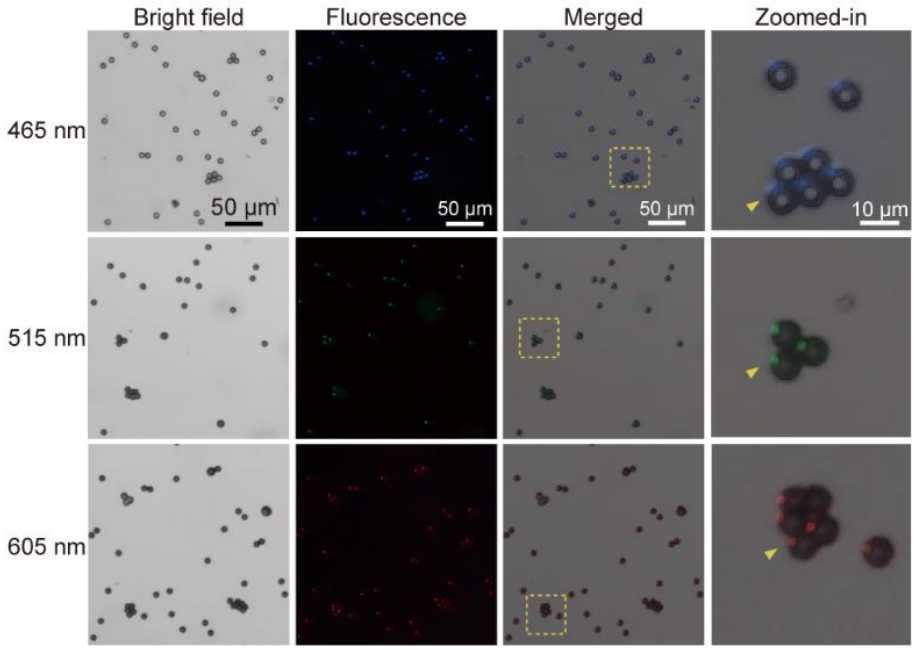

Fig. 3-11. Fluorescent PS beads image with different spectrums, and yellow arrows denote aggregated beads. The 50 µm scale bar is for the first three columns, and the 10 µm scale bar is for the last column. The fluorescent signals of PS beads in the Zoomed-in column are not located in the centre of the beads (yellow indicators), caused by the oblique illumination and the beads' 3D-rounded shapes. When the illumination light excited fluorescent beads obliquely, the light does not directly illuminate the beads' centres but their edges. Therefore, fluorescent signals appear on the beads' peripherals. These fluorescent signals are all located in the upper left of the beads.

3.3.3 Foreground feature extraction and bead counting

PS bead samples were used to show πM's real-time foreground feature extraction and counting performances. Table. 3-2. shows the quantitative counting results of the images captured in the centre FOV (800µm2). The CNN counting method demonstrates superior robustness compared to OpenCV, as it can effectively recognize aggregated beads. At lower (low and medium) concentrations, the CLIJ2 method exhibits better performance. However, at higher concentrations, the CNN also outperforms the CLIJ2 method, primarily because the CNN can recognize aggregated targets, which highlights the adaptability and versatility of the CNN method for various sample concentrations

and complexities.

Fig. 3-12 shows foreground feature extraction and counting results at different concentrations. Fig. 3-12(a) shows local FOV sample images (low: 0.225×106 beads/mL, medium: 0.9×106 beads/mL, high: 3.6×106 beads/mL). The corresponding foreground feature extraction results are shown in the following rows. The *cv2.morphologyEx* function processes OpenCV input masks to eliminate the donut shape (shown in the CNN input mask). This configuration can enhance the counting accuracy of OpenCV. After segmentation, OpenCV and CNN masks were used as inputs for bead counting.

Furthermore, PS bead samples with different aggregated numbers were used to validate OpenCV, the CNN, and the CLIJ2 method in counting aggregate beads (from one to eight). Fifty other groups for each aggregated number were tested. Fig. 3-12(b) shows the hot maps of counting accuracy for OpenCV (26% accuracy for three aggregated beads), CNN (80% accuracy for six aggregated beads), and CLIJ2(64% accuracy for six aggregated beads). These results show that the CNN is better for aggregated target counting and segmentation.

Table. 3-2. Bead counting results. At each concentration, results were obtained by five captured images with different centre FOVs. GT is the ground truth, Avg is the average value, and Std is the standard deviation.

	225 beads/μl		450 beads/μl		900 beads/μl		1800 beads/μl		3600 beads/μl	
	Avg	Std	Avg	Std	Avg	Std	Avg	Std	Avg	Std
GT	57	15.7	104.6	13.5	153.8	9.7	298.2	6.9	558.8	5.7
OpenCV	49.4	12	77	9.1	103.2	6.6	217.8	5.9	293.4	5.9
CNN	57.6	16.6	108.8	15.6	158.8	8.1	304.8	4.8	571.6	5.8
CLIJ2	57	15.7	103.8	12.3	149.6	10	282.8	6.6	504	6.1

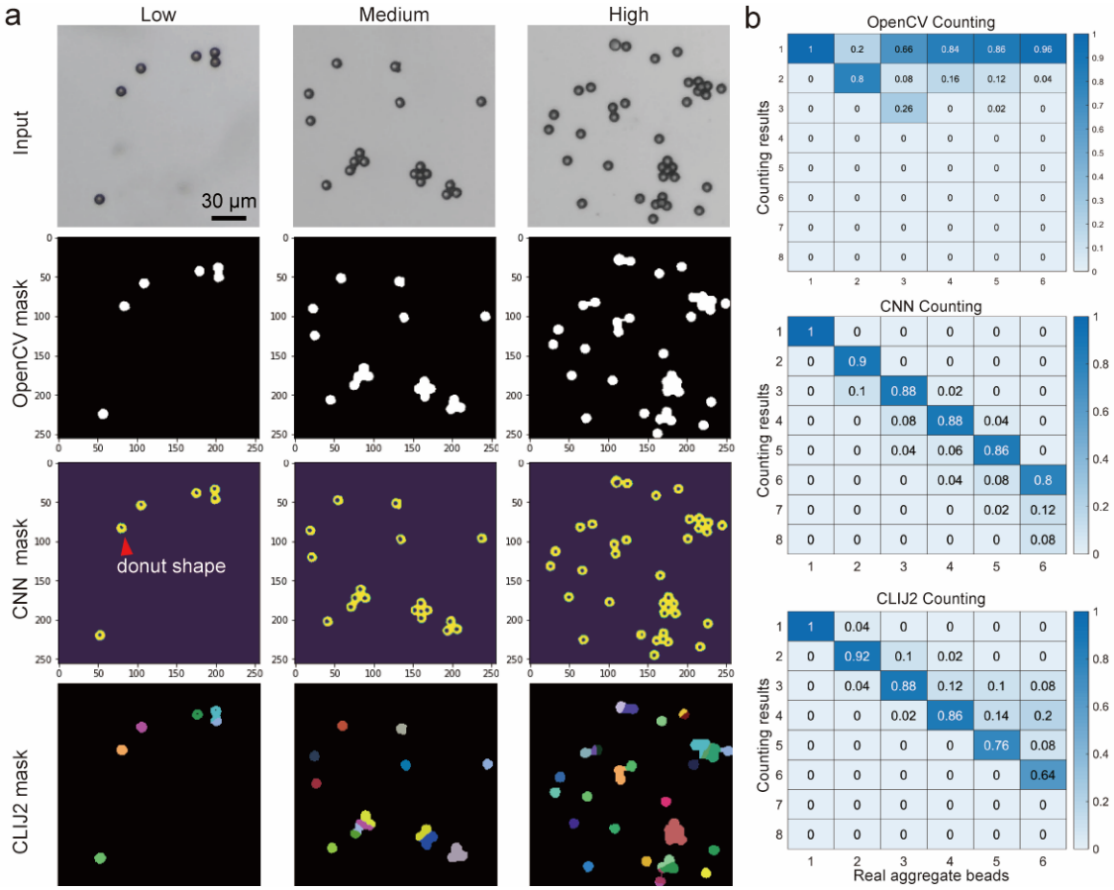

Fig. 3-12. πM's foreground feature extraction and quantitative counting results. (a) Sample images of local FOV and corresponding foreground feature extraction maps. Input: captured images. OpenCV, CNN, and CLIJ2 mask: Corresponding foreground feature extraction masks. (b) Accuracy hot maps of counting aggregated beads for our CNN, OpenCV, and CLIJ2 methods.

3.3.4 Red blood cells (RBC) extraction and counting

Further, πM's functionalities on actual biological samples were evaluated. Prepared human RBCs smear samples with Wright' Strain were used as targets. These samples were bought from the Carolina, USA (https://www.carolina.com/histology-microscope-slides/frog-blood-film-smear-microscope-slide/313128.pr). According to previous bead experiments, the OpenCV method performs the worst. Therefore, only the CNN and CLIJ2 methods were considered here. Forty-five sub-region images from 10

samples were randomly selected for RBC extraction and counting. Table. 3-3 provides the statistical results, and the GT was established by examining the samples using a benchtop microscope and a tally counter. Corresponding box and Whisker plot are shown in Fig.3-13. Compared to CLIJ2, the CNN method exhibits superior robustness and accuracy when applied to biological samples, showing its effectiveness in practical applications.

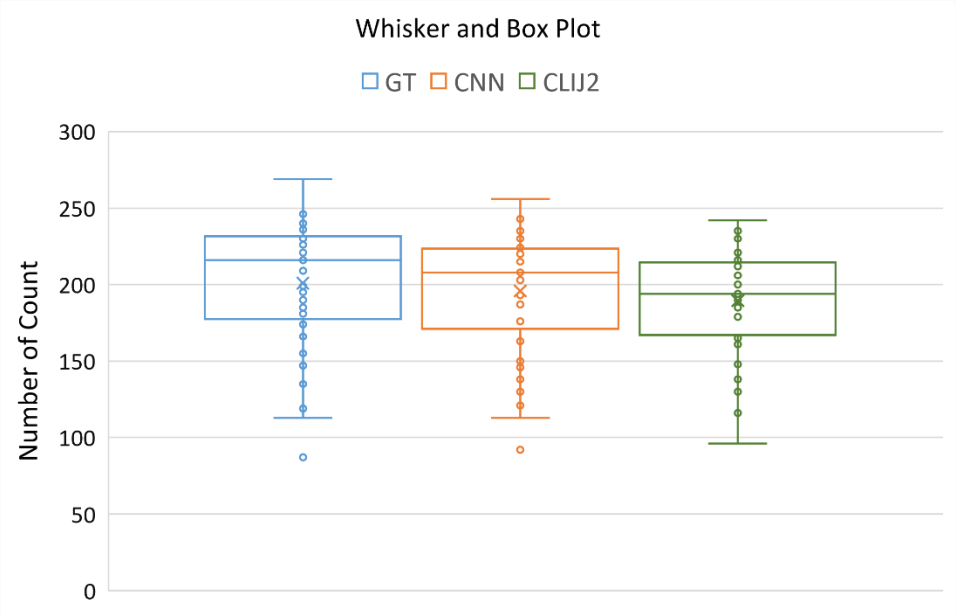

Fig. 3-13. Whisker and box plot of RBCs counting.

Table. 3-3. RBC counting results.

	Ground truth	CNN method	CLIJ2 method
Average counting results of 45 sub-regions	201	196	189
Counting standard deviation of 45 sub-regions	41	38	33

Fig. 3-14 shows original images of RBCs captured by πM and corresponding feature extraction maps using different methods. In the CNN mask row, RBCs are depicted by yellow labels, and these masks are used as the input for the counting neural network (Fig. 3-7). Each RBC is coded in the CLIJ2 mask row with a unique colour, and adjacent RBCs do not share the same colour. The extraction mask and counting results are obtained simultaneously. Although CLIJ2 is a model-free approach, prior knowledge about two parameters defining the distance of segregate cells and the precision of the segmentation boundary is needed. These two parameters should be fine-tuned to achieve optimal results. However, the data-driven CNN does not have this problem. The same result was consistently obtained for the same image in different trails.

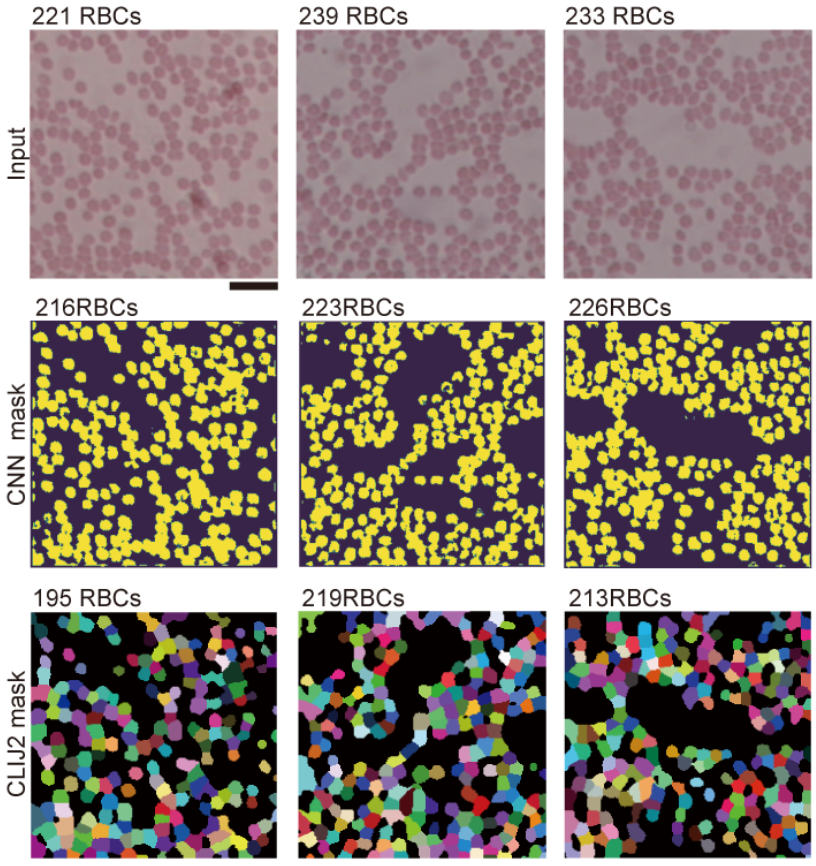

Fig. 3-14. Images of human RBCs. The first row is the original pictures captured by πM, and the second and third rows are foreground feature extraction processed by our CNN and CLIJ2 methods. The number above each picture is the corresponding RBC counting result of the ground truth, CNN, and CLIJ2 methods. The scale bar under the

top-left image is 20μm.

Here, a crucial limitation is that the testing of the πM on denser RBC samples and its comparison with high-quality images from an benchtop microscope. The omission of these tests is attributed to the initial scope of the study focusing on establishing the foundational capabilities of the πM in less challenging conditions, potential technical constraints of the πM system, resource limitations, and the developmental stage of the microscope. Future research will need to incorporate these elements, testing the microscope on denser RBC samples and comparing its performance against high-end microscopes like the Olympus, to ensure the robustness and applicability of the πM system in a wider range of clinical and research settings.

3.4 Discussion and prospect

LPMs are low-cost, user-friendly, and compact. In resource-limited areas, they are powerful tools for biomedical research. πM's components can be easily reconfigured, and its optic-mechanical structure is simple. It contains a powerful AI-embedded system NJN and achieves image acquisition and real-time analysis without data transfer. Different from other portable microscopes, πM has several unique features. Users can: (1) easily customize their ANNs for specific applications, such as feature extraction, pattern recognition, and cell counting. (2) πM does not rely on network communication. The NJN, a robust calculation module, obtains real-time analysis. Users do not need to upload their captured images to servers and clouds. (3) πM can be an ANN training machine. Users can seamlessly capture images and customize and train their networks.

Despite its innovative design and application, the πM exhibits certain limitations that merit attention. One notable constraint is the lack of comparative analysis with benchtop microscopes under identical conditions, which restricts a comprehensive evaluation of its performance. Furthermore, the resolution achieved by the πM,

although commendable for its design and cost, falls short when compared with theoretical expectations. This discrepancy could be attributed to various factors such as optical aberrations and the quality of illumination, which are common challenges in compact microscopy designs.

To solve these limitations, future iterations of the πM could focus on enhancing the optical components and illumination strategies to mitigate aberrations and improve resolution. Incorporating adaptive optics could be a viable solution to dynamically correct for aberrations in real-time. Moreover, optimizing the illumination system to ensure uniform and adequate lighting could significantly enhance image quality. Expanding the comparative studies to include a broader range of conditions and benchmarks against conventional microscopes would also provide deeper insights into the πM's capabilities and areas for improvement. Additionally, integrating advanced image processing algorithms and deep learning techniques could compensate for hardware limitations, offering improved image reconstruction and feature detection. These advancements could further solidify the πM's utility in diverse applications, from clinical diagnostics to environmental monitoring, particularly in resource-limited settings.

PS bead samples validated πM’s feature extraction and target counting functionalities. Experimental results show that the CNN is much more robust than OpenCV or CLIJ2 in bead counting. Six aggregated beads can be correctly counted with 80% accuracy. Furthermore, human RBC smear samples were imaged by πM. Different FOVs from RBC samples were selected randomly for recognition and counting. According to the statistical analysis, πM achieved closer results to the ground truth than CLIJ2. Both bead and RBC experiments show that πM has potential in biomedical image analysis, especially for those images and targets with sophisticated and dense features.

In this project, the primary objective was to develop an affordable and portable device for RBC imaging and counting, specifically focusing on this application. Considering project funding constraints, experimental conditions, and ethical concerns related to biological experiments, more complex biological experiments were not included in this study. However, several prepared teaching microscope slides were chosen for comparison, demonstrating the system's potential for powerful biomedical imaging.

Furthermore, while the segmentation and counting functions were initially achieved using brightfield images, the inclusion of fluorescent bead imaging suggests that πM has the capacity for fluorescent imaging and diagnostics. Soon, the goal is to upgrade πM to enable the detection of sickle cell diseases and hazardous microorganisms in drinking water in resource-limited regions at a relatively low cost. This expansion will incorporate more fluorescent imaging and diagnostic capabilities into the system, enhancing its utility in healthcare and diagnostics.

In the AI aspect, a U-Net network and a VGG network were effectively cascaded to provide segmentation results along with target counting numbers. This design not only simplifies the system's data processing but also preserves its robustness. It is important to note, however, that this method has been validated for well-prepared samples, meaning those with minimal contaminants. In real-world clinical applications, the distribution of complex contaminants on sample slides can present challenges for AI algorithms in accurately extracting targets.

The absence of detailed quantification regarding the data processing speed, exposure times, and sample irradiance levels in our πM system is an aspect that requires further elaboration to enhance the comprehensiveness of our research findings. The term 'real-time' in the context of our study was used to denote the system's capability to process and analyse images without perceivable delay, thus facilitating immediate interpretation

and decision-making. However, it is acknowledged that a more precise quantification of processing times, including exposure durations and sample irradiance measurements, would provide a clearer understanding of the system's efficiency and operational capabilities.

The processing speed of the NJN is a critical parameter, especially when considering the application of the πM in scenarios requiring rapid data analysis, such as in clinical diagnostics or environmental monitoring. The absence of specific metrics regarding processing speed in our initial study was primarily due to the preliminary nature of the system's evaluation, where the focus was more on demonstrating feasibility and potential applications.

In future studies, the aim is to address these issues without substantially increasing the complexity of the network. We will implement benchmark tests to measure the time taken by the NJN from image capture to the completion of data processing. This will include assessing the time required for various processes such as image acquisition, pre-processing, analysis, and displaying results. Meanwhile, conducting experiments to determine optimal exposure times for various sample types and imaging modalities are important. This will ensure that images are captured with sufficient quality for accurate analysis while minimizing potential damage to sensitive samples. We will also measure the irradiance levels for different imaging conditions to optimize image quality and ensure sample safety. This is particularly important for fluorescent imaging, where excessive irradiance can lead to photobleaching and sample damage. Moreover, some contaminants will be introduced to test the system's robustness and ability to simulate real-world scenarios.

As mentioned in section 3.3.3, the adaptability of our πM system to transition between brightfield and fluorescence imaging, through the disassembly and reassembly of the

webcam and adaptation of optical filters, introducing a limitation in maintaining precise optical alignment. One promising approach is the integration of an automated alignment system, equipped with real-time feedback mechanisms. Such a system could utilize advanced algorithms and actuators to adjust the optical components automatically, ensuring optimal alignment is achieved and maintained throughout the imaging process. This automation would significantly reduce the likelihood of alignment errors and improve the system's reliability and user-friendliness. Another avenue for improvement involves the design of a modular optical component system with precise locking mechanisms. This would allow for the quick interchange of components, such as filters, without disrupting the core alignment of the optical path. Each module could be designed to fit into a predefined position with high precision, ensuring consistent alignment even after multiple disassembly and reassembly cycles. Exploring these solutions will be a focal point of our future research endeavours. By enhancing the πM system's ability to maintain perfect alignment across different imaging modalities, we can unlock its full potential and expand its applicability across a broader range of scientific and medical fields.

These targeted investigations will not only fortify the understanding and operational efficiency of the πM system but will also contribute valuable insights to the broader scientific community engaged in the development and application of portable microscopy technologies. This concerted effort will pave the way for realizing the full potential of portable microscopy systems in real-world applications, where speed, efficiency, and precision are of paramount importance.

For RBCs counting experiments, we recognize the importance of a more detailed analysis to fully understand the algorithm's performance, especially in challenging conditions such as denser RBC samples. The variability in cell morphology, density, and the presence of overlapping cells can significantly impact segmentation accuracy.

Additionally, comparing the algorithm's performance on images captured by the πM system versus a high-end microscope like the Olympus, known for its superior image quality, could provide valuable insights into the robustness and adaptability of our segmentation algorithm.

Recognizing the importance of these aspects, we are committed to addressing them in subsequent studies. Future research will expand on the quantitative analysis, incorporating more detailed data visualizations to dissect the algorithm's performance nuances thoroughly. We plan to conduct comprehensive evaluations across a range of cell densities, including denser RBC samples, and compare the algorithm's efficacy on images obtained from both the πM system and conventional high-end microscopy systems. These efforts will not only enhance our understanding of the algorithm's strengths and limitations but also contribute to the iterative development and refinement of the πM system.

3.5 Conclusion

In this study, a 3D-printed portable AI-supported fluorescence microscope, denoted as πM, has been introduced. This compact device measures 145mm×172mm×144mm (L×W×H) and comes at an affordable cost of around $400. The imaging path of πM was achieved by reversing the front lens of a webcam. The device can resolve 228.1 lp/mm when tested with the USAF target. πM has demonstrated the capability to capture brightfield images comparable to those obtained with a benchtop microscope. Furthermore, it can observe fluorescent PS beads with a diameter of 10μm. The embedded CNN enables real-time feature extraction and accurate bead counting.

Quantitative experiments have confirmed that the CNN can significantly reduce counting inaccuracies caused by aggregated beads and exhibits superior robustness compared to the OpenCV and CLIJ2 methods. Additionally, results from experiments

involving the extraction and counting of RBCs exhibit the potential of πM in real-time biomedical image analysis and disease detection. The device shows promise in facilitating advanced healthcare and diagnostic applications.

Chapter 4. Smartphone-based Optical Sectioning (SOS) Microscopy with A Telecentric Design for Fluorescence Imaging

This study introduces a Smartphone-based Optical Sectioning (SOS) microscope employing the HiLo technique, wherein a single smartphone replaces the conventional high-cost illumination source and camera sensor. The SOS system is assembled using optical mechanical cage systems, enhanced with 3D-printed adapters to integrate the smartphone with the main SOS body seamlessly. The liquid light guide can be incorporated into the adapter, efficiently directing the smartphone's LED light to the DMD with minimal loss.

An ETL is utilized for cost-effective axial scanning instead of a mechanical translation stage. The ETL is conjugated to the objective lens's BPP, establishing a telecentric design through a 4f configuration. This design ensures consistency in magnification across different layers, preventing variations in image quality. The SOS system achieves a telecentric scanning range of 571.5 μm and an axial resolution of 11.7 μm.

The broad-spectrum LED torch of the smartphone proves highly effective in exciting fluorescent PS beads. Consequently, the SOS microscope successfully captures high-contrast images of fluorescent PS beads at varying wavelengths and enables optical sectioning imaging of accumulated fluorescent PS beads. This SOS configuration represents the pioneering smartphone-based HiLo optical sectioning microscopy, offering a potent and cost-efficient tool for biomedical research, particularly in resource-limited areas.

4.1 Introduction

Widefield fluorescence microscopy (WFM) is widely used for imaging biological samples because of its cost-effectiveness, rapid imaging speed, and minimal photodamage and photobleaching [265–267]. However, WFM's optical transfer function (OTF) indicates a limited optical sectioning ability, resulting in low-contrast images due to out-of-focus signals [268,269]. Therefore, various methods have been proposed to achieve high-contrast optical sectioning images.

One such method is confocal laser scanning microscopy (CLSM), which applies a spatial pinhole filter positioned at the conjugated focus point of the illumination to reject out-of-focus fluorescence. The scanning mechanism typically involves galvo mirrors and a motorized stage for acquiring three-dimensional (3D) images [270–272]. Line scanning confocal microscopy (LSCM) operates on a similar principle but with a slit replacing the spatial pinhole in CLSM. The sample is scanned in two directions instead of three, enhancing scanning speed [273,274].

Two-photon excitation microscopy (TPEM) provides another effective approach to obtaining high-contrast images. Utilizing near-infrared two-photon absorption minimizes tissue scattering and strongly suppresses out-of-focus signals [275–277]. Light sheet microscopy (LSM) is another potent optical sectioning technique [23,94,278]. In LSM, the illumination and detection arms are separated orthogonally, allowing the imaging objective lens to detect only fluorescent signals from the selectively illuminated plane. This setup mitigates phototoxicity and photobleaching while enhancing imaging contrast [279–281].

Compared to the previously mentioned methods, structured illumination microscopy (SIM) boasts a relatively easy configuration. This technique yields modulated and in-

focus images with notable contrast and optical sectioning capabilities [282]. Implementation involves the use of a DMD or a spatial light modulator (SLM) to project periodic patterns onto the sample plane [283,284]. To easily incorporate optical sectioning into WFM, Merts' group pioneered HiLo microscopy by leveraging SIM's optical sectioning capabilities [21,285,286]. Beyond its straightforward setup, HiLo requires only two images, as opposed to SIM's usual three, for operation. The HiLo principle involves acquiring one uniformly illuminated image and one structured-illuminated image, followed by image processing algorithms to derive the optically sectioned image [21].

HiLo is cost-effective by using a coherent laser and a diffuser to create speckles on samples [21,285,286] or using an incoherent light source and a DMD to project patterns on samples [287,288]. Lim et al. [286] have presented that HiLo's optical sectioning performance is comparable to CLSM [21,286,289]. HiLo has demonstrated its efficacy in applications such as 3D image cytometry [290], observation of neuron cell activities [291,292], exploration of 3D cell mechanical properties [293], enhancement of retinal imaging quality [294]. Furthermore, HiLo can integrate with endoscopy [289,295] and optical scanning microscopy [296,297]. Despite its relative simplicity compared to other optical sectioning modalities, the costs associated with its light source, DMD or SLM, and advanced camera sensor remain noteworthy.

Many smartphones have high-performance image sensors and camera lenses, and their costs are relatively low, which makes smartphone-based microscopy an effective and affordable choice for various applications such as bioimaging [1,51,81], disease detection [37,298], and point-of-care testing [6]. Moreover, smartphones can easily integrate with different imaging modalities, including bright-field microscopy [299], fluorescence microscopy [82,300], phase microscopy [70,71,73,241], and Fourier ptychographic microscopy [74].

However, most of these devices primarily rely on the cameras and sensors of smartphones, necessitating additional external LEDs for illumination, which limits their potential despite their strong capabilities [56,86,301]. To enhance the simplicity of smartphone-based microscopy, screen LCD and LED flashlights smartphones have been used for illumination [74,84].

Here, I present the smartphone-based optical sectioning (SOS) microscopy concept. To our knowledge, this is the first HiLo microscope utilizing a smartphone, providing cost-effective optical-sectioned widefield imaging. The smartphone functions as a CMOS sensor, reducing the overall cost compared to traditional HiLo microscopes. Using the smartphone's Bayer filter and small pixel size allows for the acquisition of high-resolution coloured images without the need for external colour filters.

Adapters were designed to integrate the smartphone into the main microscope body. These adapters facilitate the incorporation of the smartphone into the system. A liquid light guide was introduced into the adapter to direct the smartphone's flashlight to the DMD. Simultaneously, a reverse smartphone lens was affixed to the camera, conjugating the intermediate image plane with the smartphone's sensor at 1X magnification.

The ETL was conjugated with the objective lens's Back Focal Plane (BPP) for a telecentric axial scan. This configuration ensures a stable lateral magnification of SOS at various depths. A spectrometer was employed to test the smartphone's LED torch, revealing its broad spectrum, effectively exciting fluorescent PS beads with diverse wavelengths.

The SOS microscope has a telecentric scanning range of 571.5 μm and an axial resolution of 11.7 μm. Its capabilities were successfully demonstrated in acquiring high-

contrast widefield fluorescent images featuring 10μm PS beads with emission wavelengths of 465nm, 515nm, and 605nm. Optically sectioned images of accumulated PS beads were achieved within a 25 μm axial range, employing a 5μm step.

To our knowledge, the proposed SOS is the first smartphone-based HiLo optical sectioning microscopy (£1,965), which can save around £7,035 when comparing with a traditional HiLo system (£9,000). It is a powerful tool for biomedical research in resource-limited areas.

4.2 Materials and Methods

4.2.1 HiLo Principle

In HiLo, two images captured under uniform and structured illumination were used to extract the in-focus high-frequency components (IHC) and in-focus low-frequency components (ILC) and generate an optical-sectioning image $I_{HiLo}(x, y)$:

$$I_{HiLo}(x, y) = \eta I_{Lo}(x, y) + I_{Hi}(x, y), \tag{4-1}$$

where $I_{Lo}(x, y)$ is the in-focus low-frequency image and $I_{Hi}(x, y)$ is the in-focus high-frequency image, and x and y are spatial coordinates at the image plane. The parameter η is used to avoid the discontinuity at all frequencies, calculated by [295]:

$$\eta = \frac{HP_{Kc}}{LP_{Kc}}, \tag{4-2}$$

where HP_{Kc} and LP_{Kc} are Gaussian high-pass and low-pass filters, respectively, and

K_c, the cut-off frequency, should be less than or equal to the frequency of the structured illumination pattern. It should be notice that K_c is adjusted by the frequency of the DMD patterns. In section 4.3.4, for fluorescent beads imaging, K_c is set as 45.36μm/lp, and the high-pass filter is directly applied to the Fourier transform of the data for acquiring $I_{Hi}(x, y)$ components.

According to the wide-field microscope's OTF, high-frequency features decay rapidly, defocused from the image plane [302]. Thus, a high-pass filter can be applied on the uniformly-illuminated image to obtain ICH:

$$I_{Hi}(x, y) = \Im^{-1}\{HP_{Kc}\{\Im[I_u(x, y)]\}\}, \tag{4-3}$$

where $\Im$ and $\Im^{-1}$ are two-dimensional Fourier transform and inverse Fourier transform, respectively. HP_{Kc} denotes a Gaussian high-pass filter with the cutoff frequency Kc. I_u is the image under uniform illumination, and it can be divided into the in-focus term I_{focus}, and the defocused term $I_{defocus}$:

$$I_u(x, y) = I_{focus}(x, y) + I_{defocus}(x, y), \tag{4-4}$$

Similarly, the structurally-illuminated image under sinusoidal illumination is:

$$I_s(x, y) = I_{focus}(x, y) + M\sin(2\pi kx) I_{focus}(x, y) + I_{defocus}(x, y), \tag{4-5}$$

where *M* is the modulation depth and *k* is the pattern spatial frequency. The sinusoidal pattern can modulate in-focus images, whereas defocused images does not.

It should be noticed that the DMD can only generate binary patterns, which means that SI patterns should be stripe patterns. However, when using a DMD to project a stripe pattern onto the sample plane of a microscope, the transformation of the stripe pattern into a sinusoidal pattern is often attributed to the diffraction effects caused by the DMD itself, as well as the optical system of the microscope. The DMD consists of thousands of tiny mirrors that can tilt to direct light either towards or away from the projection lens. The edges of these mirrors can cause diffraction, which is the bending of light as it passes around the edges of an object. The small size of the mirrors is on the order of the wavelength of light, which can lead to significant diffraction effects, transforming the sharp edges of the stripe pattern into more sinusoidal patterns. Moreover, imperfections in the optical system of the microscope, such as lens aberrations, can distort the projected pattern. These aberrations can blur the edges of the stripes, contributing to the sinusoidal appearance. From the aspect of Fourier optics, when light is projected through any system with a finite aperture (like the DMD and the microscope optics), the system performs a Fourier transform on the light pattern. A stripe pattern, being like a square wave, has a Fourier transform that includes sinusoidal components. The optical system can emphasize these sinusoidal components, especially under coherent illumination conditions.

To extract the ILC from $I_u(x, y)$, a weighting function should be used to reject defocused low-frequency components. The weighting function serves to optimally combine the high-resolution information from the SI image with the low-noise background of the uniformly illuminated image. This process enhances the visibility of fine details in the specimen while suppressing the noise, resulting in clearer, more detailed images. Mathematically, the weighting function can be represented as a spatially varying parameter that determines the contribution of each type of illumination (uniform or speckle) at each point in the final image. Since the image modulated by the

sinusoidal pattern have the maximum contrast at the focal plane, we can relate this weighting function with the contrast. This weighting function can be obtained by using the rectified subtraction method [289], the single-sideband demodulation method [295], and the local contrast method [21]. Here, considering the robustness, calculation speed, and simplicity, we used the difference image with a band-pass filter for the contrast weighting function to remove the sample-induced contrast and obtain a better axial resolution [292]:

$$C(x,y) = std\left\langle \Im^{-1}\{BPF\{\Im[|I_u(x,y) - I_s(x,y)|]\}\}\right\rangle, \tag{4-6}$$

where std represents the stand deviation operation and BPF is a 2D Gaussian band-pass filter. The band-pass filter can remove the DC spectral components, which is not defocus. The optical sectioning performance of low-frequency components can be enhanced by tuning the bandpass filter's width, and it can be denoted as:

$$BPF(k_x,k_y) = \exp(-\frac{k_x^2+k_y^2}{2\sigma^2}) - \exp(-\frac{k_x^2+k_y^2}{\sigma^2}), \tag{4-7}$$

where (k_x,k_y) is the spectral coordinate and σ is the band-pass filter's width.

Weighted uniformly-illuminated images without $I_{defocus}$ can be obtained by multiplying the uniformly-illuminated image with $C(x,y)$. Then, a low-pass filter is applied to the weighted uniformly-illuminated image to diminish structurally-illuminated-induced sinusoidal noise to acquire ILC:

$$I_{Lo}(x,y) = \Im^{-1}\{LP_{Kc}\{\Im[C(x,y)I_u(x,y)]\}\}, \tag{4-8}$$

where LP_{Kc} is the low-pass filter with cutoff frequency Kc.

4.2.2 Optical Setup of the System

Fig. 4-1(a) illustrates the optical configuration of SOS. A smartphone (iPhone 13Pro, Apple) serves as both the illumination source and the sensor. The LED light emitted by the smartphone is initially directed through a liquid light guide (3mm×6', liquid light guide, Edmund Optics). This light is then filtered using a selected filter and collimated through the Köhler illumination setup (refer to section 4.2.4 for details) to illuminate the DMD (DLP LightCrafter 6500, Texas Instruments). The modulated reflective light from the DMD subsequently passes through a dichromatic mirror. L1 is an achromatic lens pair (MAP10303-A, Thorlabs), and L2 is an aspherical convex lens (ACL3026U-A, Thorlabs). To maintain consistency between the input and reflective light planes, the DMD is rotated at 45° because each pixel on the DMD is activated along the diagonal line (see Fig. 4-1(b)). The illumination light is also introduced at a 24° angle from the direction normal to the DMD, allowing for reflection at 0°. Two 4f systems, namely L3-RL2 (L3: AC508-180A, RL2: AC508-100A, Thorlabs) and OL-RL1 (OL: UPLanSApo/20X/0.75, Olympus, RL1: AC508-100A, Thorlabs), are employed for structured illumination. The ETL (EL-16-40-TC-VIS-5D-M27, Optotune) acts as a nonmechanical axial scanning device with a rapid response. It is conjugated to the Back Focal Plane (BFP) of the objective lens, ensuring a telecentric setup and maintaining constant lateral magnification during axial scanning (refer to section 4.2.3 for details).

The objective lens collects the excited fluorescent signal, and the first image is located at the BFP of RL1. Then the image is again imaged at the BFP of TL (AC508-180A, Thorlabs) through RL2-TL 4f system. The ETL is located at the confocal plane of RL2, TL, and L3. To acquire the image using a smartphone, the same reversed smartphone lens is put in front of the camera to combine a 1:1 symmetric relay system. So the image

can finally be recorded by the smartphone sensor. The smartphone sensor is equipped with the Bayer filter so that coloured images can be directly acquired. Furthermore, adapters are designed and fabricated for integrating the smartphone and the liquid light guide to the cage system of the microscope's main body without sacrificing any concentric of the optical path (Fig. 4-1(c), section 4.2.5 for detail).

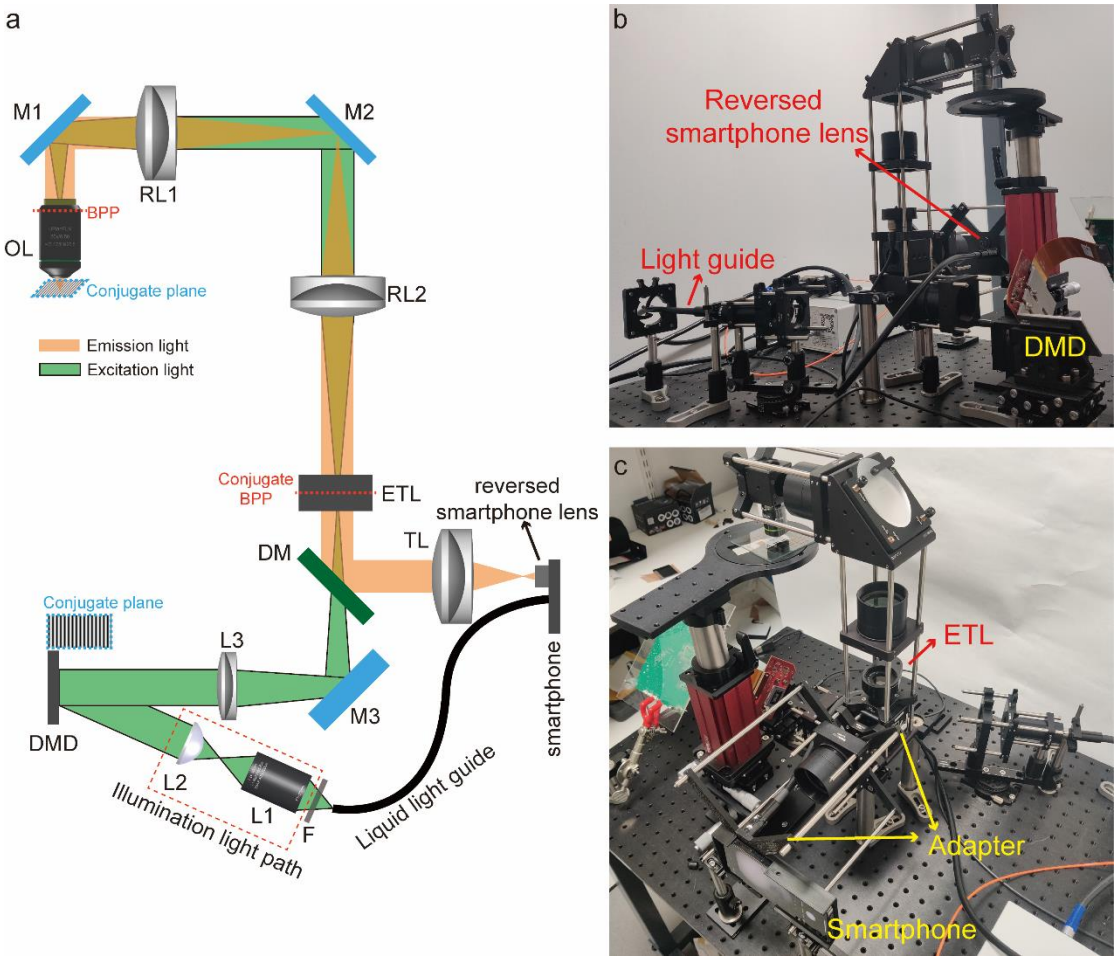

Fig. 4-1. Optical setup of the proposed SOS microscope. (a) The diagram of the SOS microscope. The DMD plane, which is conjugate to the sample plane, is illuminated by the collimated light. L3, RL2 and RL1, OL consist of two 4f systems. The illumination is introduced at 24° to ensure the DMD can reflect the light at 0°. For telecentric design, the ETL is conjugate to the BPP. The image is recorded by a smartphone equipped with a reversed smartphone lens. (b) and (c) shows the experiment setup. Adapters are designed to make the smartphone seamlessly integrate with the SOS main body (section 4.2.5 for detail). OL: objective lens; M1-M3: mirror; RL1-RL2, L1-L3: lens; F: filter;

TL: tube lens; DM: dichromatic mirror; DMD: digital mirror device; ETL: electrical tunable lens; BPP: back pupil plane.

4.2.3 Telecentric Design and Theoretical Axial Scanning Range

The telecentric design can realized axial scanning with invariant lateral magnification. Here, an ETL was used for axial scanning by tuning the input current to change its surface shape. To maintain lateral magnification at different depths, the entrance and exit pupils should be located infinitely at object and image space, respectively. Therefore, the system setup should be strictly in the 4f configuration.

Fig. 4-2 illustrates the telecentric design of the imaging path. ETL should be conjugated with the objective lens's BPP to obtain the telecentric design. It is hard to put ETL directly at BPP; therefore, the 4f configuration (RL1-RL2 lens pair) was used to relay BPP, at which ETL and BPP are conjugated. Meanwhile, ETL is also located at the FFP of the TL to guarantee that the image space is telecentric. It should be noted that the clear aperture size of the conjugate BPP cannot surpass ETL's clear aperture. Here, the BPP diameter of the objective lens is 9 mm and ETL's clear aperture size is 16 mm. RL1 and RL2 with both 100 mm focal lengths was used to combine a 1:1 4f configuration, and its confocal plane coincident with the intermediate image plane I.

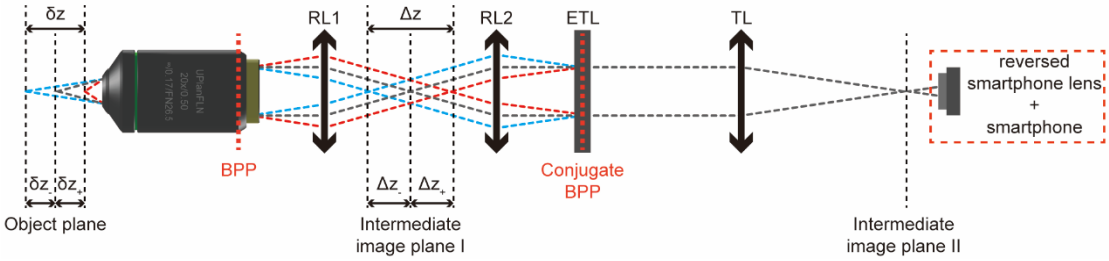

Fig. 4-2. Telecentric imaging optical path. RL1 and RL2 is configured as a 4f system to relay the objective lens' back pupil plane to ETL. The red and blue lines depict the

minimum and maximum axial scanning ranges.

To calculate the theoretical scanning range in object space, the relationship between the axial displacement of the object plane and the intermediate image plane should be found. As shown in Fig. 4-2, δz_+ and Δz_+ can be related by:

$$\delta z_+ = \frac{n_o}{n_i M_{OL-RL1}^2} \Delta z_+ , \tag{4-9}$$

M_{OL-RL1} is the lateral magnification of the objective lens and the first relay lens (RL1), n_o and n_i are the refractive indices in the object and the image space, respectively. Here, for simplicity, both of them are unity. The scanning range will be different for the sample's refractive index.

The intermediate image plane I can be tuned by ETL, and RL2 and ETL can be treated as a compound lens. According to Gullstrand's equation [303]:

$$f_{RL2-ETL} = \frac{f_{ETL} f_{RL2}}{f_{ETL} + f_{RL2} - d_{ETL-RL2}} , \tag{4-10}$$

$f_{RL2-ETL}$ is the focal length of the RL2-ETL-compound lens, f_{ETL} and f_{RL2} are the focal lengths of ETL and RL, and $d_{ETL-RL2}$ is the distance between ETL and RL2. Since ETL is located at the BFP of RL2, Eq. (4-10) can be rewritten as:

$$f_{RL2-ETL} = \frac{f_{ETL} f_{RL2}}{f_{ETL} + f_{RL2} - f_{RL2}} = f_{RL2} , \tag{4-11}$$

Therefore, tuning ETL's optical power changes the compound lens's front principal plane instead of changing its focal length. This is equivalent to the axial displacement of the intermediate image plane I. As shown in Fig. 4-2, Δz_+ can be written as [303]:

$$\Delta z_+ = \frac{f_{RL2}^2}{f_{ETL}}, \tag{4-12}$$

Combining Eq. (4-9) and Eq. (4-12) we obtain:

$$\delta z_+ = \frac{1}{M_{OL-RL1}^2} \bullet \frac{\phi_{ETL}}{\phi_{RL2}^2}, \tag{4-13}$$

ϕ denote the corresponding optical power.

Therefore, the scanning range in the object space can be written as:

$$\delta z = \left|\delta z_-\right| + \left|\delta z_+\right| = \frac{1}{M_{OL-RL1}^2}\left(\left|\frac{\phi_{ETL-\max}}{\phi_{RL2}^2}\right| + \left|\frac{\phi_{ETL-\min}}{\phi_{RL2}^2}\right|\right), \tag{4-14}$$

$\phi_{ETL-\min}$ and $\phi_{ETL-\max}$ are the minimum and maximum optical power of ETL.

4.2.4 Illumination Path Design

Fig. 4-3 shows the exact illumination path for the HiLo microscopy. The light guide's light must be collimated, and the final beam diameter *D* should fill the DMD's active area. Furthermore, this diameter *D* cannot be too large to prevent illumination energy loss. Therefore, *D* was set to be the diagonal length of DMD's active area. The Köhler setup was applied to acquire high-quality illumination. L1 was used as a collector to

image the light source to the FFP of the condenser (L2), and the final collimated light illuminated the DMD. To choose appropriate elements for L1 and L2, the relationship between the illumination half angle u and beam diameter D can be found according to the Gaussian optics. The magnification of the collector (L1) can be calculated as:

$$m_c = \frac{n_1 \sin u}{n_1' \sin u'}, \tag{4-15}$$

where n_1 and n_1' are the refractive index in the object and image space of L1, respectively. When the light is collimated by L2, the relationship between u' and D is:

$$\sin u' = \sin[\arctan(\frac{D}{2 f_{condenser}})], \tag{4-16}$$

$f_{condenser}$ is L2's focal length. The medium is air. Combining Eq. (4-15) and Eq. (4-16):

$$\sin u = m_c \sin[\arctan(\frac{D}{2 f_{condenser}})], \tag{4-17}$$

where the angle u can be obtained from experiments (Section 4.3.2 for detail) and D should be slightly longer than the diagonal length of the DMD active area, which is 12mm.

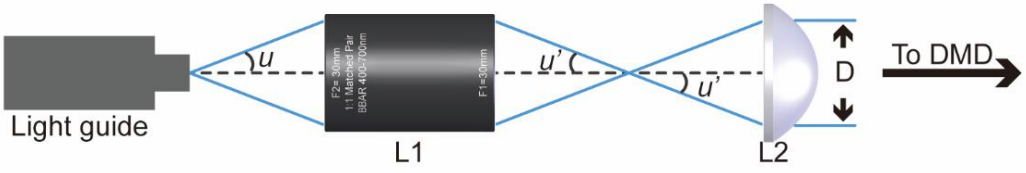

Fig. 4-3. Illumination light path. After calculating and experiments, appropriate L1 (MAP10303-A, Thorlabs) and L2 (ACL3026U-A, Thorlabs) are chosen. L1 has 1X magnification, and the NA of L2 is 0.55.

4.2.5 Smartphone Adapter Design

I employed CAD design (Autodesk, Inventor Professional 2020) and 3D-printed two adapters. Fig. 4-4(a) shows the connections between these adapters. Two holders were designed to accommodate the iPhone. These adapters are designed similarly to the Thorlabs cage system adapter. So that the smartphone can be easily combined with the microscope's main body without losing any concentricity. Fig. 4-4(b) illustrates the smartphone holder with the light guide and the reversed smartphone lens.

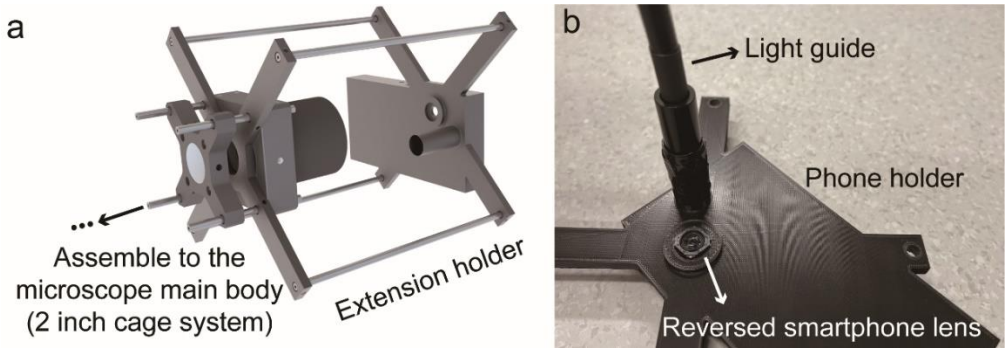

Fig. 4-4. Home-made adapters. (a) The diagram of harnessing the smartphone to the microscope's main body. (b) The light guide and the reversed smartphone lens are aligned through the smartphone holder.

4.3 Results

4.3.1 Performance of the Axial Scanning

The theoretical axial scanning range can be obtained from Eq. (4-14). The effective ETL current (I) ranges from -250 mA to 250 mA, corresponding to the optical power from -3.3 to 3.5 dpt. The lateral magnification of the lens pair OL-RL1 is 11.1, and the

optical power of RL2 is 10 dpt. The theoretical axial scanning range is calculated as 561 μm.

The experimental axial scanning range is also measured to compare with the theoretical results. A uniform pattern was uploaded onto the DMD to generate wide-field illumination. A resolution target (R3L3S5P, Thorlabs) was imaged at the different axial positions by tuning the current of the ETL and the z-axis translation stage. In the experiment, *I* was adjusted to be -250, 125, 0, 125, and 250 mA. After each current adjustment, the target was axially removed by adjusting the translation stage (Edmund Optics) to get a clear image, and the relationship between *I* and the axial displacement (*d*) can be found (Fig. 4-5(c)). The translation stage here is for finding the relationship between the axial movement and the ETL current. It can be exempted during experiments.

Fig. 4-5(a) shows five in-focus images at different depths; the central image is the in-focus image without tuning the *I* (0mA). All images were captured without any horizontal or vertical movements. To prove the telecentric property of the proposed system during axial scanning, as shown in Fig. 4-5(a), three line profiles were traced at the same position when the *I* were -250mA, 0mA, and 250mA. As shown in Fig. 4-5(b), the size of each circle fixed, meaning that the lateral magnification is constant. The data is normalized by $\frac{I_{max}-I_{min}}{I_{max}+I_{min}}$ for better visualization. I_{max} and I_{min} is maximum and minimum intensity respectively. Fig. 4-5(c) shows the ETL current versus the axial displacement. The axial position was set as a reference plane (*d* is zero) when *I* is zero. The measured axial scanning range is 571.5 μm, close to the theoretical value of 561 μm with a 2% error.

Fig. 4-5(d) shows the non-normalized line profiles of fig. 4-5(b). Obviously, the contrast is very low, and this could be attributed to several factors, including the limitations of

smartphone sensors, optical aberration, or misalignment of the optical path.

Smartphone-based optical sectioning microscopy, as detailed in this study, utilizes smartphone sensors instead of high-cost camera sensors. While this is cost-effective and innovative, smartphone sensors may not always match the sensitivity and dynamic range of more specialized imaging sensors used in traditional microscopy. This can lead to lower contrast in captured images, especially in scenarios requiring high sensitivity to subtle changes in light intensity. More detailed discussions can be found in section 4.4.

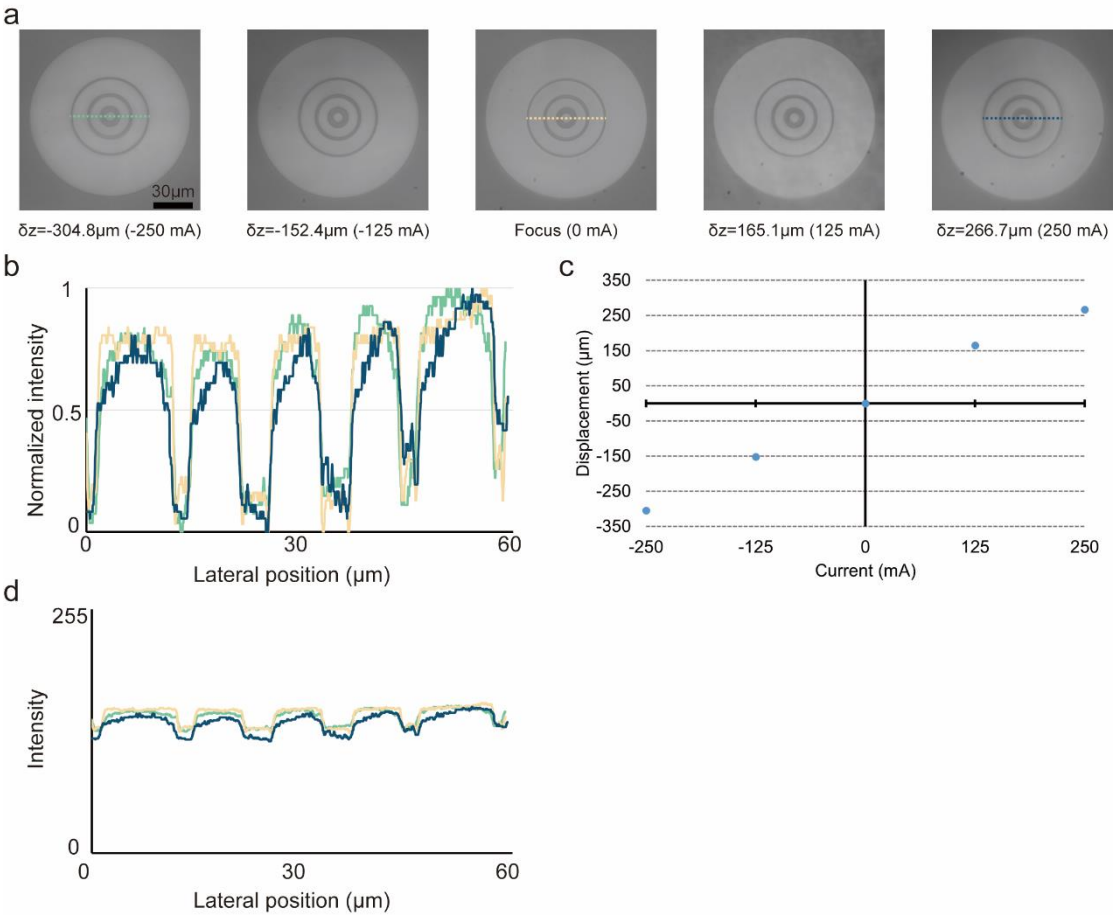

Fig. 4-5. Performance of axial scanning and telecentric property. (a) In-focus images at different depths. The ETL current is first changed, then the target is moved axially to acquire a clear picture. (b) Corresponding line profiles in Fig. 4-5(a). (c) Relationship between the ETL current and axial displacement. (d) Non-normalized line profiles for (b).

4.3.2 Characterization of the Illumination Path

a. Radial Intensity Distribution

According to Eq. (4-17), the light source's radial intensity distribution decides how to choose the appropriate optical components to illuminate the whole DMD area with proper beam diameter. The low-loss liquid light guide (5mm * 6' UV, Edmund Optics) was contacted to the smartphone's LED. The output illumination radial intensity distribution was tested, as shown in Fig. 4-6(c). The radial intensity distribution directly irradiated from the smartphone was compared as shown in Fig. 4-6(a). Fig. 4-6(b) and (d) show the corresponding distributions and corresponding distributions in the polar coordinate system. The light guide can easily guide the illumination source to the aimed position. Besides, the power distribution from the light guide is more focused (14.2° FWHM) than the phone LED (21.6°).

When coupling the LED light of a smartphone into the liquid light guide, the issue of light loss is not readily avoidable. The NA of the liquid light guide is noted to be 0.55, indicating a range of ±33 degrees. Hence, the occurrence of light loss is anticipated, as seen at the extreme end of the distribution in fig.4-6(d). It is believed that bending loss contributes to this issue. In practice, maintaining the light guide in a perfectly straight alignment is challenging, resulting in inevitable light attenuation. Additionally, the gap between the light guide's surface and the LED light source may cause the loss. Achieving a seamless contact between the light guide surface and the LED light source proved challenging during experimentation, leading to light leakage. Furthermore, the difference in diameters between the LED light source at 7mm and the 3mm core of the light guide further compounds the issue of light loss.

Moreover, the power and the Etendue problem of illumination are also essential, and

these will directly decide the illumination efficiency. These are limitations of our current study, and detailed discussions can be found in section 4.4.

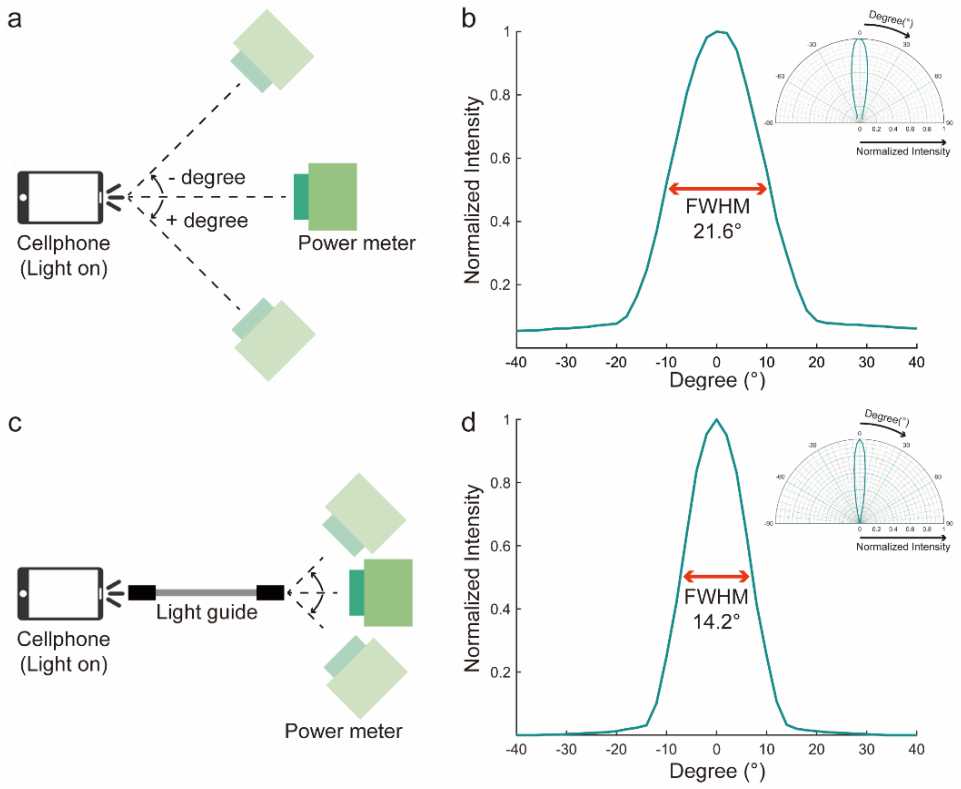

Fig. 4-6. The measured radial intensity distribution by the power meter (LASERPOINT, Italy). Intensity distribution tests with (a) and without (c) the light guide. (b) The distribution of (a). (d) The distribution of (c). FWHM means the full-width-half-maximum. The subplots in (b) and (d) are in the polar coordinate system.

b. Spectral Intensity Distribution

The spectrometer (HR2000, Ocean Optics) was used to test the smartphone LED's spectrum. Fig. 4-7 shows the spectrum range of the iPhone 13pro LED. Like most white LEDs, the peak emission appears at ~450nm wavelength, and the normalised intensity in the visible spectrum range is higher than 50% except the dip around 480 nm.

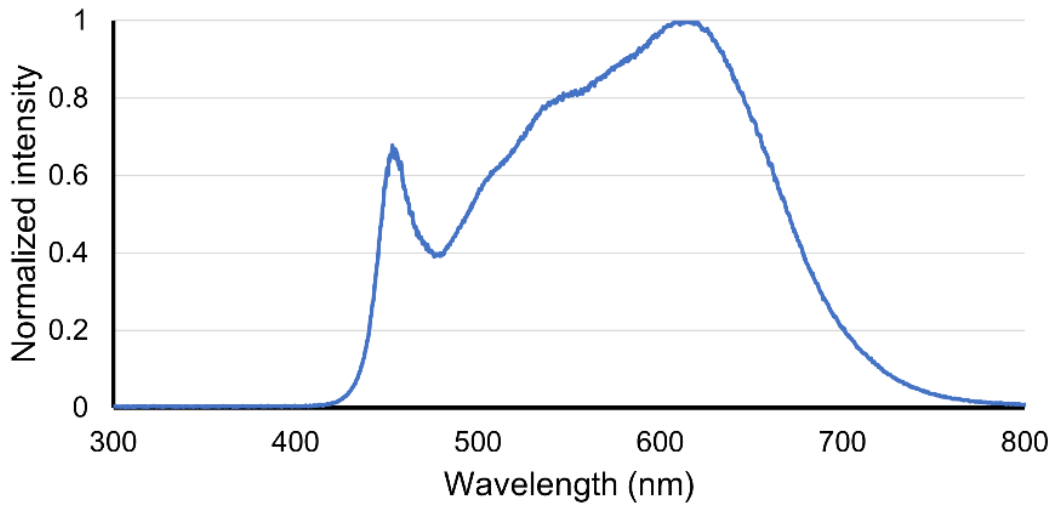

Fig. 4-7. The spectrum of the iPhone 13pro LED.

4.3.3 Optical Sectioning Capability

To test SOS' optical sectioning capability, I put a silver-coated mirror (PFR10-P01, Thorlabs) on the sample stage and projected DMD patterns with different periods to its surface. Since the pattern contrast decreased with defocus, contrast maps was extracted from pattern images and quantified the optical sectioning capability accordingly [289]. The green light (532nm) was used as reference [304]. An emission filter (FL532-3, Thorlabs) was inserted in front of the liquid guide. The focal plane was axially scanned with a 5μm step for a 15.12μm/lp pattern and a 10μm step for 75.6μm/lp and 241.92μm/lp patterns. The normalized contrast for each axial image is calculated by $C = (I_{max} - I_{min})/(I_{max} + I_{min})$. Fig. 4-8(a) shows the relationship between the normalized contrast and the axial position for three patterns with different frequencies. A higher frequency shows better optical section capability. This is because the higher spatial frequency modulation of the OTF in widefield microscopy decays with defocus more quickly, enabling better optical sectioning power. In this study, the DMD's pixel size is 7.56μm, so the highest frequency is 15.12μm/lp. Fig. 4-8(b) shows images with three frequencies captured at three axial positions. The pattern structure at 15.12μm/lp almost vanishes when the defocus distance is -10μm, whereas the periodic structure at

241.92μm/lp is still observable at the defocus distance -100μm.

From these images, we can also find that the contrast is relatively low, especially when the frequency is higher. As mentioned in section 4.3.1, smartphone sensors may not be as capable as specialized microscopy cameras in detecting subtle changes in intensity, particularly in low-light conditions or when imaging faint fluorescence signals. This limitation can lead to images with lower contrast, especially for patterns with lower spatial frequencies where the distinction between illuminated and non-illuminated regions is less pronounced.

Moreover, the optical system's resolution, defined by the diffraction limit, impacts how well high spatial frequency patterns are resolved. As the spatial frequency of a pattern approaches the system's resolution limit, it becomes increasingly difficult for the microscope to distinguish between the high and low regions of the pattern, leading to reduced contrast. This effect is exacerbated for higher spatial frequencies, which are closer to or beyond the resolution limit of the optical system.

In HiLo, high spatial frequency components of the illumination pattern decay more rapidly with defocus compared to lower frequencies. While this rapid decay is beneficial for optical sectioning, it also means that at any significant defocus distance, high-frequency patterns lose contrast more quickly than lower-frequency patterns. Essentially, the high-frequency components are more sensitive to slight deviations from the focal plane, leading to a reduction in contrast when the sample is not precisely in focus.

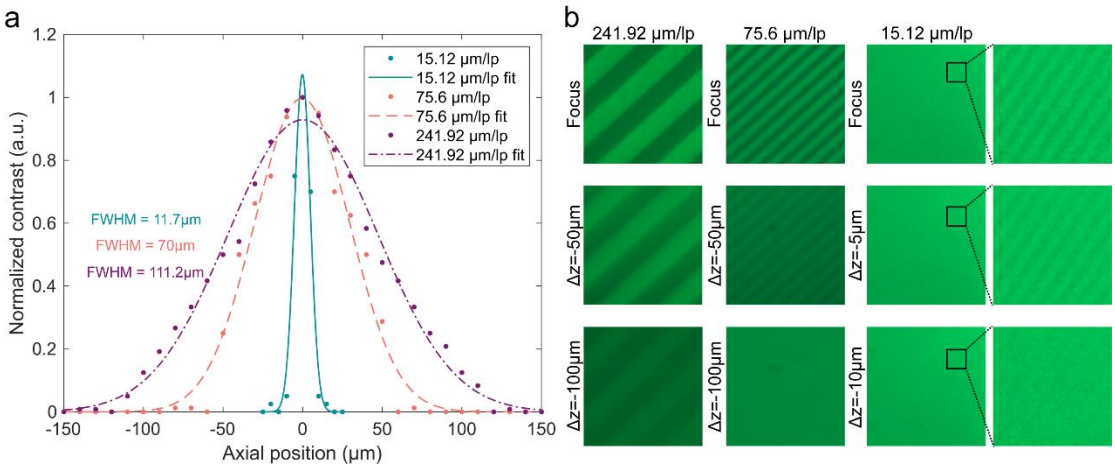

Fig. 4-8. SOS' optical sectioning capability. (a) The axial contrast profiles of DMD patterns for three spatial frequencies were obtained by imaging the reflected signal from the mirror sample. The Gaussian fitting was used for each experimental dataset. The Gaussian function's FWHM is also shown. (b) The images with three frequencies in (a) are captured at focus, and two defocus planes.

4.3.4 Fluorescent beads imaging

Fluorescent PS beads with 465 nm, 515 nm, and 605 nm excitation wavelengths (FluoSpheres, Thermo Fisher) were used to test SOS' imaging performances. The bead's size is 10μm in diameter. The samples were diluted ten times with deionised water and set on microscopic glass slides. For structured illumination, the DMD pattern period was set to 6 pix/lp (45.36μm/lp). For uniform illumination, all pixels on DMD were turned 'on'. Fig. 4-9 shows the captured images of fluorescent bead samples. The widefield images were imaged under uniform illumination, and the SI images were under structured illumination. The HiLo algorithm was used to obtain the final HiLo images by taking both widefield and SI images. The code source and the ImageJ plugin can be found in appendix. To excite different fluorescent beads, different optical filters were inserted into the illumination path which was shown in Fig. 4-1(a), letter F (Fig. 4-9(a), FBH430-10; Fig. 4-9(b), FBH500-40; Fig. 4-9(c), FBH580-10, Thorlabs). Because of the Bayer filter on the smartphone sensor, emission filters were unnecessary.

Fig. 4-9(d)- (f) shows corresponding line profiles in Fig. 4-9(a)-(c).

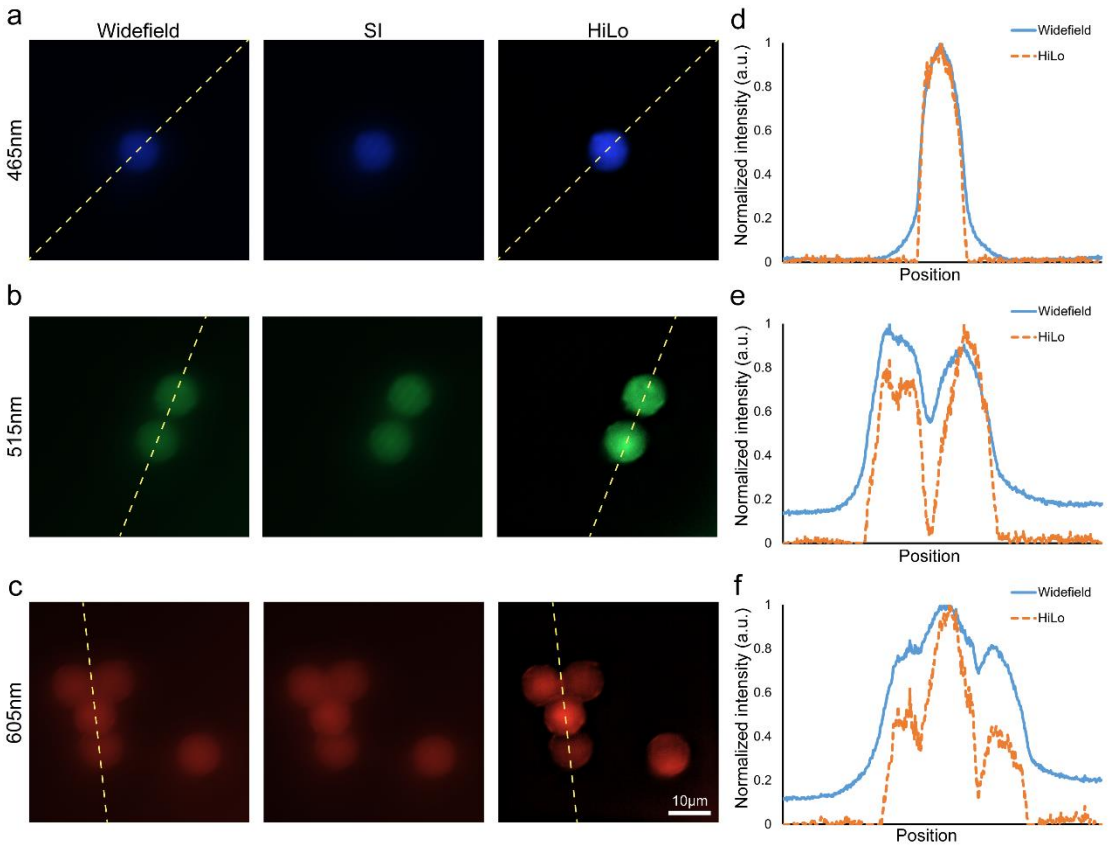

Fig. 4-9. Fluorescent bead images at different wavelengths. (a) The bead samples with 430nm excitation and 465nm emission. (b) The bead samples with 505nm excitation and 515nm emission. (c) The bead samples with 580nm excitation and 605nm emission. Corresponding line profiles of widefield and HiLo images are shown in (d)-(f). SI: Structured illumination.

4.3.5 Optically sectioned imaging of accumulated fluorescent beads

To test SOS' optical sectioning performances, the fluorescent beads (FluoSpheres, Thermo Fisher, 505/515) of different layers were optically sectioned and then imaged. The 10μL bead solution without dilution was dipped onto the microscopic glass side and waited until it was dry. Therefore, beads start to accumulate and flow much slower.

The current (*I)* was set to -10.5, -7.0, -3.5, 0.0, 3.5, 7.0 mA , and the focus plane from -15 μm to -10 μm with a 5 μm step. At each step, beads were illuminated by uniform and structured illumination (45.36 μm/lp). Fig. 4-10 shows widefield, structured illumination, and HiLo-processed images of accumulated beads at different depths. The HiLo images show much better optical sectioning capacity compared with widefield images. Out-of-focus signals are significantly suppressed. Several artefacts in the final HiLo images can also be found in the same position of widefield images (red rectangular), and there is no such artefact when samples are sparse (Fig. 4-9). In [305], researchers found that thick fluorescent objects could reduce speckle contrast, hampering the optical sectioning performance, but only in speckle illumination. In [287], in which the illumination setup is the same as our SOS, researchers found that the SI pattern of higher frequency can deliver a better axial resolution but more susceptible to out-of-focus background and thus produce severe artefacts in HiLo optical-sectioning images. Although these studies found artefacts in experiments, the cause of artefacts should be further examined. We speculate that this issue might be attributed to the camera of an iPhone smartphone, given the difficulty in adjusting its parameters and the challenge in accessing raw data. Furthermore, since the smartphone camera is optimized for general photography, it may pose challenges when used for capturing biological images. An in-depth examination of this phenomenon is provided in Section 4.4.

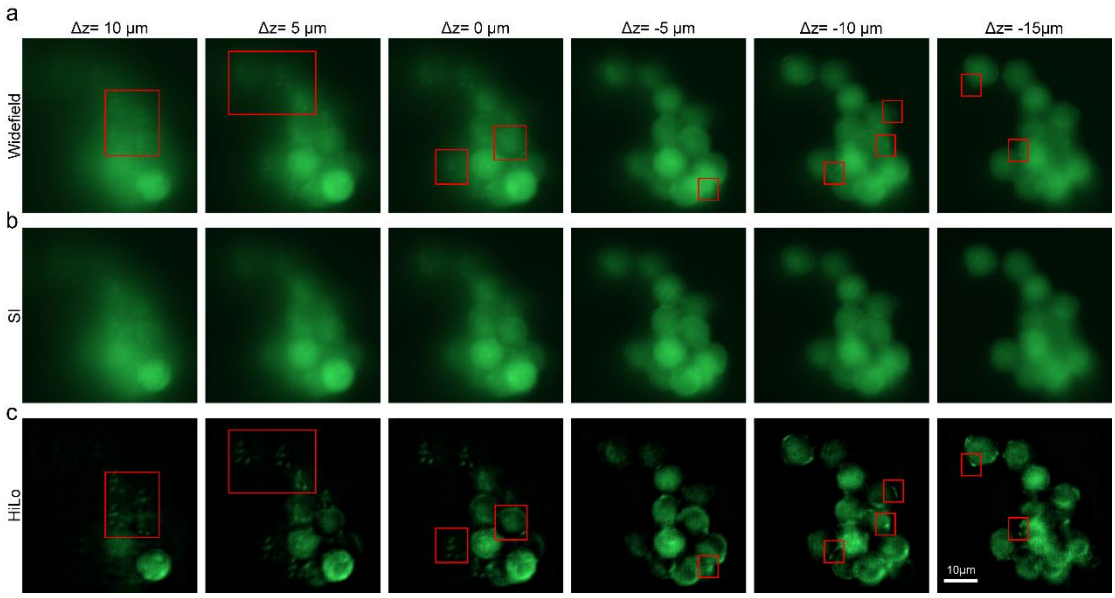

Fig. 4-10. Images of accumulated fluorescent beads at different depths. (a) widefield images. (b) SI images. (c) HiLo processed images.

4.4 Discussion and Future Aspects

Using microscopes for biomedical research and disease diagnosis poses challenges in resource-limited areas due to a lack of necessary resources. Especially for advanced optical sectioning microscopes, light sources, scientific sensors, precise translation stages, and optical components are usually costly. In response, a smartphone-based HiLo optical sectioning microscope, SOS, was proposed as a cost-effective solution utilizing a smartphone and an electrically tunable lens. Table. 4-1 summarizes the components used in the SOS and traditional HiLo systems and their corresponding costs. To make a cost comparison, because the traditional HiLo microscope can be built up in different ways, here we assume that the whole optical path structure is same and other components (objective lens, mirror, cage rod, lenses, filter, mechanical holders, et al.) in both SOS and traditional HiLo systems are identical. In that case, SOS demonstrates significant cost savings of approximately £7,035.

The primary structure of SOS was designed and constructed using a compact cage

system. We developed and manufactured adapters to integrate the smartphone into this cage structure seamlessly. A liquid light guide was employed to channel the light from the smartphone torch to the Digital Micromirror Device (DMD) for structured illumination. The advantage of this approach is that we can freely guide light by using the liquid light guide to the aimed position. In this study, we only test the radial intensity distribution because the aim is to quickly demonstrate our proof-of-concept prototype and determine appropriate lenses for collimation so that the collimated beam size can exactly cover the DMD's effective area. However, to examine whether the illumination source can effectively excite biological fluorescent dyes, the light power output and the Etendue of the light coming out of the fibre still needed to be carefully examined. These aspects are out of the scope of this work, and we will provide quantitative studies soon.

In SOS, the ETL serves as an axial scanner, allowing the selection of sample planes and adjustment of the focal plane. The ETL is precisely conjugated to the BPP of the objective lens through a 4f configuration. This telecentric setup ensures the preservation of lateral magnification irrespective of the axial plane's position. Consequently, both the FOV and resolution remain constant. An additional benefit is that Z-stack images can be directly generated without post-processing. Moreover, the broadband LED light source employed in SOS proves highly effective in exciting various PS beads, providing versatility in imaging capabilities.

The proof-of-concept SOS prototype has demonstrated its ability to successfully section and image 10μm PS fluorescent beads, indicating its significant potential for imaging more complex fluorescently labelled biological samples. However, as discussed in Section 4.3.5, when fluorescent beads are too dense, artefacts can be found in the final HiLo results. We conclude that the illumination and sample properties cause these artefacts. In addition, we suspect that images captured by the iPhone are not raw data and are processed by the post-processing algorithm. Therefore, some artefacts may be

introduced when these processed images are inputs for HiLo algorithms. Shi R., et al [287] also discovered these artefacts in their experiments. They concluded that these artefacts can be avoided by carefully choosing appropriate patterns and the frequency of the structure illumination according to biological samples. However, the cause of these artefacts is still unknown and needs further examination. In future studies, we will examine this aspect thoroughly. We will also use some Android smartphones and develop software to acquire raw format photos to discuss artefact problems.

To testify whether SOS can image actual biological samples, this aspect needs further investigation. In the future, we will use SOS to conduct biological experiments with thicker biological samples (such as fluorescently labelled zebrafish). To develop a compact portable SOS, we will 3D print or machine some components holders instead of using Thorlabs cage system.

This is a pioneer study about using a smartphone instead of a light source and a camera to realize HiLo optical sectioning microscopy. The cost is lower than that of traditional HiLo microscopy. However, we aim to minimize further its cost in the future. The most expensive parts of SOS are the DMD and the light guide. To save money and enable HiLo in low-resource settings, we can substitute the DMD with the diffusive or periodic pattern glass plates, and the light guide can be easily fabricated by low-cost polymers such as PDMS or PMMA. Furthermore, micro-LEDs are broadly used for illumination and display because of their brightness and small volume. We can use a micro-LED mini display and cheaper relay optics to generate and relay structured illumination. If this method is cheaper, additional light sources and light guides can be replaced, and more illumination structures can be generated by using a computer to control the micro-LED mini display.

The ETL and telecentric design maintain the lateral magnification and fast axial

scanning. However, an ETL still costs nearly £950, which is expensive for laboratories without sufficient funds. Cicuta P et al [109]. developed an open-source microscope, OpenFlexure, which allows easy customization and fast development of low-cost microscopes. For instance, Stirling J et al. [110]used the OpenFlexure Delta Stage and developed a multi-modal microscope. Matsui T et al. [120] established an optical sectioning microscope with the OpenFlexure stage. The other open-source microscope project, UC2 [101,114], also provides good options for customizing different low-cost microscopes. Therefore, in our future studies, we will make full use of these platforms and create appropriate modules to replace the ETL.

Considering the fast development of smartphones, the iPhone 13Pro will eventually be out of date and using advanced smartphones in every resource-limited area is also unrealistic. To leverage the limitations of our smartphone HiLo and expand its application scenarios, we will focus on making it more general in future. For 3D-printed adapter parts, we will design a more compact and general part for different smartphones. We will apply clutch structures and adjustable mechanisms into adapters to harness different smartphones seamlessly. In this study, there is only one adapter for simultaneously combining the light guide and an iPhone 13 Pro. Considering that the cellphone's LED torch varies from type to type, we will separate the adapter into two parts, one for the smartphone's main body and the other for the light guide. Users can harness the phone and light guide to their corresponding adapters and combine two adapters. This configuration can make our method more general without considering smartphone types.

The low-contrast issue observed in the images underscores significant challenges inherent in the application of SOS microscopy. The contrast degradation can be attributed to factors including the limitations of smartphone camera sensors, the optical resolution limits of the system, the behaviour of high spatial frequencies under defocus,

and the interaction of light with biological samples. Looking forward, addressing the low-contrast issue in SOS microscopy necessitates a multifaceted approach that encompasses both hardware optimization and computational strategies.

From a hardware perspective, enhancing the light source's intensity and uniformity could improve the overall illumination quality, thereby boosting image contrast. Additionally, integrating more sensitive and high-dynamic-range sensors, possibly through advanced smartphone models or specialized imaging attachments, could mitigate the limitations currently imposed by smartphone cameras. On the computational front, the development of sophisticated image processing algorithms tailored for SOS microscopy could offer significant improvements. These algorithms could employ advanced techniques such as deconvolution, contrast enhancement, and noise reduction to improve the quality of the captured images. Furthermore, machine learning and AI could play a pivotal role in automatically optimizing the imaging parameters and processing strategies based on the sample's characteristics and the desired imaging outcomes.

Another promising avenue is the exploration of adaptive optics and other real-time correction techniques to compensate for optical aberrations and misalignments in the imaging path. These technologies could dynamically adjust the optical setup in response to detected aberrations, ensuring optimal imaging conditions, and enhancing contrast.

In conclusion, this is a pioneer study about testing the possibility of using smartphones to realize the HiLo optical sectioning microscopy. We find several limitations in SOS's performance and configuration that will be further developed in future. These limitations can be solved, and the portable, low-cost HiLo microscope will be developed soon.

Table. 4-1 Costs of the proposed SOS and traditional HiLo systems.

	SOS	Traditional HiLo
Light source	N/A	Tungsten-Halogen Source: ~ £5,000
Camera sensor	N/A	12 MP colour CMOS camera: ~ £2,000
Smartphone	Iphone 13pro: ~ £615	N/A
Light guide	~ £400	N/A
Axial translation stage	Electrically tunable lens: ~ £950	Motorised translation stage: ~ £2000
Total	~ £1,965	~ £9,000

4.5 Conclusion

The proposed smartphone-based optical sectioning microscope, inspired by the HiLo principle, presents a compelling alternative to traditional HiLo systems, resulting in cost savings exceeding £7,035. In SOS, the dual functionalities of the illumination source and camera sensor are seamlessly integrated into a smartphone. An ETL serves as the axial translation stage, enabling axial scanning and focus plane selection.

The telecentric setup employed in SOS ensures the preservation of lateral magnification regardless of the axial plane's position, eliminating the need for post-processing in imaging registration. SOS achieves an impressive axial range of 571.5 μm, closely approximating the theoretical value of 561 μm with a minimal 2% error. The axial resolution of SOS reaches 11.7 μm. Successful imaging of various PS beads was demonstrated, and optically sectioned images of accumulated beads were recorded within a 25 μm axial range using a 5 μm step.

Chapter 5. Optimizing microlens arrays for incoherent HiLo microscopy

HiLo microscopy is a potent, budget-friendly, and easily configurable method for obtaining high-contrast optically-sectioned images. Nonetheless, conventional HiLo microscopes rely on either coherent light sources with diffusive glass plates or incoherent light sources utilizing DMD and SLM, which tend to be more costly.

This study introduces a novel, cost-effective HiLo microscopy approach employing MLAs and incoherent LED light sources. I simulated SI patterns and HiLo image generation based on Fresnel diffraction and incoherent imaging. To investigate the impact of MLAs on HiLo images, I employed three commonly used MLAs with specific microlens pitch and NA parameters, generating periodic illumination patterns. According to simulations, using MLAs and incoherent light sources can significantly enhance image contrast compared to traditional widefield fluorescence microscopes. Surprisingly, the NA of the MLA was found to have an insignificant effect on HiLo images, while a larger lens pitch resulted in higher image contrast. However, an optimized lens pitch is crucial, as excessively high pitches led to artifacts in HiLo images.

This numerical study represents the pioneering exploration of MLA-based HiLo microscopy. Its findings hold potential benefits for researchers seeking to employ MLAs and incoherent light sources in configuring cost-effective HiLo microscopes.

5.1 Introduction

HiLo is a widefield fluorescence microscope with an optical-sectioning (OS) function.

It is a robust method for rejecting background noise and acquiring high-resolution OS images [296,306]. HiLo can reveal fast biological processes in neuron cells [291,292], discover 3D cell mechanical properties by rejecting out-of-focus signals [293], improve retinal image quality [294], and realize 3D image cytometers [290]. HiLo can also achieve rapid and non-destructive imaging of freshly excised tissues with high efficiency and a good resolution [307]. In addition to its biomedical applications, HiLo extends its utility to measuring engineering microstructure surface profiles [308].

The configuration of HiLo is like widefield epi-fluorescence microscopy (Fig. 5-1). The only difference is that in HiLo, the illumination light is adjusted to generate patterns on the sample plane. Any widefield epi-fluorescence microscope can be adapted to function as HiLo, facilitating optically-sectioned imaging by modifying the illumination path. Furthermore, HiLo seamlessly integrates with various biomedical imaging modalities, including endoscopy [289,295,309], 3D volumetric microscopy [310,311], and optical scanning microscopy [312]. Unlike optical-sectioning (OS) microscopy techniques like confocal [24], two-photon [276], and light sheet microscopy [23], HiLo eliminates the need for pinhole assignments, an expensive laser module, and dual objective lenses for illumination and excitation [313].

Like SI microscopy, HiLo employs a light source that projects a distinct SI pattern onto the in-focus sample plane. However, what sets HiLo apart is its ability to reconstruct high-contrast OS images with just two images, one acquired with widefield illumination and the other with SI, in contrast to the three required by OS SI microscopes [314]. Thanks to advancements in deep learning (DL) algorithms and sophisticated image processing, HiLo has evolved to achieve OS imaging using a single image [288,315]. These characteristics collectively position HiLo as a cost-effective and user-friendly imaging technique.

HiLo's SI pattern determines the OS image's contrast and axial resolution [316]. Several studies have concluded that we can optimize the properties of speckle illumination [285,305] and frequency, modulation depth, and SI patterns [287,295] for the best OS images. There are two common ways to obtain SI patterns in HiLo: 1) using a coherent light source with a diffuser [21,317] to create speckle patterns or 2) using an incoherent light source with diffraction optical devices [292,318] to develop periodic patterns. However, coherent light sources, spatial light modulators (SLMs), and digital mirror devices (DMDs) increase the cost and system complexity. MLAs can also modulate light into different patterns. Researchers have exploited lithography [319] and laser etching techniques [320] to fabricate MLAs quickly. Moreover, the moulding method can also produce PDMS and PMMA-based MLAs [321]. Using appropriate MLAs instead of DMD or SLMs for HiLo can minimize costs and simplify the optical path.

Furthermore, it is possible to substitute the expensive coherent light source in HiLo with a more economical uncoherent LED light source. This substitution, utilizing (MLAs in conjunction with LEDs, has the potential to markedly diminish both the cost and complexity associated with HiLo microscopy. However, properly selecting a specific MLA with appropriate parameters is the key to successfully implementing this approach.

This numerical simulation study assesses the integration of uncoherent LEDs and MLAs for a low-cost HiLo system. I first simulated how MLAs generate periodic illumination patterns on the illuminated sample volume. According to several studies about MLAs fabrication [322,323], the three most common types of MLAs were chosen here: the cross-, cylinder-, and hexagon-types (Fig.5-1). I examined how MLA's NA and its microlens pitch affects the spatial distribution of these illumination patterns. Then I generated a simulated fluorescent block, multiplying it with the MLA-generated illumination pattern and using the HiLo algorithm to obtain high-contrast optical-

sectioning images. To balance the computational efficiency and mesh fineness, MLA's NA was tuned within a small range (0.006-0.01). The microlens pitch is set from 60μm to 140μm with a 20μm step. After passing through the optical illumination path with 0.1 times magnification, the illumination pattern period is from 6μm to 14μm with a 2μm step.

According to the simulation results, the HiLo image contrast is not significantly affected by MLA's NA but still has a minor enhancement with a higher NA. Notably, the relationship between the microlens pitch and image contrast is more pronounced. A higher pitch leads to enhanced image contrast, but if the illumination period reaches 14μm/period, the contrast begins to deteriorate. Additionally, we explored three types of MLAs to understand how pattern distribution influences image quality. All three MLA types exhibit similar performance, except when the illumination period reaches its optimum value (12μm/period), where the cross-type MLA outperforms the others. The most favourable results are achieved using the cross-type MLA with a 0.1 NA and a pitch of 120μm. This numerical study is anticipated to inspire further theoretical investigations and contribute to the future development of cost-effective MLA-based HiLo microscopes.

5.2 Theory

5.2.1 Fundamentals of HiLo microscope

The mathematic deduction and theoretical model of HiLo are discussed in chapter 4. In this study, the only different is the SI image is illuminated by MLA-generated illumination pattern. To avoid misunderstand, these formulations were rewrote again in a new coordinate system with different letters (Fig. 5-2).

In HiLo, two images combine an OS image ($I_{HiLo}(u, v)$):

$$I_{HiLo}(u,v) = I_{Hi}(u,v) + \eta I_{Lo}(u,v), \tag{5-1}$$

where $I_{Hi}(u,v)$ is the in-focus high-frequency image, $I_{Lo}(u,v)$ is the in-focus low-frequency image, and u,v are spatial coordinates. The parameter η can avoid discontinuities in the frequency domain, which can be calculated by [295]:

$$\eta = \frac{HP_{k_c}}{LP_{k_c}}, \tag{5-2}$$

where HP_{k_c} and LP_{k_c} are Gaussian HPF and LPF, respectively, and k_c, the cut-off frequency, should be less than or equal to the frequency of the structured illumination pattern. LP_{k_c} is complementary to HP_{k_c}. Because $I_{Hi}(u,v)$ is intuitively axially resolved, it can be acquired easily by:

$$I_{Hi}(u,v) = \mathcal{F}^{-1}\{HP_{k_c}[I_u(k_u,k_v)]\}, \tag{5-3}$$

where $I_u(k_u,k_v)$ is the captured image in the frequency domain under uniform illumination and $\mathcal{F}^{-1}\{\}$ is the inverse Fourier operator. To get $I_{Lo}(u,v)$, which cannot be axially resolved, we need a weighting function to select the in-focus portion of $I_u(u,v)$ below the cut-off frequency. First, we get a bias-free difference image $I_\Delta(u,v)$ by subtracting $I_s(u,v)$, the captured image in the spatial domain under structured illumination, from $I_u(u,v)$:

$$I_\Delta(u,v) = I_u(u,v) - I_s(u,v), \tag{5-4}$$

where $I_u(u,v)$ and $I_s(u,v)$ are the captured images under uniform and structured illumination in the spatial domain. According to Eq. (5-4), we can estimate the illumination-induced contrast $C(u,v)$ by:

$$C(u,v) = \sigma\{I_{\Delta}(u,v)\}, \tag{5-5}$$

where $\sigma\{\}$ means the standard deviation.

In this study, the $C(u,v)$ is different with $C(x,y)$ in chapter 4. $I_{\Delta}(u,v)$ here is not filtered by the band-pass filter. Because in this study, I care about how the MLA-generated illumination pattern changes the result. If all difference images are not filtered by the band-pass filter, there is no relative change, and this can make the calculation more efficient.

According to Eq. (4) and Eq. (5), we can guarantee that the modulated component is locally centred about zero and make the evaluation insensitivity to differences in the global illumination profile [289]. Then we weighted $I_u(u,v)$ with $C(u,v)$ and input it to the low-pass filter to acquire $I_{Lo}(u,v)$:

$$I_{Lo}(u,v) = \mathcal{F}^{-1}\{LP_{k_c}[C(k_u,k_v)I_u(k_u,k_v)]\}, \tag{5-6}$$

where $C(k_u,k_v)$ is $C(u,v)$ in the frequency domain.

5.2.2 Theory of Pattern Projection and Image Formation

In examining the impact of MLAs on HiLo microscope image quality, I conducted a comprehensive mathematical deduction elucidating the principles of structured illumination and image formation. Spectral domain multiplications were chosen instead of spatial domain convolutions to enhance computational efficiency.

Fig. 5-1 illustrates the physical model of this study. The MLA modulates the collimated

beam and forms a specific pattern on its focal plane. The Fresnel diffraction theory was used in this part. To create different patterns, three common types of MLAs (cross-, cylinder- and hexagon types) were used. The illumination part of the 4f microscope system (L1 and OL) conjugates the illumination pattern to the sample plane, and the camera captures the excited fluorescent signal through the imaging part of the 4f microscope system (OL and Tube lens). The incoherent imaging theory was used in the illumination and imaging parts.

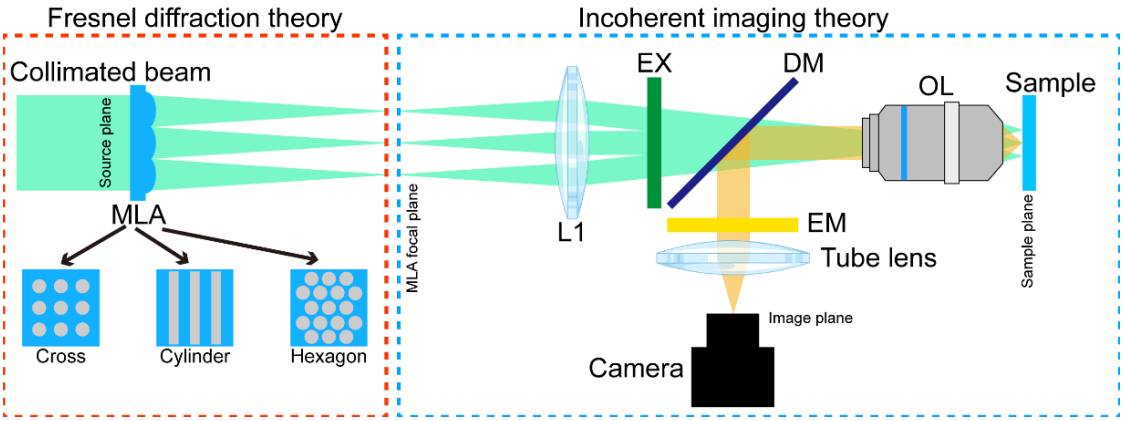

Fig. 5-1. The physical model of this study. Red and blue dashed rectangles denote physical theories used in different parts. I used three different MLAs to generate different illumination patterns. This optical path is for structured illumination. The uniform illumination can be easily obtained by removing the MLA, and the collimated beam can be focused on the back pupil plane of the OL by L1. For simplicity, I denote four planes in the figure (source plane, MLA focal plane, sample plane, and image plane), which are the same as Fig. 5-2. (MLA: microlens array; L1: convex lens; EX: excitation filter; DM: dichroic mirror; OL: objective lens; EM: emission filter).

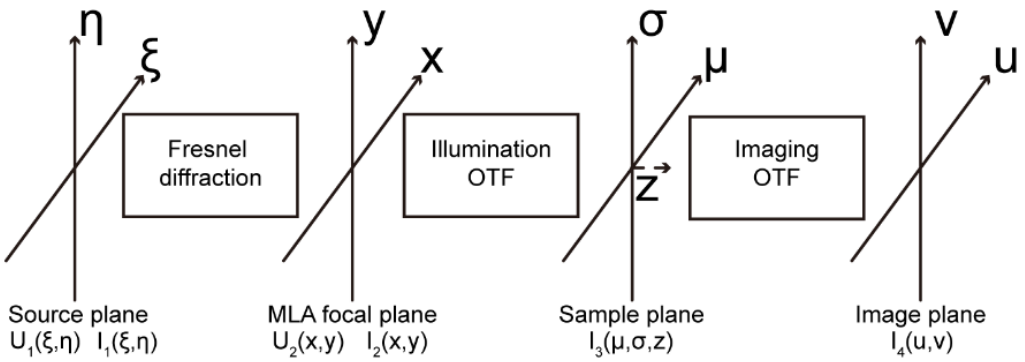

Fig. 5-2. Coordinate system of illumination and imaging process.

Firstly, let us see the image formation on the image plane. Fig. 5-2 is the coordinate system for a mathematical deduction. The image acquired under SI is:

$$I_{4s}(u,v) = \sum_{z_i=0}^{n} \iint PSF_{em}(u-\mu, v-\sigma)|_{z=z_i} I_3(\mu,\sigma,z_i) O(\mu,\sigma,z_i)\, d\mu d\sigma, \quad (5\text{-}7)$$

where PSF_{em} is the 2D emission point spread function with a defocus term (different z). O and I_3 are the 3D objects and illumination distribution, respectively, and z_i is the defocus distance between the focus and target plane (z_i = 0 is in focus).

To obtain the intensity distribution on the image plane, I convoluted the corresponding structure-illuminated sample plane for each slice with a defocused PSF_{em}, and summed them up from $z_i = 0$ to $z_i = n$. When $I_3(\mu,\sigma,z_i)$ is 1 for different z_i, we can obtain the image under uniform illumination ($I_{4u}(u,v)$). For simplicity, we assume the imaging system is telecentric and has unit magnification. From Eq. (5-6), $I_3(\mu,\sigma,z_i)$ can determine the final HiLo image.

The incident beam is assumed to be a monochromatic plane wave, and only the distribution inside each microlens of the MLA is considered. For the cross-type MLA, the amplitude distribution before the MLA can be written as:

$$U_1(\xi,\eta) = \sum_i \sum_j circ\left[\frac{\sqrt{(\xi-id)^2+(\eta-jd)^2}}{w}\right] = \begin{cases} 1 & inside\ each\ micro\ lens \\ 0 & other\ wise \end{cases}, \tag{5-8}$$

where w is the radius of each microlens, d is the distance of the neighboring microlens, i and j denote the indices of microlenses in two perpendicular directions (i =0, j =0 for central microlenses). The phase transformation of the cross-type MLA can be written as:

$$\phi(\xi,\eta) = \sum_i \sum_j exp\left\{-j\frac{2\pi}{\lambda_{ex}}[(\xi - id)^2 + (\eta - jd)^2]\right\}, and\ d > 2w, \tag{5-9}$$

where λ_{ex} is the illumination wavelength. According to Eq. (5-8) and Eq. (5-9), we can obtain the Fraunhofer diffraction pattern at the focal plane of the MLA:

$$U_2(x,y) = \frac{exp\left[\frac{j\pi}{\lambda_{exf}}(x^2+y^2)\right]}{j\lambda_{exf}} \times \sum_i \sum_j \iint circ\left[\frac{\sqrt{(\xi-id)^2+(\eta-jd)^2}}{w}\right] \times exp\left\{-j\frac{2\pi}{\lambda_{exf}}[(\xi - id)x + (\eta - jd)y]\right\} d(\xi - id)d(\eta - jd), \tag{5-10}$$

The integrand term in Eq. (5-10) is the Fourier transform of the input field at frequencies $k_{\xi-id} = \frac{x-id}{\lambda_{exf}}$, $k_{\eta-jd} = \frac{y-jd}{\lambda_{exf}}$, and it can be written as:

$$U_2(x,y) = \frac{exp\left[\frac{j\pi}{\lambda_{exf}}(x^2+y^2)\right]}{\lambda_{exf}} \sum_i \sum_j \mathcal{F}\left\{circ\left[\frac{\sqrt{(\xi-id)^2+(\eta-jd)^2}}{w}\right]\right\}, \tag{5-11}$$

To calculate the Fourier transform of the $circ[\ ]$ function, I separate each microlens into unique polar coordinates and use the Hankel transform to obtain the corresponding Fourier transform. Eq. (5-11) can be further derived as:

$$U_2(x,y) = \sum_i \sum_j \frac{exp\left[\frac{j\pi}{\lambda_{exf}}(x^2+y^2)\right]}{j\lambda_{exf}} \times w^2 \frac{J_1\left[\frac{2\pi w}{\lambda_{exf}}\sqrt{(x-id)^2+(y-jd)^2}\right]}{\frac{w}{\lambda_{exf}}\sqrt{(x-id)^2+(y-jd)^2}}, \quad (5\text{-}12)$$

where J_1 is the first-order Bessel function. For incoherent imaging, only the distribution of the illumination intensity is cared; thus, the intensity at the MLA focal plane is:

$$I_2(x,y) = |U_2(x,y)U_2^*(x,y)| = \sum_i \sum_j \left(\frac{w^2}{\lambda_{exf}}\right)^2 \left\{\frac{J_1\left[\frac{2\pi w}{\lambda_{exf}}\sqrt{(x-id)^2+(y-jd)^2}\right]}{\frac{w}{\lambda_{exf}}\sqrt{(x-id)^2+(y-jd)^2}}\right\}^2, \quad (5\text{-}13)$$

For the HiLo microscope, the incoherent imaging theory is used to conjugate this pattern to the sample plane for SI.

Assuming the blue dashed rectangular region in Fig. 5-1 is a telecentric configuration. The objective lens is used for illuminating and imaging the samples. According to the incoherent imaging theory, the intensity distribution on the sample plane is:

$$\begin{aligned} I_3(\mu,\sigma,z)|_{z=z_i} &= \iint \left|h(\mu-x,\sigma-y)|_{z=z_i}\right|^2 \times I_{3-geometric}(\mu,\sigma)dxdy \\ &= \iint \left|h(\mu-x,\sigma-y)|_{z=z_i}\right|^2 \times I_2(Mx,My)dxdy, \end{aligned} \quad (5\text{-}14)$$

where $h|_{z=z_i}$ is the coherent impulse response function for the defocus distance z, the coordinate (μ,σ) is related with $(\mu = Mx, \sigma = My)$, and M is the lateral magnification. $z_i = 0$ is the in-focus plane. $I_{3-geometric}(\mu,\sigma)$ is the scaled ideal geometric image copy of $I_2(x,y)$. Due to the telecentric configuration, $I_{3-geometric}(\mu,\sigma)$ remains the same for different z distances. The corresponding spectrum of Eq. (5-14) can be expressed as:

$$G_3(f_\mu, f_\sigma)\big|_{z=z_i} = \mathcal{H}_{ill}(f_\mu, f_\sigma)\big|_{z=z_i} G_g(f_\mu, f_\sigma), \tag{5-15}$$

where $\mathcal{H}_{ill}(f_\mu, f_\sigma)\big|_{z=z_i}$ is the illumination OTF at a defocus distance z_i. Thus, Eq. (5-14) can be rewritten as:

$$I_3(\mu, \sigma, z)|_{z=z_i} = \mathcal{F}^{-1}\left\{\mathcal{H}_{ill}(f_\mu, f_\sigma)\big|_{z=z_i} G_g(f_\mu, f_\sigma)\right\}, \tag{5-16}$$

To get the defocused-OTF, we should know the corresponding CTF. Assuming the optical system is aberration-free, and the CTF of the system is:

$$\mathcal{H}_{ill}(f_\mu, f_\sigma) = circ\left(\frac{\lambda_{ex} z_{xp}\sqrt{f_\mu^2+f_\sigma^2}}{w_{xp}}\right) exp\left\{j\frac{2\pi}{\lambda_{ex}} W_d\left[\frac{(\lambda_{ex} z_{xp})^2 (f_\mu^2+f_\sigma^2)}{w_{xp}^2}\right]\right\}, \tag{5-17}$$

where z_{xp} and w_{xp} are the exit pupil distance and exit pupil radius, respectively, $NA_{obj} \approx w_{xp}/z_{xp}$, NA_{obj} is the numerical aperture of the objective lens, and W_d is the Seidel defocus coefficient. Also, we have $W_d = \left(NA_{obj}^2/2\right)\cdot z_i$ [324]. Eq. (5-17) can be therefore rewritten as:

$$\mathcal{H}_{ill}(f_\mu, f_\sigma) = circ\left(\frac{\sqrt{f_\mu^2+f_\sigma^2}}{f_0}\right) exp\{j\pi z_i \lambda_{ex}(f_\mu^2 + f_\sigma^2)\}, \tag{5-18}$$

where f_0 is $\lambda z_{xp}/w_{xp}$. The sign assignment of wavefront error is the same as [324]. For convenience, I recall it here. In Fig. 5-3, when the defocused wavefront converges to the right side of the ideal focus point and the corresponding defocused wavefront on the left side, W_d and z_i are positive.

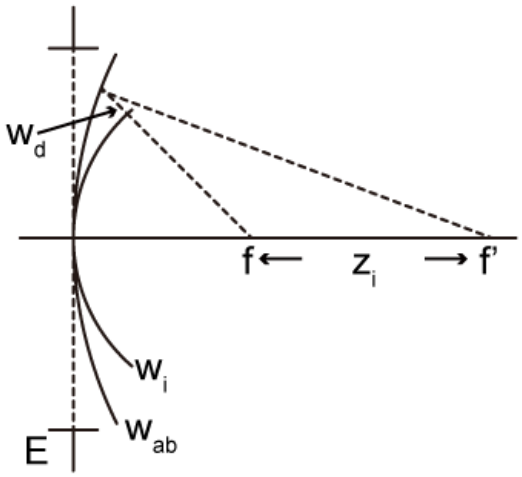

Fig. 5-3. Illustration of defocus. *E* is the exit pupil, wavefront w_i converges to the focus point *f*, and the defocus wavefront w_{ab} is centred on the axis at the defocus point f'.

According to the analytic expression for the OTF of a circular asymmetric optical system with defocused aberration, which was first given by Hopkins [325], the OTF of the HiLo illumination can be rewritten as:

$$\mathcal{H}_{ill}(\rho) = \frac{4}{\pi a} cos\left(\frac{1}{2}\alpha\rho\right)\left\{\beta J_1(\alpha) + \sum_{n=1}^{\infty}(-1)^{n+1}\frac{sin(2n\beta)}{2n}\left[J_{2n-1}(\alpha) - J_{2n+1}(\alpha)\right]\right\}$$
$$-\frac{4}{\pi a} sin\left(\frac{1}{2}\alpha\rho\right)\sum_{n=1}^{\infty}(-1)^{n}\frac{sin[(2n+1)\beta]}{2n+1}\left[J_{2n}(\alpha) - J_{2(n+1)}(\alpha)\right], \tag{5-19}$$

where $\alpha = \frac{2\pi w_{xp}^2 z_i}{\lambda_{ex} z_{xp}^2}\rho$, $\beta = \cos^{-1}\left(\frac{\rho}{2}\right)$, $\rho = \sqrt{s^2 + \tau^2}$, s and τ are normalized spatial frequency components defined as $\lambda_{ex} z_{xp} f_{\mu} / w_{xp}$ and $\lambda_{ex} z_{xp} f_{\sigma} / w_{xp}$, respectively.

The high-order Bessel function makes Eq. (5-19) converge rather slowly. In simulations, we set z_i = 0.5λ for each step, and the approximation of Eq. (5-19) can also obtain

accurate results [39]. $\mathcal{H}_{ill}\left(f_{\mu},f_{\sigma}\right)\Big|_{z=z_i}$ in Eq. (5-16) is:

$$\mathcal{H}_{ill}(f_{\mu},f_{\sigma})\big|_{z=z_i}=\mathcal{H}_{ill}(\rho)=\begin{cases}2(1-0.69\rho+0.076\rho^2+0.043\rho^3)\left[\frac{J_1(\alpha-0.5\alpha\rho)}{(\alpha-0.5\alpha\rho)}\right] & ,|\rho|<2\\ 0 & ,|\rho|\geq 2\end{cases}, \tag{5-20}$$

I calculated the Fourier transform of $I_2(Mx,My)$ to obtain $G_g(f_{\mu},f_{\sigma})$ in Eq. (5-16). Recalling Eq. (5-13) and using the autocorrelation theorem, the Fourier transform of $I_2(Mx,My)$ is:

$$\mathcal{F}\{I_2(Mx,My)\}=\mathcal{F}\{|U_2(Mx,My)|^2\}=\frac{1}{M^4}\left[ACF\langle G_2\left(\frac{f_x}{M},\frac{f_y}{M}\right)\rangle\right], \tag{5-21}$$

where $ACF\langle\ \rangle$ is the auto-correlation function operator and $G_2\left(\frac{f_x}{M},\frac{f_y}{M}\right)$ is the scaling spectrum of U_2. Using the convolution and successive transform theorems, neglecting the constant term in Eq. (5-11), we can obtain the following:

$$G_2\left(\frac{f_x}{M},\frac{f_y}{M}\right)=\mathcal{F}\left\{exp\left[\frac{j\pi M^2(x^2+y^2)}{\lambda_{exf}}\right]\right\}\otimes\sum_i\sum_j circ\left[\frac{\sqrt{[M(x-id)]^2+[M(y-jd)]^2}}{Mw}\right], \tag{5-22}$$

Where $\otimes$ is the convolution operator. Combing Eqs. (5-16), (5-20), (5-21), and (5-22), we can rewrite the 3D illumination pattern on the sample volume as:

$$I_3(\mu,\sigma,z)|_{z=z_i}=\mathcal{F}^{-1}\left\{\mathcal{H}_{ill}(\rho)\times ACF\langle\mathcal{F}\left\{exp\left[\frac{j\pi M^2(x^2+y^2)}{\lambda_{exf}}\right]\right\}\otimes \sum_i\sum_j circ\left[\frac{\sqrt{[M(x-id)]^2+[M(y-jd)]^2}}{Mw}\right]\rangle\right\}, \tag{5-23}$$

From Eq. (5-7), we can rewrite it in the spectrum domain:

$$I_{4s}(u,v) = \sum_{z_i=0}^{n} \mathcal{F}^{-1}\left\{\mathcal{H}_{ima}(\rho)\mathcal{F}\{O(\mu,\sigma,z_i)I_3(\mu,\sigma,z)|_{z=z_i}\}\right\}, \quad (5\text{-}24)$$

where $\mathcal{H}_{ima}(\rho)$ is the same as Eq. (5-20), except that the emission wavelength λ_{em} substitutes the illumination wavelength λ_{ex} .

5.3 Simulations

5.3.1 3D illumination pattern on the sample volume

I simulated different 3D illumination patterns on the sample volume. The illumination wavelength is 520nm, the illumination NA is 0.5, and the sample volume is 200*200*100μm (width*length*height). MLA's NA was set from 0.006 to 0.01 with a step of 0.001. Each microlens is 50μm in diameter; the microlens pitch (distance between adjacent microlens) is from 60μm to 140μm with a 20μm step. Fig. 5-4 shows several normalized 3D illumination patterns created by different MLAs. The x-y section shows the intensity distribution on the focus plane ($z_i = 0\mu m$), and the x-z section shows the axial intensity distribution of the central slice (y = 0) from $z_i = 0\mu m$ to $z_i = 100\mu m$. The magnification of the illumination light path is 0.1; therefore, the pattern period on the sample plane in Fig. 5-4 is ten times smaller than MLA's lens pitch (6μm, 10μm, and 14μm).

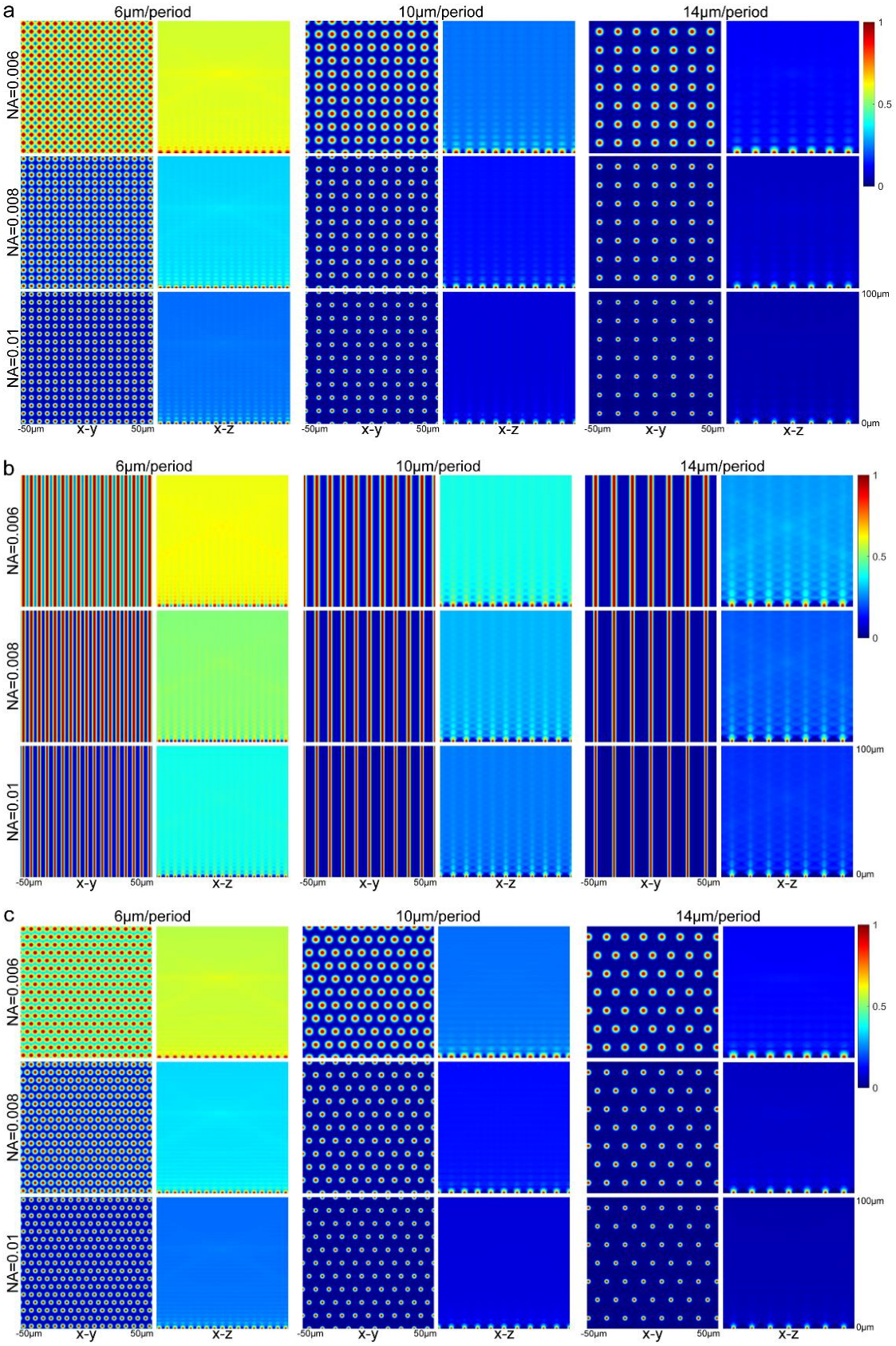

Fig. 5-4. 3D illumination intensity distribution on the sample volume created by cross-type (a), cylinder-type (b), and hexagon-type (c) MLAs. Each picture is self-normalized,

and the NA is MLA's numerical aperture. The period is the distance between adjacent focus points on the x-y focus plane, which MLA creates.

When using MLA to create SI on the sample, its microlens pitch and NA determine the modulation depth (MD). Fig. 5-5 shows horizontal line profiles of the focus plane (x-y section, y = 0 in Fig. 5-4). In the same MLA type, a higher microlens pitch increases MD. Beyond that, increasing NA also causes a higher MD. According to Eqs (5-8) and (5-18), the intensity distribution formed by each microlens at the sample plane is an Airy pattern. Therefore, if the period (corresponding to MLA's microlens pitch) and NA are too large, the side lobes of each focus point will sum up and cause oscillation (purple arrows in Fig. 5-5). MD is defined as $MD(\%) = \left(I_{max} - I_{min} \right) / \left(I_{max} + I_{min} \right)$, where I_{max} and I_{min} are the profile's maximum and minimum intensities. Fig. 5-6 shows relationships between MD, NA, and the period for different MLAs. As expected, increasing the period and NA can obtain higher MD rates. Because of the structure's similarity, illumination patterns formed by the cross-type and hexagon-type MLAs have similar MD rates and trends. When the period and the NA are both low, cylinder-type MLAs can create patterns with higher MD rates (> 50%).

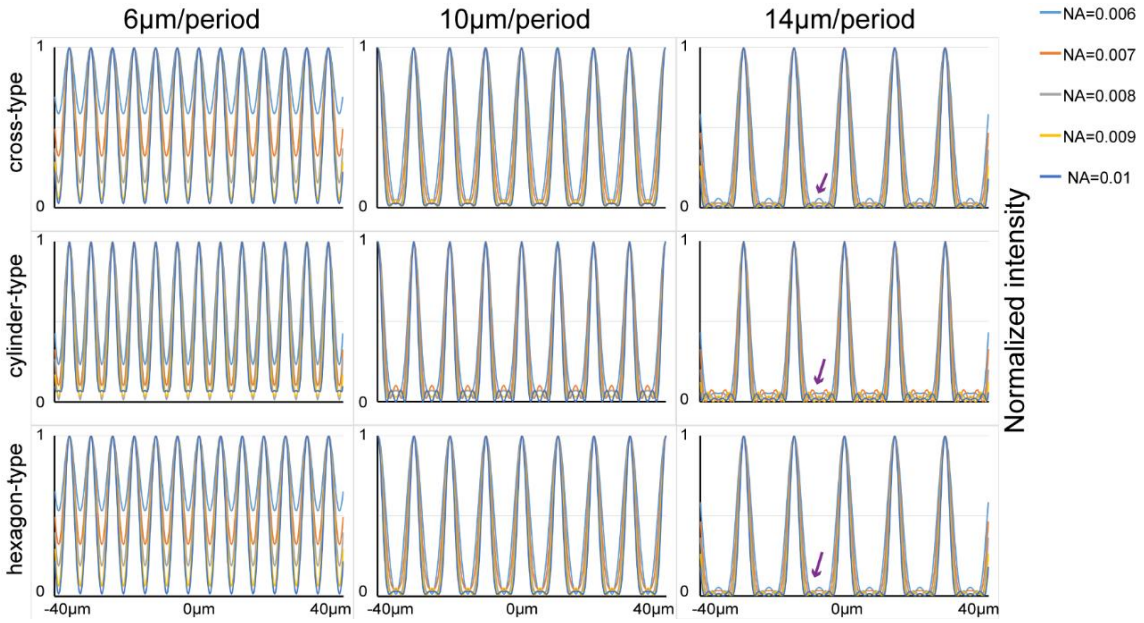

Fig. 5-5. Horizontal line profiles of illumination patterns on the in-focus plane (x-y section, y=0). Different colour lines represent microlens NA.

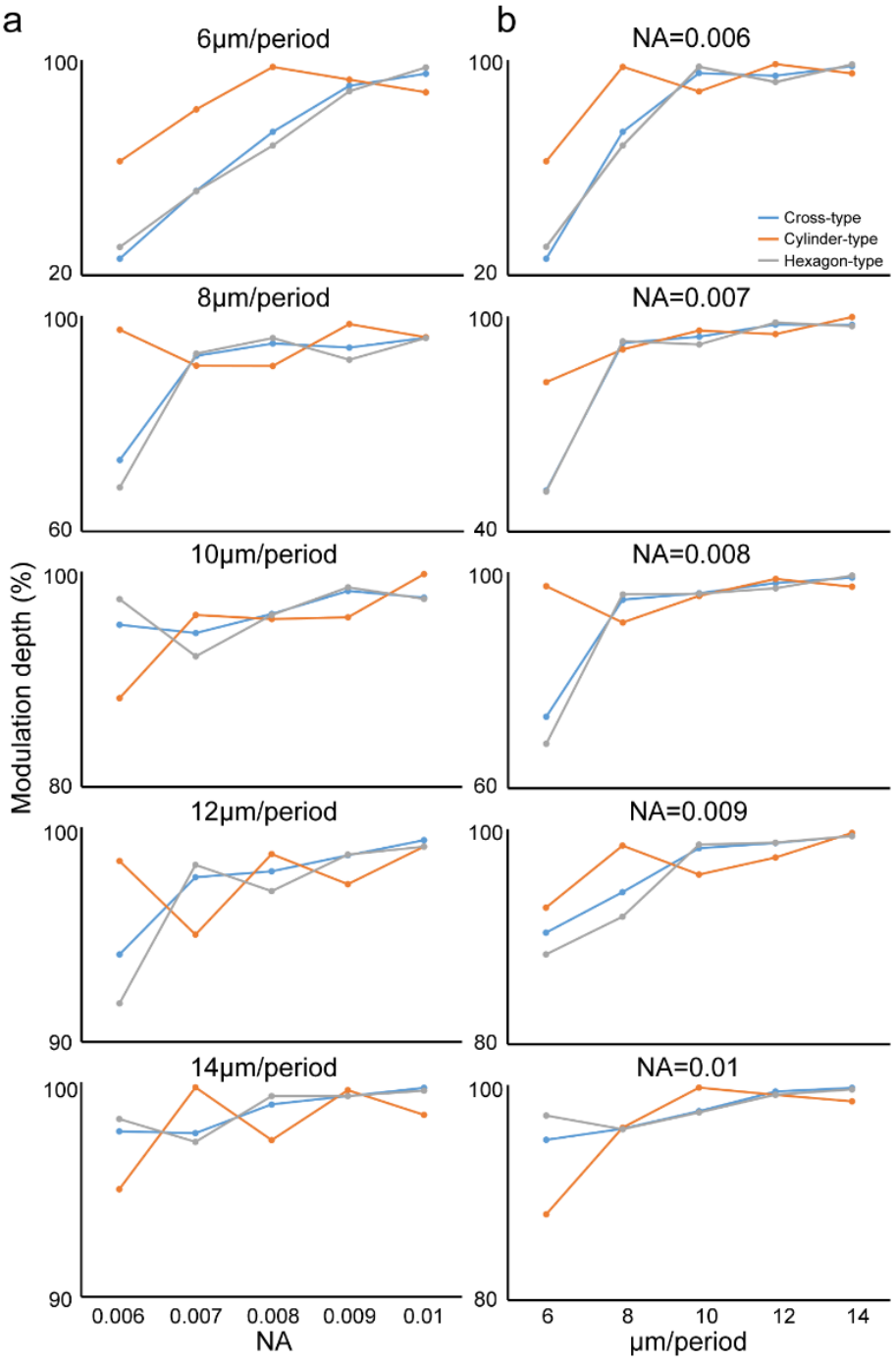

Fig. 5-6. Relationships between MD and microlens NA (a), MD and pattern period (b). Different color lines represent MLA's type. Scales are different for better visualization.

5.3.2 The axial resolution of illumination patterns on the sample volume

The relationship between MLA and axial resolution of illumination patterns on the sample volume is also numerically studied. Fig. 5-7 shows the central (x = y = 0) axial line profiles of illumination patterns on the sample volume. The axial range is 0μm to 10μm. Purple arrows denote the first global minimal value along the axial line. This position is denoted as z_{min}, whose corresponding intensity is I_{z-min}.

Similarly, the in-focus position z_{max} has the maximum intensity I_{z-max}. δI is $I_{z-max} - I_{z-min}$. To quantify the axial resolution, we defined the axial FWHM as $2z_{FWHM}$. z_{FWHM} is the axial position when the axial intensity is half the difference between maximum and first side lobe minimum intensity. For clearance, these definitions are annotated in Fig. 5-7, centre picture. Fig. 5-7 shows that Cross-type and Hexagon-type line profiles are similar, and Cylinder-type lines are always higher than the others. As expected, a higher NA increases δI. Beyond that, z_{min} seems only determined by the period of the illumination pattern, and a higher period would bring a larger z_{min}. We did a quantitative analysis to discover how the MLA type affects the axial resolution of illumination patterns. Table. 5-1. summarizes how z_{min} behaves in terms of the MLA type, the periods, and NA. Obviously, z_{min} depends only on the period of the illumination pattern.

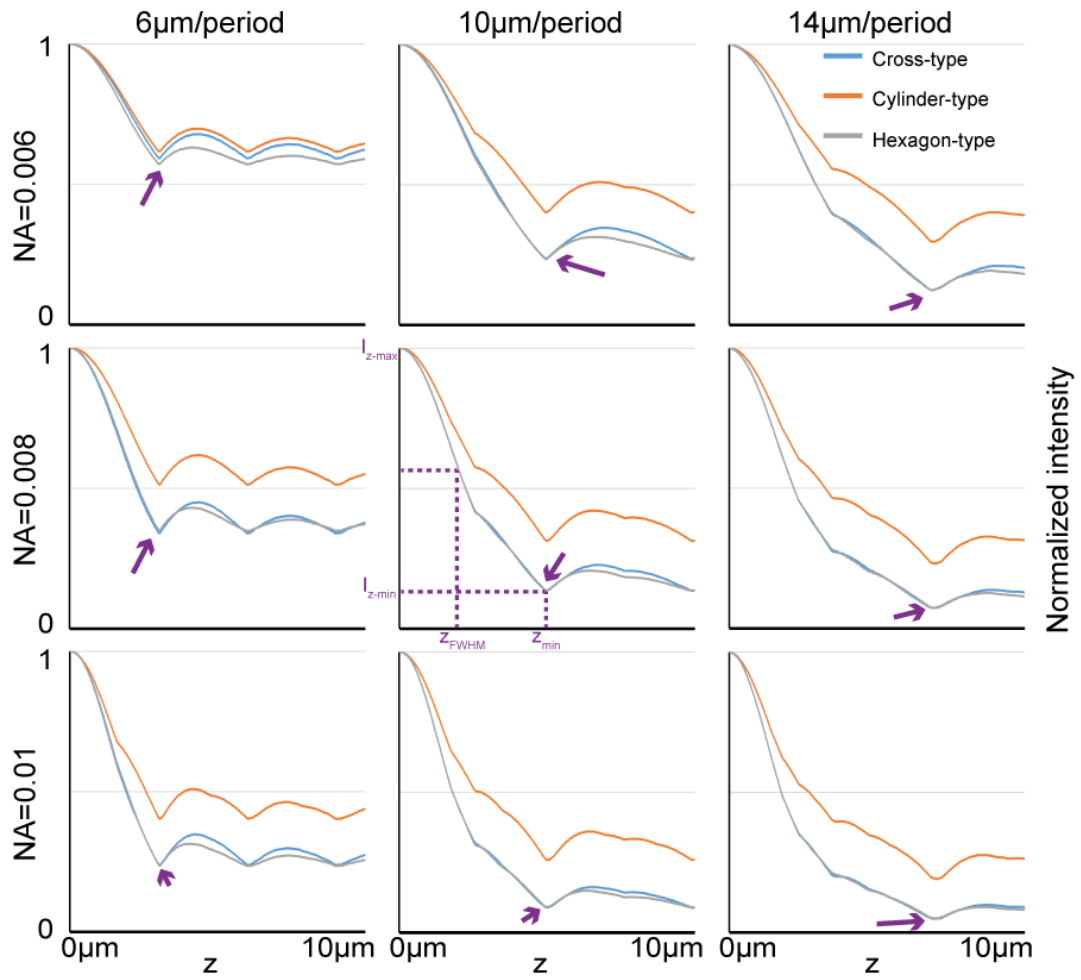

Fig. 5-7. Axial line profiles of illumination patterns at x = y = 0. The purple arrow denotes the first global minimal position along the axial line. The central picture shows detailed positions about z_{min}, z_{FWHM}, I_{z-min}, and I_{z-max}.

Table. 5-1. The value of z_{min} (μm as the unit) in terms of the MLA type, the period, and NA. Cro, cyl, and hex denote cross-type, cylinder-type, and hexagon-type MLAs.

Period / NA	6μm/period			8μm/period			10μm/period			12μm/period			14μm/period		
	cro	cyl	hex	cro	cyl	hex	cro	cyl	hex	cro	cyl	hex	cro	cyl	hex
0.006	3	3	3	4	4	4	4.95	4.95	4.95	5.85	5.85	5.85	6.8	6.9	6.8
0.007	3	3	3	4	4	4	4.95	4.95	4.95	5.85	5.95	5.85	6.9	6.9	6.8
0.008	3	3	3	4	4	4	4.95	4.95	4.95	5.95	5.95	5.85	6.9	6.95	6.9
0.009	3	3	3	4	4	4	4.95	4.95	4.95	5.95	6	5.95	6.95	6.95	6.9
0.01	3	3	3	4	4	4	4.95	5.05	4.95	5.95	6	5.95	6.95	7	6.95

Fig. 5-8 shows the axial resolution (z_{FWHM}) changing with different MLA's NA and illumination pattern periods. The higher the MLA's NA or, the lower the illumination pattern period, the better the axial resolution. In Fig. 5-8(a), the gradient is steeper with a higher period. On the other hand, the gradient is gentle with higher NA in Fig. 5-8(b). In addition, the cylinder-type MLA has worse axial resolution when compared to the others. Because the cylinder-type MLA creates periodic features on the focus plane only in a one-dimensional direction. The intensity variation only exists in one direction; however, in cross-type and hexagon-type, this variation is in two orthogonal directions, and the propagating light field changes more quickly. Therefore, z_{FWHM} in cross- and hexagon-types are smaller z_{FWHM} in the cylindrical type.

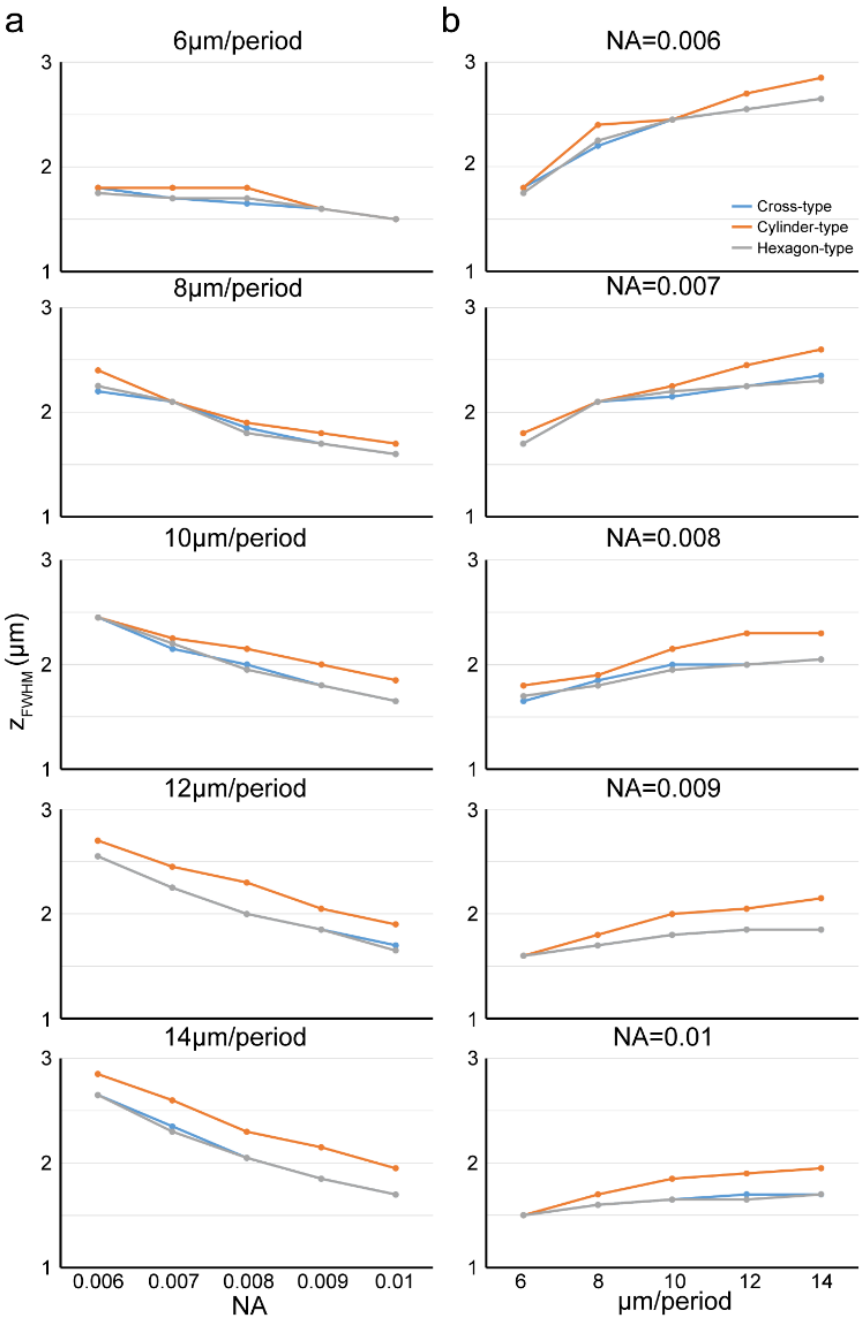

Fig. 5-8. Relationships between axial resolution (z_{FWHM}) and microlens NA (a), axial resolution (z_{FWHM}) and pattern period (b). Different color lines represent MLA's type.

5.3.3 HiLo imaging simulation

To understand the effects of MLA-generated SI patterns on the HiLo image, a fluorescent block was modelled for simulating incoherent widefield and HiLo imaging (Fig. 5-9(a) and (b)). According to Eq. (5-6), the sample was multiplied with a specific

3D illumination pattern. Then, I used the incoherent imaging theory to acquire SI images on the camera plane. Similarly, the same method was used to obtain widefield images (Fig. 5-9(c)), except that the fluorescent block was multiplied by the all-one matrix instead of the MLA-generated SI pattern. In the simulations, the illumination and the imaging NA were set to 0.5, and the excitation and emission wavelengths are 520nm and 580nm, respectively. The magnification in the illumination light path is 10, and 1 in the imaging light path.

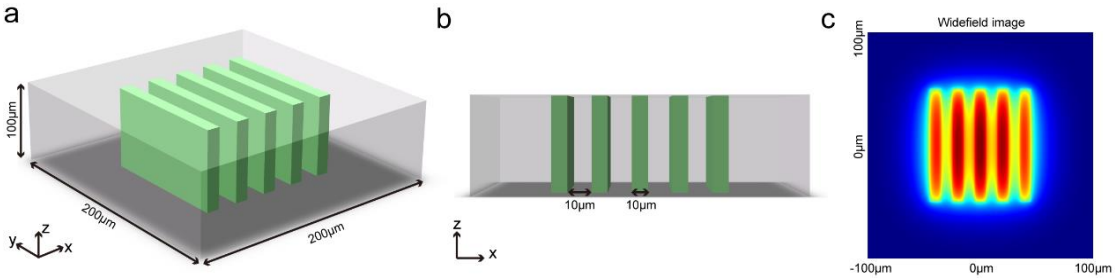

Fig. 5-9. Simulated fluorescent block for HiLo imaging (a and b). The green parts can be excited by 520nm wavelength illumination. The residual grey transparent parts cannot create a fluorescent signal. The emission wavelength is 580nm. (c) The self-normalized widefield image on the camera plane.

Fig. 5-10 shows images of the fluorescent block on the camera plane. SI columns are images under SI illumination, and HiLo columns show final HiLo pictures. The widefield image used as input for HiLo algorithms is shown in Fig. 5-9(c). In Fig. 5-10(a), the fluorescent target is excited by a cross-type illumination pattern, and others are excited by cylinder-type (Fig. 5-10(b)) and hexagon-type (Fig. 5-10(c)). When the pattern's period is 14μm/period, I found uneven artifacts on these HiLo images (white arrows). Especially when the pattern is the hexagon type (Fig. 5-10(c)), artifacts seem the worst. The cross-type pattern also generates recognizable ununiform intensity (Fig. 5-10(a)). In cylinder-type patterns, these imperfections are the mildest. Artifacts are caused by side lobes that sum up and cause oscillations (Purple arrows in Fig. 5-5). With larger lens pitch and higher NA, more side lobes will exist between each microlens,

and the oscillation will become more serious. These artifacts are the mildest in cylinder-type patterns because side lobes and oscillation only exist in one dimension but two dimensions in both cross-type and hexagon-type. Furthermore, cross-type has fewer artifacts when compared with hexagon-type since its two-dimensional patterns are orthogonal and can be decomposed into x and y directions. However, in hexagon-type, these artifacts are correlated. To quantitively analyse how MLA-generated illumination patterns affect HiLo images, I traced line profiles on each HiLo image (Red line in Fig. 5-10(a). Same tracing positions in all HiLo images.).

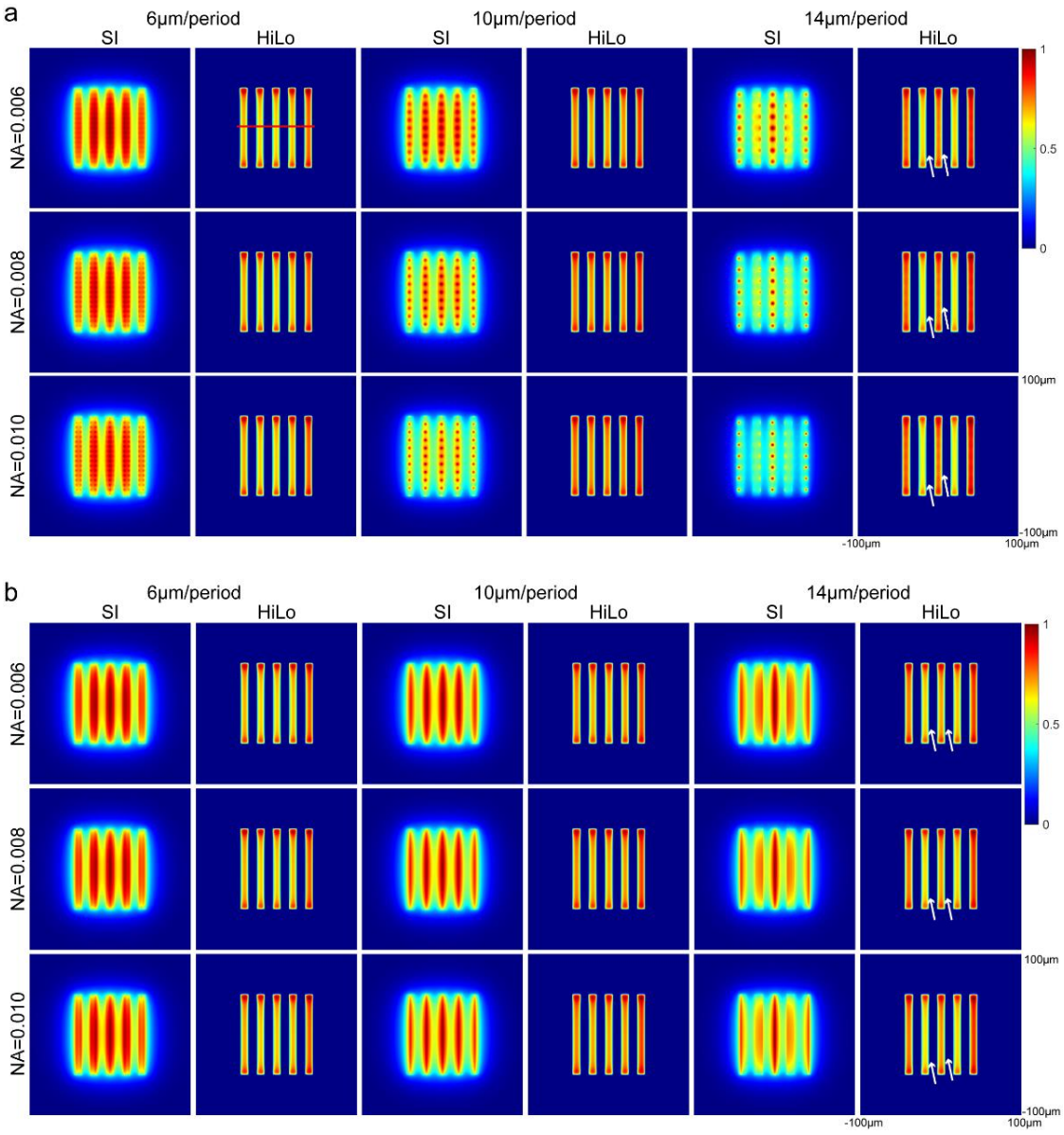

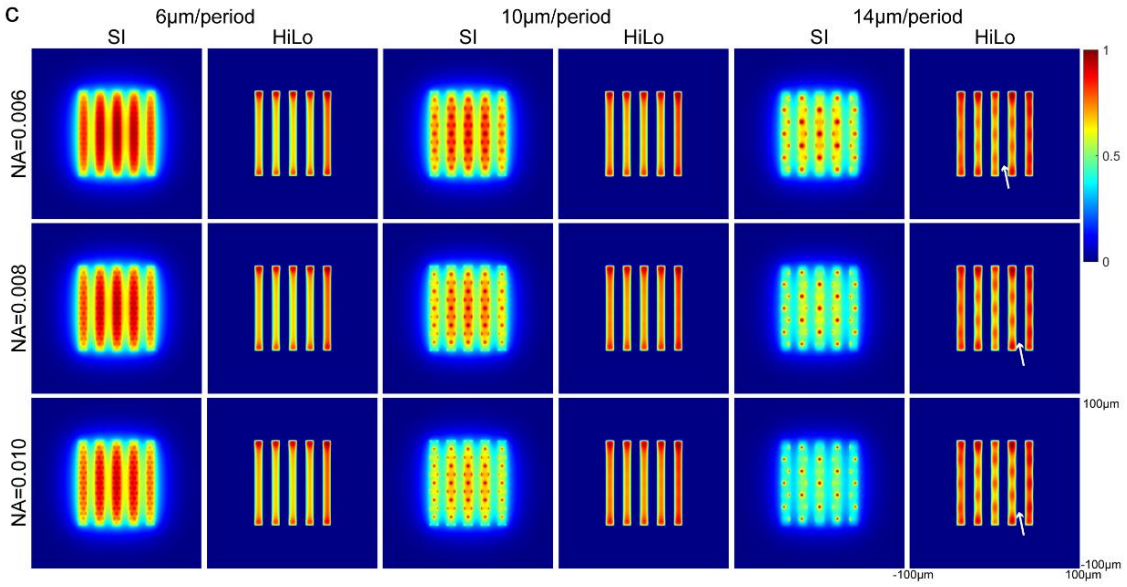

Fig. 5-10. Captured images on the camera plane. The corresponding widefield image is shown in Fig. 5-9(c). SI columns show images under different SI illumination. HiLo columns are the final HiLo images. Headlines are periods of corresponding illumination patterns. 8 μm/period and 12 μm/period are not shown. Different NAs are corresponding to MLA's numerical aperture. NA = 0.007 and NA = 0.009 are not shown. (a) Cross-type illumination pattern. (b) Cylinder-type. (c) Hexagon-type. Each image is normalized. White arrows depict imperfections.

In Fig. 5-10, these images are similar; therefore, captured images of 8μm/period, 12μm/period, NA=0.007, and NA=0.009 are not shown. However, line profiles were traced on every condition, NA from 0.006 to 0.01 with a step of 0.001, and period from 6μm/period to 14μm/period with 2μm/period step. According to the line profiles shown in Fig. 5-11, the NA of MLA does not seem to affect the quality of the final HiLo image. Fig. 5-11(a) (12μm/period column) shows a minor contrast enhancement with a higher NA. However, some artifacts are created if the period is too high (14μm/period). In Fig. 5-11(a), the contrast of the second and fourth lobes (purple arrows) is lower than others, and their trends become inverse (the higher the NA, the lower the contrast). In Fig. 5-11(b), we can see clearly that a higher period can enhance the final HiLo image contrast, and this tendency is more evident for the cross-type illumination. Like Fig. 5-11(a),

artifacts appear when the period is 14μm/period.

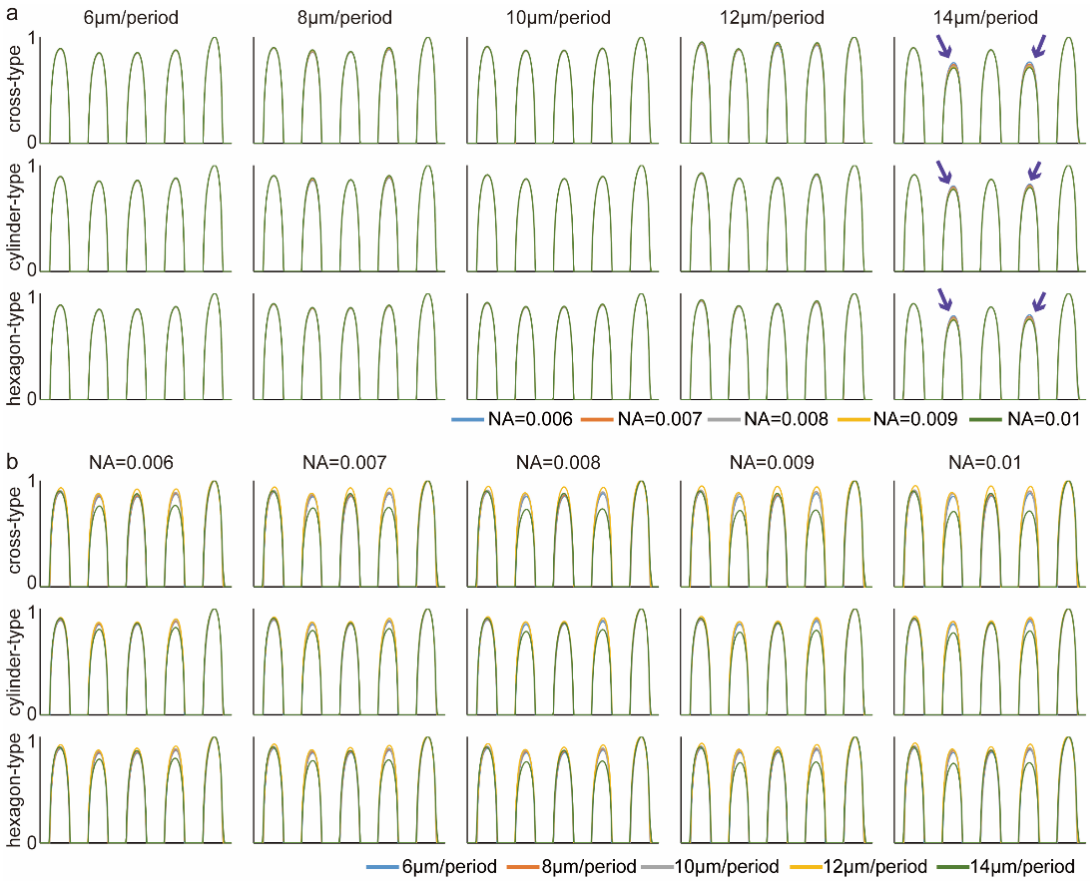

Fig. 5-11. Line profiles (along the red line in Fig. 5-10) of HiLo images under different illumination patterns. In (a), we can see that the NA of MLA does not significantly affect the image quality. Interestingly, when the period is 14μm/period, the contrast of the second and fourth lobes (counted from left to right) is lower than others. (Depicted by purple arrows). The same phenomenon can be found in (b). In (b), the image contrast becomes better with a higher period, except 14μm/period.

Furthermore, the normalized local maximum intensity of the middle lobe in Fig. 5-11 was recorded. Table. 5-2 shows how the intensity changes with different periods and NA. The period affects the intensity more significantly than MLA's NA. The best parameter setting is the cross-type pattern with 0.01NA and 12μm/period.

Table. 5-2. The normalized local maximum intensity of the middle lobe in Fig. 5-11.

Abbreviations are the same in Table. 5-1

Period / NA	6μm/period			8μm/period			10μm/period			12μm/period			14μm/period		
	cro	cyl	hex	cro	cyl	hex	cro	cyl	hex	cro	cyl	hex	cro	cyl	hex
0.006	0.84	0.844	0.838	0.85	0.852	0.85	0.863	0.862	0.862	0.916	0.868	0.888	0.873	0.859	0.867
0.007	0.842	0.846	0.841	0.853	0.855	0.853	0.866	0.864	0.866	0.928	0.872	0.895	0.875	0.861	0.868
0.008	0.844	0.848	0.843	0.855	0.856	0.856	0.869	0.865	0.869	0.936	0.875	0.898	0.877	0.861	0.869
0.009	0.845	0.85	0.844	0.857	0.857	0.859	0.871	0.867	0.871	0.942	0.877	0.9	0.878	0.862	0.869
0.01	0.847	0.852	0.846	0.858	0.858	0.86	0.872	0.868	0.873	0.946	0.879	0.901	0.879	0.863	0.87

5.4 Discussion and prospect

HiLo microscopy stands out as a potent and uncomplicated instrument for optical sectioning. Conventionally, two methods are employed to generate SI patterns: one involves a coherent light source and a rotated scattering glass to produce speckle patterns, while the other utilizes an incoherent light source and a DMD to create customized periodic patterns. However, using a coherent light source and DMD increases system cost and bulkiness. In this research, I designed different types of microlens generating a structural illumination pattern for HiLo. This alternative configuration promises to reduce both the cost and system complexity associated with HiLo microscopy.

In this study, I choose three distinct MLA types—cross, cylinder, and hexagon—each characterized by varying physical parameters such as NA and microlens pitch size. These MLAs served as diffractive components for generating SI patterns. To begin, I employed the Fresnel diffraction theory to explore the influence of different MLAs on SI patterns. The MD exhibited an increase with higher NA values when the microlens pitch was sufficiently small. Similarly, with low NA, the MD experienced a significant boost with a broader lens pitch. However, it was observed that when both NA and

microlens pitch were excessively high, the MD remained unaffected.

NA and the microlens pitch size need to be carefully chosen. A higher NA would minimize focus point size, and a higher period can lead these focus points side lobes to accumulate between each microlens, causing oscillations (Fig. 5-5 purple arrows). These oscillations will create artifacts on the final HiLo images (Fig. 5-10 red arrows). Here, I chose NA from 0.006 to 0.01 to prevent the focal point size is too small. In terms of other MLAs type, the cross-type and hexagon-type perform similarly, and the cylinder-type MLA can generate SI patterns with a better modulation depth when NA or the microlens pitch is low. I also discussed the axial resolution of SI patterns. As expected, when the microlens pitch lens is unaltered, a higher NA can deliver a better axial resolution. This trend is evident with a bigger microlens pitch. Conversely, the axial resolution becomes worse with a higher microlens pitch when NA is unaltered, and this phenomenon is more pronounced in low NA conditions. When MLA's parameters are the same, the cylinder-type MLA has the worst axial resolution, and the cross-type and the hexagon-type MLA perform similarly.

Continuously, I multiplied the simulation-generated fluorescent block with SI patterns, using the incoherent imaging theory and HiLo algorithms to investigate the links between HiLo images and MLAs. We found subtle differences among these HiLo images with different MLA's NA, and a higher NA can enhance the image contrast negligibly. Regarding the microlens pitch, a higher distance leads to better image contrast. Interestingly, a large microlens pitch can introduce artifacts and ununiform intensity to final HiLo images. We also found that the hexagon-type MLA is the most susceptible to artifacts. Using the cross-type MLA with NA of 0.01 and the microlens pitch of 120 μm to generate SI patterns can obtain the best HiLo images. In cylinder-type and hexagon-type, the best parameter is NA = 0.01 with a 120μm microlens pitch. Besides, due to the simplicity of corresponding periodic patterns, less oscillation can be

found in cylinder-type-generated illumination patterns. We can obtain HiLo images with the mildest artifacts using cylinder-type MLA.

Microlens arrays have found diverse applications in microscopy, enhancing imaging capabilities through improved resolution and contrast. The success of MLAs in SIM underscores their potential in advancing microscopy techniques [326]. By creating fine, structured illumination patterns, MLAs facilitate super-resolution imaging, a principle we aim to extend to HiLo microscopy. This approach promises significant advancements in observing dynamic biological processes with minimal phototoxicity and rapid imaging capabilities.

Overall, in this study, we found that the cylinder-type MLA can be used for HiLo imaging with the mildest artifacts due to the simplicity of the corresponding structure. However, this aspect also leads to its corresponding light intensity field only varying in one dimension, which minimizes the axial resolution. Cross-type and hexagon-type MLAs can obtain a better axial resolution but tend to produce more artifacts. Therefore, there exists a trade-off between the artifacts-free and better axial resolution. Researchers should carefully choose the appropriate MLA for HiLo imaging.

This study finds a new method for HiLo imaging. During the simulation, we found several interesting phenomena, which will be further investigated through theoretical analysis and mathematical deduction in future. These include: 1) A quantitative link between the microlens pitch and NA (e.g., ratio); 2) Theoretical and mathematical analysis about why the z_{min} in Fig. 5-7 is unrelated to NA; 3) If translating different distances of each line of the microlens in cross-type MLA, how this affects the final HiLo image?

Throughout our research, we encountered several challenges, notably in the fabrication

process, where maintaining uniformity and precision across the MLA proved demanding. Additionally, the integration of the MLA with existing microscopy setups posed alignment and calibration hurdles, impacting the overall feasibility and accessibility of the proposed solution. Moving forward, our research will focus on refining the fabrication process to enhance the scalability and usability of MLAs in microscopy.

The validation of the current simulation study is a crucial aspect to consider. While simulation software such as Zemax and COMSOL are powerful tools for comparison, their application was not deemed suitable for this study for several reasons. Firstly, the study introduces a novel low-cost HiLo microscopy technique that leverages MLAs and incoherent LED light sources. This approach may fundamentally differ from the methodologies typically modelled in Zemax and COMSOL, potentially rendering direct comparisons less meaningful or relevant. Furthermore, the simulations conducted in this research are intricately tailored to the specific characteristics of MLAs and their impact on HiLo microscopy, a level of specificity that might not align with the broad-spectrum applications of Zemax and COMSOL, thus making any comparison less insightful.

Additionally, the focus of this study leans more towards the practical implementation and optimization of MLAs for HiLo microscopy rather than on theoretical simulations alone. Although Zemax and COMSOL are renowned for their detailed optical simulations, this research emphasizes experimental outcomes over theoretical modelling. The core objective of this research is to establish the feasibility and benefits of employing MLAs alongside incoherent LED sources for HiLo microscopy. Given that Zemax and COMSOL may not offer specialized features necessary for simulating the unique aspects of this methodology, comparisons with these tools might not align with the intended scope of this study. Hence, prioritizing experimental validation of the

MLA-based HiLo microscopy technique over theoretical comparisons is essential, as demonstrating the practical effectiveness and advantages through experimental validation aligns more closely with the research objectives.

Experimental validation of the simulated designs will be a critical next step, alongside exploring innovative materials and fabrication techniques to overcome current limitations. The goal is to transition from theoretical models to practical implementations, unlocking new possibilities in high-resolution, low-phototoxicity imaging for biological research.

5.5 Conclusion

In conclusion, this study proposes the practical and cost-effective application of MLAs in generating SI for HiLo microscopy. It systematically examines how MLA parameters, including MLA type, NA, and microlens pitch, impact the final HiLo images, identifying optimal MLA parameters. Notably, this marks the first exploration of utilizing specific MLAs to achieve HiLo microscopy. Future investigations will develop deeper, including a broader NA range, larger microlens pitch, the ratio between NA and the lens pitch, and various microlens arrangements.

This study contributes valuable insights into the optimization of MLA-based HiLo microscopy and serves as a guide for researchers seeking to establish such microscope systems. The potential impact of these tools lies in their ability to facilitate the acquisition of high-quality biomedical images cost-efficiently and efficiently, further advancing research capabilities in the field.

Chapter 6. Conclusion

6.1 Discussions and limitations

In resource-limited regions and developing countries, the application of microscopy for disease detection and biomedical research faces obstacles due to inadequate financial resources. Establishing sophisticated microscopic imaging systems and healthcare laboratories is challenging in these settings. Nevertheless, the progress in high-speed communication, AI techniques, and the Internet of Things (IoT) has paved the way for remote diagnostics and analysis. This breakthrough enables individuals to utilize affordable devices to capture original image data and transmit it to a server for analysis. Notably, GPUs have recently augmented the computing capabilities of embedded systems, empowering them with real-time functionality.

LPMs emerge as robust tools for bioimaging applications, especially in resource-limited and underdeveloped areas. Their mechanical bodies are predominantly crafted through 3D printing technology, rendering them user-friendly and compact. In healthcare settings, these microscopes find versatile applications in POCT, disease detection, and on-the-spot organism identification. For instance, LPMs prove effective in achieving real-time detection and counting of RBC, identifying sickle cell disease, and detecting microorganisms in drinking water. Their portability and ease of use make them valuable assets in scenarios where traditional imaging setups may need to be more practical and financially feasible.

Tasks requiring low-computational image processing, such as target recognition, image segmentation, and target counting, can be efficiently handled by embedded systems or consumer electronics devices like smartphones, enabling real-time data analysis. DL algorithms can seamlessly integrate into these devices to cater to various real-time

applications. LPMs can capture original images or videos for scenarios demanding high-computational image processing. These data sets can then be uploaded to a cloud server for more intensive data processing. Subsequently, the processed results can be transmitted back to users for diagnostics. This approach optimally leverages the computational capabilities of both local devices and cloud-based servers for effective and timely data analysis.

In this PhD study, a literature review was first conducted in Chapter 2. Different types of LPMs were discussed from a hardware configuration perspective and classified into smartphone-based LPMs, customized LPMs, and lensless LPMs. Moreover, how to choose the appropriate LPM based on its characteristics for various biomedical applications was considered. Four commonly proposed applications for LPMs were reviewed, including POCT and healthcare, pathology, cell monitoring, and microfluidic applications.

6.1.1 Portable AI-enhanced fluorescence microscope for real-time target detection

Chapter 3 proposed a portable AI fluorescence microscope (πM) based on a webcam and the NJN. It is a customized LPM and has a powerful AI-enhanced real-time analysis function. The NJN makes πM can be customized appropriately for different applications, and data transfer to the cloud and servers for analysis are exempted because of the NJN's edge computing power. πM has an easy optical path and mechanical design, weighing only ~250 grams with dimensions of 145mm × 172 mm × 144 mm (L×W×H). It has x5 magnification and can resolve 228.1 lp/mm microscopic features. The brightfield imaging of microscopic samples and human RBCs and fluorescence imaging of PS beads can be proposed on πM. A convolution neural network was demonstrated on πM to realize foreground feature extraction and counting functions

without data transfer and image processing. Compared with the OpenCV and CLIJ2 algorithms, the customized CNN methods can recognize six aggregated beads with 80% accuracy (OpenCV: three aggregated beads with 26% accuracy; CLIJ2: six aggregated beads with 64% accuracy). In human RBCs counting and recognition, the CNN shows results closer to the GT than the CLIJ2 method (GT: 201; CNN: 196; CLIJ2: 189). These experimental results provide a proof-of-principle debut of πM.

The primary problem addressed by this study is the lack of accessible, cost-effective, and portable microscopy solutions capable of real-time analysis in resource-limited settings. Traditional benchtop microscopes, while precise, are often expensive, bulky, and require significant expertise to operate. Additionally, they typically need external devices for data processing, which can further complicate their use in fieldwork or in regions with limited access to technological infrastructure.

The πM system offers a solution by providing a portable, affordable, and user-friendly alternative that does not compromise on the quality of brightfield and fluorescence imaging. Its design, which utilizes a reversed webcam lens and an NVIDIA Jetson Nano for computation, allows for real-time image processing without the need for data transfer to external computers. This feature is particularly beneficial for applications in remote or resource-limited areas where immediate analysis is crucial, such as in diagnosing diseases or monitoring environmental samples.

However, there are still several limitations. The πM achieves a physical magnification of ×5, which is sufficient for various applications but may not match the higher magnification and resolution capabilities of more advanced benchtop microscopes. This limitation could affect the system's utility in applications requiring detailed cellular or molecular imaging.

While the customized convolutional neural network (CNN) shows robust performance in feature extraction and target counting in the tested scenarios, the generalizability of this AI model to different types of samples and conditions remains a question. The performance of the system in the presence of complex biological samples with high variability and in conditions not included in the training dataset could be a potential limitation. Moreover, real-time data analysis, a critical feature of this system, faces several constraints. These include computational limitations inherent to portable devices, potential data transfer delays, the need for highly efficient algorithms, significant power consumption, and the challenges of ensuring accuracy across diverse conditions. Additionally, there's a risk of users becoming overly reliant on automated analyses, possibly at the expense of critical human expertise. Overcoming these challenges necessitates a comprehensive approach, focusing on technological advancements, algorithmic optimizations, user education, and improved power management strategies. As these issues are addressed over time, the utility and application scope of real-time analysis in portable microscopy are expected to expand, enhancing its impact in both research and practical field applications.

Real-time video processing, as opposed to static image analysis, involves the continuous and instantaneous analysis of video frames to extract and interpret dynamic changes within the sample being observed. This feature is particularly crucial for observing biological processes in live specimens, such as cellular motility, blood flow, or microbial interactions, where the temporal aspect of the observation provides critical insights into the biological phenomena. Implementing real-time video processing in πM poses several challenges. Firstly, the computational load increases significantly with video processing, as each frame of the video needs to be analysed in real-time. This demands highly efficient algorithms and potent processing units that can handle high-throughput data without latency, which might be a constraint given the compact and portable nature of the πM system. Moreover, video processing requires advanced data

compression and storage solutions to manage the large volumes of data generated, without overwhelming the device's storage capacities or compromising the video quality. This is particularly challenging in field settings where data offloading options might be limited.

The system's performance, as demonstrated with PS beads and RBCs, relies on well-prepared samples. In real-world applications, especially in field settings, the presence of contaminants or poorly prepared samples could significantly affect the system's accuracy and reliability.

In hardware aspects, while the use of off-the-shelf components and 3D printing technology contributes to the system's affordability and portability, it may also limit the system's adaptability and scalability to more demanding applications. Users with specific needs might find it challenging to modify or upgrade the system without extensive technical knowledge. Beyond that, its long-term durability and reliability under various environmental conditions have not been addressed. The impact of factors such as temperature fluctuations, humidity, and mechanical shocks on the system's performance over time is unclear.

In conclusion, the πM system represents a significant advancement in making microscopy more accessible and practical for a wide range of applications, particularly in resource-limited settings. However, its limitations regarding optical performance, AI generalization, dependency on sample preparation, hardware customization, and long-term reliability need to be considered when evaluating its suitability for specific applications. Future developments could focus on enhancing the system's versatility, scalability, and robustness to extend its utility in both educational and research contexts.

6.1.2 Smartphone-based HiLo

A smartphone-based LPM with optical sectioning ability (SOS) was presented in Chapter 4. SOS microscope uses the HiLo principle to realize the optical sectioning function, with a single smartphone replacing a high-cost illumination source and a camera sensor. It has an easy optical path and mechanical design. The liquid light guide relayed the broadband smartphone LED into the DMD devices for SI. For realizing the telecentric axial scan, the ETL was conjugated to the BPP of the objective lens, which can stabilize SOS's lateral magnification at different depths. SOS has a 571.5μm telecentric scanning range and a 5.5μm axial resolution, which costs around £7,035 cheaper than a traditional HiLo microscope equipped with a scientific camera sensor and an illumination source. The high-contrast fluorescent PS beads imaging with different wavelengths and optical sectioning imaging of accumulated fluorescent PS beads were proposed by HiLo. The proposed SOS is the first smartphone-based HiLo optical sectioning microscopy. It is a powerful, low-cost tool for biomedical research in resource-limited areas.

The primary problem solved by this study is the high cost and complexity associated with traditional HiLo optical sectioning microscopes. By incorporating a smartphone to serve both as the illumination source and the camera sensor, the study effectively reduces the financial barrier to accessing high-quality optical sectioning microscopy. This democratization of advanced microscopy techniques is particularly beneficial for biomedical research and diagnostics in under-resourced areas, where such technology could significantly impact healthcare outcomes. Moreover, the study introduces a telecentric design with an ETL for axial scanning, maintaining constant lateral magnification across different axial planes. This feature ensures high-quality imaging without the need for complex post-processing, further simplifying the use of the system while ensuring the fidelity of the captured images.

Despite its innovative approach and significant contributions, the study encounters several limitations that warrant further investigation and improvement.

The occurrence of artefacts in the final HiLo images, particularly when imaging dense fluorescent beads, presents a significant limitation. These artefacts could potentially obscure or distort crucial details in the sample, leading to misinterpretation of the data. The study attributes these artefacts to the properties of the illumination and the sample, as well as the image processing algorithms implemented by the smartphone's camera software. Addressing this issue requires a deeper understanding of the interaction between the structured illumination patterns, sample properties, and the smartphone's imaging algorithms.

The illumination Etendue is also a problem. The study highlights concern regarding the effective excitation of biological fluorescent dyes and the adequacy of the light power output from the smartphone's LED torch. This limitation could affect the system's versatility and applicability to a wide range of biological samples, particularly those requiring specific excitation wavelengths or higher power illumination. A comprehensive analysis of the light guide's Etendue and the illumination system's power output is necessary to ensure the system's effectiveness across various applications. Moreover, the reliance on a smartphone's LED as an illumination source might introduce variability in image quality due to ambient light conditions. The SOS Microscope utilizes the smartphone's LED torch as an illumination source, which is not designed for microscopy. This can lead to challenges in achieving uniform, controlled illumination that is crucial for consistent and reliable imaging, particularly for fluorescence microscopy. Unlike controlled illumination sources in traditional microscopes that provide consistent lighting, the varying intensity and colour temperature of environmental light could affect the consistency and reliability of

imaging results when using SOS in different settings.

In generalizability and compatibility aspects, the current design of the SOS Microscope is tailored to a specific smartphone model, which may limit its generalizability and adaptability to other devices. As smartphone technology rapidly evolves, the system's design must be adaptable to accommodate a wide range of devices to ensure its long-term applicability and relevance. Beyond that, the mechanical stability of the setup, relying on 3D-printed adapters and off-the-shelf optical components, might not match the precision and stability of dedicated microscopy systems. This could lead to issues with image blurring, alignment, and repeatability, particularly during extended imaging sessions or when handling sensitive samples that require high precision.

While the study demonstrates the capability of SOS for optical sectioning with good axial resolution, the inherent optical limitations of smartphone cameras, such as limited numerical aperture and depth of field, might restrict the maximum achievable resolution and depth penetration compared to traditional high-end microscopes. This could be particularly challenging when dealing with complex biological samples that require high-resolution imaging at various depths. Smartphone cameras are optimized for general photography, not microscopy. The quality of lenses and sensors in smartphones, while impressive for consumer photography, may not match the precision and clarity required for high-resolution microscopy, especially when imaging at the cellular or sub-cellular level. Furthermore, the vast diversity in smartphone models and their camera specifications introduces variability in imaging performance. This lack of standardization can lead to inconsistent imaging results and complicate the replication of experiments across different devices. In software and data processing aspects, the study hints at potential artefacts introduced by smartphone image processing algorithms. Beyond this, the overall capacity for on-device data processing, storage, and sophisticated image analysis might be limited by the smartphone's hardware and

software capabilities. Smartphones automatically process images to enhance visual appeal for general photography, which may include noise reduction, sharpening, and colour correction. These processing algorithms can introduce artefacts or alter the raw data in ways that may be undesirable for scientific imaging, where authenticity and accuracy of the raw data are paramount.

In conclusion, the development of the SOS Microscope represents a significant step forward in making advanced optical sectioning microscopy more accessible and affordable. However, addressing the identified limitations, such as the artefact and illumination etendue problems, and enhancing the system's compatibility with various smartphone models, requires a multi-faceted approach, including hardware improvements for enhanced stability and resolution, software development for robust image processing and analysis, and the development of guidelines and training materials for users. Additionally, exploring the integration of the SOS system with existing microscopy platforms could leverage the strengths of both traditional and smartphone-based approaches to overcome some of these challenges. Further research and development in these areas will be essential to optimize the system's performance and expand its applicability in biomedical research and diagnostics.

6.1.3 Microlens arrays for incoherent HiLo microscopy

Following Chapter 4, a numerical study about using proper MLAs to realize HiLo microscopy was presented. This study aimed to substitute the DMD device in the traditional HiLo with the MLA, decreasing the cost of the traditional HiLo microscopy. Instead of using the DMD, different MLAs can also be used for SI pattern generation. SI patterns and HiLo image generation were simulated based on Fresnel diffraction and incoherent imaging theories. Three common MLAs (cross-, cylinder-, and hexagon type) with specific microlens pitch and NA were used to generate periodic illumination patterns in simulation. According to simulation results, increasing MLA’s lens pitch can

enhance the HiLo image’s contrast and optically sectioned ability, and this pitch size has a valve value. Hexagon-type MLA is the most susceptible to artifacts, but HiLo images can be acquired with the mildest artifacts using cylinder-type MLA. This study can guide a more detailed analysis for further investigation in the theoretical research field, including a more comprehensive NA range, a larger microlens pitch, the ratio between NA and the lens pitch, and multiple microlens arrangements. Moreover, this study can support more researchers in establishing low-cost MLA-based HiLo microscope systems in the experiment and engineering aspects.

This study's novel approach of employing MLAs for SI in HiLo microscopy represents a significant stride towards simplification and cost reduction in optical imaging. The rigorous simulation-based comparison across various MLA types (cross, cylinder, and hexagon) and configurations (differing NAs and microlens pitches) provides a comprehensive understanding of how these parameters influence image quality and contrast. Particularly, the revelation that the microlens pitch has a pronounced effect on image contrast, with an optimal pitch identified, underscores the nuanced balance between MLA design and imaging efficacy. However, it's important to critically assess the assumption that a single optimal configuration (cross-type MLA, 0.01 NA, 120 μm pitch) could universally apply across diverse imaging scenarios. Biological samples are notoriously varied in their optical properties, and what works best in a simulation may not translate directly to all practical applications.

The study's acknowledgment of potential artifacts introduced by certain MLA configurations is commendable for its transparency. However, this issue raises deeper questions about the trade-offs between cost-efficiency and image fidelity. The presence of artifacts in images, especially when using hexagon-type MLAs, could limit the technique's applicability or require additional post-processing to mitigate these effects, potentially offsetting some cost advantages. Moreover, the reliance on numerical

simulations, while practical for an initial feasibility study, introduces a level of abstraction from real-world complexities. The biological imaging field is replete with examples where theoretical models provide an incomplete picture due to biological variability, sample preparation differences, and unforeseen optical interactions. Thus, experimental validation is not just a formality but a crucial step that could reveal additional challenges or necessitate further refinements to the proposed technique.

6.2 Future works

This PhD research develops two distinct types of LPMs and introduces a theoretical study to guide further research endeavours to minimize the cost of LPMs. Although the study has achieved advancements in enhancing compactness, reducing costs, and broadening the modality of LPMs, several challenges need further exploration and resolution. Identifying and subsequently addressing these challenges will contribute to the ongoing refinement and optimization of LPMs for diverse applications.

6.2.1 Portable AI-enhanced fluorescence microscope for real-time target detection

The first work (Chapter 3) proposed a real-time CNN for target recognition and counting. For future enhancements of πM, a critical and thoughtful approach is required, particularly in enhancing its real-time data analysis capabilities. Drawing from case studies, such as the use of machine learning algorithms in low-power edge devices in remote environmental monitoring, it's evident that optimizing computational efficiency without compromising analytical depth is paramount. For instance, employing lightweight neural networks like MobileNets, which have shown promise in mobile vision applications, could offer a pathway to achieving robust real-time analysis within the πM's computational constraints.

To address challenges in real-time analysis, future work could explore the application of edge computing and machine learning algorithms specifically optimized for video processing. For example, techniques like background subtraction and frame differencing could be employed to reduce the computational load by focusing the analysis on changes between consecutive frames rather than processing each frame in its entirety. Case studies in applications like environmental monitoring, where real-time video processing has been used to track wildlife movements or monitor water quality, could provide valuable insights into practical implementations. These examples illustrate the potential of real-time video analysis to provide not only static snapshots but also dynamic insights into the observed subjects, thereby enriching the data and its interpretability.

Incorporating real-time video processing into the πM system would undoubtedly enhance its capabilities, making it a more versatile tool for a wider range of applications, from educational purposes to sophisticated scientific research and diagnostics. It would allow users not only to observe but also to interact with and manipulate samples in real-time, opening up new possibilities for exploratory learning and research.

Expanding the scope of biological experiments is another critical area for future work. The device's efficacy in diverse biological contexts can be benchmarked against established microscopy techniques in clinical diagnostics, such as malaria parasite detection or tuberculosis diagnosis, where the nuances of sample variability are well-documented. These case studies can provide a framework for designing comprehensive testing protocols for the πM system, ensuring its utility across a broad spectrum of biological research and medical diagnostics.

In addressing hardware limitations, inspiration can be drawn from the field of consumer

electronics, where advancements in miniaturized camera technologies have revolutionized mobile phone imaging. Applying similar innovations to the optical components of the πM could enhance its imaging capabilities while maintaining portability and affordability. Moreover, integrating rugged design principles from outdoor and military-grade equipment could improve the device's durability for field applications, as seen in portable water quality testing kits used in disaster-stricken regions.

Furthermore, to ensure the system's applicability in precision experiments, a series of methodical validation studies should be conducted. For example, comparing the πM's performance in counting circulating tumour cells against gold-standard flow cytometry could offer valuable insights into its precision and reliability. These studies not only serve to validate the device but also to highlight areas for iterative improvement.

By critically examining these aspects and incorporating lessons from relevant case studies and examples, future developments of the πM system can be more effectively aligned with the practical needs and challenges of field-based microscopy, paving the way for broader adoption and impact in scientific research and healthcare diagnostics.

6.2.2 Smartphone-based HiLo

To address the inherent limitations associated with utilizing smartphones for microscopy, future research and development efforts must be comprehensive and interdisciplinary. A significant focus should be placed on enhancing optical quality, which could be achieved by designing specialized optical attachments tailored to smartphone cameras. These attachments could include adaptive lenses to improve resolution and image quality, thus compensating for the limitations of built-in smartphone lenses. Moreover, the development of clip-on illumination modules would provide more uniform and controllable lighting, essential for various microscopy

techniques, particularly fluorescence microscopy.

The variability in smartphone models poses a challenge to consistent imaging performance, necessitating hardware standardization and the creation of modular smartphone microscopy kits. These kits would ensure adaptability to different devices, while standardized components such as illumination sources, lens adapters, and sample holders would guarantee compatibility and repeatability. Furthermore, dedicated microscopy applications need to be developed to bypass or minimize native image processing algorithms in smartphones, allowing for the capture and storage of raw image data. Integrating basic image analysis tools within these apps would empower users to conduct essential computations directly on their devices.

Illumination control is crucial for microscopy, prompting the need for software-controlled illumination systems within the smartphone microscopy setup. These systems would enable precise control over various illumination parameters, catering to different techniques and sample requirements. Addressing the issue of thermal management is also critical, as prolonged imaging sessions could lead to overheating. Incorporating thermal management solutions would ensure the smartphone and biological samples remain unaffected by temperature increases.

The mechanical stability of the setup is paramount, and future work should focus on enhancing the design and manufacturing of components such as adapters and holders. Using more robust materials or incorporating fine adjustment mechanisms could significantly improve precision and stability. Additionally, the user interface of smartphone microscopy apps should be specifically designed for scientific users, incorporating ergonomic considerations and possibly voice commands or external control devices to enhance usability.

Although the presented smartphone-based HiLo optical sectioning microscope significantly reduces costs compared to traditional systems, future efforts will aim to reduce costs even further by exploring alternative components such as using diffusive or periodic pattern glass plates instead of a DMD and fabricating light guides from low-cost polymers like PDMS or PMMA. Additionally, employing micro-LED mini displays and more affordable relay optics could further reduce the necessity for additional light sources and enable the generation of various structured illumination patterns.

Moreover, the application of SOS in imaging actual biological samples, such as fluorescently labelled zebrafish, will be explored to validate its effectiveness in real-world bioimaging scenarios.

6.3.3 Microlens arrays for incoherent HiLo microscopy

Chapter 5 provides a theoretical study of using MLAs to decrease the cost of HiLo microscopy. For future research, a multifaceted approach is essential to bridge the gap between the promising results obtained from simulations and the complex realities of practical microscopy applications. Firstly, a comprehensive series of experimental validations should be conducted across a diverse array of biological samples to assess the robustness and applicability of the proposed MLA-based HiLo microscopy technique. This would involve not only confirming the simulation results but also exploring the technique's performance under varied sample conditions, including different types of tissues, live-cell imaging, and long-term time-lapse studies. Additionally, further investigations into the mitigation strategies for artifacts, especially those associated with specific MLA configurations, are crucial. Developing advanced image processing algorithms or exploring alternative MLA designs could provide solutions. Another promising avenue is the integration of this technique with other imaging modalities or the incorporation of adaptive optics to enhance resolution and

contrast dynamically. Moreover, exploring the potential for miniaturization and portability of the MLA-based HiLo setup could open new avenues for in-field biological research and point-of-care diagnostics. Ultimately, the goal should be to not only validate and refine the proposed method but also to expand its capabilities and applications, making it a versatile tool in the arsenal of optical microscopy techniques.

References

[1] de Haan K, Ceylan Koydemir H, Rivenson Y, et al. Automated screening of sickle cells using a smartphone-based microscope and deep learning[J]. NPJ digital medicine, 2020, 3(1): 76.

[2] Tan W C C, Nerurkar S N, Cai H Y, et al. Overview of multiplex immunohistochemistry/immunofluorescence techniques in the era of cancer immunotherapy[J]. Cancer Communications, 2020, 40(4): 135-153.

[3] Minaee S, Boykov Y, Porikli F, et al. Image segmentation using deep learning: A survey[J]. IEEE transactions on pattern analysis and machine intelligence, 2021, 44(7): 3523-3542.

[4] Bai X, Wang X, Liu X, et al. Explainable deep learning for efficient and robust pattern recognition: A survey of recent developments[J]. Pattern Recognition, 2021, 120: 108102.

[5] Razzak M I, Naz S, Zaib A. Deep learning for medical image processing: Overview, challenges and the future[J]. Classification in BioApps: Automation of decision making, 2018: 323-350.

[6] Ayardulabi R, Khamespanah E, Abbasinia S, et al. Point-of-care applications of smartphone-based microscopy[J]. Sensors and Actuators A: Physical, 2021, 331: 113048.

[7] Shan Y, Wang B, Huang H, et al. On-site quantitative Hg2+ measurements based on selective and sensitive fluorescence biosensor and miniaturized smartphone fluorescence microscope[J]. Biosensors and Bioelectronics, 2019, 132: 238-247.

[8] Shrestha R, Duwal R, Wagle S, et al. A smartphone microscopic method for simultaneous detection of (oo) cysts of Cryptosporidium and Giardia[J]. PLoS Neglected Tropical Diseases, 2020, 14(9): e0008560.

[9] Atta M A, Imtiaz M, Hassan A, et al. Image segmentation by using threshold techniques[J]. Lahore Garrison University Research Journal of Computer Science and Information Technology, 2018, 2(2): 1-6.

[10] Kanopoulos N, Vasanthavada N, Baker R L. Design of an image edge detection filter using the Sobel operator[J]. IEEE Journal of solid-state circuits, 1988, 23(2): 358-367.

[11] Deng C X, Wang G B, Yang X R. Image edge detection algorithm based on improved canny operator[C]//2013 International Conference on Wavelet Analysis and Pattern Recognition. IEEE, 2013: 168-172.

[12] Dong W, Shisheng Z. Color image recognition method based on the prewitt operator[C]//2008 International Conference on Computer Science and Software Engineering. IEEE, 2008, 6: 170-173.

[13] Fully convolutional architecture vs sliding-window CNN for corneal endothelium cell segmentation

[14] Cell segmentation and tracking using CNN-based distance predictions and a graph-based matching strategy

[15] An Automatic Nucleus Segmentation and CNN Model based Classification Method of White Blood Cell

[16] Quality counts: new parameters in blood cell counting

[17] Evaluation of diagnostic criteria in polycythemia vera

[18] Distribution of dehydration rates generated by maximal Gardos-channel activation in normal and sickle red blood cells

[19] Automated Blood Cell Counts: State of the Art

[20] Spurious counts and spurious results on haematology analysers: a review. Part II: white blood cells, red blood cells, haemoglobin, red cell indices and reticulocytes

[21] Lim D, Chu K K, Mertz J. Wide-field fluorescence sectioning with hybrid speckle and uniform-illumination microscopy[J]. Optics letters, 2008, 33(16): 1819-1821.

[22] Saxena M, Eluru G, Gorthi S S. Structured illumination microscopy[J]. Advances in Optics and Photonics, 2015, 7(2): 241-275.

[23] Olarte O E, Andilla J, Gualda E J, et al. Light-sheet microscopy: a tutorial[J]. Advances in Optics and Photonics, 2018, 10(1): 111-179.

[24] Jonkman J, Brown C M, Wright G D, et al. Tutorial: guidance for quantitative confocal microscopy[J]. Nature protocols, 2020, 15(5): 1585-1611.

[25] Pan L W, Shen X, Lin L. Microplastic lens array fabricated by a hot intrusion process[J]. Journal of microelectromechanical systems, 2004, 13(6): 1063-1071.

[26] Xie D, Chang X, Shu X, et al. Rapid fabrication of thermoplastic polymer refractive microlens array using contactless hot embossing technology[J]. Optics Express, 2015, 23(4): 5154-5166.

[27] Zhu X, Li Z, Hu Y, et al. Facile fabrication of defogging microlens arrays using electric field-driven jet printing[J]. Optics & Laser Technology, 2020, 123: 105943.

[28] Luo Y, Wang L, Ding Y, et al. Direct fabrication of microlens arrays with high numerical aperture by ink-jetting on nanotextured surface[J]. Applied Surface Science, 2013, 279: 36-40.

[29] Shao J, Ding Y, Zhai H, et al. Fabrication of large curvature microlens array using confined laser swelling method[J]. Optics letters, 2013, 38(16): 3044-3046.

[30] Li J, Wang W, Mei X, et al. Rapid fabrication of microlens arrays on PMMA substrate using a microlens array by rear-side picosecond laser swelling[J]. Optics and Lasers in Engineering, 2020, 126: 105872.

[31] Luo J, Guo Y, Wang X. Rapid fabrication of curved microlens array using the 3D printing mold[J]. Optik, 2018, 156: 556-563.

[32] Zhang H, Qi T, Zhu X, et al. 3D printing of a PDMS cylindrical microlens array with 100% fill-factor[J]. ACS Applied Materials & Interfaces, 2021, 13(30): 36295-36306.

[33] Sun R, Yang H, Rock D M, et al. Manufacturing PDMS micro lens array using spin coating under a multiphase system[J]. Journal of Micromechanics and Microengineering, 2017, 27(5): 055012.

[34] Skolrood L, Wang Y, Zhang S, et al. Single-molecule and particle detection on true portable microscopy platforms[J]. Sensors and Actuators Reports, 2022, 4: 100063.

[35] Yang K, Wu J, Santos S, et al. Recent development of portable imaging platforms for cell-based assays[J]. Biosensors and Bioelectronics, 2019, 124: 150-160.

[36] Kolluri N, Klapperich C M, Cabodi M. Towards lab-on-a-chip diagnostics for malaria elimination[J]. Lab on a Chip, 2018, 18(1): 75-94.

[37] Gopinath S C B, Tang T H, Chen Y, et al. Bacterial detection: From microscope to smartphone[J]. Biosensors and Bioelectronics, 2014, 60: 332-342.

[38] Salido J, Bueno G, Ruiz‐Santaquiteria J, et al. A review on low‐cost microscopes for Open Science[J]. Microscopy research and technique, 2022, 85(10): 3270-3283.

[39] Bian Y, Xing T, Jiao K, et al. Computational portable microscopes for point-of-care-test and tele-diagnosis[J]. Cells, 2022, 11(22): 3670.

[40] Del Rosario M, Heil H S, Mendes A, et al. The field guide to 3D printing in optical microscopy for life sciences[J]. Advanced Biology, 2022, 6(4): 2100994.

[41] Gordon P, Venancio V P, Mertens-Talcott S U, et al. Portable bright-field, fluorescence, and cross-polarized microscope toward point-of-care imaging diagnostics[J]. Journal of Biomedical Optics, 2019, 24(9): 096502-096502.

[42] Contreras-Naranjo J C, Wei Q, Ozcan A. Mobile phone-based microscopy, sensing, and diagnostics[J]. IEEE Journal of Selected Topics in Quantum Electronics, 2015, 22(3): 1-14.

[43] Sivakumar R, Lee N Y. Recent progress in smartphone-based techniques for food safety and the detection of heavy metal ions in environmental water[J]. Chemosphere, 2021, 275: 130096.

[44] Yadav P, Yadav L, Laddha H, et al. Upsurgence of smartphone as an economical, portable, and consumer-friendly analytical device/interface platform for digital sensing of hazardous environmental ions[J]. Trends in Environmental Analytical Chemistry, 2022, 36: e00177.

[45] Kuroda A, Alexandrov M, Nishimura T, et al. Rapid on-site detection of airborne asbestos fibers and potentially hazardous nanomaterials using fluorescence microscopy-based biosensing[J]. Biotechnology Journal, 2016, 11(6): 757-767.

[46] Shin Y H, Gutierrez-Wing M T, Choi J W. Recent progress in portable fluorescence sensors[J]. Journal of The Electrochemical Society, 2021, 168(1): 017502.

[47] Yang J, Wang K, Xu H, et al. Detection platforms for point-of-care testing based on colorimetric, luminescent and magnetic assays: A review[J]. Talanta, 2019, 202: 96-110.

[48] Roda A, Michelini E, Zangheri M, et al. Smartphone-based biosensors: A critical review and perspectives[J]. TrAC Trends in Analytical Chemistry, 2016, 79: 317-325.

[49] Wang B, Li Y, Zhou M, et al. Smartphone-based platforms implementing microfluidic detection with image-based artificial intelligence[J]. Nature Communications, 2023, 14(1): 1-18.

[50] Banik S, Melanthota S K, Arbaaz, et al. Recent trends in smartphone-based detection for biomedical applications: a review[J]. Analytical and Bioanalytical Chemistry, 2021, 413: 2389-2406.

[51] Dai B, Jiao Z, Zheng L, et al. Colour compound lenses for a portable fluorescence microscope[J]. Light: Science & Applications, 2019, 8(1): 75.

[52] Szydlowski N A, Jing H, Alqashmi M, et al. Cell phone digital microscopy using an oil droplet[J]. Biomedical Optics Express, 2020, 11(5): 2328-2338.

[53] Switz N A, D'Ambrosio M V, Fletcher D A. Low-cost mobile phone microscopy with a reversed mobile phone camera lens[J]. PloS one, 2014, 9(5): e95330.

[54] Snow J W, Koydemir H C, Karinca D K, et al. Rapid imaging, detection, and quantification of Nosema ceranae spores in honey bees using mobile phone-based fluorescence microscopy[J]. Lab on a Chip, 2019, 19(5): 789-797.

[55] Leonard J, Koydemir H C, Koutnik V S, et al. Smartphone-enabled rapid quantification of microplastics[J]. Journal of Hazardous Materials Letters, 2022, 3: 100052.

[56] Koydemir H C, Gorocs Z, Tseng D, et al. Rapid imaging, detection and quantification of Giardia lamblia cysts using mobile-phone based fluorescent microscopy and machine learning[J]. Lab on a Chip, 2015, 15(5): 1284-1293.

[57] Lee W M, Upadhya A, Reece P J, et al. Fabricating low cost and high performance elastomer lenses using hanging droplets[J]. Biomedical optics express, 2014, 5(5): 1626-1635.

[58] Sung Y L, Jeang J, Lee C H, et al. Fabricating optical lenses by inkjet printing and heat-assisted in situ curing of polydimethylsiloxane for smartphone microscopy[J]. Journal of biomedical optics, 2015, 20(4): 047005-047005.

[59] Salafi T, Zeming K K, Lim J W, et al. Portable Smartphone‐Based Platform for Real‐Time Particle Detection in Microfluidics[J]. Advanced Materials Technologies, 2019, 4(3): 1800359.

[60] Long J, Parker H E, Ehrlich K, et al. Frugal filtering optical lenses for point-of-care diagnostics[J]. Biomedical Optics Express, 2020, 11(4): 1864-1875.

[61] Ephraim R K D, Duah E, Cybulski J S, et al. Diagnosis of Schistosoma haematobium infection with a mobile phone-mounted Foldscope and a reversed-lens CellScope in Ghana[J]. The American journal of tropical medicine and hygiene, 2015, 92(6): 1253.

[62] D'Ambrosio M V, Bakalar M, Bennuru S, et al. Point-of-care quantification of blood-borne filarial parasites with a mobile phone microscope[J]. Science translational medicine, 2015, 7(286): 286re4-286re4.

[63] McKay G N, Mohan N, Butterworth I, et al. Visualization of blood cell contrast in nailfold capillaries with high-speed reverse lens mobile phone microscopy[J]. Biomedical optics express, 2020, 11(4): 2268-2276.

[64] Rabha D, Biswas S, Hatiboruah D, et al. An affordable, handheld multimodal microscopic system with onboard cell morphology and counting features on a mobile device[J]. Analyst, 2022, 147(12): 2859-2869.

[65] Liu Y, Rollins A M, Levenson R M, et al. Pocket MUSE: an affordable, versatile and high-performance fluorescence microscope using a smartphone[J]. Communications biology, 2021, 4(1): 334.

[66] Wei Q, Qi H, Luo W, et al. Fluorescent imaging of single nanoparticles and viruses on a smart phone[J]. ACS nano, 2013, 7(10): 9147-9155.

[67] Wei Q, Luo W, Chiang S, et al. Imaging and sizing of single DNA molecules on a mobile phone[J]. ACS nano, 2014, 8(12): 12725-12733.

[68] Kühnemund M, Wei Q, Darai E, et al. Targeted DNA sequencing and in situ mutation analysis using mobile phone microscopy[J]. Nature communications, 2017, 8(1): 13913.

[69] Knowlton S, Joshi A, Syrrist P, et al. 3D-printed smartphone-based point of care tool for fluorescence-and magnetophoresis-based cytometry[J]. Lab on a Chip, 2017, 17(16): 2839-2851.

[70] Meng X, Huang H, Yan K, et al. Smartphone based hand-held quantitative phase microscope using the transport of intensity equation method[J]. Lab on a Chip, 2017, 17(1): 104-109.

[71] Phillips Z F, D'Ambrosio M V, Tian L, et al. Multi-contrast imaging and digital refocusing on a mobile microscope with a domed LED array[J]. PloS one, 2015, 10(5): e0124938.

[72] Bian Y, Jiang Y, Huang Y, et al. Smart-phone phase contrast microscope with a singlet lens and deep learning[J]. Optics & Laser Technology, 2021, 139: 106900.

[73] Rabha D, Rather M A, Mandal M, et al. Programmable illumination smartphone microscopy (PISM): A multimodal imaging platform for biomedical applications[J]. Optics and Lasers in Engineering, 2022, 151: 106931.

[74] Lee K C, Lee K, Jung J, et al. A smartphone-based Fourier ptychographic microscope using the display screen for illumination[J]. ACS Photonics, 2021, 8(5): 1307-1315.

[75] Trofymchuk K, Glembockyte V, Grabenhorst L, et al. Addressable nanoantennas with cleared hotspots for single-molecule detection on a portable smartphone microscope[J]. Nature communications, 2021, 12(1): 950.

[76] Chowdhury F A, Chau K J. Variable focus microscopy using a suspended water droplet[J]. Journal of Optics, 2012, 14(5): 055501.

[77] Ekgasit S, Kaewmanee N, Jangtawee P, et al. Elastomeric PDMS planoconvex lenses fabricated by a confined sessile drop technique[J]. ACS applied materials & interfaces, 2016, 8(31): 20474-20482.

[78] Kamal T, Watkins R, Cen Z, et al. Design and fabrication of a passive droplet dispenser for portable high resolution imaging system[J]. Scientific reports, 2017, 7(1): 41482.

[79] Sung Y L, Garan J, Hu Z, et al. Modeling the surface of fast-cured polymer droplet lenses for precision fabrication[J]. Applied optics, 2018, 57(35): 10342-10347.

[80] Malacara Z, Malacara-Hernández D, Malacara-Hernández Z. Handbook of optical design[M]. CRC press, 2003.

[81] Sung Y, Campa F, Shih W C. Open-source do-it-yourself multi-color fluorescence smartphone microscopy[J]. Biomedical optics express, 2017, 8(11): 5075-5086.

[82] Müller V, Sousa J M, Koydemir H C, et al. Identification of pathogenic bacteria in complex samples using a smartphone based fluorescence microscope[J]. RSC advances, 2018, 8(64): 36493-36502.

[83] Nguyen H, Sung Y, O'Shaughnessy K, et al. Smartphone nanocolorimetry for on-demand lead detection and quantitation in drinking water[J]. Analytical chemistry, 2018, 90(19): 11517-11522.

[84] Rabha D, Biswas S, Chamuah N, et al. Wide-field multi-modal microscopic imaging using smartphone[J]. Optics and Lasers in Engineering, 2021, 137: 106343.

[85] Navruz I, Coskun A F, Wong J, et al. Smart-phone based computational microscopy using multi-frame contact imaging on a fiber-optic array[J]. Lab on a Chip, 2013, 13(20): 4015-4023.

[86] Wei Q, Acuna G, Kim S, et al. Plasmonics enhanced smartphone fluorescence microscopy[J]. Scientific reports, 2017, 7(1): 2124.

[87] Rivenson Y, Ceylan Koydemir H, Wang H, et al. Deep learning enhanced mobile-phone microscopy[J]. Acs Photonics, 2018, 5(6): 2354-2364.

[88] Ghonge T, Koydemir H C, Valera E, et al. Smartphone-imaged microfluidic biochip for measuring CD64 expression from whole blood[J]. Analyst, 2019, 144(13): 3925-3935.

[89] Knowlton S M, Sencan I, Aytar Y, et al. Sickle cell detection using a smartphone[J]. Scientific reports, 2015, 5(1): 15022.

[90] Miller A R, Davis G L, Oden Z M, et al. Portable, battery-operated, low-cost, bright field and fluorescence microscope[J]. PloS one, 2010, 5(8): e11890.

[91] Zhu W, Pirovano G, O'Neal P K, et al. Smartphone epifluorescence microscopy for cellular imaging of fresh tissue in low-resource settings[J]. Biomedical optics express, 2020, 11(1): 89-98.

[92] Brown J W P, Bauer A, Polinkovsky M E, et al. Single-molecule detection on a portable 3D-printed microscope[J]. Nature Communications, 2019, 10(1): 5662.

[93] Ambrose B, Baxter J M, Cully J, et al. The smfBox is an open-source platform for single-molecule FRET[J]. Nature communications, 2020, 11(1): 5641.

[94] Pitrone P G, Schindelin J, Stuyvenberg L, et al. OpenSPIM: an open-access light-sheet microscopy platform[J]. Nature methods, 2013, 10(7): 598-599.

[95] Prakash K. Laser-free super-resolution microscopy[J]. Philosophical Transactions of the Royal Society A, 2021, 379(2199): 20200144.

[96] Diederich B, Müllenbroich C, Vladimirov N, et al. CAD we share? Publishing reproducible microscope hardware[J]. Nature Methods, 2022, 19(9): 1026-1030.

[97] Hohlbein J, Diederich B, Marsikova B, et al. Open microscopy in the life sciences: quo vadis?[J]. Nature methods, 2022, 19(9): 1020-1025.

[98] Diekmann R, Till K, Müller M, et al. Characterization of an industry-grade CMOS camera well suited for single molecule localization microscopy–high performance super-resolution at low cost[J]. Scientific reports, 2017, 7(1): 14425.

[99] Schröder D, Deschamps J, Dasgupta A, et al. Cost-efficient open source laser engine for microscopy[J]. Biomedical Optics Express, 2020, 11(2): 609-623.

[100] Nicovich P R, Walsh J, Böcking T, et al. NicoLase—an open-source diode laser combiner, fiber launch, and sequencing controller for fluorescence microscopy[J]. PLoS One, 2017, 12(3): e0173879.

[101] Diederich B, Lachmann R, Carlstedt S, et al. A versatile and customizable low-cost 3D-printed open standard for microscopic imaging[J]. Nature communications, 2020, 11(1): 5979.

[102] Zhang Y S, Ribas J, Nadhman A, et al. A cost-effective fluorescence mini-microscope for biomedical applications[J]. Lab on a Chip, 2015, 15(18): 3661-3669.

[103] Lu Q, Liu G, Xiao C, et al. A modular, open-source, slide-scanning microscope for diagnostic applications in resource-constrained settings[J]. PloS one, 2018, 13(3): e0194063.

[104] Jiao Z, Zang Z, Wang Q, et al. PAIM (πM): Portable AI-enhanced fluorescence microscope for real-time target detection[J]. Optics & Laser Technology, 2023, 163: 109356.

[105] O'Connor T, Javidi B. COVID-19 screening with digital holographic microscopy using intra-patient probability functions of spatio-temporal bio-optical attributes[J]. Biomedical Optics Express, 2022, 13(10): 5377-5389.

[106] O'Connor T, Shen J B, Liang B T, et al. Digital holographic deep learning of red blood cells for field-portable, rapid COVID-19 screening[J]. Optics Letters, 2021, 46(10): 2344-2347.

[107] O'Connor T, Santaniello S, Javidi B. COVID-19 detection from red blood cells using highly comparative time-series analysis (HCTSA) in digital holographic microscopy[J]. Optics Express, 2022, 30(2): 1723-1736.

[108] Son J, Mandracchia B, Jia S. Miniaturized modular-array fluorescence microscopy[J]. Biomedical Optics Express, 2020, 11(12): 7221-7235.

[109] Collins J T, Knapper J, Stirling J, et al. Robotic microscopy for everyone: the OpenFlexure microscope[J]. Biomedical Optics Express, 2020, 11(5): 2447-2460.

[110] McDermott S, Ayazi F, Collins J, et al. Multi-modal microscopy imaging with the OpenFlexure Delta Stage[J]. Optics Express, 2022, 30(15): 26377-26395.

[111] Gordon P D, De Ville C, Sacchettini J C, et al. A portable brightfield and fluorescence microscope toward automated malarial parasitemia quantification in thin blood smears[J]. PloS one, 2022, 17(4): e0266441.

[112] Ouyang W, Bowman R W, Wang H, et al. An Open-Source Modular Framework for Automated Pipetting and Imaging Applications[J]. Advanced biology, 2022, 6(4): 2101063.

[113] Tristan-Landin S B, Gonzalez-Suarez A M, Jimenez-Valdes R J, et al. Facile assembly of an affordable miniature multicolor fluorescence microscope made of 3D-printed parts enables detection of single cells[J]. PloS one, 2019, 14(10): e0215114.

[114] Wang H, Lachmann R, Marsikova B, et al. UCsim2: 2D structured illumination microscopy using UC2[J]. bioRxiv, 2021: 2021.01. 08.425840.

[115] Rosenegger D G, Tran C H T, LeDue J, et al. A high performance, cost-effective, open-source microscope for scanning two-photon microscopy that is modular and readily adaptable[J]. PloS one, 2014, 9(10): e110475.

[116] Auer A, Schlichthaerle T, Woehrstein J B, et al. Nanometer-scale Multiplexed Super-Resolution Imaging with an Economic 3D-DNA-PAINT Microscope[J]. ChemPhysChem, 2018, 19(22): 3024-3034.

[117] Ly V T, Baudin P V, Pansodtee P, et al. Picroscope: low-cost system for simultaneous longitudinal biological imaging[J]. Communications biology, 2021, 4(1): 1261.

[118] Meng Q, Harrington K, Stirling J, et al. The OpenFlexure Block Stage: sub-100 nm fibre alignment with a monolithic plastic flexure stage[J]. Optics Express, 2020, 28(4): 4763-4772.

[119] Sharkey J P, Foo D C W, Kabla A, et al. A one-piece 3D printed flexure translation stage for open-source microscopy[J]. Review of Scientific Instruments, 2016, 87(2).

[120] Matsui T, Fujiwara D. Optical sectioning robotic microscopy for everyone: the structured illumination microscope with the OpenFlexure stages[J]. Optics Express, 2022, 30(13): 23208-23216.

[121] Diep T T, Needs S H, Bizley S, et al. Rapid Bacterial Motility Monitoring Using Inexpensive 3D-Printed OpenFlexure Microscopy Allows Microfluidic Antibiotic Susceptibility Testing[J]. Micromachines, 2022, 13(11): 1974.

[122] Delmans M, Haseloff J. μCube: A framework for 3D printable optomechanics[J]. Journal of Open Hardware, 2018, 2(1): 2-2.

[123] Sanderson T, Rayner J C. PlasmoTron: an open-source platform for automated culture of malaria parasites[J]. BioRxiv, 2017: 241596.

[124] Ouyang W, Mueller F, Hjelmare M, et al. ImJoy: an open-source computational platform for the deep learning era[J]. Nature methods, 2019, 16(12): 1199-1200.

[125] Ojaghi A, Williams E K, Kaza N, et al. Label-free deep-UV microscopy detection and grading of neutropenia using a passive microfluidic device[J]. Optics Letters, 2022, 47(22): 6005-6008.

[126] Aidukas T, Eckert R, Harvey A R, et al. Low-cost, sub-micron resolution, wide-field computational microscopy using opensource hardware[J]. Scientific reports, 2019, 9(1): 7457.

[127] Jang Y, Han S, Song C, et al. Miniaturized optimal incident light angle‐fitted dark field system for contrast‐enhanced real‐time monitoring of 2D/3D‐projected cell motions[J]. Journal of Biophotonics, 2022, 15(10): e202200091.

[128] Salido J, Toledano P T, Vallez N, et al. MicroHikari3D: an automated DIY digital microscopy platform with deep learning capabilities[J]. Biomedical Optics Express, 2021, 12(11): 7223-7243.

[129] Niu M, Luo G, Shu X, et al. Portable quantitative phase microscope for material metrology and biological imaging[J]. Photonics Research, 2020, 8(7): 1253-1259.

[130] Zheng G, Lee S A, Yang S, et al. Sub-pixel resolving optofluidic microscope for on-chip cell imaging[J]. Lab on a Chip, 2010, 10(22): 3125-3129.

[131] Cui X, Lee L M, Heng X, et al. Lensless high-resolution on-chip optofluidic microscopes for Caenorhabditis elegans and cell imaging[J]. Proceedings of the National Academy of Sciences, 2008, 105(31): 10670-10675.

[132] Heng X, Erickson D, Baugh L R, et al. Optofluidic microscopy—a method for implementing a high resolution optical microscope on a chip[J]. Lab on a Chip, 2006, 6(10): 1274-1276.

[133] Bishara W, Zhu H, Ozcan A. Holographic opto-fluidic microscopy[J]. Optics express, 2010, 18(26): 27499-27510.

[134] Greenbaum A, Luo W, Khademhosseinieh B, et al. Increased space-bandwidth product in pixel super-resolved lensfree on-chip microscopy[J]. Scientific reports, 2013, 3(1): 1717.

[135] McLeod E, Luo W, Mudanyali O, et al. Toward giga-pixel nanoscopy on a chip: a computational wide-field look at the nano-scale without the use of lenses[J]. Lab on a Chip, 2013, 13(11): 2028-2035.

[136] Bishara W, Su T W, Coskun A F, et al. Lensfree on-chip microscopy over a wide field-of-view using pixel super-resolution[J]. Optics express, 2010, 18(11): 11181-11191.

[137] Zheng G, Lee S A, Antebi Y, et al. The ePetri dish, an on-chip cell imaging platform based on subpixel perspective sweeping microscopy (SPSM)[J]. Proceedings of the National Academy of Sciences, 2011, 108(41): 16889-16894.

[138] Lee S A, Zheng G, Mukherjee N, et al. On-chip continuous monitoring of motile microorganisms on an ePetri platform[J]. Lab on a Chip, 2012, 12(13): 2385-2390.

[139] Han C, Yang C. Viral plaque analysis on a wide field-of-view, time-lapse, on-chip imaging platform[J]. Analyst, 2014, 139(15): 3727-3734.

[140] Lee S A, Erath J, Zheng G, et al. Imaging and identification of waterborne parasites using a chip-scale microscope[J]. PloS one, 2014, 9(2): e89712.

[141] Luo W, Greenbaum A, Zhang Y, et al. Synthetic aperture-based on-chip microscopy[J]. Light: Science & Applications, 2015, 4(3): e261-e261.

[142] Ozcan A, McLeod E. Lensless imaging and sensing[J]. Annual review of biomedical engineering, 2016, 18: 77-102.

[143] Boominathan V, Robinson J T, Waller L, et al. Recent advances in lensless imaging[J]. Optica, 2022, 9(1): 1-16.

[144] Yuan X, Brady D J, Katsaggelos A K. Snapshot compressive imaging: Theory, algorithms, and applications[J]. IEEE Signal Processing Magazine, 2021, 38(2): 65-88.

[145] Qi D, Zhang S, Yang C, et al. Single-shot compressed ultrafast photography: a review[J]. Advanced Photonics, 2020, 2(1): 014003-014003.

[146] Lange D, Storment C W, Conley C A, et al. A microfluidic shadow imaging system for the study of the nematode Caenorhabditis elegans in space[J]. Sensors and Actuators B: Chemical, 2005, 107(2): 904-914.

[147] Ozcan A, Demirci U. Ultra wide-field lens-free monitoring of cells on-chip[J]. Lab on a Chip, 2008, 8(1): 98-106.

[148] Kun J, Smieja M, Xiong B, et al. The use of motion analysis as particle biomarkers in lensless optofluidic projection imaging for point of care urine analysis[J]. Scientific reports, 2019, 9(1): 17255.

[149] Seo S, Su T W, Tseng D K, et al. Lensfree holographic imaging for on-chip cytometry and diagnostics[J]. Lab on a Chip, 2009, 9(6): 777-787.

[150] Dolega M E, Allier C, Kesavan S V, et al. Label-free analysis of prostate acini-like 3D structures by lensfree imaging[J]. Biosensors and Bioelectronics, 2013, 49: 176-183.

[151] Kesavan S V, Navarro F P, Menneteau M, et al. Real-time label-free detection of dividing cells by means of lensfree video-microscopy[J]. Journal of biomedical optics, 2014, 19(3): 036004-036004.

[152] Berdeu A, Laperrousaz B, Bordy T, et al. Lens-free microscopy for 3D+ time acquisitions of 3D cell culture[J]. Scientific reports, 2018, 8(1): 16135.

[153] Greenbaum A, Zhang Y, Feizi A, et al. Wide-field computational imaging of pathology slides using lens-free on-chip microscopy[J]. Science translational medicine, 2014, 6(267): 267ra175-267ra175.

[154] Kesavan S V, Momey F, Cioni O, et al. High-throughput monitoring of major cell functions by means of lensfree video microscopy[J]. Scientific reports, 2014, 4(1): 5942.

[155] Sobieranski A C, Inci F, Tekin H C, et al. Portable lensless wide-field microscopy imaging platform based on digital inline holography and multi-frame pixel super-resolution[J]. Light, science & applications, 2015, 4: e346.

[156] Adams J K, Boominathan V, Avants B W, et al. Single-frame 3D fluorescence microscopy with ultraminiature lensless FlatScope[J]. Science advances, 2017, 3(12): e1701548.

[157] Jiang S, Zhu J, Song P, et al. Wide-field, high-resolution lensless on-chip microscopy via near-field blind ptychographic modulation[J]. Lab on a Chip, 2020, 20(6): 1058-1065.

[158] O'Connor T, Hawxhurst C, Shor L M, et al. Red blood cell classification in lensless single random phase encoding using convolutional neural networks[J]. Optics Express, 2020, 28(22): 33504-33515.

[159] Douglass P M, O'Connor T, Javidi B. Automated sickle cell disease identification in human red blood cells using a lensless single random phase encoding biosensor and convolutional neural networks[J]. Optics Express, 2022, 30(20): 35965-35977.

[160] Kuo G, Liu F L, Grossrubatscher I, et al. On-chip fluorescence microscopy with a random microlens diffuser[J]. Optics express, 2020, 28(6): 8384-8399.

[161] Adams J K, Yan D, Wu J, et al. In vivo lensless microscopy via a phase mask generating diffraction patterns with high-contrast contours[J]. Nature Biomedical Engineering, 2022, 6(5): 617-628.

[162] Coskun A F, Sencan I, Su T W, et al. Lensfree fluorescent on-chip imaging of transgenic Caenorhabditis elegans over an ultra-wide field-of-view[J]. PloS one, 2011, 6(1): e15955.

[163] Coskun A F, Sencan I, Su T W, et al. Wide-field lensless fluorescent microscopy using a tapered fiber-optic faceplate on a chip[J]. Analyst, 2011, 136(17): 3512-3518.

[164] Sasagawa K, Ohta Y, Kawahara M, et al. Wide field-of-view lensless fluorescence imaging device with hybrid bandpass emission filter[J]. AIP Advances, 2019, 9(3).

[165] Papageorgiou E P, Zhang H, Giverts S, et al. Real-time cancer detection with an integrated lensless fluorescence contact imager[J]. Biomedical optics express, 2018, 9(8): 3607-3623.

[166] Sasagawa K, Kimura A, Haruta M, et al. Highly sensitive lens-free fluorescence imaging device enabled by a complementary combination of interference and absorption filters[J]. Biomedical optics express, 2018, 9(9): 4329-4344.

[167] Han C, Pang S, Bower D V, et al. Wide field-of-view on-chip Talbot fluorescence microscopy for longitudinal cell culture monitoring from within the incubator[J]. Analytical chemistry, 2013, 85(4): 2356-2360.

[168] Penwill L A, Batten G E, Castagnetti S, et al. Growth phenotype screening of Schizosaccharomyces pombe using a Lensless microscope[J]. Biosensors and Bioelectronics, 2014, 54: 345-350.

[169] Zhang X, Khimji I, Gurkan U A, et al. Lensless imaging for simultaneous microfluidic sperm monitoring and sorting[J]. Lab on a Chip, 2011, 11(15): 2535-2540.

[170] Roy M, Seo D, Oh C H, et al. Low-cost telemedicine device performing cell and particle size measurement based on lens-free shadow imaging technology[J]. Biosensors and Bioelectronics, 2015, 67: 715-723.

[171] Su T W, Seo S, Erlinger A, et al. High - throughput lensfree imaging and characterization of a heterogeneous cell solution on a chip[J]. Biotechnology and bioengineering, 2009, 102(3): 856-868.

[172] Jin G, Yoo I H, Pack S P, et al. Lens-free shadow image based high-throughput continuous cell monitoring technique[J]. Biosensors and Bioelectronics, 2012, 38(1): 126-131.

[173] Lee L M, Cui X, Yang C. The application of on-chip optofluidic microscopy for imaging Giardia lamblia trophozoites and cysts[J]. Biomedical microdevices, 2009, 11: 951-958.

[174] Mudanyali O, Tseng D, Oh C, et al. Compact, light-weight and cost-effective microscope based on lensless incoherent holography for telemedicine applications[J]. Lab on a Chip, 2010, 10(11): 1417-1428.

[175] Wu Y, Ozcan A. Lensless digital holographic microscopy and its applications in biomedicine and environmental monitoring[J]. Methods, 2018, 136: 4-16.

[176] Göröcs Z, Ozcan A. On-chip biomedical imaging[J]. IEEE reviews in biomedical engineering, 2012, 6: 29-46.

[177] Greenbaum A, Ozcan A. Maskless imaging of dense samples using pixel super-resolution based multi-height lensfree on-chip microscopy[J]. Optics express, 2012, 20(3): 3129-3143.

[178] Xu W, Jericho M H, Meinertzhagen I A, et al. Digital in-line holography for biological applications[J]. Proceedings of the National Academy of Sciences, 2001, 98(20): 11301-11305.

[179] Verrier N, Coëtmellec S, Brunel M, et al. Digital in-line holography in thick optical systems: application to visualization in pipes[J]. Applied optics, 2008, 47(22): 4147-4157.

[180] Kim M K. Principles and techniques of digital holographic microscopy[J]. SPIE reviews, 2010, 1(1): 018005.

[181] Trujillo C, Piedrahita-Quintero P, Garcia-Sucerquia J. Digital lensless holographic microscopy: numerical simulation and reconstruction with ImageJ[J]. Applied Optics, 2020, 59(19): 5788-5795.

[182] Kreis T M. Frequency analysis of digital holography[J]. Optical Engineering, 2002, 41(4): 771-778.

[183] Ebrahimi S, Dashtdar M. Lens-free digital holographic microscopy for cell imaging and tracking by Fresnel diffraction from a phase discontinuity[J]. Optics Letters, 2021, 46(15): 3516-3519.

[184] Greenbaum A, Sikora U, Ozcan A. Field-portable wide-field microscopy of dense samples using multi-height pixel super-resolution based lensfree imaging[J]. Lab on a Chip, 2012, 12(7): 1242-1245.

[185] Latychevskaia T, Fink H W. Solution to the twin image problem in holography[J]. Physical review letters, 2007, 98(23): 233901.

[186] Guizar-Sicairos M, Fienup J R. Understanding the twin-image problem in phase retrieval[J]. JOSA A, 2012, 29(11): 2367-2375.

[187] Zalevsky Z, Mendlovic D, Dorsch R G. Gerchberg–Saxton algorithm applied in the fractional Fourier or the Fresnel domain[J]. Optics Letters, 1996, 21(12): 842-844.

[188] Yang G, Dong B, Gu B, et al. Gerchberg–Saxton and Yang–Gu algorithms for phase retrieval in a nonunitary transform system: a comparison[J]. Applied optics, 1994, 33(2): 209-218.

[189] Gureyev T E, Roberts A, Nugent K A. Partially coherent fields, the transport-of-intensity equation, and phase uniqueness[J]. JOSA A, 1995, 12(9): 1942-1946.

[190] Zuo C, Li J, Sun J, et al. Transport of intensity equation: a tutorial[J]. Optics and Lasers in Engineering, 2020, 135: 106187.

[191] Tobon-Maya H, Zapata-Valencia S, Zora-Guzmán E, et al. Open-source, cost-effective, portable, 3D-printed digital lensless holographic microscope[J]. Applied Optics, 2021, 60(4): A205-A214.

[192] Rivenson Y, Wu Y, Wang H, et al. Sparsity-based multi-height phase recovery in holographic microscopy[J]. Scientific reports, 2016, 6(1): 37862.

[193] Kim G, Isaacson K, Palmer R, et al. Lensless photography with only an image sensor[J]. Applied optics, 2017, 56(23): 6450-6456.

[194] Asif M S, Ayremlou A, Sankaranarayanan A, et al. Flatcam: Thin, lensless cameras using coded aperture and computation[J]. IEEE Transactions on Computational Imaging, 2016, 3(3): 384-397.

[195] Tajima K, Shimano T, Nakamura Y, et al. Lensless light-field imaging with multi-phased fresnel zone aperture[C]//2017 IEEE International Conference on Computational Photography (ICCP). IEEE, 2017: 1-7.

[196] Wu J, Zhang H, Zhang W, et al. Single-shot lensless imaging with fresnel zone aperture and incoherent illumination[J]. Light: Science & Applications, 2020, 9(1): 53.

[197] DeWeert M J, Farm B P. Lensless coded-aperture imaging with separable Doubly-Toeplitz masks[J]. Optical Engineering, 2015, 54(2): 023102-023102.

[198] Shimano T, Nakamura Y, Tajima K, et al. Lensless light-field imaging with Fresnel zone aperture: quasi-coherent coding[J]. Applied optics, 2018, 57(11): 2841-2850.

[199] Boominathan V, Adams J K, Robinson J T, et al. Phlatcam: Designed phase-mask based thin lensless camera[J]. IEEE transactions on pattern analysis and machine intelligence, 2020, 42(7): 1618-1629.

[200] Chi W, George N. Optical imaging with phase-coded aperture[J]. Optics express, 2011, 19(5): 4294-4300.

[201] Gill P R, Stork D G. Lensless ultra-miniature imagers using odd-symmetry spiral phase gratings[C]//Computational Optical Sensing and Imaging. Optica Publishing Group, 2013: CW4C. 3.

[202] Antipa N, Kuo G, Heckel R, et al. DiffuserCam: lensless single-exposure 3D imaging[J]. Optica, 2018, 5(1): 1-9.

[203] Chi W, George N. Phase-coded aperture for optical imaging[J]. Optics Communications, 2009, 282(11): 2110-2117.

[204] Tian F, Hu J, Yang W. GEOMScope: large field‐of‐view 3D lensless microscopy with low computational complexity[J]. Laser & photonics reviews, 2021, 15(8): 2100072.

[205] Singh A K, Pedrini G, Takeda M, et al. Scatter-plate microscope for lensless microscopy with diffraction limited resolution[J]. Scientific Reports, 2017, 7(1): 10687.

[206] Baraniuk R G, Cevher V, Duarte M F, et al. Model-based compressive sensing[J]. IEEE Transactions on information theory, 2010, 56(4): 1982-2001.

[207] Zhang Z, Zhou Y, Jiang S, et al. Invited Article: Mask-modulated lensless imaging with multi-angle illuminations[J]. APL Photonics, 2018, 3(6).

[208] Cai Z, Chen J, Pedrini G, et al. Lensless light-field imaging through diffuser encoding[J]. Light: Science & Applications, 2020, 9(1): 143.

[209] Coskun A F, Su T W, Ozcan A. Wide field-of-view lens-free fluorescent imaging on a chip[J]. Lab on a Chip, 2010, 10(7): 824-827.

[210] Shanmugam A, Salthouse C. Lensless fluorescence imaging with height calculation[J]. Journal of Biomedical Optics, 2014, 19(1): 016002-016002.

[211] Martinelli L, Choumane H, Ha K N, et al. Sensor-integrated fluorescent microarray for ultrahigh sensitivity direct-imaging bioassays: Role of a high rejection of excitation light[J]. Applied Physics Letters, 2007, 91(8).

[212] Lee S A, Ou X, Lee J E, et al. Chip-scale fluorescence microscope based on a silo-filter complementary metal-oxide semiconductor image sensor[J]. Optics letters, 2013, 38(11): 1817-1819.

[213] Sencan I, Coskun A F, Sikora U, et al. Spectral demultiplexing in holographic and fluorescent on-chip microscopy[J]. Scientific reports, 2014, 4(1): 3760.

[214] Kulmala N, Sasagawa K, Treepetchkul T, et al. Lensless dual-color fluorescence imaging device using hybrid filter[J]. Japanese journal of applied physics, 2022, 61(SC): SC1020.

[215] Coskun A F, Sencan I, Su T W, et al. Lensless wide-field fluorescent imaging on a chip using compressive decoding of sparse objects[J]. Optics express, 2010, 18(10): 10510-10523.

[216] Pang S, Han C, Kato M, et al. Wide and scalable field-of-view Talbot-grid-based fluorescence microscopy[J]. Optics letters, 2012, 37(23): 5018-5020.

[217] Howard A G, Zhu M, Chen B, et al. Mobilenets: Efficient convolutional neural networks for mobile vision applications[J]. arXiv preprint arXiv:1704.04861, 2017.

[218] Simonyan K, Zisserman A. Very deep convolutional networks for large-scale image recognition[J]. arXiv preprint arXiv:1409.1556, 2014.

[219] Krizhevsky A, Sutskever I, Hinton G E. Imagenet classification with deep convolutional neural networks[J]. Advances in neural information processing systems, 2012, 25.

[220] Ilyas S, Sher M, Du E, et al. Smartphone-based sickle cell disease detection and monitoring for point-of-care settings[J]. Biosensors and Bioelectronics, 2020, 165: 112417.

[221] Dacal E, Bermejo-Peláez D, Lin L, et al. Mobile microscopy and telemedicine platform assisted by deep learning for the quantification of Trichuris trichiura infection[J]. PLoS neglected tropical diseases, 2021, 15(9): e0009677.

[222] Cui M, Zhang D Y. Artificial intelligence and computational pathology[J]. Laboratory Investigation, 2021, 101(4): 412-422.

[223] Zheng G, Shen C, Jiang S, et al. Concept, implementations and applications of Fourier ptychography[J]. Nature Reviews Physics, 2021, 3(3): 207-223.

[224] Wang D, Lippard S J. Cellular processing of platinum anticancer drugs[J]. Nature reviews Drug discovery, 2005, 4(4): 307-320.

[225] Qian Y, Karpus J, Kabil O, et al. Selective fluorescent probes for live-cell monitoring of sulphide[J]. Nature communications, 2011, 2(1): 495.

[226] Joeris K, Frerichs J G, Konstantinov K, et al. In-situ microscopy: Online process monitoring of mammalian cell cultures[J]. Cytotechnology, 2002, 38: 129-134.

[227] Dittrich P S, Manz A. Lab-on-a-chip: microfluidics in drug discovery[J]. Nature reviews Drug discovery, 2006, 5(3): 210-218.

[228] Mark D, Haeberle S, Roth G, et al. Microfluidic lab-on-a-chip platforms: requirements, characteristics and applications[J]. Microfluidics based microsystems: fundamentals and applications, 2010: 305-376.

[229] Das P K, Meher S, Panda R, et al. A review of automated methods for the detection of sickle cell disease[J]. IEEE reviews in biomedical engineering, 2019, 13: 309-324.

[230] Amaral A, Ramalho - Santos J. Assessment of mitochondrial potential: implications for the correct monitoring of human sperm function[J]. International journal of andrology, 2010, 33(1): e180-e186.

[231] Knowlton S M, Sadasivam M, Tasoglu S. Microfluidics for sperm research[J]. Trends in biotechnology, 2015, 33(4): 221-229.

[232] Cybulski J S, Clements J, Prakash M. Foldscope: origami-based paper microscope[J]. PloS one, 2014, 9(6): e98781.

[233] Ghosh K K, Burns L D, Cocker E D, et al. Miniaturized integration of a fluorescence microscope[J]. Nature methods, 2011, 8(10): 871-878.

[234] Shen H, Gao J. Portable deep learning singlet microscope[J]. Journal of Biophotonics, 2020, 13(6): e202000013.

[235] Nuñez I, Matute T, Herrera R, et al. Low cost and open source multi-fluorescence imaging system for teaching and research in biology and bioengineering[J]. PloS one, 2017, 12(11): e0187163.

[236] Lee M, Yaglidere O, Ozcan A. Field-portable reflection and transmission microscopy based on lensless holography[J]. Biomedical optics express, 2011, 2(9): 2721-2730.

[237] Greenbaum A, Akbari N, Feizi A, et al. Field-portable pixel super-resolution colour microscope[J]. PloS one, 2013, 8(9): e76475.

[238] Cacace T, Bianco V, Mandracchia B, et al. Compact off-axis holographic slide microscope: design guidelines[J]. Biomedical Optics Express, 2020, 11(5): 2511-2532.

[239] Lee S A, Yang C. A smartphone-based chip-scale microscope using ambient illumination[J]. Lab on a Chip, 2014, 14(16): 3056-3063.

[240] Dong S, Guo K, Nanda P, et al. FPscope: a field-portable high-resolution microscope using a cellphone lens[J]. Biomedical optics express, 2014, 5(10): 3305-3310.

[241] Jung D, Choi J H, Kim S, et al. Smartphone-based multi-contrast microscope using color-multiplexed illumination[J]. Scientific reports, 2017, 7(1): 7564.

[242] Diederich B, Wartmann R, Schadwinkel H, et al. Using machine-learning to optimize phase contrast in a low-cost cellphone microscope[J]. PloS one, 2018, 13(3): e0192937.

[243] Wu Y, Luo Y, Chaudhari G, et al. Bright-field holography: cross-modality deep learning enables snapshot 3D imaging with bright-field contrast using a single hologram[J]. Light: Science & Applications, 2019, 8(1): 25.

[244] Liu T, De Haan K, Rivenson Y, et al. Deep learning-based super-resolution in coherent imaging systems[J]. Scientific reports, 2019, 9(1): 3926.

[245] Rivenson Y, Liu T, Wei Z, et al. PhaseStain: the digital staining of label-free quantitative phase microscopy images using deep learning[J]. Light: Science & Applications, 2019, 8(1): 23.

[246] Li Y, Zheng R, Wu Y, et al. A low-cost, automated parasite diagnostic system via a portable, robotic microscope and deep learning[J]. Journal of biophotonics, 2019, 12(9): e201800410.

[247] Göröcs Z, Tamamitsu M, Bianco V, et al. A deep learning-enabled portable imaging flow cytometer for cost-effective, high-throughput, and label-free analysis of natural water samples[J]. Light: Science & Applications, 2018, 7(1): 66.

[248] Göröcs Z, Baum D, Song F, et al. Label-free detection of Giardia lamblia cysts using a deep learning-enabled portable imaging flow cytometer[J]. Lab on a Chip, 2020, 20(23): 4404-4412.

[249] Zhang Y, Ouyang M, Ray A, et al. Computational cytometer based on magnetically modulated coherent imaging and deep learning[J]. Light: Science & Applications, 2019, 8(1): 91.

[250] Wu Y, Ray A, Wei Q, et al. Deep learning enables high-throughput analysis of particle-aggregation-based biosensors imaged using holography[J]. Acs Photonics, 2018, 6(2): 294-301.

[251] O'Connor T, Anand A, Andemariam B, et al. Deep learning-based cell identification and disease diagnosis using spatio-temporal cellular dynamics in compact digital holographic microscopy[J]. Biomedical Optics Express, 2020, 11(8): 4491-4508.

[252] Ronneberger O, Fischer P, Brox T. U-net: Convolutional networks for biomedical image segmentation[C]//Medical image computing and computer-assisted intervention–MICCAI 2015: 18th international conference, Munich, Germany, October 5-9, 2015, proceedings, part III 18. Springer International Publishing, 2015: 234-241.

[253] Ljosa V, Sokolnicki K L, Carpenter A E. Annotated high-throughput microscopy image sets for validation[J]. Nature methods, 2012, 9(7): 637-637.

[254] Haase R, Royer L A, Steinbach P, et al. CLIJ: GPU-accelerated image processing for everyone[J]. Nature methods, 2020, 17(1): 5-6.

[255] Falk T, Mai D, Bensch R, et al. U-Net: deep learning for cell counting, detection, and morphometry[J]. Nature methods, 2019, 16(1): 67-70.

[256] Isensee F, Jaeger P F, Kohl S A A, et al. nnU-Net: a self-configuring method for deep learning-based biomedical image segmentation[J]. Nature methods, 2021, 18(2): 203-211.

[257] Zhou Y, Huang W, Dong P, et al. D-UNet: a dimension-fusion U shape network for chronic stroke lesion segmentation[J]. IEEE/ACM transactions on computational biology and bioinformatics, 2019, 18(3): 940-950.

[258] Xu Y K T, Chitsaz D, Brown R A, et al. Deep learning for high-throughput quantification of oligodendrocyte ensheathment at single-cell resolution[J]. Communications biology, 2019, 2(1): 116.

[259] Baheti B, Innani S, Gajre S, et al. Eff-unet: A novel architecture for semantic segmentation in unstructured environment[C]//Proceedings of the IEEE/CVF Conference on Computer Vision and Pattern Recognition Workshops. 2020: 358-359.

[260] Li X, Chen H, Qi X, et al. H-DenseUNet: hybrid densely connected UNet for liver and tumor segmentation from CT volumes[J]. IEEE transactions on medical imaging, 2018, 37(12): 2663-2674.

[261] Zhou Z, Siddiquee M M R, Tajbakhsh N, et al. Unet++: Redesigning skip connections to exploit multiscale features in image segmentation[J]. IEEE transactions on medical imaging, 2019, 39(6): 1856-1867.

[262] He K, Zhang X, Ren S, et al. Deep residual learning for image recognition[C]//Proceedings of the IEEE conference on computer vision and pattern recognition. 2016: 770-778.

[263] Otsu N. A threshold selection method from gray-level histograms[J]. Automatica, 1975, 11(285-296): 23-27.

[264] De Berg M. Computational geometry: algorithms and applications[M]. Springer Science & Business Media, 2000.

[265] Webb D J, Brown C M. Epi-fluorescence microscopy[J]. Cell Imaging Techniques: Methods and Protocols, 2013: 29-59.

[266] Schneckenburger H, Weber P, Wagner M, et al. Light exposure and cell viability in fluorescence microscopy[J]. Journal of microscopy, 2012, 245(3): 311-318.

[267] Icha J, Weber M, Waters J C, et al. Phototoxicity in live fluorescence microscopy, and how to avoid it[J]. BioEssays, 2017, 39(8): 1700003.

[268] Gustafsson M G L, Shao L, Carlton P M, et al. Three-dimensional resolution doubling in wide-field fluorescence microscopy by structured illumination[J]. Biophysical journal, 2008, 94(12): 4957-4970.

[269] Agard D A, Hiraoka Y, Shaw P, et al. Fluorescence microscopy in three dimensions[J]. Methods in cell biology, 1989, 30: 353-377.

[270] Amos W B, White J G. How the confocal laser scanning microscope entered biological research[J]. Biology of the Cell, 2003, 95(6): 335-342.

[271] Carlsson K, Danielsson P E, Lenz R, et al. Three-dimensional microscopy using a confocal laser scanning microscope[J]. Optics letters, 1985, 10(2): 53-55.

[272] Bayguinov P O, Oakley D M, Shih C C, et al. Modern laser scanning confocal microscopy[J]. Current protocols in cytometry, 2018, 85(1): e39.

[273] Dusch E, Dorval T, Vincent N, et al. Three-dimensional point spread function model for line-scanning confocal microscope with high-aperture objective[J]. Journal of microscopy, 2007, 228(2): 132-138.

[274] Gareau D S, Krueger J G, Hawkes J E, et al. Line scanning, stage scanning confocal microscope (LSSSCM)[J]. Biomedical Optics Express, 2017, 8(8): 3807-3815.

[275] So P T C, Dong C Y, Masters B R, et al. Two-photon excitation fluorescence microscopy[J]. Annual review of biomedical engineering, 2000, 2(1): 399-429.

[276] Helmchen F, Denk W. Deep tissue two-photon microscopy[J]. Nature methods, 2005, 2(12): 932-940.

[277] Moreaux L, Sandre O, Blanchard-Desce M, et al. Membrane imaging by simultaneous second-harmonic generation and two-photon microscopy[J]. Optics Letters, 2000, 25(5): 320-322.

[278] Vettenburg T, Dalgarno H I C, Nylk J, et al. Light-sheet microscopy using an Airy beam[J]. Nature methods, 2014, 11(5): 541-544.

[279] Jemielita M, Taormina M J, DeLaurier A, et al. Comparing phototoxicity during the development of a zebrafish craniofacial bone using confocal and light sheet fluorescence microscopy techniques[J]. Journal of biophotonics, 2013, 6(11-12): 920-928.

[280] Xiong B, Han X, Wu J, et al. Improving axial resolution of Bessel beam light-sheet fluorescence microscopy by photobleaching imprinting[J]. Optics Express, 2020, 28(7): 9464-9476.

[281] Chen B C, Legant W R, Wang K, et al. Lattice light-sheet microscopy: imaging molecules to embryos at high spatiotemporal resolution[J]. Science, 2014, 346(6208): 1257998.

[282] Gustafsson M G L. Surpassing the lateral resolution limit by a factor of two using structured illumination microscopy[J]. Journal of microscopy, 2000, 198(2): 82-87.

[283] York A G, Parekh S H, Nogare D D, et al. Resolution doubling in live, multicellular organisms via multifocal structured illumination microscopy[J]. Nature methods, 2012, 9(7): 749-754.

[284] Dan D, Lei M, Yao B, et al. DMD-based LED-illumination super-resolution and optical sectioning microscopy[J]. Scientific reports, 2013, 3(1): 1116.

[285] Ventalon C, Mertz J. Dynamic speckle illumination microscopy with translated versus randomized speckle patterns[J]. Optics express, 2006, 14(16): 7198-7209.

[286] Lim D, Ford T N, Chu K K, et al. Optically sectioned in vivo imaging with speckle illumination HiLo microscopy[J]. Journal of biomedical optics, 2011, 16(1): 016014-016014-8.

[287] Shi R, Kong L. Evaluating structured-illumination patterns in optimizing optical-sectioning of HiLo microscopy[J]. Journal of Physics D: Applied Physics, 2021, 54(41): 414001.

[288] Chai C, Chen C, Liu X, et al. Deep learning based one-shot optically-sectioned structured illumination microscopy for surface measurement[J]. Optics Express, 2021, 29(3): 4010-4021.

[289] Ford T N, Lim D, Mertz J. Fast optically sectioned fluorescence HiLo endomicroscopy[J]. Journal of biomedical optics, 2012, 17(2): 021105-021105.

[290] Choi H, Wadduwage D N, Tu T Y, et al. Three-dimensional image cytometer based on widefield structured light microscopy and high-speed remote depth scanning[J]. Cytometry Part A, 2015, 87(1): 49-60.

[291] Lauterbach M A, Ronzitti E, Sternberg J R, et al. Fast calcium imaging with optical sectioning via HiLo microscopy[J]. PloS one, 2015, 10(12): e0143681.

[292] Shi R, Jin C, Xie H, et al. Multi-plane, wide-field fluorescent microscopy for biodynamic imaging in vivo[J]. Biomedical Optics Express, 2019, 10(12): 6625-6635.

[293] Michaelson J, Choi H, So P, et al. Depth-resolved cellular microrheology using HiLo microscopy[J]. Biomedical Optics Express, 2012, 3(6): 1241-1255.

[294] Zhou X, Bedggood P, Metha A. Improving high resolution retinal image quality using speckle illumination HiLo imaging[J]. Biomedical Optics Express, 2014, 5(8): 2563-2579.

[295] Santos S, Chu K K, Lim D, et al. Optically sectioned fluorescence endomicroscopy with hybrid-illumination imaging through a flexible fiber bundle[J]. Journal of biomedical optics, 2009, 14(3): 030502-030502-3.

[296] Mertz J, Kim J. Scanning light-sheet microscopy in the whole mouse brain with HiLo background rejection[J]. Journal of biomedical optics, 2010, 15(1): 016027-016027-7.

[297] Bhattacharya D, Singh V R, Zhi C, et al. Three dimensional HiLo-based structured illumination for a digital scanned laser sheet microscopy (DSLM) in thick tissue imaging[J]. Optics Express, 2012, 20(25): 27337-27347.

[298] Chung S, Breshears L E, Gonzales A, et al. Norovirus detection in water samples at the level of single virus copies per microliter using a smartphone-based fluorescence microscope[J]. Nature Protocols, 2021, 16(3): 1452-1475.

[299] Cai F, Wang T, Lu W, et al. High-resolution mobile bio-microscope with smartphone telephoto camera lens[J]. Optik, 2020, 207: 164449.

[300] Vietz C, Schütte M L, Wei Q, et al. Benchmarking smartphone fluorescence-based microscopy with DNA origami nanobeads: reducing the gap toward single-molecule sensitivity[J]. ACS omega, 2019, 4(1): 637-642.

[301] Kim J, Go T, Lee S J. Volumetric monitoring of airborne particulate matter concentration using smartphone-based digital holographic microscopy and deep learning[J]. Journal of Hazardous Materials, 2021, 418: 126351.

[302] Stokseth P A. Properties of a defocused optical system[J]. JOSA, 1969, 59(10): 1314-1321.

[303] Greivenkamp J E. Field guide to geometrical optics[C]. Bellingham, WA: SPIE, 2004.

[304] Kim J Y, Lee C, Park K, et al. Fast optical-resolution photoacoustic microscopy using a 2-axis water-proofing MEMS scanner[J]. Scientific reports, 2015, 5(1): 7932.

[305] Mazzaferri J, Kunik D, Belisle J M, et al. Analyzing speckle contrast for HiLo microscopy optimization[J]. Optics express, 2011, 19(15): 14508-14517.

[306] Schniete J, Franssen A, Dempster J, et al. Fast optical sectioning for widefield fluorescence mesoscopy with the mesolens based on HiLo microscopy[J]. Scientific reports, 2018, 8(1): 16259.

[307] Zhang Y, Kang L, Lo C T K, et al. Rapid slide-free and non-destructive histological imaging using wide-field optical-sectioning microscopy[J]. Biomedical Optics Express, 2022, 13(5): 2782-2796.

[308] Kang S, Ryu I, Kim D, et al. High-speed three-dimensional surface profile measurement with the HiLo optical imaging technique[J]. Current Optics and Photonics, 2018, 2(6): 568-575.

[309] Hsiao H, Lin C Y, Vyas S, et al. Telecentric design for digital‐scanning‐based HiLo optical sectioning endomicroscopy with an electrically tunable lens[J]. Journal of Biophotonics, 2021, 14(2): e202000335.

[310] Philipp K, Smolarski A, Koukourakis N, et al. Volumetric HiLo microscopy employing an electrically tunable lens[J]. Optics express, 2016, 24(13): 15029-15041.

[311] Lin W, Wang D, Meng Y, et al. Multi-focus microscope with HiLo algorithm for fast 3-D fluorescent imaging[J]. PloS one, 2019, 14(9): e0222729.

[312] Qiao W, Jin R, Luo T, et al. Single-scan HiLo with line-illumination strategy for optical section imaging of thick tissues[J]. Biomedical Optics Express, 2021, 12(4): 2373-2383.

[313] Mertz J. Optical sectioning microscopy with planar or structured illumination[J]. Nature methods, 2011, 8(10): 811-819.

[314] Neil M A A, Juškaitis R, Wilson T. Method of obtaining optical sectioning by using structured light in a conventional microscope[J]. Optics letters, 1997, 22(24): 1905-1907.

[315] Hu Y, Liang D, Wang J, et al. Background-free wide-field fluorescence imaging using edge detection combined with HiLo[J]. Journal of Biophotonics, 2022, 15(8): e202200031.

[316] Karadaglić D, Wilson T. Image formation in structured illumination wide-field fluorescence microscopy[J]. Micron, 2008, 39(7): 808-818.

[317] Ventalon C, Mertz J. Quasi-confocal fluorescence sectioning with dynamic speckle illumination[J]. Optics letters, 2005, 30(24): 3350-3352.

[318] Shabani H, Doblas A, Saavedra G, et al. Improvement of two-dimensional structured illumination microscopy with an incoherent illumination pattern of tunable frequency[J]. Applied Optics, 2018, 57(7): B92-B101.

[319] Chang S I, Yoon J B. Shape-controlled, high fill-factor microlens arrays fabricated by a 3D diffuser lithography and plastic replication method[J]. Optics Express, 2004, 12(25): 6366-6371.

[320] Lim C S, Hong M H, Kumar A S, et al. Fabrication of concave micro lens array using laser patterning and isotropic etching[J]. International Journal of Machine Tools and Manufacture, 2006, 46(5): 552-558.

[321] Kuo W K, Lin S Y, Hsu S W, et al. Fabrication and investigation of the bionic curved visual microlens array films[J]. Optical Materials, 2017, 66: 630-639.

[322] Yuan W, Li L H, Lee W B, et al. Fabrication of microlens array and its application: a review[J]. Chinese Journal of Mechanical Engineering, 2018, 31(1): 1-9.

[323] Sohn I B, Choi H K, Noh Y C, et al. Laser assisted fabrication of micro-lens array and characterization of their beam shaping property[J]. Applied Surface Science, 2019, 479: 375-385.

[324] FitzGerrell A R, Dowski E R, Cathey W T. Defocus transfer function for circularly symmetric pupils[J]. Applied Optics, 1997, 36(23): 5796-5804.

[325] Hopkins H H. The frequency response of a defocused optical system[J]. Proceedings of the Royal Society of London. Series A. Mathematical and Physical Sciences, 1955, 231(1184): 91-103.

[326] York A G, Chandris P, Nogare D D, et al. Instant super-resolution imaging in live cells and embryos via analog image processing[J]. Nature methods, 2013, 10(11): 1122-1126.

Appendix

Journal publications

1. Jiao Z, Zang Z, Wang Q, et al. PAIM (πM): Portable AI-enhanced fluorescence microscope for real-time target detection[J]. Optics & Laser Technology, 2023, 163: 109356.
2. Jiao Z, Pan M, Yousaf K, et al. Smartphone-based Optical Sectioning (SOS) Microscopy with A Telecentric Design for Fluorescence Imaging[J]. arXiv preprint arXiv:2310.01928, 2023.
3. Jiao Z, Chen X, Li D D U. Optimizing microlens arrays for incoherent HiLo microscopy[J]. Results in Optics, 2024: 100622.
4. Zang Z, Xiao D, Wang Q, et al. Compact and robust deep learning architecture for fluorescence lifetime imaging and FPGA implementation[J]. Methods and Applications in Fluorescence, 2023, 11(2): 025002.

Conference submission

1. Zang Z, Xiao D, Wang Q, et al. Hardware inspired neural network for efficient time-resolved biomedical imaging[C]//2022 44th Annual International Conference of the IEEE Engineering in Medicine & Biology Society (EMBC). IEEE, 2022: 1883-1886.
2. Xiao D, Zang Z, Wang Q, et al. Smart wide-field fluorescence lifetime imaging system with CMOS single-photon avalanche diode arrays[C]//2022 44th Annual International Conference of the IEEE Engineering in Medicine & Biology Society (EMBC). IEEE, 2022: 1887-1890.

Supplementary information

List of PAIM components (Fixed cost for brightfield imaging and counting of RBCs):

Product	Item	Price	Supplier
White LED	LEDW7E	$1.4	Thorlabs
Aspheric condenser lens	ACL2520U-DG15	$17.19	Thorlabs
Biconcave lens	LD2746	$24.48	Thorlabs
AI unit (Cable included)	Jetson Nano	$110.65	Taobao, China
USB Webcam (Cable included)	ELP,4K, Sony-IMX317	$65.99	Taobao, China
LED socket	LEDMT1F	$52.41	Thorlabs
Translation stage	DT12	$73.89	Thorlabs
Angle bracket	DT12A	$38.5	Thorlabs
3D Print part		$12.63	Department of Mechanical Engineering

These items are fixed cost for PAIM (Brightfield imaging for RBCs imaging and count), total cost is $397.14. If users want to realize fluorescent imaging, the white LED can be substituted by other LED with specific wavelength. Also, corresponding optical filter can be inserted into the specific position of designed adapter (Fig. 3-6c).

Data for the PAIM

The data for the webcam lens testing and PAIM STL files can be downloaded in the

following link:

https://github.com/ZiaoJiao/PAIM

The training data set can be downloaded in the following link:

https://bbbc.broadinstitute.org/BBBC005

For the neural network code and software to run the RBCs counting and segmentation functionalities, we are securing multiple Chinese patents, necessitating confidentiality at this stage. In the future, our plan includes launching a commercial software package accessible through license purchase. However, we are open to disclosing select components of the code, encompassing the neural network architectures tailored for segmentation and counting tasks and the code for calculating IoU:

Code for segmentation neural network:

```
########################################
import torch
import torch.nn as nn


class double_conv(nn.Module):
    '''
    Double Convolution layer with both 2 BN and Activation Layer in between
    Conv2d==>BN==>Activation==>Conv2d==>BN==>Activation
    '''
    def __init__(self, in_channel, out_channel):
        super(double_conv, self).__init__()
        self.conv = nn.Sequential(
            nn.Conv2d(in_channel, out_channel, 3, padding=1),
```

```
                nn.ReLU(inplace=True),
                nn.BatchNorm2d(out_channel),
                nn.Conv2d(out_channel, out_channel, 3, padding=1),
                nn.ReLU(inplace=True),
                nn.BatchNorm2d(out_channel)
            )
        def forward(self, x):
            x = self.conv(x)
            return x

class down_conv(nn.Module):
    '''
    A maxpool layer followed by a Double Convolution.
    MaxPool2d==>double_conv.
    '''
    def __init__(self, in_channel, out_channel):
        super(down_conv, self).__init__()
        self.down = nn.Sequential(
            nn.MaxPool2d(2),
            double_conv(in_channel, out_channel)
        )
    def forward(self, x):
        x = self.down(x)
        return x

class up_sample(nn.Module):
    def __init__(self, in_channel, out_channel):
        super(up_sample, self).__init__()
```

```
        self.up = nn.Upsample(scale_factor=2, mode='bilinear', align_corners=True)
        self.double_conv = double_conv(in_channel, out_channel)

    def forward(self, x1, x2):
            x1 = self.up(x1)
            x = torch.cat([x1, x2], dim=1)
            x = self.double_conv(x)
            return x

class UNet_density(nn.Module):
    '''Main Unet Model'''
    def __init__(self, in_channel, out_channel):
        super(UNet_density, self).__init__()
        ## DownSampling Block
        self.down_block1 = double_conv(in_channel, 16)
        self.down_block2 = down_conv(16, 32)
        self.down_block3 = down_conv(32, 64)
        self.down_block4 = down_conv(64, 128)
        self.down_block5 = down_conv(128, 256)
        self.down_block6 = down_conv(256, 512)

        ## UpSampling Block
        self.up_block1 = up_sample(1024+512, 512)
        self.up_block2 = up_sample(512+256, 256)
        self.up_block3 = up_sample(256+128, 128)
        self.up_block4 = up_sample(128+64, 64)
        self.up_block5 = up_sample(64+32, 32)
        self.up_block6 = up_sample(32+16, 16)
```

```
    def forward(self, x):
        #Down
        x1 = self.down_block1(x)
        x2 = self.down_block2(x1)
        x3 = self.down_block3(x2)
        x4 = self.down_block4(x3)
        x5 = self.down_block5(x4)
        x6 = self.down_block6(x5)

        #Up
        x8 = self.up_block1(x7, x6)
        x9 = self.up_block2(x8, x5)
        x10 = self.up_block3(x9, x4)
        x11 = self.up_block4(x10, x3)
        x12 = self.up_block5(x11, x2)
        x13 = self.up_block6(x12, x1)
        x14 = self.up_block7(x13)

        return out
########################################
```

Code for counting neural network:

```
########################################
import torch
```

```
import torch.nn as nn
from torch.autograd import Variable
import math


cfg = {
    'VGG11': [64, 'M', 128, 'M', 256, 256, 'M', 512, 512, 'M', 512, 512, 'M'],
    'VGG13': [64, 64, 'M', 128, 128, 'M', 256, 256, 'M', 512, 512, 'M', 512, 512, 'M'],
    'VGG16': [64, 64, 'M', 128, 128, 'M', 256, 256, 256, 'M', 512, 512, 512, 'M', 512,
512, 512, 'M'],
    'VGG19': [64, 64, 'M', 128, 128, 'M', 256, 256, 256, 256, 'M', 512, 512, 512, 512,
'M', 512, 512, 512, 512, 'M'],
}

img_size = (256, 256)

class VGG(nn.Module):
    def __init__(self, vgg_name):
        super(VGG, self).__init__()

        self.input_image = nn.Sequential(
            nn.Conv2d(1, 16, kernel_size=3, stride = 1, padding=1),
            nn.BatchNorm2d(16),
            nn.ReLU(inplace=True),
            nn.Conv2d(16, 32, kernel_size=3, stride = 1, padding=1),
            nn.BatchNorm2d(32),
            nn.ReLU(inplace=True)
```

```
        )

        self.input_mask = nn.Sequential(
            nn.Conv2d(1, 16, kernel_size=3, stride = 1, padding=1),
            nn.BatchNorm2d(16),
            nn.ReLU(inplace=True),
            nn.Conv2d(16, 32, kernel_size=3, stride = 1, padding=1),
            nn.BatchNorm2d(32),
            nn.ReLU(inplace=True)
        )

        self.convs = self._make_layers(cfg[vgg_name])

        in_dim = 512 * math.floor(img_size[0]/2**5)*math.floor(img_size[1]/2**5)
        self.dense = nn.Sequential(
            nn.Linear(in_dim, 1024),
            nn.BatchNorm1d(1024),
            nn.LeakyReLU(0.1),
            nn.Linear(1024, 512),
            nn.BatchNorm1d(512),
            nn.LeakyReLU(0.1),
            nn.Linear(512, 1),
            nn.ReLU()
        )

    def _make_layers(self, cfg):
        layers = []
        in_channels = 64
```

```
        flag = 0
        for x in cfg:
            if x == 'M':
                layers += [nn.MaxPool2d(kernel_size=2, stride=2)] # h=h/2
            else:
                layers += [nn.Conv2d(in_channels, x, kernel_size=3, stride = 1,
padding=1),
                           nn.BatchNorm2d(x),
                           nn.ReLU(inplace=True)]
                in_channels = x
                flag += 1

        return nn.Sequential(*layers)

    def forward(self, x1,x2):
        '''
        x1: density map
        x2: mask
        '''
        out1 = self.input_image(x1)
        out2 = self.input_mask(x2)
        out = torch.cat((out1, out2), dim=1)

        out = self.convs(out)
        out = out.view(out.size(0), -1)
        out = self.dense(out)
        return out
########################################
```

Code for IoU calculation:

```
########################################
ret, mask_opencv = cv2.threshold(test_image, 0, 255, cv2.THRESH_BINARY)

intersection_opencv = np.logical_and(test_images_mask_annots, mask_opencv)
union = np.logical_or(test_images_mask_annots, mask_opencv)
iou_score_opencv = np.sum(intersection_opencv) / np.sum(union)
print('IoU_opencv is %s' % iou_score_opencv)

intersection_unet = np.logical_and(test_images_mask_annots, test_recon_mask)
union = np.logical_or(test_images_mask_annots, test_recon_mask)
iou_score_unet = np.sum(intersection_unet) / np.sum(union)
print('IoU_unet is %s' % iou_score_unet)
########################################
```

Protocol for setup your own PAIM

1. Printing the 3D Parts:

Utilize a 3D printer to fabricate the necessary components for the microscope. Ensure you have the correct 3D models and that your printer settings are optimized for the material and precision required.

2. Assemble All Components:

Carefully assemble the 3D-printed parts along with any additional hardware required for the microscope. Follow any assembly guides or schematics provided with the 3D models to ensure correct assembly.

3. Configure the Operating System and Software Environment on Jetson Nano

To set up your Jetson Nano, you need to configure the operating system and the necessary software environment. Visit the official Jetson Nano starting guide (https://developer.nvidia.com/embedded/learn/get-started-jetson-nano-devkit) for detailed instructions on how to do this.

4. Connecting Peripherals to Jetson Nano:

Webcam: Connect your webcam to one of the USB ports on the Jetson Nano to enable video input.

Keyboard and Mouse: Plug in a keyboard and mouse into the available USB ports for navigation and input.

Screen: Attach a screen to the HDMI port on the Jetson Nano for display purposes.

5. Configuring the Python Coding Environment on Jetson Nano

Configuring a robust Python coding environment on your Jetson Nano is crucial for efficiently developing and running your applications. Follow these steps to set up a conducive Python workspace:

- Update and Upgrade Jetson Nano

Before installing any new software, it's good practice to update and upgrade your system packages to ensure compatibility and security.

code here

```
sudo apt-get update
sudo apt-get upgrade
```

code end

- Install Python

Jetson Nano usually comes with Python pre-installed. Verify the installation and version using:

code here

```
python3 --version
```

code end

If Python is not installed or you need a different version, use the following command to install it:

code here

sudo apt-get install python3

code end

- Setting up pip

Pip is a package installer for Python. You can install it with:

code here

sudo apt-get install python3-pip

code end

Once installed, you can use pip to install Python packages:

code here

pip3 install <package-name>

code end

- Virtual Environments

It's a best practice to use virtual environments for your Python projects to manage dependencies efficiently.

Install the virtual environment package:

code here

sudo apt-get install python3-venv

code end

Create a new virtual environment:

code here

python3 -m venv myenv

code end

Activate the virtual environment:

code here

source myenv/bin/activate

code end

- Install development tools

Install development tools like IDEs or text editors. Popular choices include Visual Studio Code, PyCharm, or simpler editors like Nano or Vim. For Visual Studio Code, you can follow the official installation guide provided by Microsoft: https://code.visualstudio.com/docs/setup/linux

- Jupyter Notebook/Lab

For interactive coding sessions, Jupyter Notebook or Lab is an excellent tool. Install it within your virtual environment:

code here

pip install jupyterlab

code end

To run Jupyter Lab:

code here

jupyter lab

code end

- Additional Libraries and Frameworks

Depending on your project, you may need additional libraries like NumPy, Pandas, or frameworks like TensorFlow or PyTorch. Install them using pip within your virtual environment:

code here

pip install numpy pandas tensorflow pytorch

code end

- Test Your Setup

Once everything is installed, test your setup by running a simple Python script or a Jupyter notebook to ensure all components are working correctly. For more detailed instructions and troubleshooting, refer to the official NVIDIA documentation for Jetson

Nano (https://developer.nvidia.com/embedded/learn/get-started-jetson-nano-devkit).

Code source and plugin for SOS

The HiLo plugin used for SOS can be found in the following link:
https://sites.bu.edu/biomicroscopy/resources/4/

Also, a Matlab tutorial can be found in the following link:
https://github.com/SWC-Advanced-Microscopy/HiLo_SIM

Mechanical design parts for SOS

The mechanical design parts for SOS can be downloaded from the following link:
https://github.com/ZiaoJiao/SOS

Code for Chapter 5 simulation

The code used for simulation in chapter 5 can be downloaded from the following link:
https://github.com/ZiaoJiao/MLA_HiLo